Conjugated Metal–Organic Macrocycles as Solution-Processable Semiconductors

Leo Porter-Zasada

A dissertation

submitted in partial fulfillment of the

requirements for the degree of

Doctor of Philosophy

University of Washington

2024

Reading Committee:

Dianne J. Xiao, Chair

Brandi M. Cossairt

Matthew Golder

Program Authorized to Offer Degree:

Chemistry

University of Washington

Abstract

Conjugated Metal–Organic Macrocycles as Solution-Processable Semiconductors

Leo Porter-Zasada

Chair of the Supervisory Committee:

Dianne J. Xiao

Department of Chemistry

There has been recent widespread interest in porous self-assembling crystalline materials for a wide variety of applications, but a striking lack of solution processability can greatly hinder attempts to scale these materials commercially. Tremendous research progress has been made with two-dimensional metal–organic frameworks (2D MOFs) which are desirable for their crystallinity, porosity, and conductivity which opens the door to applications in electrocatalysis, chemical sensing, and energy storage and conversion. MOFs are extended materials and typically lack solution processability meaning they cannot be dissolved in organic solvents without destroying the framework overall. This problem has generated renewed interest in macrocycles and cages which are dimensionally reduced molecular units that can self-assemble into unique materials, demonstrating similar or improved properties. This work describes the synthesis of a new class of conjugated metal–organic macrocycles with remarkable tunability, including access

to solution-processable materials, device fabrication, and studies on crystal growth and morphology.

Chapter 1 provides an overview of shape-persistent macrocycles and progress into their accessible morphologies and applications. Emphasis is placed on their ability to self-assemble into supramolecular arrays, and the influence of hydrogen-bonding on self-assembly and crystallinity. Metal–organic macrocycles based on Pd and Pt are discussed first, followed by organic macrocycles and varying applications depending on what functional groups comprise the ring.

Chapter 2 discusses the synthesis and characterization of new Cu-based metal–organic macrocycles which mimic 2D MOF pores but offer enhanced solution processability and ease of field-effect transistor (FET) device fabrication. The strategy involves truncating HHTP (2,3,6,7,10,11-hexahydroxytriphenylene), a common tritopic MOF ligand to a ditopic alternative H_4TOTP (TOTP^{n-} = 2,3,5,6-tetraoxidotriphenylene) and coordinating to square planar copper centers to make a family of macrocycles with tunable carbon side chains. Extending chains to eighteen carbons enables solubility in common organic solvents and fabrication of FETs.

Chapter 3 details the expansion of the side chain library with a focus on gaining deeper insight into the crystal packing and crystal morphology. Side chains are carefully chosen to increase steric bulk, polarity, or hydrogen-bonding. Steric bulk is found to disrupt the π–π stacking, polar side-chains can be installed and maintain hexagonal packing, and hydrogen-bonding improves order, dramatically increasing crystallite size which allows characterization by optical microscopy and scanning electron microscopy (SEM) for the first time.

Appendix A includes an introduction to field-effect transistor architecture and measurement. Preliminary atomic force microscopy results are shown, where slower drying

methods from higher boiling solvents provide greater alignment across larger distances. This may be an avenue to improve charge mobility in the reported metal–organic macrocycles.

Table of Contents

List of Figures

List of Tables

Acknowledgements

Thank you to the entire Xiao Group and Professor Dianne Xiao, and I particularly want to thank Jack Geary for being there from the very beginning. Joining a group as the first student is never easy and I'm glad he was there with me.

The loneliness that has underscored my graduate school experience has been broken up by a few important people. Rhys Green has been my friend since we were about nine years old and has remained a steadfast presence throughout my time here. Whether he was in LA or New Zealand, he has always been available for a Discord chat, reassuring words, and often some video games. Sometimes when we talk about life, we actually reach conclusions, and I've learned how valuable and rare that is. He is a brilliant listener, and a warm and caring person, and he deserves a thank you for being there through many difficult times.

Ben Mitchell became my best friend in Seattle during the pandemic on our long, socially distanced walks around Ballard. We have had countless discussions about life, school, working, and every aspect of navigating our problems. I am lucky to have such a friend in my life.

My family has been very supportive throughout this whole experience, and I thank them for everything they have given me. Thank you to my siblings for their love and care, my brothers- and sisters-in-law for their interest in what I do and treating me like a little brother, and my niece and recently nephew for being adorable and loving.

Thank you to my parents for supporting me through this entire experience. All the phone calls and family Zooms have lifted my spirits. My dad has helped me with writing projects, and both have helped with my presentation skills. Most of all I have seen them both grow a great deal in the last five years, and I really appreciate the effort that went into that. They also put so much work into caring for Grandmère as she aged and I'm thankful for that too.

Thank you also to my grandmother (Grandmère as we called her) for being such an all-around loving and warm person. She could keep a secret, she listened and cared, and she was proud of everything I did, big and small. She passed away last year, but I don't want to say she would have been so proud because she didn't need to see me finish to be proud, she was proud all along.

This would be incomplete without thank-you's to music and to my therapist. Learning to play music became an integral part of my experience during the pandemic and has brought comfort. I've also listened to more music and podcasts than could possibly be counted and both became necessary tools for survival. My therapist has taught me about being present and engaged with all things as they happen and opened me to feeling more bad and more good.

Dedication

To the people who supported me even when I didn't know how to ask

Chapter 1: An Introduction to Shape-Persistent Macrocycles and Their Supramolecular Assembly

1.1 Introduction

Two dimensional metal–organic frameworks (2D MOFs) have garnered significant interest due to their unique combination of porosity, tunability and impressive conductivities,[1–7] but suffer from a lack of solution processability, ultimately limiting device fabrication and scaleup. With possible applications in electrocatalysis,[8–12] chemical sensing,[13–18] and energy storage and conversion,[19–22] harnessing 2D MOF conductivity requires good electrical contacts at the interface of material and device, and electrical continuity throughout the material which can be difficult to achieve across crystallite grain boundaries in an extended 2D material. While 2D MOFs have achieved surface areas around ~600 m^2 g^{-1},[23] much of this area is inaccessible to any analytes beyond small gas molecules. Attempts have been made to grow ordered thins films which minimize grain boundaries,[24–27] but these processes are arduous and unscalable.

In contrast, supramolecular assemblies of shape-persistent macrocycles may offer greater solution processability thanks to their lower initial dimensionality and side-chains tuned to optimize solvent interactions.[28–31] 2D MOF-based chemiresistive sensors generally only react at surface sites without fully utilizing the high internal surface area.[32] Metal–organic macrocycles have a greater surface-to-volume ratio allowing better exposure of active sites, and greater tunability of the surface chemistry through side-chain modification. Metal–organic macrocycles are an exciting but underexplored frontier which can push the limits of our understanding of synthesis, self-assembly, and charge transport. This introduction provides an overview of the structure, design of side chains, and applications of some of the metal–organic, and organic macrocycles synthesized so far.

1.2 Pd- and Pt-based metal–organic macrocycles

Most metal–organic macrocycles reported are based on Pd or Pt, but macrocycles based on first-row transition metals are rare. Stang *et. al.*, demonstrated the first example of hexagonal metal–organic macrocycles by square-planar coordination about the metal.[33] Two Pt complexes with 120° and 180° chelation angles were used where the vertices of the hexagon are made with the bent 120° unit. This initial example demonstrates the enthalpic preference for the formation of macrocycles over oligomerization. Macrocycles did not crystallize or precipitate, instead remaining dissolved in the dichloromethane reaction solvent and characterized by NMR spectroscopy and were therefore solution-processable.

Pt_4 macrocycles were found to self-assemble into columnar stacks by Frischmann *et. al.* by using chelating asymmetric aromatic ligands to promote π–π stacking and connect four Pt centers into a square.[34] The authors employed a "head-to-tail" approach in ligand design, with a monodentate attachment on the tail and a tridentate attachment at the head which lead to directed self-assembly. These Pt_4 macrocycles demonstrate liquid crystalline behavior through the installation of greasy 2-hexyldecyl chains to the periphery of each ligand and high quality nematic mesophases were obtained in chlorobenzene. This first report of liquid crystallinity for Pt-pyridyl macrocycles also shows the importance of organic peripheral chains in adding functionality and can provide an extremely versatile avenue for targeted materials design.

In more recent work by Hu *et. al.*, this concept of platinum-based liquid crystalline macrocycles was extended to rhomboidal and hexagonal macrocycles which were used for holographic storage of colored images.[35] These were constructed using a 60° and 120° diplatinum(II) acceptor respectively, each coordinated to an identical curved aromatic chelating ligand which when paired with the alternate geometries about the Pt complex give rise to two unique macrocyclic geometries. These macrocycles also feature long and complex peripheral

chains, consisting of a polyethylene glycol (PEG) unit, ester, phenyl ring, additional PEG, phenyl rings, and finally hydrocarbon tails. The length and complexity of these peripheral chains shows the range of possibilities available but may also caution that proper peripheral chain choice can be difficult to achieve the desired properties. Liquid crystallinity was confirmed by polarized optical microscopy (POM), wide-angle X-ray diffraction (1D WAXD), and differential scanning calorimetry (DSC) which showed a glass transition temperature at 1.9 °C for the rhomboidal macrocycle due to the high molecular weight. The rhomboidal macrocycle demonstrated superior holographic performance and can be mixed with a polymer which imparts constructive interference, while the macrocycle imparts destructive interference during exposure to interference patterns of a 460 nm laser. These patterns may be used for anticounterfeiting applications because they are generally not replicable by laser scanning or copying.

There are a number of Pt and Pd based bowls, cages, triangles, rectangles, and rhomboids[36,37] which have been explored primarily for biomedical and anti-cancer applications, with other hexagons reported for artificial light harvesting.[38] This range of macrocyclic structures is exciting, but applications are limited by the high cost of noble metals which inhibit manufacturing at scale. Examples of non-noble metals as the building unit for metal–organic macrocycles are rare, but in principle they can share the square planar coordination environment about the metal and provide a similar wealth of opportunities.

1.3 Organic shape-persistent macrocycles

Purely organic macrocycles also eliminate the need for noble metals and can self-assemble into nanotubes with applications in ion transport, energy storage, and biologically relevant intramembrane transport.[28–31] Despite more modern interest compared to noble metal based macrocycles, organic systems can be difficult and costly to assemble, often necessitating harsh reaction conditions to form the irreversible covalent bonds into the appropriate topology and to

avoid excessive oligomerization or polymerization.[39] Reversible self-assembly is attractive for building in additional functionality through dimensional control.

1.4 Macrocycles for separations

Examples of molecular sieves derived from macrocycles and cages are numerous[40] and in one particularly compelling example Jiang *et. al.* were able to align macrocycles into an ultrathin nanofilm and demonstrated selectivity for methanol in separations and excellent enrichment of cannabidiol oil compared to commercial membranes.[41] Cyclodextrin rings were functionalized with reactive amine groups whose hydrogen-bonding assisted in highly ordered self-assembly of films. A major pitfall for size-selective sieving is misaligned macrocycles or holes and gaps preventing size selectivity. These functionalized cyclodextrin rings give accurate molecular sieving results because of their supramolecular assembly from macrocycles, into nanotubes, and finally into oriented thin films which largely eliminate such defects. These films are remarkably only a few nanometers thick but survived deformation with a pinning rod and could be used in high-value pharmaceutical separations.

The interior of nanotubes composed of organic macrocycles can be tuned as shown by Itoh et. al. who installed inward facing C–F bonds which exhibit polar hydrophobicity and cause increased H_2O flow through the pore channels.[42] These macrocycles were synthesized by microwave amide condensation of a derivative of 3,5-diamino-4-fluorobenzamide and 2,4-difluoroterphthalic acid together with pentaluorophneyl diphenylphosphinate (FDPP) to form rings of four different pore diameters 0.90–1.90 nm wide depending on the microwave conditions. Strong hydrogen-bonding and π–π interactions stacks macrocycles into nanochannels which allow for ultrafast flow of water clusters as studied by DFT models and molecular dynamics simulations. Additionally, these fluorous nanorings reject Cl^- ions and have excellent salt reflectance due to the strong electrostatic barrier from the fluorinated interior and may have applications in desalination.

In this report, synthetic control at the molecular level imparts new functionality after supramolecular self-assembly.

Shape-persistent oligoamide macrocycles featuring strong hydrogen-bonding and π–π stacking have been reported by Gong and coworkers to transport Na^+ ions across a lipid bilayer.[43–45] The authors were able to measure transmembrane conductance by concentration-dependent peak broadening in ^{23}Na NMR experiments. Based on the voltage across a membrane separating two KCl solutions in the presence of macrocycle, open and closed states were observed likely due to assembly and disassembly of macrocycles opening and closing channels across the membrane. These systems are uniquely capable of this change in dimensionality between molecules in solution, and a material transporting ions across larger distances. The same group extended enforced stacking based on hydrogen-bonding and π–π interactions by synthesizing planar arylene ethynylene macrocycles by Pd-catalyzed Sonagashira coupling of trimeric precursors.[46] A series of side-chains all containing an amide and ester group and varying length alkyl tails were attached to enforce six-fold hydrogen-bonding around the perimeter of the aromatic core. Atomic force microscopy (AFM) was used to show macrocycle alignment into ordered nanotubes composing nanofilaments on the micron scale. Formed channels selectively transported protons over chloride ions, and the authors found a minimum of nine molecules must assemble to form a functional channel.

1.5 Electrical conductivity in macrocycles

Compared to ion transport or molecular sieving, there are relatively fewer conductive organic macrocycles reported, likely due to the difficulty in installing reliable mechanisms for charge transport in the absence of metal ions. A clever approach was taken by Louie *et. al.* through para-linked anilines, similar to the conductive polymer polyaniline (PANI), but formed into oligoanilines as a hexagon rather than a linear chain.[47] Conductivity is responsive to pH, where conversion to the emeraldine salt in the presence of trifluoroacetic acid (TFA) turns on the conductivity, similar to PANI. Two-contact conductivity measurements of the protonated state determined the bulk conductivity to be 1.7×10^{-5} S cm^{-1}. Single crystal conductivity measurements also showed an impressive 7.5×10^{-2} S cm^{-1}. Zn ions also were found to diffuse through the pores and increase the conductivity in the bulk by electrochemical impedance spectroscopy. The switchable conductivity based on proton doping is an exciting feature in these para-linked aniline macrocycles, which are attractive for many electrochemical applications including chemical sensing.

Nuckolls and coworkers have reported other electrically conductive macrocycles including three examples based on perylenediimide (PDI) which vary by the number of PDI and connecting groups for macrocyclization.[48–50] Macrocycles were explored for organic photovoltaics (OPVs) and organic field effect transistors (OFETs). When grown as a film, these PDI-based macrocycles demonstrated electron mobilities from 10^{-3}–10^{-2} cm^2 V^{-1} s^{-1}. One of these PDI-based macrocycles so-called $(\text{PDI-BBr}_4)_3$ even showed a modest BET surface area of 20 m^2/g, highlighting some accessible pore volume. The $(\text{PDI-Ph-B-Ph})_2$ and $(\text{PDI-BP})_4$ macrocycles were also explored for optoelectronic applications in OPV devices where the devices outperformed acyclic controls in photocurrent generation as a solar cell.[51]

Carbazolylene-ethynylene shape-persistent macrocycles were used as the building block for 2D covalent organic frameworks (COFs) in work from Huang *et. al.* who found a four-point probe conductivity of 7.8×10^{-4} S cm^{-1} after I_2 doping.[52] Conductivity is much lower, around 10^{-10} S cm^{-1} in the absence of I_2, likely as a result of a lack of charge carrier mobility, density, and significant grain boundaries for 2D organic materials. Macrocycles were functionalized as a tetraacetal via peripheral chains which were synthesized into COFs by polycondensation with hydrazine or benzidine, yielding COFs with a BET surface area as high as 983 m^2 g^{-1}. This process was done at 120 °C for three days which is energy intensive but shows another approach to assemble macrocycles into extended structures via covalent bonds rather than H-bonding or π–π stacking.

1.6 Chemical reactions inside macrocycle pores

The self-assembly of macrocycles into nanotubes with an internal cavity also provides an opportunity for tailored microenvironments to host chemical reactions, attempting to mimic enzymatic environments found in nature. Yang *et. al.* used bisurea macrocycles to host stereoselective photodimerization of 2-cyclohexenone.[53] The confined environment of the relatively small pore from the chosen macrocycle's assembly selectively yields the head-to-tail photodimer. Selectivity for the transketone was 96% with the host and only 35% in its absence, whereas hosting the same reaction in zeolites favors the *cis*- product with 82% selectivity. The structure of the host did not change by PXRD after the vapor loading of the guest molecule and subsequent photoreaction, and the product was easily recovered as the host remained crystalline and heterogeneous with the solution, allowing recyclability.

Oxidative polymerization was performed inside the pores of self-assembled triphenylamine *bis*-urea macrocycles by Islam *et. al.* as a means of hosting and modulating the reaction.[54] The polymers polypyrrole (PPy) and poly(ethylenedioxythiophene) (PEDOT) were

formed inside the pore using iodine as an oxidizing agent, with single-crystal X-ray diffraction studies confirming the incorporation of monomers into the nanopores. Oxidative polymerizations were performed at elevated temperatures (90 °C) which did result in crystal fractures forming along the needle axis. Macrocycles are fully soluble in DMSO which enabled ease of polymer extraction and reuse of macrocycles as a host. The polymers retained bulk organization once extracted, with PXRD peaks at a d-spacing which matched the host, and SAXS showed the polymers also retained host morphology. The polymers could also be left inside the host cavity, rendering the system conductive. The solution processability of these macrocycles was key to their use and recyclability for hosting chemical reactions.

1.7 Macrocycles structurally related to COFs

Macrocycles structurally related to COF-5 were synthesized by Chavez *et. al*. by truncating the tritopic hexahydroxytriphenylene (HHTP) linker to a ditopic linker they called dihexyloxy tetrahydroxytriphenylene (C6THTP).[55] This linker was paired with a variety of boronic acids to make a series of four hexagonal macrocycles which self-assemble into nanotubes with a π–π stacking distance of 3.37 Å. These macrocycles stack similarly to COF-5, but with much more dynamic processability as studied by AFM. One macrocycle with included hexa(ethylene glycol) monomethyl ether chains (HxgTHTP) showed increased dispersibility in a variety of organic solvents such as acetone, THF, or $CHCl_3$ once again showing the versatility of installing peripheral side-chains to alter solvent interactions. Macrocycles assembled with 1,4-phenylenebis(boronic acid) (PBBA) were shown to assemble into nanotubes several hundred nanometers long. These nanotubes disperse back into macrocycles and smaller aggregates after sonication, then reassemble into nanotubes by AFM. This process is likely driven by the π–π interactions which are strong enough to encourage self-assembly, but weak enough to be disturbed by sonication, creating a dynamic and malleable material. While no electrical conductivity is reported, the work in Chapters

2 and 3 are structurally related to these boronate ester macrocycles in their use of truncated ditopic triphenylene linkers to compose hexagonal π-stacking macrocycles.

1.7 Conclusion

Synthesis of shape-persistent organic macrocycles has made significant progress in the last decade, but synthesis of metal–organic macrocycles has fallen off. Challenges remain in organic macrocycles often due to difficult synthetic requirements, and Pt and Pd based metal–organic macrocycles use costly noble metals, limiting their potential. Impressive feats have been achieved in designing systems which specific targeted applications through the tremendous tunability of the chemical and morphological features. Numerous synthetic handles on the interior or exterior of the ring present the chance for tailored design to improve molecular and charge transport properties. Designing systems which form supramolecular assemblies by non-covalent interactions have the potential for reversibility and access to a broad range of applications. There is a significant opportunity for designing metal–organic macrocycles based on non-noble metals, and that work is presented in the following chapters.

1.8 References

(1) Xie, L. S.; Skorupskii, G.; Dincă, M. Electrically Conductive Metal–Organic Frameworks. *Chem. Rev.* **2020**, *120* (16), 8536–8580. https://doi.org/10.1021/acs.chemrev.9b00766.

(2) Hmadeh, M.; Lu, Z.; Liu, Z.; Gándara, F.; Furukawa, H.; Wan, S.; Augustyn, V.; Chang, R.; Liao, L.; Zhou, F.; Perre, E.; Ozolins, V.; Suenaga, K.; Duan, X.; Dunn, B.; Yamamto, Y.; Terasaki, O.; Yaghi, O. M. New Porous Crystals of Extended Metal-Catecholates. *Chem. Mater.* **2012**, *24* (18), 3511–3513. https://doi.org/10.1021/cm301194a.

(3) Sheberla, D.; Sun, L.; Blood-Forsythe, M. A.; Er, S.; Wade, C. R.; Brozek, C. K.; Aspuru-Guzik, A.; Dincă, M. High Electrical Conductivity in Ni3(2,3,6,7,10,11-Hexaiminotriphenylene)2, a Semiconducting Metal–Organic Graphene Analogue. *J. Am. Chem. Soc.* **2014**, *136* (25), 8859–8862. https://doi.org/10.1021/ja502765n.

(4) Xing, D.; Wang, Y.; Zhou, P.; Liu, Y.; Wang, Z.; Wang, P.; Zheng, Z.; Cheng, H.; Dai, Y.; Huang, B. Co3(Hexaiminotriphenylene)2: A Conductive Two-Dimensional π–d Conjugated Metal–Organic Framework for Highly Efficient Oxygen Evolution Reaction. *Applied Catalysis B: Environmental* **2020**, *278*, 119295. https://doi.org/10.1016/j.apcatb.2020.119295.

(5) Stodolka, M.; Choi, J. Y.; Flood, J.; Pham, H. T. B.; Park, J. Iron-Based 2D Conductive Metal–Organic Framework Nanostructure with Enhanced Pseudocapacitance. *ACS Appl. Nano Mater.* **2022**, *5* (2), 2156–2162. https://doi.org/10.1021/acsanm.1c03862.

(6) Wang, L.; Sarkar, A.; Grocke, G. L.; Laorenza, D. W.; Cheng, B.; Ritchhart, A.; Filatov, A. S.; Patel, S. N.; Gagliardi, L.; Anderson, J. S. Broad Electronic Modulation of Two-Dimensional Metal–Organic Frameworks over Four Distinct Redox States. *J. Am. Chem. Soc.* **2023**, *145* (15), 8486–8497. https://doi.org/10.1021/jacs.3c00495.

(7) Dong, R.; Pfeffermann, M.; Liang, H.; Zheng, Z.; Zhu, X.; Zhang, J.; Feng, X. Large-Area, Free-Standing, Two-Dimensional Supramolecular Polymer Single-Layer Sheets for Highly Efficient Electrocatalytic Hydrogen Evolution. *Angewandte Chemie International Edition* **2015**, *54* (41), 12058–12063. https://doi.org/10.1002/anie.201506048.

(8) Clough, A. J.; Yoo, J. W.; Mecklenburg, M. H.; Marinescu, S. C. Two-Dimensional Metal–Organic Surfaces for Efficient Hydrogen Evolution from Water. *J. Am. Chem. Soc.* **2015**, *137* (1), 118–121. https://doi.org/10.1021/ja5116937.

(9) Miner, E. M.; Fukushima, T.; Sheberla, D.; Sun, L.; Surendranath, Y.; Dincă, M. Electrochemical Oxygen Reduction Catalysed by Ni3(Hexaiminotriphenylene)2. *Nat Commun* **2016**, *7* (1), 10942. https://doi.org/10.1038/ncomms10942.

(10) Dong, R.; Zheng, Z.; Tranca, D. C.; Zhang, J.; Chandrasekhar, N.; Liu, S.; Zhuang, X.; Seifert, G.; Feng, X. Immobilizing Molecular Metal Dithiolene–Diamine Complexes on 2D Metal–Organic Frameworks for Electrocatalytic H2 Production. *Chemistry – A European Journal* **2017**, *23* (10), 2255–2260. https://doi.org/10.1002/chem.201605337.

(11) Downes, C. A.; Clough, A. J.; Chen, K.; Yoo, J. W.; Marinescu, S. C. Evaluation of the H2 Evolving Activity of Benzenehexathiolate Coordination Frameworks and the Effect of Film Thickness on H2 Production. *ACS Appl. Mater. Interfaces* **2018**, *10* (2), 1719–1727. https://doi.org/10.1021/acsami.7b15969.

(12) M. Miner, E.; Wang, L.; Dincă, M. Modular O 2 Electroreduction Activity in Triphenylene-Based Metal–Organic Frameworks. *Chemical Science* **2018**, *9* (29), 6286–6291. https://doi.org/10.1039/C8SC02049C.

(13) Benedetto, G.; Mirica, K. A. Conductive Framework Materials for Chemiresistive Detection and Differentiation of Toxic Gases. *Acc. Chem. Res.* **2024**. https://doi.org/10.1021/acs.accounts.4c00319.
(14) Campbell, M. G.; Sheberla, D.; Liu, S. F.; Swager, T. M.; Dincă, M. Cu3(Hexaiminotriphenylene)2: An Electrically Conductive 2D Metal–Organic Framework for Chemiresistive Sensing. *Angewandte Chemie International Edition* **2015**, *54* (14), 4349–4352. https://doi.org/10.1002/anie.201411854.
(15) Campbell, M. G.; Liu, S. F.; Swager, T. M.; Dincă, M. Chemiresistive Sensor Arrays from Conductive 2D Metal–Organic Frameworks. *J. Am. Chem. Soc.* **2015**, *137* (43), 13780–13783. https://doi.org/10.1021/jacs.5b09600.
(16) Smith, M. K.; Mirica, K. A. Self-Organized Frameworks on Textiles (SOFT): Conductive Fabrics for Simultaneous Sensing, Capture, and Filtration of Gases. *J. Am. Chem. Soc.* **2017**, *139* (46), 16759–16767. https://doi.org/10.1021/jacs.7b08840.
(17) Rubio-Giménez, V.; Almora-Barrios, N.; Escorcia-Ariza, G.; Galbiati, M.; Sessolo, M.; Tatay, S.; Martí-Gastaldo, C. Origin of the Chemiresistive Response of Ultrathin Films of Conductive Metal–Organic Frameworks. *Angewandte Chemie* **2018**, *130* (46), 15306–15310. https://doi.org/10.1002/ange.201808242.
(18) Meng, Z.; Aykanat, A.; Mirica, K. A. Welding Metallophthalocyanines into Bimetallic Molecular Meshes for Ultrasensitive, Low-Power Chemiresistive Detection of Gases. *J. Am. Chem. Soc.* **2019**, *141* (5), 2046–2053. https://doi.org/10.1021/jacs.8b11257.
(19) Sheberla, D.; Bachman, J. C.; Elias, J. S.; Sun, C.-J.; Shao-Horn, Y.; Dincă, M. Conductive MOF Electrodes for Stable Supercapacitors with High Areal Capacitance. *Nature Mater* **2017**, *16* (2), 220–224. https://doi.org/10.1038/nmat4766.
(20) Park, J.; Lee, M.; Feng, D.; Huang, Z.; Hinckley, A. C.; Yakovenko, A.; Zou, X.; Cui, Y.; Bao, Z. Stabilization of Hexaaminobenzene in a 2D Conductive Metal–Organic Framework for High Power Sodium Storage. *J. Am. Chem. Soc.* **2018**, *140* (32), 10315–10323. https://doi.org/10.1021/jacs.8b06020.
(21) Feng, D.; Lei, T.; Lukatskaya, M. R.; Park, J.; Huang, Z.; Lee, M.; Shaw, L.; Chen, S.; Yakovenko, A. A.; Kulkarni, A.; Xiao, J.; Fredrickson, K.; Tok, J. B.; Zou, X.; Cui, Y.; Bao, Z. Robust and Conductive Two-Dimensional Metal−organic Frameworks with Exceptionally High Volumetric and Areal Capacitance. *Nat Energy* **2018**, *3* (1), 30–36. https://doi.org/10.1038/s41560-017-0044-5.
(22) Shinde, S. S.; Lee, C. H.; Jung, J.-Y.; Wagh, N. K.; Kim, S.-H.; Kim, D.-H.; Lin, C.; Lee, S. U.; Lee, J.-H. Unveiling Dual-Linkage 3D Hexaiminobenzene Metal–Organic Frameworks towards Long-Lasting Advanced Reversible Zn–Air Batteries. *Energy Environ. Sci.* **2019**, *12* (2), 727–738. https://doi.org/10.1039/C8EE02679C.
(23) Sun, L.; Campbell, M. G.; Dincă, M. Electrically Conductive Porous Metal–Organic Frameworks. *Angewandte Chemie International Edition* **2016**, *55* (11), 3566–3579. https://doi.org/10.1002/anie.201506219.
(24) de Lourdes Gonzalez-Juarez, M.; Morales, C.; Flege, J. I.; Flores, E.; Martin-Gonzalez, M.; Nandhakumar, I.; Bradshaw, D. Tunable Carrier Type of a Semiconducting 2D Metal–Organic Framework Cu3(HHTP)2. *ACS Appl. Mater. Interfaces* **2022**, *14* (10), 12404–12411. https://doi.org/10.1021/acsami.2c00089.
(25) Zhao, W.; Chen, T.; Wang, W.; Bi, S.; Jiang, M.; Zhang, K. Y.; Liu, S.; Huang, W.; Zhao, Q. Layer-by-Layer 2D Ultrathin Conductive Cu3(HHTP)2 Film for High-Performance

Flexible Transparent Supercapacitors. *Advanced Materials Interfaces* **2021**, *8* (11), 2100308. https://doi.org/10.1002/admi.202100308.
(26) Liu, J.; Chen, Y.; Feng, X.; Dong, R. Conductive 2D Conjugated Metal–Organic Framework Thin Films: Synthesis and Functions for (Opto-)Electronics. *Small Structures* **2022**, *3* (5), 2100210. https://doi.org/10.1002/sstr.202100210.
(27) Jeong, H.; Park, G.; Jeon, J.; Park, S. S. Fabricating Large-Area Thin Films of 2D Conductive Metal–Organic Frameworks. *Acc. Chem. Res.* **2024**. https://doi.org/10.1021/acs.accounts.4c00292.
(28) Bong, D. T.; Clark, T. D.; Granja, J. R.; Ghadiri, M. R. Self-Assembling Organic Nanotubes. *Angew. Chem. Int. Ed.* **2001**, *40* (6), 988–1011. https://doi.org/10.1002/1521-3773(20010316)40:6<988::AID-ANIE9880>3.0.CO;2-N.
(29) Balbo Block, M. A.; Kaiser, C.; Khan, A.; Hecht, S. Discrete Organic Nanotubes Based on a Combination of Covalent and Non-Covalent Approaches. In *Functional Molecular Nanostructures*; Schlüter, A. D., Ed.; Topics in Current Chemistry; Springer Berlin Heidelberg: Berlin, Heidelberg, 2005; Vol. 245, pp 89–150. https://doi.org/10.1007/b98167.
(30) Gong, B.; Shao, Z. Self-Assembling Organic Nanotubes with Precisely Defined, Sub-Nanometer Pores: Formation and Mass Transport Characteristics. *Acc. Chem. Res.* **2013**, *46* (12), 2856–2866. https://doi.org/10.1021/ar400030e.
(31) Talukdar, D.; Kumar, J. M.; Gole, B. Self-Assembled Macrocycles: Design Strategies and Emerging Functions. *Crystal Growth & Design* **2023**, *23* (11), 7582–7611. https://doi.org/10.1021/acs.cgd.3c00677.
(32) Meng, Z.; Stolz, R. M.; Mendecki, L.; Mirica, K. A. Electrically-Transduced Chemical Sensors Based on Two-Dimensional Nanomaterials. *Chem. Rev.* **2019**, *119* (1), 478–598. https://doi.org/10.1021/acs.chemrev.8b00311.
(33) Stang, P. J.; Persky, N. E.; Manna, J. Molecular Architecture via Coordination: Self-Assembly of Nanoscale Platinum Containing Molecular Hexagons. *J. Am. Chem. Soc.* **1997**, *119* (20), 4777–4778. https://doi.org/10.1021/ja970537l.
(34) Frischmann, P. D.; Guieu, S.; Tabeshi, R.; MacLachlan, M. J. Columnar Organization of Head-to-Tail Self-Assembled Pt_4 Rings. *J. Am. Chem. Soc.* **2010**, *132* (22), 7668–7675. https://doi.org/10.1021/ja910886g.
(35) Hu, Y.-X.; Hao, X.; Xu, L.; Xie, X.; Xiong, B.; Hu, Z.; Sun, H.; Yin, G.-Q.; Li, X.; Peng, H.; Yang, H.-B. Construction of Supramolecular Liquid-Crystalline Metallacycles for Holographic Storage of Colored Images. *J. Am. Chem. Soc.* **2020**, *142* (13), 6285–6294. https://doi.org/10.1021/jacs.0c00698.
(36) Sepehrpour, H.; Fu, W.; Sun, Y.; Stang, P. J. Biomedically Relevant Self-Assembled Metallacycles and Metallacages. *J. Am. Chem. Soc.* **2019**, *141* (36), 14005–14020. https://doi.org/10.1021/jacs.9b06222.
(37) Leininger, S.; Olenyuk, B.; Stang, P. J. Self-Assembly of Discrete Cyclic Nanostructures Mediated by Transition Metals. *Chem. Rev.* **2000**, *100* (3), 853–908. https://doi.org/10.1021/cr9601324.
(38) Acharyya, K.; Bhattacharyya, S.; Sepehrpour, H.; Chakraborty, S.; Lu, S.; Shi, B.; Li, X.; Mukherjee, P. S.; Stang, P. J. Self-Assembled Fluorescent Pt(II) Metallacycles as Artificial Light-Harvesting Systems. *J. Am. Chem. Soc.* **2019**, *141* (37), 14565–14569. https://doi.org/10.1021/jacs.9b08403.

(39) Strauss, M. J.; Evans, A. M.; Roesner, E. K.; Monsky, R. J.; Bardot, M. I.; Dichtel, W. R. Divergent Nanotube Synthesis through Reversible Macrocycle Assembly. *Acc. Mater. Res.* **2022**, *3* (9), 935–947. https://doi.org/10.1021/accountsmr.2c00062.
(40) Zhang, G.; Lin, W.; Huang, F.; Sessler, J.; Khashab, N. M. Industrial Separation Challenges: How Does Supramolecular Chemistry Help? *J. Am. Chem. Soc.* **2023**, *145* (35), 19143–19163. https://doi.org/10.1021/jacs.3c06175.
(41) Jiang, Z.; Dong, R.; Evans, A. M.; Biere, N.; Ebrahim, M. A.; Li, S.; Anselmetti, D.; Dichtel, W. R.; Livingston, A. G. Aligned Macrocycle Pores in Ultrathin Films for Accurate Molecular Sieving. *Nature* **2022**, *609* (7925), 58–64. https://doi.org/10.1038/s41586-022-05032-1.
(42) Itoh, Y.; Chen, S.; Hirahara, R.; Konda, T.; Aoki, T.; Ueda, T.; Shimada, I.; Cannon, J. J.; Shao, C.; Shiomi, J.; Tabata, K. V.; Noji, H.; Sato, K.; Aida, T. Ultrafast Water Permeation through Nanochannels with a Densely Fluorous Interior Surface. *Science* **2022**, *376* (6594), 738–743. https://doi.org/10.1126/science.abd0966.
(43) Yuan, L.; Feng, W.; Yamato, K.; Sanford, A. R.; Xu, D.; Guo, H.; Gong, B. Highly Efficient, One-Step Macrocyclizations Assisted by the Folding and Preorganization of Precursor Oligomers. *J. Am. Chem. Soc.* **2004**, *126* (36), 11120–11121. https://doi.org/10.1021/ja0474547.
(44) Sanford, A. R.; Yuan, L.; Feng, W.; Yamato, K.; Flowers, R. A.; Gong, B. Cyclic Aromatic Oligoamides as Highly Selective Receptors for the Guanidinium Ion. *Chem. Commun.* **2005**, No. 37, 4720–4722. https://doi.org/10.1039/B504411A.
(45) Helsel, A. J.; Brown, A. L.; Yamato, K.; Feng, W.; Yuan, L.; Clements, A. J.; Harding, S. V.; Szabo, G.; Shao, Z.; Gong, B. Highly Conducting Transmembrane Pores Formed by Aromatic Oligoamide Macrocycles. *J. Am. Chem. Soc.* **2008**, *130* (47), 15784–15785. https://doi.org/10.1021/ja807078y.
(46) Zhou, X.; Liu, G.; Yamato, K.; Shen, Y.; Cheng, R.; Wei, X.; Bai, W.; Gao, Y.; Li, H.; Liu, Y.; Liu, F.; Czajkowsky, D. M.; Wang, J.; Dabney, M. J.; Cai, Z.; Hu, J.; Bright, F. V.; He, L.; Zeng, X. C.; Shao, Z.; Gong, B. Self-Assembling Subnanometer Pores with Unusual Mass-Transport Properties. *Nat Commun* **2012**, *3* (1), 949. https://doi.org/10.1038/ncomms1949.
(47) Louie, S.; Zhong, Y.; Bao, S. T.; Schaack, C.; Montoya, A.; Jin, Z.; Orchanian, N. M.; Liu, Y.; Lei, W.; Harrison, K.; Hone, J.; Angerhofer, A.; Evans, A. M.; Nuckolls, C. P. Coaxially Conductive Organic Wires Through Self-Assembly. *J. Am. Chem. Soc.* **2023**, *145* (9), 4940–4945. https://doi.org/10.1021/jacs.2c12437.
(48) Ball, M.; Zhong, Y.; Fowler, B.; Zhang, B.; Li, P.; Etkin, G.; Paley, D. W.; Decatur, J.; Dalsania, A. K.; Li, H.; Xiao, S.; Ng, F.; Steigerwald, M. L.; Nuckolls, C. Macrocyclization in the Design of Organic N-Type Electronic Materials. *J. Am. Chem. Soc.* **2016**, *138* (39), 12861–12867. https://doi.org/10.1021/jacs.6b05474.
(49) Zhang, B.; Hernández Sánchez, R.; Zhong, Y.; Ball, M.; Terban, M. W.; Paley, D.; Billinge, S. J. L.; Ng, F.; Steigerwald, M. L.; Nuckolls, C. Hollow Organic Capsules Assemble into Cellular Semiconductors. *Nat Commun* **2018**, *9* (1), 1957. https://doi.org/10.1038/s41467-018-04246-0.
(50) Ball, M. L.; Zhang, B.; Xu, Q.; Paley, D. W.; Ritter, V. C.; Ng, F.; Steigerwald, M. L.; Nuckolls, C. Influence of Molecular Conformation on Electron Transport in Giant, Conjugated Macrocycles. *J. Am. Chem. Soc.* **2018**, *140* (32), 10135–10139. https://doi.org/10.1021/jacs.8b06565.

(51) Ball, M.; Zhang, B.; Zhong, Y.; Fowler, B.; Xiao, S.; Ng, F.; Steigerwald, M.; Nuckolls, C. Conjugated Macrocycles in Organic Electronics. *Acc. Chem. Res.* **2019**, *52* (4), 1068–1078. https://doi.org/10.1021/acs.accounts.9b00017.
(52) Huang, S.; Choi, J. Y.; Xu, Q.; Jin, Y.; Park, J.; Zhang, W. Carbazolylene-Ethynylene Macrocycle Based Conductive Covalent Organic Frameworks. *Angewandte Chemie* **2023**, *135* (22), e202303538. https://doi.org/10.1002/ange.202303538.
(53) Yang, J.; Dewal, M. B.; Shimizu, L. S. Self-Assembling Bisurea Macrocycles Used as an Organic Zeolite for a Highly Stereoselective Photodimerization of 2-Cyclohexenone. *J. Am. Chem. Soc.* **2006**, *128* (25), 8122–8123. https://doi.org/10.1021/ja062337s.
(54) Islam, M. F.; Adame-Ramirez, E.; Williams, E. R.; Kittikhunnatham, P.; Wijesekera, A.; Zhang, S.; Ge, T.; Stefik, M.; Smith, M. D.; Pellechia, P. J.; Greytak, A. B.; Shimizu, L. S. Inclusion Polymerization of Pyrrole and Ethylenedioxythiophene in Assembled Triphenylamine *Bis* -Urea Macrocycles. *Macromolecules* **2022**, *55* (24), 11013–11022. https://doi.org/10.1021/acs.macromol.2c02042.
(55) Chavez, A. D.; Smith, B. J.; Smith, M. K.; Beaucage, P. A.; Northrop, B. H.; Dichtel, W. R. Discrete, Hexagonal Boronate Ester-Linked Macrocycles Related to Two-Dimensional Covalent Organic Frameworks. *Chem. Mater.* **2016**, *28* (14), 4884–4888. https://doi.org/10.1021/acs.chemmater.6b01831.

Chapter 2: Conjugated metal–organic macrocycles: Synthesis, characterization, and electrical conductivity

2.1 Introduction.

By facilitating rapid electronic, ionic, and molecular transport, nanoporous conductors enable key technologies, including electrochemical energy storage and conversion,[1–3] chemical sensing,[4,5] and electrochemically driven molecular separations.[6,7] Electrically conductive metal–organic frameworks (MOFs) are a rapidly emerging class of nanoporous conductors with excellent chemical tunability, high surface areas, and exciting charge transport behavior.[8] However, metal–organic frameworks are typically isolated as brittle and poorly dispersible microcrystalline powders, presenting significant challenges to thin film fabrication and device integration.[5] This stands in contrast to established organic semiconductors, which are compatible with scalable and low-cost solution-based processing methods.[9,10] Beyond these practical considerations, existing conductive MOFs also lack the emerging multifunctional materials properties of semiconducting polymers, including stretchability[11–13] and the ability to self-heal.[14,15]

Coupling the attractive porosity, molecular tunability, and electrical conductivity of metal–organic frameworks with the advantageous physical properties of soft matter would open the door to diverse new applications and processing methods.[16] Toward this goal, we are pursuing the dimensional reduction of electrically conductive, triphenylene-based 2D metal–organic frameworks into discrete, hexagonal macrocycles. The planar macrocyclic core should favor the formation of π-stacked structures that preserve out-of-plane charge transport and large interior channels, while the richly tunable exterior can be modified to enhance solubility and alter surface properties.

Reprinted (adapted) with permission from:
Leo B. Zasada, Lorenzo Guio, Ashlyn A. Kamin, Diwash Dhakal, Madison Monahan, Gerald T. Seidler, Christine K. Luscombe, and Dianne J. Xiao, *Journal of the American Chemical Society,* **2022** *144* (10), 4515–4521.

The self-assembly of rigid, shape-persistent organic macrocycles into tubular structures with nanoscale pores is well-studied, and such materials have been investigated for organic electronics, molecular recognition, and ion transport applications.[17–22] A rich diversity of organic reactions have been successfully applied to macrocycle synthesis, including C–C cross-coupling, olefin and alkyne metathesis, and amide, imine, and boronate ester formation.[20,23,24] In contrast, the use of coordination chemistry, rather than organic chemistry, to construct rigidly planar, fully conjugated metal–organic macrocycles has been less explored. Many Pd and Pt-based macrocycles have been reported,[25–28] and interesting phase behavior,[29,30] photophysical properties,[31] and biological activity[32] have been observed. However, the exploration of non-noble metal scaffolds remains relatively rare.

Here, we report the synthesis and characterization of CuTOTP-OR ($TOTP^{n-}$ = 2,3,6,7-tetraoxidotriphenylene, R = linear C2, C4, C6, and C18 alkyl chains), a family of conjugated, copper-based metal–organic macrocycles. The planar structures self-assemble to form ordered,

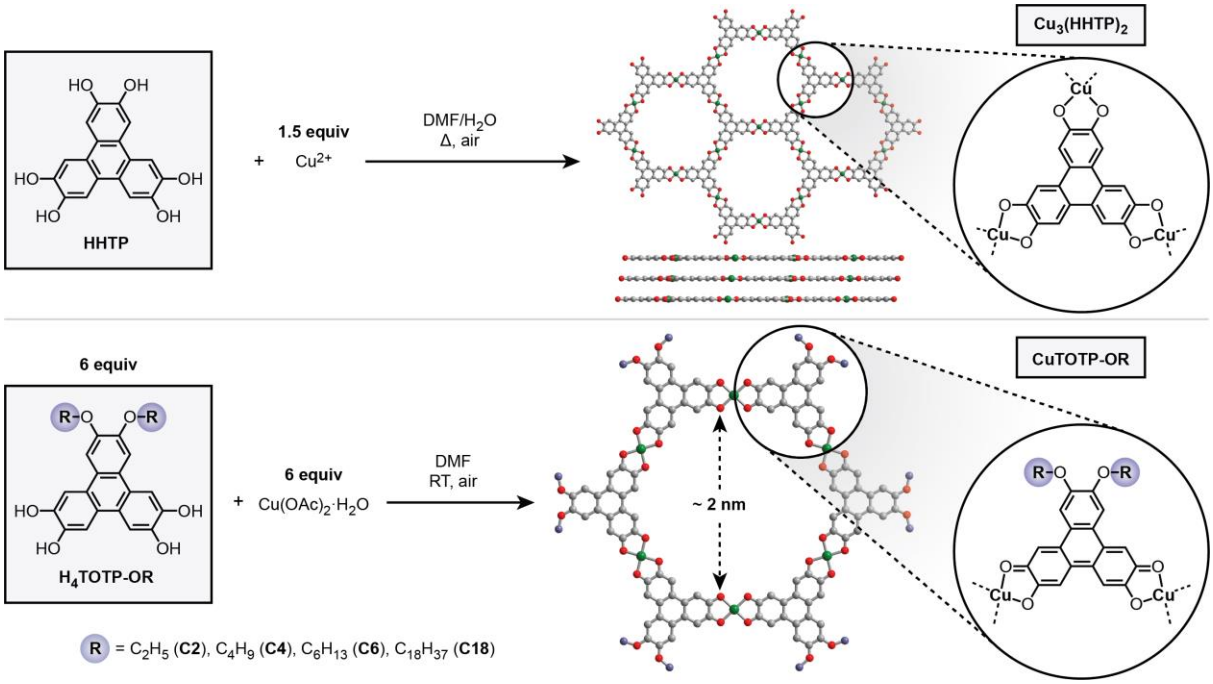

Figure 2.1. *Top:* Synthesis and structure of the 2D conductive metal–organic framework $Cu_3(HHTP)_2$. The material adopts a 2D honeycomb structure with a slipped π–π stacking arrangement between layers (ref. 43). *Bottom:* Overview of our synthetic strategy to truncate $Cu_3(HHTP)_2$ into discrete copper-based macrocycles CuTOTP-OR (R = C2, C4, C6, C18).

electrically conductive nanochannels. Average pellet conductivities of $2(1)\times10^{-3}$ S cm^{-1} are observed in CuTOTP-OC2, the shortest alkyl chain variant. Longer alkyl chain variants such as CuTOTP-OC18 readily disperse in organic solvents, facilitating the fabrication of thin-film field-effect transistor (FET) devices. Ambipolar charge transport is observed, with electron and hole mobilities on the order of $\sim10^{-3}$ cm^2 V^{-1} s^{-1}. Together, these findings show that a simple macrocyclic core can replicate key physical properties of metal–organic frameworks while affording greater processability.

2.2 Results and discussion.

2.2.1 Synthesis and structure.

Our overall synthetic strategy towards fully conjugated, planar metal–organic macrocycles is outlined in **Fig. 2.1**. To preserve extended π–d conjugation, each Cu^{2+} metal center is bridged by planar triphenylene-based ligands that closely resemble HHTP (HHTP = 2,3,6,7,10,11-hexahydroxytriphenylene), a tritopic linker commonly used to construct conductive 2D MOFs like $Cu_3(HHTP)_2$.[33] However, because one of the three catechol units is intentionally capped with alkyl groups, the formation of an extended network is instead truncated into 0D, planar macrocycles. This approach was inspired by recent work from Dichtel, Northrop, and coworkers, who used a similar strategy to achieve boronate ester-based macrocycles that are structurally reminiscent of 2D covalent organic frameworks.[24,34]

Combining the tetrahydroxytriphenylene ligands shown in **Fig. 2.1**, which we have abbreviated H_4TOTP-OR ($TOTP^{n-}$ = 2,3,6,7-**t**etra**o**xido**t**ri**p**henylene, R = alkyl group), with $Cu(OAc)_2\cdot H_2O$ in dimethylformamide (DMF) under air readily produces the desired copper-based macrocycles CuTOTP-OR in excellent yields (67–88% yield). To probe the influence of peripheral functionalization on macrocycle structure, packing, and solution processability, we further

synthesized a family of four macrocycles that differ only in the length of the capping linear alkyl chain (R = C2, C4, C6, and C18).

Powder X-ray diffraction (PXRD) patterns of the resulting dark blue-black solids show three prominent low-angle peaks with a 1:1/√3:1/2 ratio in d-spacing, consistent with hexagonal packing (**Fig. 2.2a**). A broader feature at higher angles, which we have assigned as the (001) reflection, reveals a short interlayer distance of ~3.20 Å. This value is nearly identical to what has been observed in structurally related copper-based 2D metal–organic frameworks (3.19 Å) and is indicative of strong π–π stacking interactions between the planar macrocycles.[35] The broadness of the (001) peak suggests poor long-range ordering in the π-stacking *c* direction. In addition to a perfectly eclipsed arrangement between stacked macrocycles, numerous translational and rotational displacements are also possible. Further work and more crystalline materials are needed to accurately determine the preferred π–π stacking pattern in these materials.

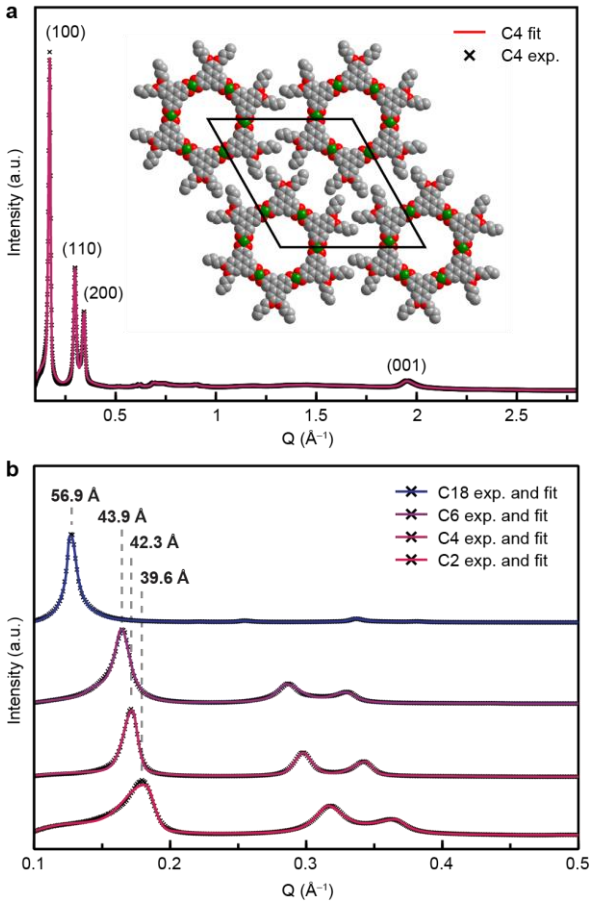

Figure 2.2. (a) PXRD pattern of DMF-solvated CuTOTP-OC4 and optimized structural model. (b) PXRD patterns and peak positions for DMF-solvated CuTOTP-OR.

Pawley refinements were performed to obtain more precise unit cell dimensions of DMF-solvated CuTOTP-OR (**Figs. 2.S1–2.S4**). As expected, the in-plane lattice parameter systematically increases as the peripheral alkyl chains lengthen ($a = b$ = 40–57 Å), while the

interlayer distance remains relatively constant (c = 3.20–3.24 Å) (**Fig. 2.2b**). Geometry optimized structural models afford similar unit cell dimensions (**Fig. 2.S5** and 2.**S6**). Transmission electron microscopy (TEM) images of CuTOTP-OC4 drop-cast from dilute solutions reveal average diameters of 1.9(4) nm, consistent with the expected size of the planar macrocyclic core (**Fig. 2.S7**). Atomic force microscopy (AFM) images of more concentrated CuTOTP-OC4 solutions (1 mg mL^{-1}) clearly show the formation of nanotubular structures, with an average length of 23(6) nm (**Fig. 2.S9**). No porosity was observed via traditional 77 K N_2 adsorption experiments, likely due to partial pore blockage by neighboring alkyl chains. However, similar measurements at 195 K using CO_2, a smaller probe molecule, led to a surface area of 226(3) m^2/g for CuTOTP-OC2. Altogether, the data obtained from PXRD, TEM, AFM, and gas sorption measurements are fully consistent with the columnar stacking of hexagonal macrocycles to form large nanochannels of approximately 2 nm in diameter.

Compared to extended 2D MOFs, the long-range structure of CuTOTP-OR is considerably more dynamic. In particular, the weak noncovalent interactions between neighboring alkyl chains are readily perturbed by solvent. While the interlayer distance stays relatively constant, reversible expansions and contractions in the *ab* plane are observed upon altering the macrocycle solvation state (**Table 2.1**). For example, the in-plane lattice parameter of fully dried CuTOTP-OC4 increases by >5% upon DMF solvation, suggesting partial solvent infiltration between the columnar stacks.

Table 2.1. Lattice parameters of CuTOTP-OR macrocycles in dried and DMF-solvated states.

	Dry		**DMF-Solvated**	
CuTOTP-OR	***a* = *b*** (Å)	***c*** (Å)	***a* = *b*** (Å)	***c*** (Å)
R = C2	38.46(3)	3.19(1)	39.56(2)	3.22(1)
R = C4	40.16(2)	3.17(1)	42.30(2)	3.23(1)
R = C6	42.93(2)	3.17(1)	43.89(2)	3.20(1)
R = C18	55.86(6)	3.21(1)	56.91(2)	3.24(1)

We hypothesized that by tuning both the solvent identity and macrocycle peripheral functionalization, we should be able to fully separate the individual columnar stacks and achieve stable colloidal dispersions. With sonication, average particle sizes of around 90, 200, and 300 nm were observed by dynamic light scattering (DLS) for THF-dispersed CuTOTP-OC2, C4, and C6, respectively. However, these dispersions were not stable and further aggregation was observed over time. In contrast, dispersions of CuTOTP-OC18 in THF appear indefinitely stable across all concentrations tested (up to 10 mg/mL). Furthermore, DLS measurements revealed an average hydrodynamic diameter of 5(1) nm, consistent with short, isolated columnar stacks of macrocycles. Similar diameters (4–5 nm) were also observed in other organic solvents, such as $CHCl_3$ and toluene (**Table 2.S1**). The ease by which CuTOTP-OR forms high concentration inks may afford future processability advantages relative to traditional metal–organic frameworks.

2.2.2 Spectroscopic characterization.

Depending on the synthesis conditions, significant Cu(II)/Cu(I) mixed valency has been observed in the copper-based 2D frameworks $Cu_3(HHTP)_2$ and $Cu_3(HITP)_2$ (HITP = 2,3,6,7,10,11-hexaiminotriphenylene).[36] To determine whether similar mixed valency is observed in CuTOTP-OR, we probed the metal oxidation state using Cu K-edge X-ray absorption near-edge spectroscopy (XANES) (**Fig. 2.3**). The edge energy (as defined by the first peak of the first derivative spectra) is typically around 8981 eV for Cu(I) and 8985 eV for Cu(II) compounds.[37] The XANES spectra of all four CuTOTP-OR materials (R = C2, C4, C6, C18) were nearly identical, with edge energies between 8985–8986 eV (**Fig. 2.3** and **Fig. 2.S11**). Overall, the observed XANES spectral features, the simple first-neighbor only extended X-ray absorption fine structure (EXAFS) oscillations, and the average Cu–O bond lengths obtained from EXAFS fitting ($d_{Cu–O}$ = 1.94(1) Å, see **Table 2.S2**) are very similar to $Cu(acac)_2$ ($acac^{1–}$ = acetylacetonate) and other reference compounds containing square planar Cu(II) centers **(Figs. 2.S10–2.S13).**[38]

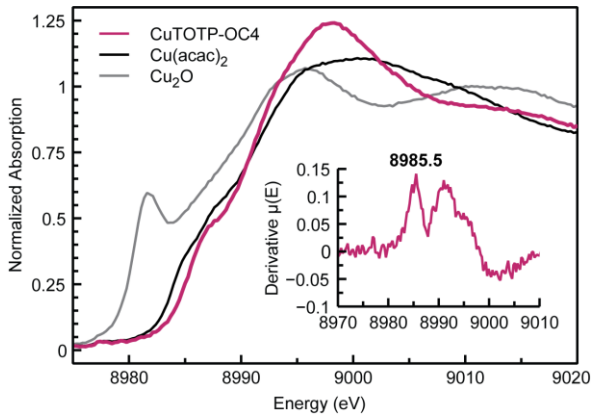

Figure 2.3. XANES spectra of CuTOTP-OC4 (purple) compared to reference Cu_2O (gray) and $Cu(acac)_2$ (black) compounds. *Inset*: Derivative spectra of CuTOTP-OC4, showing a first peak at 8985.5 eV.

High-resolution X-ray photoelectron spectroscopy (XPS) measurements of the Cu 2p region were carried out to further corroborate our Cu(II) assignment (**Fig. 2.S15**). The Cu $2p_{3/2}$ peak of Cu(II) compounds is characterized by multiplet broadening and strong satellite features at higher binding energies.[39,40] In contrast, the Cu $2p_{3/2}$ peak of Cu(I) compounds is narrower and displays a very weak shake-up satellite. By comparing the relative areas of the main $2p_{3/2}$ peak and the shake-up satellite, we estimate that ≥90% of the copper centers in CuTOTP-OR are in the +2 oxidation state (see **Table 2.S6** and the Supporting Information for more analysis details). We note that the complexity of Cu 2p XPS spectra can introduce large errors (±15%) in curve-fitting and quantification.[40] Nevertheless, taken together, our XANES and XPS data provide strong support for a predominantly Cu(II) oxidation state assignment.

After establishing the metal oxidation state in CuTOTP-OR, we next turned to the ligand. The two redox-active dioxolene units present in H_4TOTP-OR can each adopt three distinct redox states: the dianionic catecholate (cat^{2-}), monoanionic semiquinone (sq^{1-}), and neutral quinone (q^0) (**Fig. 2.4a**). These three states are readily distinguished by infrared spectroscopy. As the dioxolene unit is sequentially oxidized, its C–O stretching frequency (ν_{C-O}) systematically increases. In general, metal–catecholate, semiquinone, and quinone complexes display ν_{C-O} bands between 1250–1275, 1400–1500, and 1630–1640 cm^{-1}, respectively.[41] The infrared spectrum of CuTOTP-OC4 displays a strong feature at 1430 cm^{-1}, consistent with a metal–semiquinone C–O stretch

(**Fig. 2.4b**). A band at 1246 cm^{-1} is also observed, which we have assigned as the ν_{C-O} of the alkyl-capped catechol unit. Similar features are also observed in the other alkyl variants of CuTOTP-OR (**Fig. 2.S16**). Based on the infrared spectra, we propose the ligand is aerobically oxidized during synthesis to the dianionic TOTP-OR^{2-} form, where the bridging dioxolene units are in the $[sq, sq]^{2-}$ state.

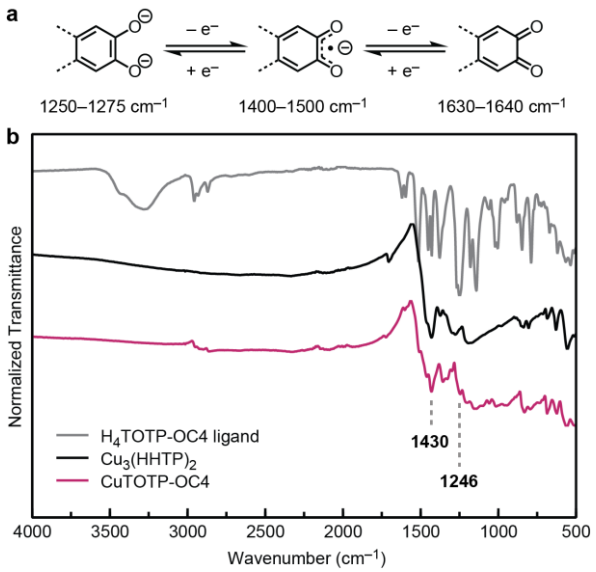

Figure 2.4. (a) Characteristic ν_{C-O} bands for metal–catecholate, semiquinone, and quinone complexes. (b) Infrared spectra of the H_4TOTP-OC4 ligand, $Cu_3(HHTP)_2$ framework, and CuTOTP-OC4 macrocycle shown in gray, black, and purple, respectively.

UV-vis electronic absorption spectra are also consistent with a semiquinone assignment. Metal–semiquinone complexes typically show an intense band at ~300 nm, assigned as an intraligand transition, as well as a broader band between 600–700 nm, assigned as a metal-to-ligand charge transfer (MLCT).[41] Indeed, the UV-vis spectra of CuTOTP-OC4 displays strong absorbances at both 317 and 598 nm (**Fig. 2.S18**). Similar features are observed in the structurally related $Cu_3(HHTP)_2$ metal–organic framework (356 and 622 nm).

Both the macrocycle CuTOTP-OR and the metal–organic framework $Cu_3(HHTP)_2$ display a broad absorption >1600 cm^{-1} that is not observed in the parent H_4TOTP-OR or HHTP ligands (**Figs. 2.4b** and **2.S16**). In $Cu_3(HHTP)_2$, this feature has been attributed to a low-energy electronic transition, though its exact nature remains unclear.[36] Previously proposed assignments have included low-lying transitions of charge carriers as well as intervalence charge-transfer,[36] though the latter explanation is less likely for CuTOTP-OR, as no ligand or metal-based mixed valency

appears to be present in these macrocycles. The broad electronic absorbance suggests a low activation energy for charge transport, motivating further study into the electrical conductivity of these materials.

2.2.3 Charge transport measurements.

Two-point conductivity measurements were performed at room temperature on pressed pellets of CuTOTP-OR using a custom screw cell equipped with brass electrodes. Surprisingly, despite the truncated structure, pressed pellets of CuTOTP-OC2 (10^{-3} S cm^{-1}) are nearly as conductive as $Cu_3(HHTP)_2$ powders (10^{-3}–10^{-2} S cm^{-1}) (**Table 2.2, Table 2.S7**, and **Fig. 2.S19**).[8,43] Similar conductivity values of ~10^{-4} S cm^{-1} were obtained for the R = C4 and C6 variants. While the pellet conductivity of CuTOTP-OC18 is only 10^{-7} S cm^{-1} due to the presence of long, insulating alkyl chains, higher values should be possible in thin films with controlled alignment and morphology.[44,45]

Table 2.2. Average room temperature (298 K) conductivity values obtained from pressed pellets of CuTOTP-OR and either pressed pellets or single crystals of $Cu_3(HHTP)_2$.

Sample	**Conductivity** (S cm^{-1})
CuTOTP-OC2[a]	$2(1) \times 10^{-3}$
CuTOTP-OC4[a]	$6(2) \times 10^{-4}$
CuTOTP-OC6[a]	$4(1) \times 10^{-4}$
CuTOTP-OC18[a]	$1(1) \times 10^{-7}$
$Cu_3(HHTP)_2$ (pellet)[b]	10^{-3}–10^{-2}
$Cu_3(HHTP)_2$ (single crystal, out-of-plane)[c]	1.5

[a]Average of three measurements. [b]Average conductivity obtained in this work is $6(2) \times 10^{-3}$ S cm^{-1}; previously reported values tabulated in ref. 8 range between 10^{-3} to 10^{-2} S cm^{-1}. [c]Value obtained from ref. 43.

Due to similarities in their structural, spectroscopic, and bulk conductivity properties, the CuTOTP-OR macrocycles provide a rare window into the out-of-plane charge transport properties of $Cu_3(HHTP)_2$ and related 2D conductive frameworks. As described in a recent review by Dincă and coworkers, many uncertainties still remain concerning the charge carrier type, carrier concentration, and carrier mobility in conductive MOFs.[8] For example, the nature of the charge carriers (electrons or holes) in $Cu_3(HHTP)_2$ is still under active investigation. Recent reports suggest that the majority charge carrier type in $Cu_3(HHTP)_2$ depends strongly on the synthesis and

processing conditions, as well as the presence of adsorbed species.[42,46,47] Our macrocyclic system provides an opportunity to study this ambipolar behavior in more detail.

Solution-processable metal–organic macrocycles are amenable to characterization techniques routinely employed by the organic semiconductor community but challenging to access with traditional porous solids. To probe the charge carrier identity and mobility, thin-film field-effect transistors were fabricated using the CuTOTP-OC18 macrocycles as the transport layer. The detailed results of FET characterization are shown in the Supporting Information and sample transfer curves are shown in **Fig. 2.S20**. All measurements were performed under an N_2 atmosphere. Interestingly, the FETs displayed ambipolar behavior, producing comparable hole and electron mobilities. The average saturation hole mobility ($\mu_{h,sat}$) was $(6.17 \pm 0.51) \times 10^{-3}$ cm^2 V^{-1} s^{-1} and the average saturation electron mobility ($\mu_{e,sat}$) was $(2.16 \pm 0.61) \times 10^{-3}$ cm^2 V^{-1} s^{-1}. The voltage thresholds were –50 V and 30 V, respectively, and the on/off drain current ratio was on the order of 10^4. We note that the CuTOTP-OC18 devices were not exhaustively optimized, and it is likely that higher mobilities could be achieved by tuning various parameters, such as the casting solution concentration, deposition spin rate, and device layer interface.

Given the strong structural resemblance between CuTOTP-OR and $Cu_3(HHTP)_2$, these results suggest that $Cu_3(HHTP)_2$ may display similar ambipolar conduction in the out-of-plane direction.[48] Together, these studies show how discrete, solution-processable macrocycles can provide deeper insight into the charge transport properties of 2D conductive frameworks.

2.2.4 Electrochemical characterization.

The concentration of charge carriers and the overall conductivity of semiconducting polymers and metal–organic frameworks can be tuned across many orders of magnitude through simple oxidative (p-type) and reductive (n-type) doping.[49–54] Motivated by these previous studies, we were interested in understanding whether our macrocycles, which contain redox-active ligands (**Fig. 2.4a**), are stable to further chemical reduction or oxidation. We hypothesized that the large interior channels present in CuTOTP-OR should be able to accommodate the insertion of charge-balancing ions without perturbing the π–π stacking pathways critical for charge transport.

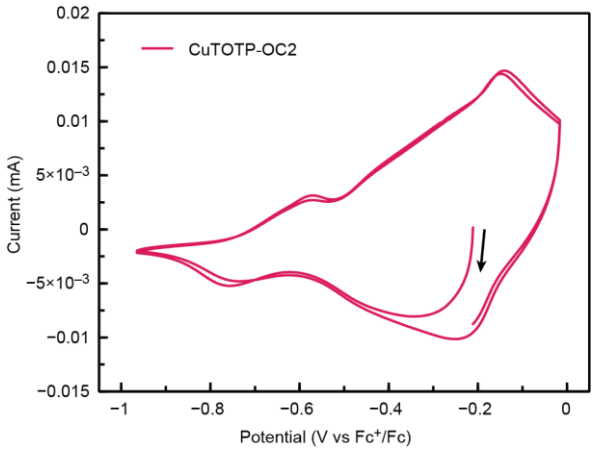

Figure 2.5. Solid-state cyclic voltammogram (2 cycles) of CuTOTP-OC2 collected at 10 mV s^{-1} in 0.05 M $NaClO_4$ in acetonitrile. The arrow indicates the direction of the forward scan.

To probe the redox properties of our macrocycles, solid-state cyclic voltammograms (CVs) of CuTOTP-OC2 were collected in 0.05 M $NaClO_4$ in acetonitrile. Working electrodes were prepared by dropcasting CuTOTP-OC2 dispersed in THF on glassy carbon electrodes. A representative CV of CuTOTP-OC2 is shown in **Fig. 2.5**. The compound displays quasi-reversible reduction events at $E_{1/2}$ = –0.20 V and –0.66 V vs. Fc^+/Fc. In contrast to the relative reductive stability, scanning to more positive potentials than ~0 V vs Fc^+/Fc led to irreversible oxidative features indicative of either macrocycle decomposition or loss of electrical contact with the electrode. While a comprehensive study is outside the scope of this work, these preliminary CV experiments suggest that reductive doping may be a promising avenue to tune the charge transport properties of CuTOTP-OR.

2.3 Conclusion.

The planar metal–organic macrocycles described here, which readily π-stack to form 1D columns, occupy a rare space in between molecules and materials. Going forward, CuTOTP-OR represents an important model system for understanding how magnetic and electronic interactions evolve as individual MOF layers self-assemble into π-stacked materials. More broadly, conjugated metal–organic macrocycles can serve as a bridge between 'hard' inorganic porous materials and 'soft' organic polymers. Future work will focus on how structural modifications across length scales influence electronic and ionic transport in this new class of soft nanoporous semiconductors.

2.4 Acknowledgments

Initial synthetic efforts were supported by the University of Washington (startup funds) and the NSF through a seed grant from the University of Washington Materials Research Science and Engineering Center DMR-1719797. Subsequent materials characterization by L.B.Z. was supported by the U.S. Department of Energy, Office of Science, Office of Basic Energy Sciences under Award Number DE-SC0021966. L.G., who performed the FET mobility measurements, was supported by the Department of Energy Office of Basic Energy Sciences under award number DE-SC0019911. D.D., who carried out the XAS measurements and analysis, was supported in part by the Joint Center for Energy Storage Research (JCESR), an Energy Innovation Hub funded by the U.S. Department of Energy, Office of Science, Basic Energy Sciences. M.M., who carried out the TEM measurements, was supported by the U.S. Department of Energy, Office of Science, Office of Basic Energy Sciences DE-SC0019288. L.B.Z., A.A.K, and D.D. were supported in part by the state of Washington through graduate fellowships from the University of Washington Clean Energy Institute.

The authors acknowledge the use of instrumentation at the following shared facilities: the Washington Research Training Testbeds, a facility operated by the University of Washington

Clean Energy Institute; the University of Washington Photonics Center; the Molecular Analysis Facility, a National Nanotechnology Coordinated Infrastructure (NNCI) site at the University of Washington, which is supported in part by funds from the National Science Foundation (awards NNCI-2025489, NNCI-1542101), the Molecular Engineering & Sciences Institute, and the Clean Energy Institute; and the MEM-C shared facilities, supported by the U.S. National Science Foundation through the UW Molecular Engineering Materials Center (MEM-C), a Materials Research Science and Engineering Center (DMR-171797). This research also used the mail-in program at Beamline 17-BM of the Advanced Photon Source, a U.S. Department of Energy (DOE) Office of Science User Facility, operated for the DOE Office of Science by Argonne National Laboratory under Contract No. DE-AC02-06CH11357. Finally, we gratefully acknowledge easyXAFS for assistance collecting EXAFS measurements, Dr. Samantha Young for assistance collecting and analyzing XPS data, Dr. Heather Niles for assistance collecting and analyzing AFM data, and Dr. Michael E. Ziebel for helpful scientific discussions.

2.5 References

(1) Yang, Z.; Ren, J.; Zhang, Z.; Chen, X.; Guan, G.; Qiu, L.; Zhang, Y.; Peng, H. Recent Advancement of Nanostructured Carbon for Energy Applications. *Chem. Rev.* **2015**, *115* (11), 5159–5223. https://doi.org/10.1021/cr5006217.

(2) Wang, L.; Han, Y.; Feng, X.; Zhou, J.; Qi, P.; Wang, B. Metal–Organic Frameworks for Energy Storage: Batteries and Supercapacitors. *Coordination Chemistry Reviews* **2016**, *307*, 361–381. https://doi.org/10.1016/j.ccr.2015.09.002.

(3) Liang, Z.; Qu, C.; Guo, W.; Zou, R.; Xu, Q. Pristine Metal-Organic Frameworks and Their Composites for Energy Storage and Conversion. *Adv. Mater.* **2018**, *30* (37), 1702891. https://doi.org/10.1002/adma.201702891.

(4) Meng, Z.; Stolz, R. M.; Mendecki, L.; Mirica, K. A. Electrically-Transduced Chemical Sensors Based on Two-Dimensional Nanomaterials. *Chem. Rev.* **2019**, *119* (1), 478–598. https://doi.org/10.1021/acs.chemrev.8b00311.

(5) Stassen, I.; Burtch, N.; Talin, A.; Falcaro, P.; Allendorf, M.; Ameloot, R. An Updated Roadmap for the Integration of Metal–Organic Frameworks with Electronic Devices and Chemical Sensors. *Chem. Soc. Rev.* **2017**, *46* (11), 3185–3241. https://doi.org/10.1039/C7CS00122C.

(6) Mendecki, L.; Ko, M.; Zhang, X.; Meng, Z.; Mirica, K. A. Porous Scaffolds for Electrochemically Controlled Reversible Capture and Release of Ethylene. *J. Am. Chem. Soc.* **2017**, *139* (48), 17229–17232. https://doi.org/10.1021/jacs.7b08102.

(7) Voskian, S.; Hatton, T. A. Faradaic Electro-Swing Reactive Adsorption for CO_2 Capture. *Energy Environ. Sci.* **2019**, *12* (12), 3530–3547. https://doi.org/10.1039/C9EE02412C.

(8) Xie, L. S.; Skorupskii, G.; Dincă, M. Electrically Conductive Metal–Organic Frameworks. *Chem. Rev.* **2020**, *120* (16), 8536–8580. https://doi.org/10.1021/acs.chemrev.9b00766.

(9) Forrest, S. R. The Path to Ubiquitous and Low-Cost Organic Electronic Appliances on Plastic. *Nature* **2004**, *428* (6986), 911–918. https://doi.org/10.1038/nature02498.

(10) Sirringhaus, H.; Kawase, T.; Friend, R. H.; Shimoda, T.; Inbasekaran, M.; Wu, W.; Woo, E. P. High-Resolution Inkjet Printing of All-Polymer Transistor Circuits. *Science* **2000**, *290* (5499), 2123–2126. https://doi.org/10.1126/science.290.5499.2123.

(11) Root, S. E.; Savagatrup, S.; Printz, A. D.; Rodriquez, D.; Lipomi, D. J. Mechanical Properties of Organic Semiconductors for Stretchable, Highly Flexible, and Mechanically Robust Electronics. *Chem. Rev.* **2017**, *117* (9), 6467–6499. https://doi.org/10.1021/acs.chemrev.7b00003.

(12) Wang, S.; Oh, J. Y.; Xu, J.; Tran, H.; Bao, Z. Skin-Inspired Electronics: An Emerging Paradigm. *Acc. Chem. Res.* **2018**, *51* (5), 1033–1045. https://doi.org/10.1021/acs.accounts.8b00015.

(13) Matsuhisa, N.; Chen, X.; Bao, Z.; Someya, T. Materials and Structural Designs of Stretchable Conductors. *Chem. Soc. Rev.* **2019**, *48* (11), 2946–2966. https://doi.org/10.1039/C8CS00814K.

(14) Yang, Y.; Urban, M. W. Self-Healing Polymeric Materials. *Chem. Soc. Rev.* **2013**, *42* (17), 7446. https://doi.org/10.1039/c3cs60109a.

(15) Kang, J.; Tok, J. B.-H.; Bao, Z. Self-Healing Soft Electronics. *Nat Electron* **2019**, *2* (4), 144–150. https://doi.org/10.1038/s41928-019-0235-0.

(16) Hosono, N.; Kitagawa, S. Modular Design of Porous Soft Materials via Self-Organization of Metal–Organic Cages. *Acc. Chem. Res.* **2018**, *51* (10), 2437–2446. https://doi.org/10.1021/acs.accounts.8b00361.

(17) Moore, J. S. Shape-Persistent Molecular Architectures of Nanoscale Dimension. *Acc. Chem. Res.* **1997**, *30* (10), 402–413. https://doi.org/10.1021/ar950232g.
(18) Yamaguchi, Y.; Yoshida, Z. Shape-Persistency and Molecular Function in Heteromacrocycles: Creation of Heteroarenecyclynes and Arene–Azaarenecyclynes. *Chem. Eur. J.* **2003**, *9* (22), 5430–5440. https://doi.org/10.1002/chem.200305099.
(19) Höger, S. Shape-Persistent Macrocycles: From Molecules to Materials. *Chem. Eur. J.* **2004**, *10* (6), 1320–1329. https://doi.org/10.1002/chem.200305496.
(20) Zhang, W.; Moore, J. S. Shape-Persistent Macrocycles: Structures and Synthetic Approaches from Arylene and Ethynylene Building Blocks. *Angew. Chem. Int. Ed.* **2006**, *45* (27), 4416–4439. https://doi.org/10.1002/anie.200503988.
(21) Iyoda, M.; Yamakawa, J.; Rahman, M. J. Conjugated Macrocycles: Concepts and Applications. *Angew. Chem. Int. Ed.* **2011**, *50* (45), 10522–10553. https://doi.org/10.1002/anie.201006198.
(22) Gong, B.; Shao, Z. Self-Assembling Organic Nanotubes with Precisely Defined, Sub-Nanometer Pores: Formation and Mass Transport Characteristics. *Acc. Chem. Res.* **2013**, *46* (12), 2856–2866. https://doi.org/10.1021/ar400030e.
(23) Jin, Y.; Wang, Q.; Taynton, P.; Zhang, W. Dynamic Covalent Chemistry Approaches Toward Macrocycles, Molecular Cages, and Polymers. *Acc. Chem. Res.* **2014**, *47* (5), 1575–1586. https://doi.org/10.1021/ar500037v.
(24) Chavez, A. D.; Smith, B. J.; Smith, M. K.; Beaucage, P. A.; Northrop, B. H.; Dichtel, W. R. Discrete, Hexagonal Boronate Ester-Linked Macrocycles Related to Two-Dimensional Covalent Organic Frameworks. *Chem. Mater.* **2016**, *28* (14), 4884–4888. https://doi.org/10.1021/acs.chemmater.6b01831.
(25) Stang, P. J.; Persky, N. E.; Manna, J. Molecular Architecture via Coordination: Self-Assembly of Nanoscale Platinum Containing Molecular Hexagons. *J. Am. Chem. Soc.* **1997**, *119* (20), 4777–4778. https://doi.org/10.1021/ja970537l.
(26) Leininger, S.; Olenyuk, B.; Stang, P. J. Self-Assembly of Discrete Cyclic Nanostructures Mediated by Transition Metals. *Chem. Rev.* **2000**, *100* (3), 853–908. https://doi.org/10.1021/cr9601324.
(27) Fujita, M.; Tominaga, M.; Hori, A.; Therrien, B. Coordination Assemblies from a Pd(II)-Cornered Square Complex. *Acc. Chem. Res.* **2005**, *38* (4), 369–378. https://doi.org/10.1021/ar040153h.
(28) Northrop, B. H.; Yang, H.-B.; Stang, P. J. Coordination-Driven Self-Assembly of Functionalized Supramolecular Metallacycles. *Chem. Commun.* **2008**, No. 45, 5896. https://doi.org/10.1039/b811712h.
(29) Frischmann, P. D.; Guieu, S.; Tabeshi, R.; MacLachlan, M. J. Columnar Organization of Head-to-Tail Self-Assembled Pt_4 Rings. *J. Am. Chem. Soc.* **2010**, *132* (22), 7668–7675. https://doi.org/10.1021/ja910886g.
(30) Hu, Y.-X.; Hao, X.; Xu, L.; Xie, X.; Xiong, B.; Hu, Z.; Sun, H.; Yin, G.-Q.; Li, X.; Peng, H.; Yang, H.-B. Construction of Supramolecular Liquid-Crystalline Metallacycles for Holographic Storage of Colored Images. *J. Am. Chem. Soc.* **2020**, *142* (13), 6285–6294. https://doi.org/10.1021/jacs.0c00698.
(31) Acharyya, K.; Bhattacharyya, S.; Sepehrpour, H.; Chakraborty, S.; Lu, S.; Shi, B.; Li, X.; Mukherjee, P. S.; Stang, P. J. Self-Assembled Fluorescent Pt(II) Metallacycles as Artificial Light-Harvesting Systems. *J. Am. Chem. Soc.* **2019**, *141* (37), 14565–14569. https://doi.org/10.1021/jacs.9b08403.

(32) Sepehrpour, H.; Fu, W.; Sun, Y.; Stang, P. J. Biomedically Relevant Self-Assembled Metallacycles and Metallacages. *J. Am. Chem. Soc.* **2019**, *141* (36), 14005–14020. https://doi.org/10.1021/jacs.9b06222.
(33) Hmadeh, M.; Lu, Z.; Liu, Z.; Gándara, F.; Furukawa, H.; Wan, S.; Augustyn, V.; Chang, R.; Liao, L.; Zhou, F.; Perre, E.; Ozolins, V.; Suenaga, K.; Duan, X.; Dunn, B.; Yamamto, Y.; Terasaki, O.; Yaghi, O. M. New Porous Crystals of Extended Metal-Catecholates. *Chem. Mater.* **2012**, *24* (18), 3511–3513. https://doi.org/10.1021/cm301194a.
(34) Smith, M. K.; Powers-Riggs, N. E.; Northrop, B. H. Rational Synthesis of Bis(Hexyloxy)-Tetra(Hydroxy)-Triphenylenes and Their Derivatives. *RSC Adv.* **2014**, *4* (72), 38281–38292. https://doi.org/10.1039/C4RA06503D.
(35) Dou, J.-H.; Arguilla, M. Q.; Luo, Y.; Li, J.; Zhang, W.; Sun, L.; Mancuso, J. L.; Yang, L.; Chen, T.; Parent, L. R.; Skorupskii, G.; Libretto, N. J.; Sun, C.; Yang, M. C.; Dip, P. V.; Brignole, E. J.; Miller, J. T.; Kong, J.; Hendon, C. H.; Sun, J.; Dincă, M. Atomically Precise Single-Crystal Structures of Electrically Conducting 2D Metal–Organic Frameworks. *Nature Materials* **2021**, *20* (2), 222–228. https://doi.org/10.1038/s41563-020-00847-7.
(36) Stolz, R. M.; Mahdavi-Shakib, A.; Frederick, B. G.; Mirica, K. A. Host–Guest Interactions and Redox Activity in Layered Conductive Metal–Organic Frameworks. *Chem. Mater.* **2020**, *32* (18), 7639–7652. https://doi.org/10.1021/acs.chemmater.0c01007.
(37) Lamberti, C.; Bordiga, S.; Bonino, F.; Prestipino, C.; Berlier, G.; Capello, L.; D'Acapito, F.; Llabrés i Xamena, F. X.; Zecchina, A. Determination of the Oxidation and Coordination State of Copper on Different Cu-Based Catalysts by XANES Spectroscopy in Situ or in Operando Conditions. *Phys. Chem. Chem. Phys.* **2003**, *5* (20), 4502–4509. https://doi.org/10.1039/B305810G.
(38) Gaur, A.; Klysubun, W.; Nitin Nair, N.; Shrivastava, B. D.; Prasad, J.; Srivastava, K. XAFS Study of Copper(II) Complexes with Square Planar and Square Pyramidal Coordination Geometries. *Journal of Molecular Structure* **2016**, *1118*, 212–218. https://doi.org/10.1016/j.molstruc.2016.04.008.
(39) Biesinger, M. C. Advanced Analysis of Copper X-Ray Photoelectron Spectra. *Surface and Interface Analysis* **2017**, *49* (13), 1325–1334. https://doi.org/10.1002/sia.6239.
(40) Brundle, C. R.; Crist, B. V. X-Ray Photoelectron Spectroscopy: A Perspective on Quantitation Accuracy for Composition Analysis of Homogeneous Materials. *Journal of Vacuum Science & Technology A* **2020**, *38* (4), 041001. https://doi.org/10.1116/1.5143897.
(41) Vlček, A. Metal and Ligand Oxidation States in Dioxolene Complexes: Meaning, Assignment and Control. *Comments on Inorganic Chemistry* **1994**, *16* (4), 207–228. https://doi.org/10.1080/02603599408035860.
(42) Rubio-Giménez, V.; Galbiati, M.; Castells-Gil, J.; Almora-Barrios, N.; Navarro-Sánchez, J.; Escorcia-Ariza, G.; Mattera, M.; Arnold, T.; Rawle, J.; Tatay, S.; Coronado, E.; Martí-Gastaldo, C. Bottom-Up Fabrication of Semiconductive Metal-Organic Framework Ultrathin Films. *Adv. Mater.* **2018**, *30* (10), 1704291. https://doi.org/10.1002/adma.201704291.
(43) Day, R. W.; Bediako, D. K.; Rezaee, M.; Parent, L. R.; Skorupskii, G.; Arguilla, M. Q.; Hendon, C. H.; Stassen, I.; Gianneschi, N. C.; Kim, P.; Dincă, M. Single Crystals of Electrically Conductive Two-Dimensional Metal–Organic Frameworks: Structural and Electrical Transport Properties. *ACS Cent. Sci.* **2019**, *5* (12), 1959–1964. https://doi.org/10.1021/acscentsci.9b01006.

(44) Kaafarani, B. R. Discotic Liquid Crystals for Opto-Electronic Applications. *Chem. Mater.* **2011**, *23* (3), 378–396. https://doi.org/10.1021/cm102117c.
(45) Diao, Y.; Shaw, L.; Bao, Z.; Mannsfeld, S. C. B. Morphology Control Strategies for Solution-Processed Organic Semiconductor Thin Films. *Energy Environ. Sci.* **2014**, *7* (7), 2145–2159. https://doi.org/10.1039/C4EE00688G.
(46) de Lourdes Gonzalez-Juarez, M.; Flores, E.; Martin-Gonzalez, M.; Nandhakumar, I.; Bradshaw, D. Electrochemical Deposition and Thermoelectric Characterisation of a Semiconducting 2-D Metal–Organic Framework Thin Film. *J. Mater. Chem. A* **2020**, *8* (26), 13197–13206. https://doi.org/10.1039/D0TA04939E.
(47) de Lourdes Gonzalez-Juarez, M.; Morales, C.; Flege, J. I.; Flores, E.; Martin-Gonzalez, M.; Nandhakumar, I.; Bradshaw, D. Tunable Carrier Type of a Semiconducting 2D Metal–Organic Framework Cu3(HHTP)2. *ACS Appl. Mater. Interfaces* **2022**, *14* (10), 12404–12411. https://doi.org/10.1021/acsami.2c00089.
(48) Huang, X.; Sheng, P.; Tu, Z.; Zhang, F.; Wang, J.; Geng, H.; Zou, Y.; Di, C.; Yi, Y.; Sun, Y.; Xu, W.; Zhu, D. A Two-Dimensional π–d Conjugated Coordination Polymer with Extremely High Electrical Conductivity and Ambipolar Transport Behaviour. *Nat Commun* **2015**, *6* (1), 7408. https://doi.org/10.1038/ncomms8408.
(49) Wegner, G. Polymers with Metal-Like Conductivity—A Review of Their Synthesis, Structure and Properties. *Angew. Chem. Int. Ed. Engl.* **1981**, *20* (4), 361–381. https://doi.org/10.1002/anie.198103611.
(50) Heeger, A. J. Semiconducting and Metallic Polymers: The Fourth Generation of Polymeric Materials (Nobel Lecture). *Angew. Chem. Int. Ed.* **2001**, *40* (14), 2591–2611. https://doi.org/10.1002/1521-3773(20010716)40:14<2591::AID-ANIE2591>3.0.CO;2-0.
(51) Kobayashi, Y.; Jacobs, B.; Allendorf, M. D.; Long, J. R. Conductivity, Doping, and Redox Chemistry of a Microporous Dithiolene-Based Metal−Organic Framework. *Chem. Mater.* **2010**, *22* (14), 4120–4122. https://doi.org/10.1021/cm101238m.
(52) Darago, L. E.; Aubrey, M. L.; Yu, C. J.; Gonzalez, M. I.; Long, J. R. Electronic Conductivity, Ferrimagnetic Ordering, and Reductive Insertion Mediated by Organic Mixed-Valence in a Ferric Semiquinoid Metal–Organic Framework. *J. Am. Chem. Soc.* **2015**, *137* (50), 15703–15711. https://doi.org/10.1021/jacs.5b10385.
(53) Xie, L. S.; Sun, L.; Wan, R.; Park, S. S.; DeGayner, J. A.; Hendon, C. H.; Dincă, M. Tunable Mixed-Valence Doping toward Record Electrical Conductivity in a Three-Dimensional Metal–Organic Framework. *J. Am. Chem. Soc.* **2018**, *140* (24), 7411–7414. https://doi.org/10.1021/jacs.8b03604.
(54) Aubrey, M. L.; Wiers, B. M.; Andrews, S. C.; Sakurai, T.; Reyes-Lillo, S. E.; Hamed, S. M.; Yu, C.-J.; Darago, L. E.; Mason, J. A.; Baeg, J.-O.; Grandjean, F.; Long, G. J.; Seki, S.; Neaton, J. B.; Yang, P.; Long, J. R. Electron Delocalization and Charge Mobility as a Function of Reduction in a Metal–Organic Framework. *Nature Mater* **2018**, *17* (7), 625–632. https://doi.org/10.1038/s41563-018-0098-1.

2.6 Supporting Information

2.6.1. General materials and methods

Reagents and solvents were purchased from commercial vendors (Millipore Sigma, TCI America, Alfa Aesar, Fisher, Oakwood Chemical, Combi-Blocks) and used without purification unless otherwise noted. Deuterated solvents ($CDCl_3$, DMSO-d_6) were purchased from Cambridge Isotope Laboratories. NMR spectra were acquired on Bruker AV300, AV301, DRX499, or AV500 instruments. ^{1}H and ^{13}C NMR spectra were referenced to residual solvent peaks. High resolution mass spectrometry data of ligands and their intermediates were collected on a Thermo Scientific LTQ Orbitrap XL instrument in positive ion mode. C, H, N combustion analysis was conducted by Atlantic Microlabs Inc.

High-resolution PXRD data were collected using the mail-in program at Beamline 17-BM of the Advanced Photon Source (APS). Kapton capillaries (1.1 mm in diameter) were sealed on one end with epoxy, packed with sample (~1 cm in height), and then sealed on the other end with epoxy. To prepare dimethylformamide (DMF)-soaked samples, the packed capillary was kept open on one end, placed horizontally in a 20 mL scintillation vial and immersed in DMF, and then heated at 35 °C for 2 h. The epoxy softens during this process, allowing DMF to enter through both ends of the capillary. After 2 h, both ends are re-sealed with epoxy. Routine powder X-ray diffraction (PXRD) data were collected on either a Bruker D8 Discover powder X-ray diffractometer located in University of Washington's Molecular Analysis Facility, or a Bruker D2 PHASER benchtop diffractometer. Powder diffraction data analysis (pattern indexing, Pawley refinement and precise unit cell determination) was carried out using MDI Jade. Structural models were constructed in Materials Studio using the Forcite module.

Attenuated total reflectance infrared (ATR-IR) spectra were recorded on a Bruker Alpha IR instrument equipped with a Platinum ATR accessory.

Dynamic light scattering (DLS) data were collected on a Malvern Zetasizer Nano ZS.

UV-Vis spectra were collected on a Cary 5000 spectrophotometer (Agilent). Samples were prepared as 4 mg/mL solutions in tetrahydrofuran (THF), sonicated, and vigorously stirred overnight and then drop cast onto quartz slides.

X-band EPR data were collected at 110K on a Bruker EMXnano spectrometer (microwave (mw) frequency, 9.64 GHz) equipped with a liquid nitrogen cooling system. A mw power of 5 mW, modulation amplitude of 8 G and a modulation frequency of 100 kHz were used. Samples were prepared by gently mixing CuTOTP-OR with pre-ground KBr to achieve a final concentration of 1 mol% macrocycle. Tubes were sparged for 5 minutes with N_2, capped, and sealed with electrical tape before obtaining spectra.

Atomic force microscopy (AFM) was collected in air on a AFM Bruker Icon in tapping mode using a silicon OTESPA probe. Samples were prepared from a 1 mg/mL solution which was shaken, and gently sonicated for 20 seconds before drop casting onto freshly cleaved mica.

TEM images were collected on a FEI Tecnai G2 F20 microscope operated at 200 keV in bright field mode. Samples were prepared by drop-casting 5 μL of sample dissolved in THF (5E-5 M)

onto a suspended ultrathin carbon film on lacey carbon support film, 400 mesh, copper grids purchased from Ted Pella Inc or CVD graphene film (1-6 monolayers) deposited on lacey carbon support film, 300 mesh, copper grids purchased from Graphene Supermarket. The samples were allowed to dry in air, without significant air flow, until dry then placed under vacuum for 1 h. Histograms, average sizes, and standard deviations for macrocycles were obtained by manual analysis of over 250 particles per sample using ImageJ.

2.6.2 Macrocycle synthesis.

Synthesis of CuTOTP-OR (R = C2, C4, C6, C18).

Synthesis of CuTOTP-OC2: A 20 mL scintillation vial was charged with H_4TOTP-OC2 (0.100 g, 0.263 mmol, 1.00 equiv), and DMF (10 mL). Separately, a 100 mL jar was charged with copper acetate monohydrate ($Cu(OAc)_2 \cdot H_2O$) (0.116 g, 0.289 mmol, 1.10 equiv) and DMF (20 mL). Both solutions were sonicated for 5 minutes, after which the ligand solution was added dropwise to the metal solution, capped, and allowed to sit at room temperature for 14 days. After 14 days, the solution was centrifuged to isolate the solid product. The product was washed with DMF (3×15 mL) and EtOAc (11×15 mL) at room temperature. The macrocycle **CuTOTP-OC2** was obtained in 67% yield (77.6 mg, 0.029 mmol) as a dark blue solid. Anal. Calc. for $(CuC_{22}H_{16}O_6)(H_2O)_{1.7}(C_3H_7NO)_{0.2}$: C, 55.95; H, 4.32; N, 0.58. Found: C, 56.09; H, 4.47; N, 0.54.

Synthesis of CuTOTP-OC4: A 20 mL scintillation vial was charged with H_4TOTP-OC4 (0.100 g, 0.229 mmol, 1.00 equiv), and DMF (10 mL). Separately, a 100 mL jar was charged with $Cu(OAc)_2 \cdot H_2O$ (0.151 g, 0.252 mmol, 1.10 equiv) and DMF (20 mL). Both solutions were sonicated for 5 minutes, after which the ligand solution was added dropwise to the metal solution, capped, and allowed to sit at room temperature. After 6-14 days, the solution was centrifuged to isolate the solid product. The product was washed with DMF (3×15 mL) and EtOAc (11×15 mL) at room temperature. The macrocycle **CuTOTP-OC4** was obtained in 83% yield (94.2 mg, 0.031 mmol) as a dark blue solid. Anal. Calc. for $(CuC_{26}H_{24}O_6)(H_2O)_{1.8}(C_3H_7NO)_{0.15}$: C, 58.90; H, 5.35; N, 0.39. Found: C, 58.78; H, 5.14; N, 0.51.

Synthesis of CuTOTP-OC6: A 20 mL scintillation vial was charged with H_4TOTP-OC6 (0.100 g, 0.203 mmol, 1.00 equiv), and DMF (10 mL). Separately, a 100 mL jar was charged with $Cu(OAc)_2 \cdot H_2O$ (0.223 g, 0.252 mmol, 1.10 equiv) and DMF (20 mL). Both solutions were sonicated for 5 minutes, after which the ligand solution was added dropwise to the metal solution, capped, and allowed to sit at room temperature. After 6-14 days, the solution was centrifuged to isolate the solid product. The product was washed with DMF (3×15 mL) and EtOAc (11×15 mL) at room temperature. The macrocycle **CuTOTP-OC6** was obtained in 85% yield (95.1 mg, 0.029 mmol) as a dark blue solid. Anal. Calc. for $(CuC_{30}H_{32}O_6)(H_2O)_{1.8}(C_3H_7NO)_{0.15}$: C, 61.41; H, 6.20; N, 0.35. Found: C, 61.28; H, 6.04; N, 0.51.

Synthesis of CuTOTP-OC18: A 20 mL scintillation vial was charged with H_4TOTP-OC18 (0.100 g, 0.121 mmol, 1.00 equiv), and THF (10.5 mL). Separately, a 20 mL scintillation vial was charged with $Cu(OAc)_2 \cdot H_2O$ (0.026 g, 0.132 mmol, 1.10 equiv) and DMF (4.5 mL). Both solutions were sonicated for 5 minutes, after which the ligand solution was added dropwise to the metal solution. This 15 mL solution was divided evenly amongst 5×4 mL vials (3 mL each) with Teflon-taped threads and allowed to heat at 60 °C for 24 h. Reactions were filtered, and the resulting powder was washed with a 1:1 mixture of THF:DMF (3×10 mL) and finally filtered and rinsed with additional DMF. The powders were transferred to a 20 mL vial and further dried under purging N_2 at 35 °C for 3 hours. The macrocycle **CuTOTP-OC18** was obtained in 88% yield (93.8 mg, 0.016 mmol) as a dark blue solid. Anal. Calc. for $(CuC_{54}H_{80}O_6)(H_2O)_{1.4}(C_3H_7NO)_{0.4}$: C, 70.29; H, 9.15; N, 0.59. Found: C, 70.14, H, 8.99, N, 0.53.

2.6.3. Ligand synthesis.

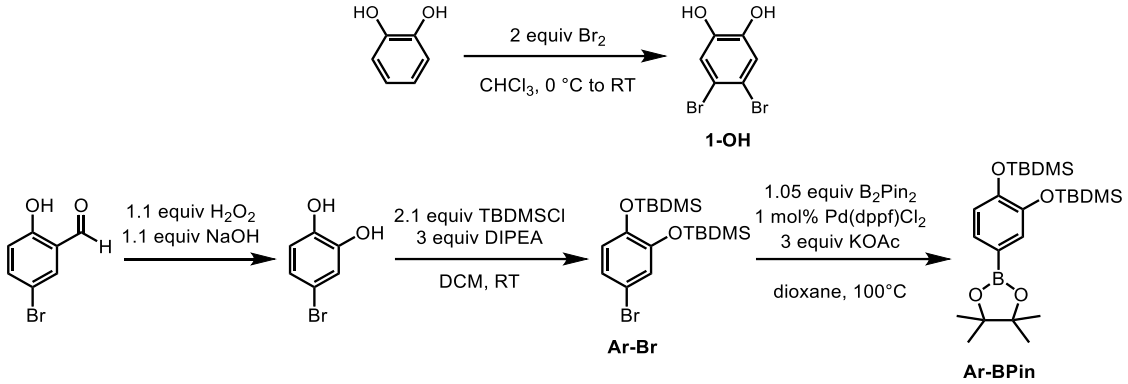

Scheme 2.S1 | Synthesis of ligand precursors **1-OH** and **Ar-Bpin**.

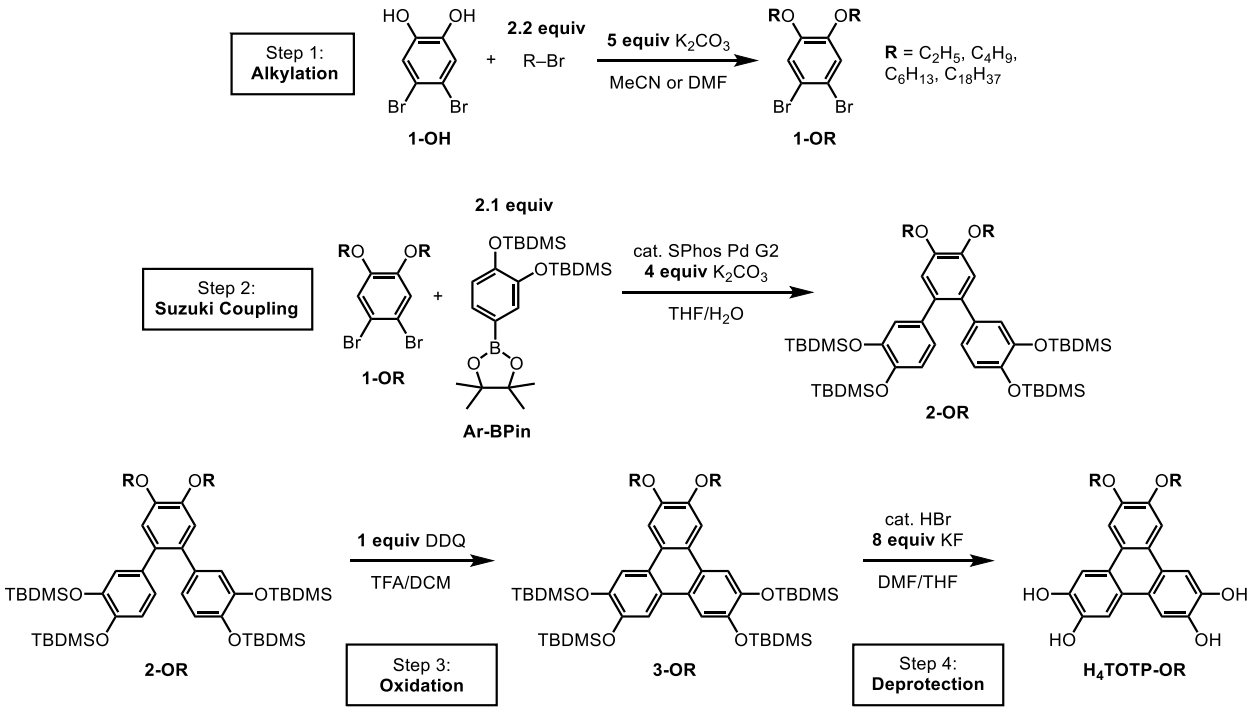

Scheme 2.S2 | Overview of H_4TOTP-OR synthesis. Starting from **1-OH** and **Ar-Bpin**, the ligand **H_4TOTP-OR** can be obtained in four steps (alkylation, Suzuki coupling, oxidation, and deprotection). The synthetic route is based on previously reported procedures.[1]

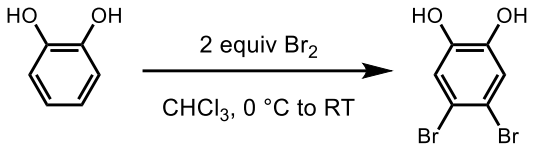

Synthesis of 4,5-dibromobenzene-1,2-diol (1-OH). In a 500 mL flask equipped with a stir bar, catechol (35.0 g, 0.318 mol, 1.00 equiv) was suspended in 200 mL of $CHCl_3$. The flask was cooled to 0 °C using an ice bath. Using an addition funnel, a solution of Br_2 (32.7 mL, 0.636 mol, 2.00 equiv) in 40 mL of $CHCl_3$ was added dropwise over 1 h with stirring. The ice bath was removed and the reaction was stirred at room temperature for 20 hr. After 20 hr, the solids were allowed to settle and the $CHCl_3$ was poured off. The solids were filtered and washed with additional $CHCl_3$ and hexanes to obtain **1-OH** as an off-white solid (69.4 g, 0.259 mol, 81% yield). *Note:* Excess bromine in the $CHCl_3$ filtrate was neutralized with aqueous sodium thiosulfate. The ^{1}H NMR is consistent with previous literature reports.[1]

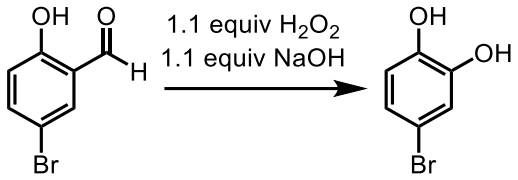

4-bromobenzene-1,2-diol. The synthesis was carried out according to previously reported procedures with slight modifications.[2,3] In a 100 mL Schlenk flask, 5-bromo-2-hydroxybenzaldehyde (15.0 g, 74.6 mmol, 1.00 equiv) was dissolved in 3 M NaOH (27.4 mL, 82.1 mmol, 1.10 equiv). The mixture was sparged with N_2 for 30 min. Under N_2, 30% H_2O_2 (8.37 mL, 82.1 mmol, 1.10 equiv) was added dropwise over the course of ~1 h with stirring. The reaction is exothermic, and the rate of addition was controlled so the solution temperature did not rise above 40–50 °C. After the first few drops, a yellow sludge formed that required occasional manual shaking. Upon further H_2O_2 addition, the yellow sludge converted into a dark solution. After H_2O_2 addition is complete, the reaction was allowed to cool to room temperature and carefully acidified to pH ~ 4 with concentrated H_2SO_4. The acidic solution was neutralized with saturated $NaHCO_3$ and extracted with Et_2O (6 x 75 mL). The organic layer was separated, dried with $MgSO_4$, and concentrated *in vacuo* to obtain an orange oil. The oil was redissolved in a small amount of DCM and concentrated *in vacuo* obtain a yellow solid, which was triturated with hexanes and filtered to yield 14.1 g of 4-bromobenzene-1,2-diol (74.6 mmol, quantitative yield). The product was used directly in the next step without further purification. The ^{1}H NMR is consistent with previous literature reports.[2]

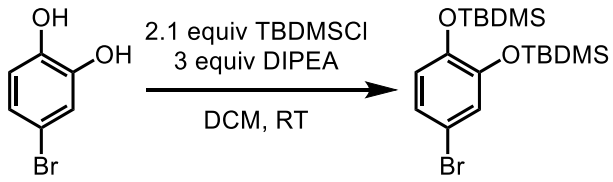

Ar-Br. In a Schlenk flask under N_2, 4-bromobenzene-1,2-diol (14.0 g, 74.1 mmol, 1.00 equiv) was dissolved in 60 mL of DCM. N,N-diisopropylethylamine (38.7 mL, 222 mmol, 3.00 equiv) was added. *Tert*-butyldimethylsilyl chloride (23.5 g, 156 mmol, 2.10 equiv) was added in portions over

5 min. The solution was stirred at room temperature overnight, and then concentrated *in vacuo*. The residue was dissolved in THF (50 mL) and water (50 mL) for 1 h at room temperature to hydrolyze excess *tert*-butyldimethylsilyl chloride. The solution was then diluted with Et_2O (100 mL), and the organic layer was washed with saturated $NaHCO_3$ (150 mL), water (100 mL), and dried with $MgSO_4$. The organic layer was concentrated *in vacuo* to obtain the product as an orange oil in quantitative yield, which was used directly in the next step without further purification. The ^1H NMR is consistent with previous literature reports.[1]

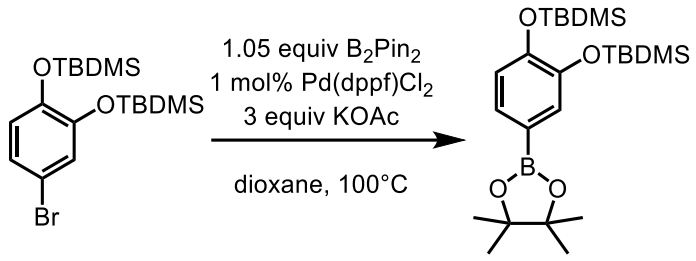

Ar-BPin. A 3-neck, 250 mL roundbottom flask equipped with a reflux condenser was charged with a stir bar, Ar-Br (28.5 g, 68.3 mmol, 1.00 equiv), B_2Pin_2 (18.2 g, 71.7 mmol, 1.05 equiv), KOAc (20.1 g, 205 mmol, 3.00 equiv), and 120 mL of 1,4-dioxane. The mixture was placed under N_2 and sparged for 30–40 min. Under positive N_2 pressure, $Pd(dppf)Cl_2$ (0.500 g, 0.683 mmol, 0.01 equiv) was added, and the reaction was heated at 100 °C for 16 h with stirring. After the reaction was complete, the solvent was removed *in vacuo* and the residue was redissolved in EtOAc (150 mL) and water (150 mL). The organic layer was separated, and the water layer was extracted with additional EtOAc (2 x 100 mL). The organic layer was dried with MgSO4, filtered through celite, and concentrated *in vacuo* to obtain an orange oil. The product was recrystallized from MeOH (~15 mL, –20 °C), and the solids rinsed with a small amount of cold MeOH. The MeOH filtrate was concentrated *in vacuo* and recrystallized a second time to obtain an additional crop of solids. The combined yield was 28.5 g (61.3 mmol, 90% yield). The ^1H NMR is consistent with previous literature reports.[1]

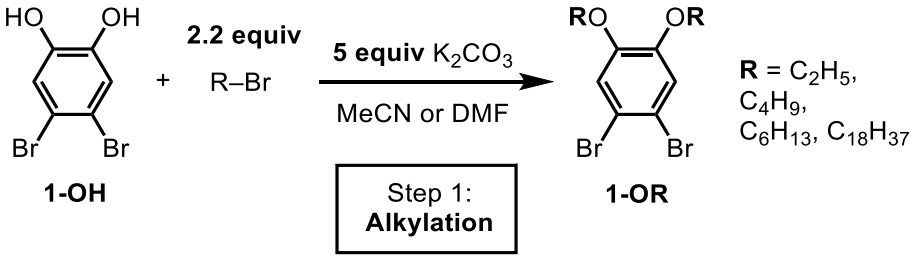

General Alkylation Procedure (Step 1): *Note:* Slight deviations from the general procedure were performed for R = C2 and C18 (see following sections for details). A 100 mL round bottom flask equipped with a stir bar and reflux condenser was charged with 4,5-dibromobenzene-1,2-diol (1.00 g, 3.74 mmol, 1.00 equiv), R–Br (8.23 mmol, 2.20 equiv), and 20 mL MeCN. The solution was sparged with N_2 for 40 minutes, and then K_2CO_3 (18.70 mmol, 5.00 equiv) was added. The solution was heated to 80 °C and stirred for 48 h. The reaction was cooled to room temperature and dried *in vacuo*. The reaction was then dissolved in Et_2O (50 mL) and washed with H_2O (2x100 mL).

The organic layer was dried over $MgSO_4$, filtered, and concentrated *in vacuo* to afford **1-OR** as an oil that was used directly in Step 2 without further purification.

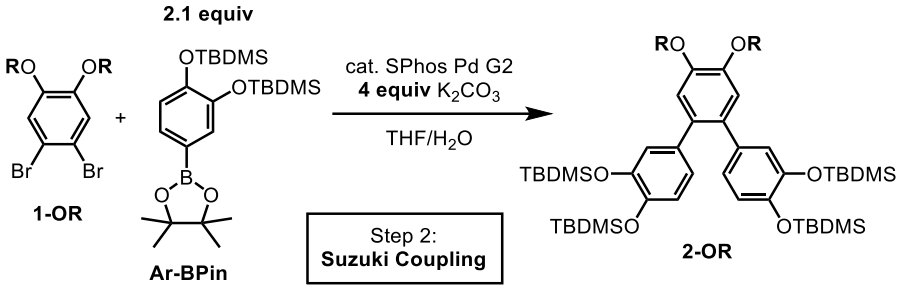

General Suzuki Coupling Procedure (Step 2): *Note:* Slight deviations from the general procedure were performed for R = C18 (see following sections for details). A 250 mL round bottom flask equipped with a stir bar and reflux condenser was charged with **1-OR** (2.63 mmol, 1.00 equiv), **Ar-BPin** (5.52 mmol, 2.10 equiv), H_2O (30 mL) and THF (90 mL). The solution was sparged with N_2 for 40 minutes, followed by addition of K_2CO_3 (10.5 mmol, 4.00 equiv) and SPhos Pd G2 (0.0526 mmol, 0.0200 equiv). The solution was heated to 70 °C and stirred for 18 h. The reaction was cooled to room temperature and THF removed *in vacuo*. The solution was then diluted with EtOAc (100 mL) and H_2O (100 mL) and the aqueous layer was extracted with additional EtOAc (2x50 mL). The combined organic layers were dried over $MgSO_4$ and concentrated *in vacuo*. The resultant brown oil was subjected to filtration through a silica plug (DCM) and used directly in Step 3 without further purification.

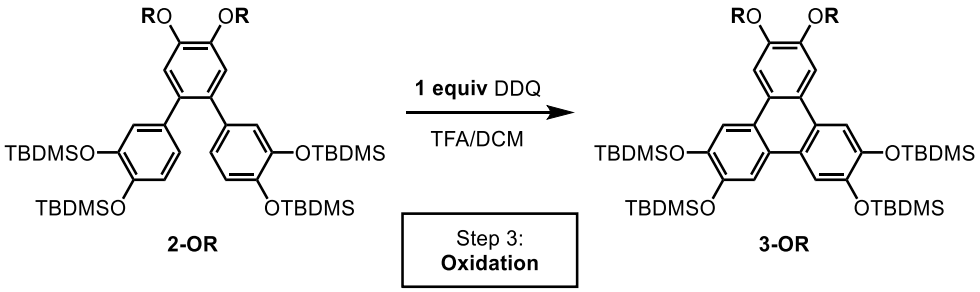

General Oxidation Procedure (Step 3): *Note:* Slight deviations from the general procedure were performed for R = C18 (see following sections for details). A 500 mL schlenk flask equipped with a stir bar was charged with **2-OR** (2.23 mmol, 1.00 equiv), anhydrous DCM (150 mL), and trifluoroacetic acid (15 mL). The solution was cooled to 0 °C and sparged with N_2 for 30 minutes. After sparging, 2,3-dichloro-5,6-dicyano-1,4-benzoquinone (2.23 mmol, 1.00 equiv) was added under N_2 after which the solution immediately turned a dark green. The reaction was kept at 0 °C for 3 h then carefully quenched with a saturated aqueous solution of $NaHCO_3$ (~200 mL). The DCM layer was separated and washed with a saturated aqueous solution of $NaHCO_3$ (3x100 mL) and H_2O (2x100 mL). The organic layer was dried over $MgSO_4$ and concentrated *in vacuo*. The resultant brown oil was subjected to filtration through a silica plug eluting with DCM and then used directly in Step 4 without further purification.

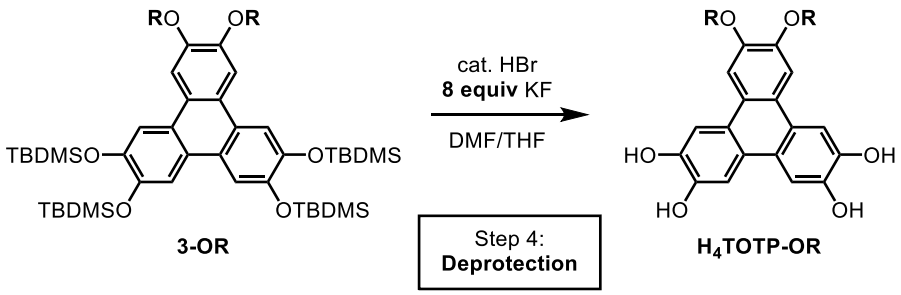

General Deprotection Procedure (Step 4): *Note:* Slight deviations from the general procedure were performed for R = C18 (see following sections for details). A 100 mL schlenk flask equipped with a stir bar was charged with **3-OR** (2.24 mmol, 1.00 equiv), DMF (10 mL) and THF (10 mL) to create a ~0.1 M solution of **3** in 1:1 DMF:THF, and sparged with N_2 for 30 minutes. Potassium fluoride (17.9 mmol, 8.00 equiv) and HBr (0.90 mmol, 0.4 equiv) were then added, and the reaction was stirred at room temperature for at least 48 h. The flask was cooled to 0 °C, and 1 M HCl (~90 mL) was added. The reaction was then extracted with EtOAc (3x100 mL), and the combined organic layers were washed with H_2O (2x100 mL). The combined organic layers were then dried over $MgSO_4$ and concentrated *in vacuo*. The product was then triturated with a 1:10 mixture of hexanes and Et_2O to yield **H_4TOTP-OR** as a light gray solid.

Characterization of R = C2 intermediates and H_4TOTP-OC2:

Intermediate **1-OC2** was synthesized according to the general alkylation procedure with slight modifications. Specifically, 16.00 equiv of R–Br was used, and the reaction was heated to 60 °C, not 80 °C. The reaction was performed on a 1.5 g (5.60 mmol) scale of 4,5-dibromobenzene-1,2-diol. The desired product was obtained as a yellow oil in 93% yield (1.69 g, 5.22 mmol). ^{1}H NMR (500 MHz, $CDCl_3$): δ 7.06 (s, 2H), 4.04 (q, J = 7.0, 4H), 1.44 (t, J = 7.0, 6H) ppm. ^{13}C NMR (75 MHz, $CDCl_3$): δ 148.79, 118.07, 114.79, 65.11, 14.61 ppm.

Intermediate **2-OC2** was synthesized according to the general Suzuki coupling procedure, on a 1.69 g (5.22 mmol) scale of **1-OC2**. The desired product was obtained as a yellow oil in 96% yield (3.60 g, 4.29 mmol). ^{1}H NMR (500 MHz, $CDCl_3$): δ 6.84 (s, 2H), 6.64 (m, 4H), 6.54 (dd, J = 3.5, 2H), 4.14 (q, J = 7.0, 4H), 1.46 (t, J = 7.1, 6H), 0.97 (s, 18H), 0.93 (s, 18H), 0.18 (s, 12H), 0.07 (s, 12H) ppm. ^{13}C NMR (75 MHz, $CDCl_3$): δ 147.57, 146.15, 145.35, 135.09, 132.83, 122.81, 122.51, 120.23, 116.13, 64.73, 53.34, 25.93, 18.40, 18.34, 14.93, -4.07, -4.18 ppm.

Intermediate **3-OC2** was synthesized according to the general oxidation procedure, on a 3.73 g (4.44 mmol) scale of **2-OC2**. The desired product was obtained as a yellow oil in in quantitative yields. ^{1}H NMR (500 MHz, $CDCl_3$): δ 7.82 (s, 2H), 7.79 (s, 2H), 7.73 (s, 2H), 4.30 (q, J = 7.0, 4H), 1.57 (t, J = 7.0, 6H), 1.06 (m, 36H), 0.31 (m, 24H) ppm. ^{13}C NMR (75 MHz, $CDCl_3$): δ 148.66, 146.83, 124.12, 114.16, 106.92, 106.84, 64.83, 26.24, 25.02, 18.84, 15.03, -3.86 ppm.

The ligand **H_4TOTP-OC2** was synthesized according to the general deprotection procedure, on a 3.68 g (4.40 mmol) scale of **3-OC2**. The desired product was obtained as a gray solid in 81% yield (1.56 g, 4.10 mmol). ^{1}H NMR (500 MHz, DMSO-d_6): δ 9.44 (s, 2H), 9.17 (s, 2H), 7.82 (s, 2H), 7.73 (s, 2H), 7.65 (s, 2H), 4.24 (q, J = 7.0, 4H), 1.43 (3, J =6.9, 6H) ppm. ^{13}C NMR (75 MHz,

DMSO-d_6): δ 147.61, 145.64, 145.42, 122.50, 122.29, 121.76, 108.39, 107.72, 106.01, 64.86, 14.84 ppm. MS (ESI/ion trap) *m/z*: $[M+H]^+$ Calcd for $C_{22}H_{20}O_6$: 381.1; found 381.1.

Characterization of R = C4 intermediates and H_4TOTP-OC4:

Intermediate **1-OC4** was synthesized according to the general alkylation procedure, on a 5.00 g (18.7 mmol) scale of 4,5-dibromobenzene-1,2-diol. The desired product was obtained as a yellow oil in 99% yield (7.00 g, 18.4 mmol). ^{1}H NMR (500 MHz, $CDCl_3$): δ 7.06 (s, 2H), 3.95 (t, J = 6.6, 4H), 1.79 (p, J = 7.0, 4H), 1.49 (sxt, J = 7.4, 4H), 0.97 (t, J = 7.4, 6H) ppm. ^{13}C NMR (75 MHz, $CDCl_3$): δ 149.33, 118.46, 114.89, 69.57, 31.27, 19.28 ppm.

Intermediate **2-OC4** was synthesized according to the general Suzuki coupling procedure, on a 1.00 g (2.63 mmol) scale of **1-OC4**. The desired product was obtained as a yellow oil in 95% yield (2.25 g, 2.51 mmol). ^{1}H NMR (500 MHz, $CDCl_3$): δ 6.84 (s, 2H), 6.64 (s, 2H), 6.62 (s, 2H), 6.5365 (dd, J = 3.4, 2H), 4.04 (t, J = 6.7, 4H), 1.82 (p, J = 7.0, 4H), 0.97 (s, 18H), 0.93 (s, 18H), 0.18 (s, 12H), 0.07 (s, 12H) ppm. ^{13}C NMR (75 MHz, $CDCl_3$): δ 148.20, 146.32, 145.51, 123.0, 122.70, 120.39, 69.39, 59.16, 31.65, 26.11, 19.43, 18.58, 18.53, 14.01, -3.89, -4.0 ppm.

Intermediate **3-OC4** was synthesized according to the general oxidation procedure, on a 2.54 g (2.84 mmol) scale of **2-OC4**. The desired product was obtained as a yellow oil in quantitative yields. ^{1}H NMR (500 MHz, $CDCl_3$): δ 7.82 (s, 2H), 7.79 (s, 2H), 7.74 (s, 2H), 4.21 (t, J = 6.7, 4H), 1.91 (p, J = 7.1, 4H), 1.58 (sxt, J = 7.3, 4H), 1.07 (s, 18H), 1.06 (s, 18H), 0.31 (s, 12H), 0.30 (s, 12H) ppm. ^{13}C NMR (75 MHz, $CDCl_3$): δ 149.08, 146.80, 124.19, 124.11, 123.55, 114.17, 107.35, 69.37, 31.50, 26.25, 19.50, 18.84, 14.02, -3.86 ppm.

The ligand **H_4TOTP-OC4** was synthesized according to the general deprotection procedure, on a 2.50 g (2.80 mmol) scale of **3-OC4**. The desired product was obtained as a gray solid in 79% yield (0.96 g, 2.20 mmol). ^{1}H NMR (500 MHz, DMSO-d_6): δ 9.43 (s, 2H), 9.19 (s, 2H), 7.82 (s, 2H), 7.74 (s, 2H) 7.64 (s, 2H), 4.17 (t, J = 6.4, 4H), 1.80 (p, J = 6.9, 4H), 1.5293 (sxt, J = 7.3, 4H), 0.99 (t, J = 7.3, 6H) ppm. ^{13}C NMR (75 MHz, DMSO-d_6): δ 148.00, 145.62, 145.39, 122.62, 122.29, 121.75, 108.38, 107.71, 106.48, 68.26, 31.02, 18.82, 13.72 ppm. MS (ESI/ion trap) *m/z*: $[M+H]^+$ Calcd for $C_{26}H_{29}O_6$: 437.2; found 437.2.

Characterization of R = C6 intermediates and H_4TOTP-OC6:

Intermediates **1-OC6**, **2-OC6**, and **3-OC6** were synthesized according to the general procedures. The obtained ^{1}H NMR was consistent with previously reported procedures.[1]

H_4TOTP-OC6. ^{1}H NMR (500 MHz, DMSO-d_6): δ 9.44 (s, 2H), 9.18 (s, 2H), 7.81 (s, 2 H), 7.73 (s, 2H), 7.64 (s, 2H), 4.16 (t, J = 6.2, 4H), 1.80 (p, J = 7.0, 4H), 1.51 (p, J = 6.9, 4H), 1.36 (m, 8H), 0.90 (t, J = 6.9, 6H) ppm. ^{13}C NMR (75 MHz, DMSO-d_6): δ 148.00, 145.60, 145.37, 122.61, 122.28, 121.75, 108.36, 107.69, 106.47, 68.52, 31.01, 28.89, 25.27, 22.06, 13.77 ppm. MS (ESI/ion trap) *m/z*: $[M+H]^+$ Calcd for $C_{30}H_{37}O_6$: 493.2; found 493.2.

Characterization of R = C18 intermediates and H_4TOTP-OC18:

Intermediate **1-OC18** was synthesized according to the general alkylation procedure with several modifications, including substitution of MeCN with DMF. The reaction was performed on a 2.00 g (7.47 mmol) scale of 4,5-dibromobenzene-1,2-diol and 20 mL of DMF, and the reaction was heated at 110 °C for 24 hr. Upon completion of the reaction, ~150 mL of H_2O was added and the precipitate was filtered, washed with water (2x100 mL), MeOH (2x50 mL), and hexanes (2x50 mL). The desired product was obtained as a white solid in 91% yield (5.25 g, 6.79 mmol). ^{1}H NMR (500 MHz, $CDCl_3$): δ 7.06 (s, 2H), 3.94 (t, J = 6.6, 4H), 1.80 (p, J = 6.9, 4H), 1.44 (p, J = 7.2, 4H), 1.26 (m, 60H), 0.88 (t, J = 6.9, 6H) ppm. ^{13}C NMR (75 MHz, $CDCl_3$): δ 149.32, 118.51, 114.90, 69.90, 32.08, 29.86, 29.76, 29.51, 29.26, 26.10, 22.83, 14.23 ppm.

Intermediate **2-OC18** was synthesized according to the general Suzuki coupling procedure with slight modifications. A 2-neck, 250 mL roundbottom equipped with a reflux condenser was charged with a stir bar, 2.50 g of **1-OC18** (3.23 mmol, 1.00 equiv), 3.12 g of **Ar-Bpin** (6.72 mmol, 2.10 equiv), 1.77 g K_2CO_3 (12.8 mmol, 4.00 equiv), and 20 mL of H_2O and 80 mL of THF. The solution was placed under N_2 and sparged for 30–40 min. Under an N_2 flow, Pd SPhos G2 (46.6 mg, 0.0646 mmol, 0.0200 equiv) was added and the reaction was heated at 60 °C for 14 hr. The reaction was diluted with Et_2O (100 mL) and H_2O (100 mL), and the organic layer was separated. The aqueous layer was extracted with additional Et_2O (2x50 mL). The combined organic extracts were dried with $MgSO_4$, filtered through celite, and concentrated *in vacuo* to obtain an oily solid in quantitative yield. ^{1}H NMR (500 MHz, $CDCl_3$): δ 6.84 (s, 2H), 6.34 (m, 4H), 5.54 (dd, J = 3.5, 2H), 4.03 (t, J = 6.6, 4H), 1.83 (p, J = 7.1, 4H), 1.47 (p, J = 7.4, 4H), 1.25 (m, 60H), 0.97 (s, 18H), 0.93 (s, 18H), 0.88 (t, J = 7.1, 6H), 0.18 (s, 12H), 0.07 (s, 12H) ppm. ^{13}C NMR (75 MHz, $CDCl_3$): δ 148.16, 146.32, 145.51, 135.33, 133.05, 123.00, 122.70, 120.40, 116.67, 69.68, 32.09, 29.88, 29.62, 29.52, 26.27, 26.12, 22.84, 18.58, 18.53, 14.24 ppm.

Intermediate **3-OC18** was synthesized according to the general oxidation procedure, on a 4.17 g (3.24 mmol) scale of **2-OC18**. The semi-solid was further washed with a small amount of acetone (~10 mL). The desired product was obtained as a light purple solid in 80% yield (3.35 g, 2.60 mmol). ^{1}H NMR (500 MHz, $CDCl_3$): δ 7.81 (s, 2H), 7.78 (s, 2H), 7.73 (s, 2H), 4.19 (q, J = 6.6, 4H), 1.92 (p, J = 9.6, 4H), 1.25 (m, 60H), 1.06 (m, 36H), 0.88 (t, J = 6.9, 6H), 0.31 (m, 24H) ppm. ^{13}C NMR (75 MHz, $CDCl_3$): δ 146.62, 124.02, 123.92, 123.36, 114.00, 107.16, 69.51, 31.91, 29.70, 29.49, 29.34, 26.08, 22.66, 18.66, 14.05, -4.03 ppm.

The ligand **H_4TOTP-OC18** was synthesized according to the general deprotection procedure with slight workup modifications, on a 3.35 g (2.60 mmol) scale of **3-OC18**. Upon addition of 1 M HCl during the standard workup procedure, the product crashed out as an off-white solid. The precipitate was filtered, washed with H_2O (3x50 mL), MeOH (3x50 mL), and hexanes (3x50 mL). The desired product was obtained as a light gray solid in 95% yield (2.05 g, 2.47 mmol). ^{1}H NMR (500 MHz, DMSO-*d_6*): δ 7.74 (s, 2H), 7.67 (s, 2H), 7.65 (s, 2H), 4.12 (t, J = 6.0, 4H), 1.82 (p, J = 6.9, 4H), 1.51 (p, J = 7.4, 4H), 1.20 (m, 64 H), 0.82 (t, J = 6.8, 3H) ppm. ^{13}C NMR could not obtained due to solubility issues. MALDI-TOF *m/z*: $[M]^-$ Calcd for $C_{54}H_{84}O_6$: 828.63; found 824.86.

2.6.4. X-ray absorption spectroscopy.

Sample preparation: XAS samples were prepared using commercially available powder samples of Cu_2O, $Cu(acac)_2$, and CuO with purity >99.9%, purchased from Fisher Scientific and used without further purification. CuTOTP-OC4 samples were synthesized and purified according to procedures described below. Samples were finely ground and mixed with powder hexagonal Boron Nitride (BN) which were then pressed into ~1 mm-thick pellets. The pellets were finally sealed in a Kapton tape envelope.

Measurement details: All XAS measurements were performed in transmission mode. The XANES measurements were performed with a laboratory-based X-ray absorption spectrometer, described in detail in Jahrman, et al.[4] The X-ray source has a Pd anode and was operated at ~100 W power (35 kV and 2.8 mA). The EXAFS measurements were performed in a similar instrument easyXAFS300 (easyXAFS, Renton, WA, USA) employing a Mo anode and operated at ~210 W power (35 kV and 6 mA). The XANES measurements for CuTOTP-OC4 shown in **Fig. 2.3** of the main text were obtained on the easyEXAFS instrument, while the measurements for CuTOTP-OR shown in **Fig. 2.S5** and **2.S6** were obtained on the UW laboratory instrument. A Si (553) spherically bent crystal analyzer (SBCA) had favorable Bragg angles and energy resolution for the required energy range. Each XAS scan spanned the energy range from 100 eV below the Cu K-edge to 150 eV above edge for XANES and up to k = 12 from edge for the EXAFS analysis. All measurements were calibrated using the first derivative of a Cu foil reference. The XAS data were background subtracted and normalized using LARCH package.[5] EXAFS fitting was performed using the LARCH package that employs the FEFF project.[6] for modeling the scattering paths. The CIF file was used from the 'American Mineralogical CIF Database' available through the LARCH package.

2.6.5. X-ray photoelectron spectroscopy.

X-ray photoelectron spectra (XPS) were collected on a Kratos Axis Ultra DLD X-ray photoelectron spectrometer using a monochromatic Al Kα x-ray source. Samples were prepared by pressing the powder onto a piece of double-sided Scotch tape. A low energy electron flood gun was used for charge neutralization of the sample. High-resolution spectra were obtained using an analysis area of ~ 700 × 300 μm and a 20 eV pass energy. Survey spectra were collected at a pass energy of 80 eV. Cu high resolution scans were collected first to minimize x-ray damage, and the Cu 2p peak was used for the following analysis. Data analysis and curve-fitting was carried out using CasaXPS.[7] A standard Shirley background was used for all samples, and Gaussian (30%)-Lorentzian (70%) (GL(70)) profiles were used for each component. Spectra are referenced to the C 1s hydrocarbon peak calibrated to 285.0 eV.

The %Cu(II) was quantified according to a previously reported procedure that uses the relative areas of the Cu $2p_{3/2}$ main peak and shake-up satellite peaks to estimate the Cu(II) and Cu(I) + Cu(0) content.[8] Specifically, the equation shown below was used, where A = the area of the main peak in the sample of interest, B = the area of the shake-up satellite peak in the sample of interest, and $A1_s/B_s$ = the ratio of the main peak/shake-up peak in a 100% pure, reference Cu(II) compound:

$$\%Cu(II) = \frac{B(1 + \frac{A1_s}{B_s})}{A + B} * 100$$

We note that the constant $A1_s/B_s$ can vary widely across reference Cu(II) compounds (e.g., $Cu(OH)_2$ 1.57, CuO 1.89, $CuBr_2$ 2.45).[8] We have chosen $Cu(acac)_2$ and $Cu(OAc)_2 \cdot H_2O$ as our reference compounds, because they mimic the ligand environment of CuTOTP-OR. We obtained very similar $A1_s/B_s$ values of 0.9 for $Cu(acac)_2$ and 1.1 for $Cu(OAc)_2 \cdot H_2O$ (**Table 2.S3**); the average value of 1.0 was used for our data analysis. We note that, due to poor signal-to-noise, errors in curve-fitting, and uncertainties in $A1_s/B_s$, our XPS data can only provide a rough estimate of the %Cu(II). Nevertheless, the values obtained (90–100% Cu(II), see **Table 2.S5**) are consistent with XANES data, which show K-edge energies and spectral features indicative of Cu(II) (**Figs. 2.S5** and **2.S6**).

2.6.6. Electrochemical characterization.

All cyclic voltammetry and conductivity measurements were carried out using a BioLogic SP-200 Potentiostat. Conductivity measurements were run on packed pellets using a 2-electrode screw cell. A polyetheretherketone (PEEK) spacer with a 2.8 mm smooth internal diameter was prepared with threading for two brass screws to compress powders from either side.[9] The tips of the screws were polished to a flat surface 2.75 mm in diameter. Cells were prepared by screwing one screw into the PEEK spacer, then adding 8-10 mg of powder, and screwing the second screw in finger-tight, and then tightening to 0.56 Nm with a controlled torque screwdriver on both screws. Sample thicknesses were measured with calipers and were typically in the range of 400–800 μm. Cells were allowed to settle for 8 h, before re-tightening to 0.56 Nm and settling for an additional 18 h at which point I-V curves measured using either current scan (CS) (R = C2, C4, C6) or cyclic voltammetry (CV) (R = C18.

Additional control experiments were conducted wherein a 1:1 mol mixture of H_4TOTP-OC2 with copper acetate monohydrate was mixed in a mortar and pestle, then packed into a conductivity cell as detailed above. Samples were non-conductive, demonstrating the importance of the long-range order in facilitating charge transport. An identical experiment was performed using a 1:1 mol mixture of the tert-Butyldimethylsilyl-protected derivative, **3**-OC2, and copper acetate monohydrate was also non-conductive.

Cyclic voltammetry was conducted in 0.05 M acetonitrile solutions of sodium perchlorate ($NaClO_4$) in a N_2 filled glovebox using a glassy carbon working electrode, Pt wire counter electrode, and Ag wire pseudo-reference electrode. Glassy carbon working electrodes were cleaned with water, acetone, and isopropanol and polished with 0.05 μm diameter alumina powder before use. Cyclic voltammetry data is collected at a scan rate of 10 mV s^{-1}.

2.6.7. Charge transport property measurements.

Heavily boron-doped silicon substrates with a 300 nm (± 5 nm) thick thermal oxide layer (University Wafer) as a gate dielectric were used for the thin-film field-effect transistors (FETs). Substrates were first scrubbed with detergent and water and then sonicated in DI water, acetone, and IPA for 15 min per solvent, followed by drying under a stream of compressed nitrogen. The substrates were then cleaned in a plasma cleaner for 15 min using air plasma. To passivate the thermal oxide, a vacuum vapor deposition of octadecyl trichlorosilane (ODTS) on the cleaned substrates was used. After the ODTS deposition, the substrates were rinsed with chloroform ($CHCl_3$) and IPA to remove any physiosorbed ODTS from the surface. The macrocycle layer was then spin-coated from a 5 mg/mL solution in $CHCl_3$ at 2500 RPM for 60 s onto the ODTS passivated substrates in a N_2 environment. Gold electrodes were thermally evaporated onto the active layer to a thickness of 100 nm at a rate of 0.5 Å s^{-1}. The gold was evaporated from an alumina coated Mo boat and the electrodes were deposited through a shadow mask. After electrode deposition, the devices were tested for charge mobility and current on/off ratio. The devices had a top-contact bottom-gate architecture with a channel width of 1000 µm and a channel length of 50 µm. They were tested in a nitrogen atmosphere using a Signatone Probe Station and two Keithley 2400 Source-Measure units. The transfer curves were collected in the saturation regime, where the linear section of the curve was fitted to estimate the charge mobility using the following equation:

$$I_D = \frac{W\ C\ \mu}{2L}(V_G - V_t)^2$$

where I_D is the drain-source current; μ_{sat} is the charge mobility; W is the channel width; L is the channel length; C is the capacitance per unit area of the insulator (SiO_2, 300 nm, 10 $nF \cdot cm^{-2}$).[10,11] V_G is the gate voltage; and V_t is the threshold voltage. The threshold voltage was obtained by fitting the linear region of the I_D^2 vs V_G curve and extrapolating to $I_D = 0$. Measurements were averaged from at least five transistors across three substrates and devices.

2.6.8. Supplementary tables.

Table 2.S1 | Summary of dynamic light scattering (DLS) measurement results for number particle size distribution (PSD). All values shown are for CuTOTP-OC18 macrocycle.

Solvent	**Diameter (nm)**	**St. Dev. (nm)**
THF	5.174	1.120
$CHCl_3$	5.367	0.787
Toluene	3.939	0.944

Table 2.S2 | Summary of EXAFS fit parameters and results for $Cu(acac)_2$ and CuTOTP-OC4.

		$Cu(acac)_2$	**CuTOTP-OC4**
Input parameters	Fit space	R	R
	R-range	1.0, 6.0	1.0, 6.0
	k-range	2.5, 11.18	2.5, 11.16
	k window, dk	'Kaiser-Bessel', 4.0	'Kaiser-Bessel', 4.0
Fit results	Coordination (N)	2.53+/-0.27	2.93 +/- 0.37
	delr	(-)0.029+/-0.009	0.012+/-0.011
	E0	7.23+/-1.27	8.44+/-1.43
	sigma2	0.0035+/-0.0012	0.0041+/-0.0017
	R	1.90+/-0.01	1.94+/-0.01

Table 2.S3 | Summary of Cu $2p_{3/2}$ XPS curve-fitting parameters for reference compounds $Cu(acac)_2$ and $Cu(OAc)_2 \cdot H_2O$.

	$Cu(acac)_2$	**$Cu(OAc)_2 \cdot H_2O$**
GL(X) value	70	70
Peak 1 (eV)	935.09	934.50
%	47.74	52.40
FWHM	1.22	2.53
Peak 2 (eV)	939.87	940.33
%	38.27	29.39
FWHM (eV)	2.71	3.50
Peak 3 (eV)	944.77	944.13
%	22.99	18.20
FWHM	3.03	2.61

Table 2.S4 | Summary of the XPS Cu $2p_{3/2}$ main peak ($A1_s$) and shake-up satellite peak areas (B_s) for reference Cu(II) compounds $Cu(acac)_2$ and $Cu(OAc)_2 \cdot H_2O$.

Sample	**Main peak area** ($A1_s$) (%)	**Shake-up peak area** (B_s) (%)	**$A1_s/B_s$**
$Cu(acac)_2$	47.74	52.26	0.91
$Cu(OAc)_2 \cdot H_2O$	52.40	47.59	1.10

Table 2.S5 | Summary of Cu $2p_{3/2}$ XPS curve-fitting parameters for CuTOTP-OR (R = C2, C4, C6, C18).

	R = C2	**R = C4**	**R = C6**	**R = C18**
GL(x) value	70	70	70	70
Peak 1 (eV)	932.62	931.12	932.36	932.59
%	5.02	6.89	6.48	16.12
FWHM	1.27	1.56	1.64	1.77
Peak 2 (eV)	934.58	932.74	934.22	934.36
%	23.59	14.74	25.91	31.81
FWHM (eV)	1.28	1.02	1.29	1.42
Peak 3 (eV)	935.34	933.32	935.05	935.87
%	21.36	31.02	17.98	6.97
FWHM	2.70	2.16	2.48	1.61
Peak 4 (eV)	940.12	938.43	939.95	939.87
%	26.72	29.55	35.65	30.55
FWHM	4.73	4.73	5.50	5.50
Peak 5 (eV)	944.05	942.25	943.84	943.93
%	23.31	17.81	13.98	14.56
FWHM	4.00	2.94	2.79	2.80

Table 2.S6 | Summary of the XPS main peak (A1) and shake-up satellite peak areas (B) for CuTOTP-OR (R = C2, C4, C6, C18). The % Cu was calculated using the equation shown below.[8] An $A1_s/B_s$ ratio of 1 was used, based on curve-fitting of reference compounds $Cu(acac)_2$ and $Cu(OAc)_2 \cdot H_2O$ (see **Table S3**).

$$\%Cu(II) = \frac{B(1 + \frac{A1_s}{B_s})}{A + B} * 100$$

Sample	**Main peak area** (A) (%)	**Shake-up peak area** (B) (%)	**% Cu(II)**
CuTOTP-OC2	49.97	50.03	100.06
CuTOTP-OC4	52.65	47.36	94.71
CuTOTP-OC6	50.37	49.63	99.26
CuTOTP-OC18	54.90	45.11	90.21

Table 2.S7 | Pellet conductivities for $Cu_3(HHTP)_2$ collected with 2-electrode screw cell. $Cu_3(HHTP)_2$ synthesized according to previously reported procedures.[12]

Sample	**Conductivity** (S cm^{-1})
$Cu_3(HHTP)_2$ pellet 1	6×10^{-3}
$Cu_3(HHTP)_2$ pellet 2	4×10^{-3}
$Cu_3(HHTP)_2$ pellet 3	7×10^{-3}

Table 2.S8 | Brunauer–Emmett–Teller (BET) surface area of CuTOTP-OC2.

BET fit values	**Values**
BET surface area	226.1698 ± 2.5043 m^2/g
Slope	0.37250 ± 0.00417 g/mmol
Y-intercept	0.00560 ± 0.00035 g/mmol
C	67.558525
Qm	2.64480 mmol/g
Correlation coefficient	0.9994359

2.6.9. Supplementary figures.

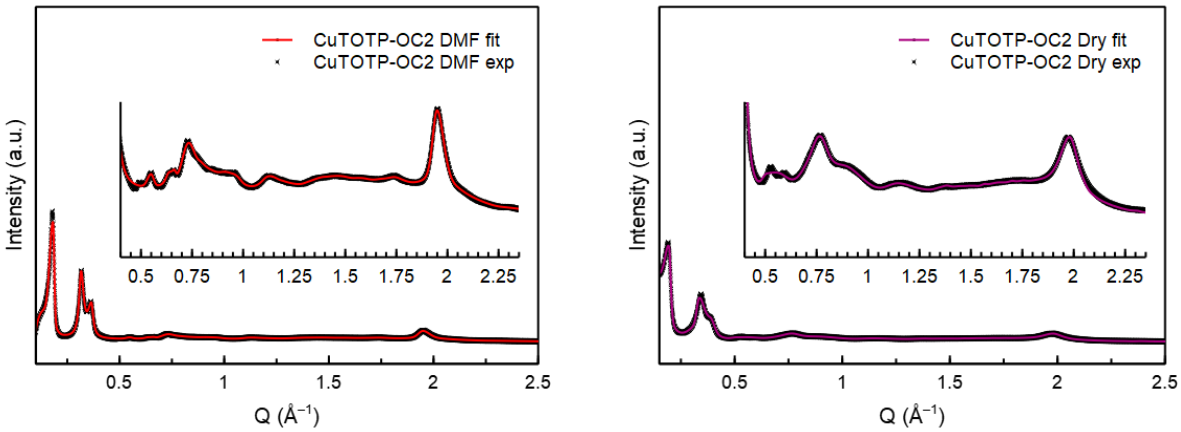

Fig. 2.S1 | Powder X-ray diffraction data obtained from DMF-soaked and dried CuTOTP-OC2 sealed inside a Kapton capillary. The black crosses and solid line represent the experimental and calculated diffraction patterns, respectively.

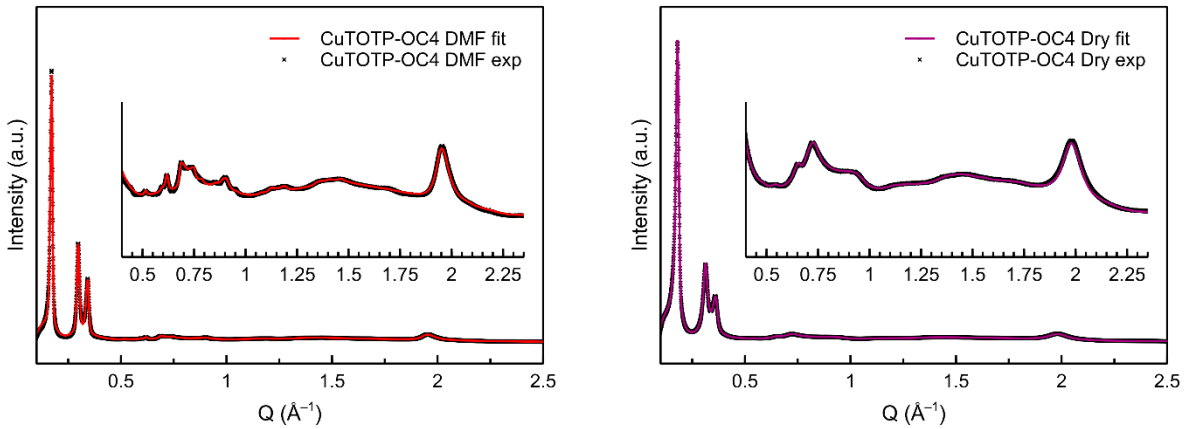

Fig. 2.S2 | Powder X-ray diffraction data obtained from DMF-soaked and dried CuTOTP-OC4 sealed inside a Kapton capillary. The black crosses and solid line represent the experimental and calculated diffraction patterns, respectively.

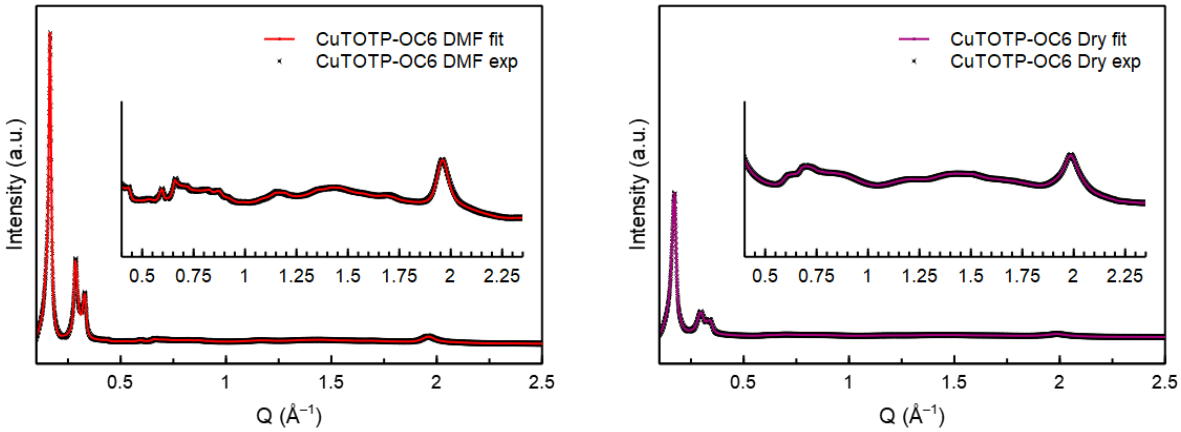

Fig. 2.S3 | Powder X-ray diffraction data obtained from DMF-soaked and dried CuTOTP-OC6 sealed inside a Kapton capillary. The black crosses and solid line represent the experimental and calculated diffraction patterns, respectively.

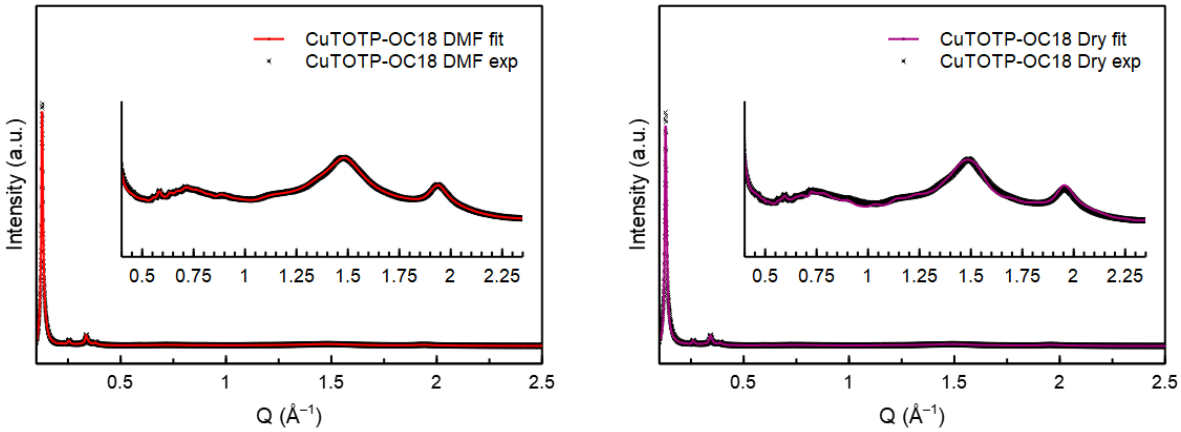

Fig. 2.S4 | Powder X-ray diffraction data obtained from DMF-soaked and dried CuTOTP-OC18 sealed inside a Kapton capillary. The black crosses and solid line represent the experimental and calculated diffraction patterns, respectively.

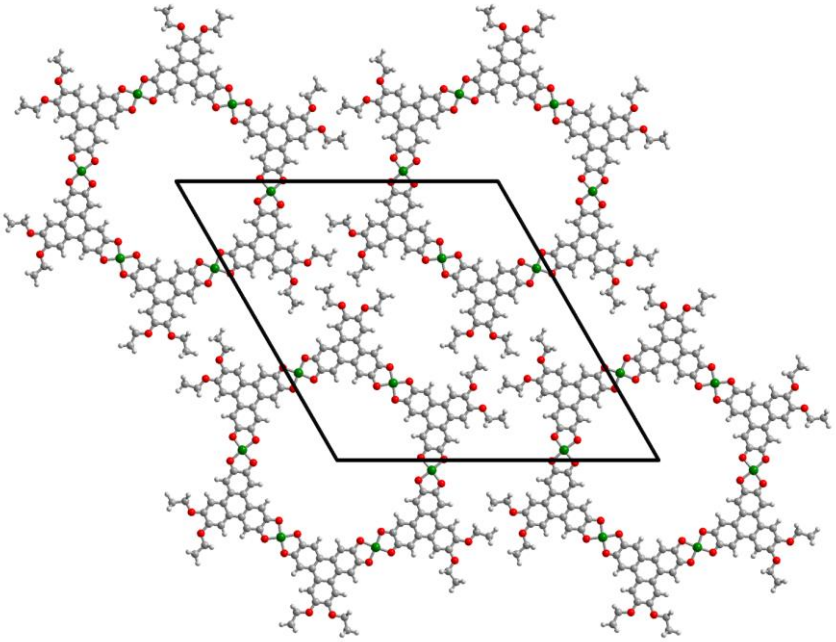

Fig. 2.S5 | Structural model of CuTOTP-OC2. Structures were optimized using the Forcite module in Materials Studio, assuming a P6/m space group. Optimized unit cell dimensions of $a = b = 36.6807$ Å (note: c was fixed at 3.20 Å) were obtained, in reasonable agreement with the experimentally observed value of $a = b = 38.46(3)$ Å.

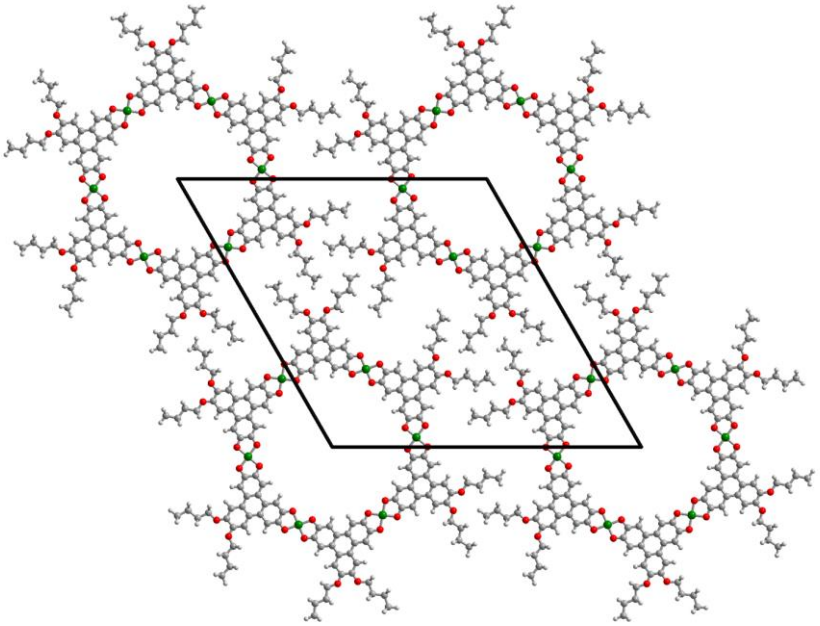

Fig. 2.S6 | Structural model of CuTOTP-OC4. Structures were optimized using the Forcite module in Materials Studio, assuming a P6/m space group. Optimized unit cell dimensions of $a = b = 38.9284$ Å (note: c was fixed at 3.20 Å) were obtained, in reasonable agreement with the experimentally observed value of $a = b = 40.16(2)$ Å.

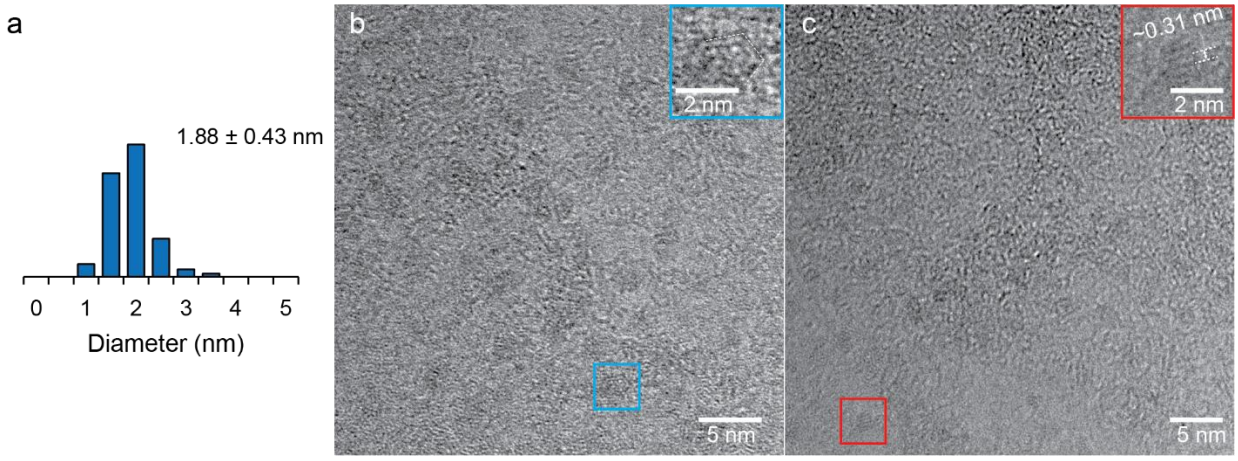

Fig. 2.S7 | TEM images of CuTOTP-OC4 macrocycle. (a) Histogram of 250 macrocycle diameter measurements showing 1.88 ± 0.43 nm, consistent with the expected size of the planar macrocyclic core. Note that peripheral carbon chains are too low contrast, and do not appear in the TEM image. (b) Highlight of macrocycle shape, with blue inset showing hexagonal edges defined against background noise. (c) Highlight of macrocycle stack side-view, with red inset showing defined edges between stacked macrocycles. ~0.31 nm distance between macrocycles matches the 3.17 Å π–π stacking distance found by XRD.

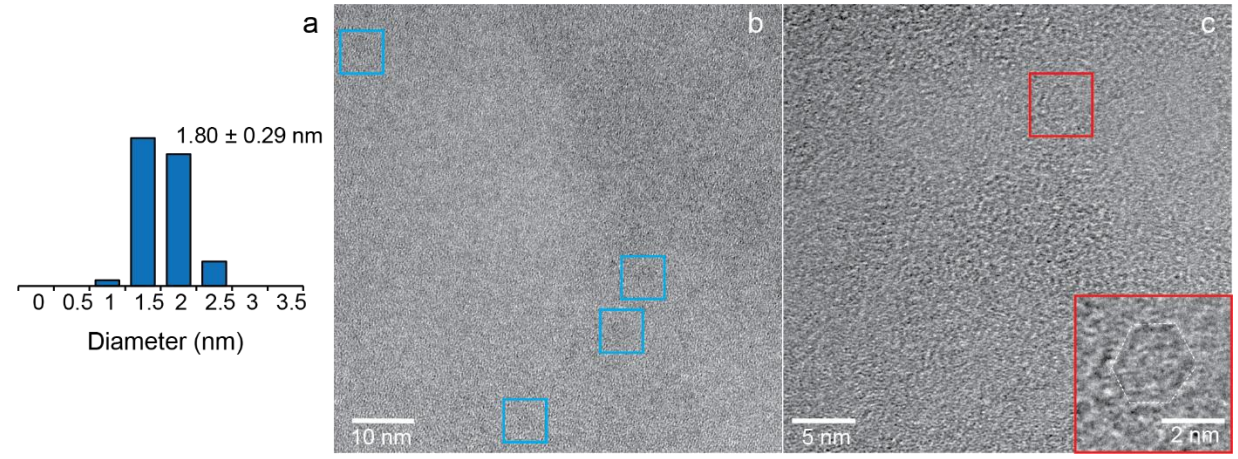

Fig. 2.S8 | TEM images of CuTOTP-OC18 macrocycle. (a) Histogram of 250 macrocycle diameter measurements showing 1.80 ± 0.29 nm, consistent with the expected size of the planar macrocyclic core. Note that peripheral carbon chains are too low contrast, and do not appear in the TEM image. (b) Low contrast C18 macrocycles highlighted in blue. Relatively lower contrast and narrower size distribution for C18 relative to C4 macrocycles may imply thinner stacks, as seen by DLS. (c) Highlight of macrocycle shape, with red inset showing hexagonal edges defined against background noise.

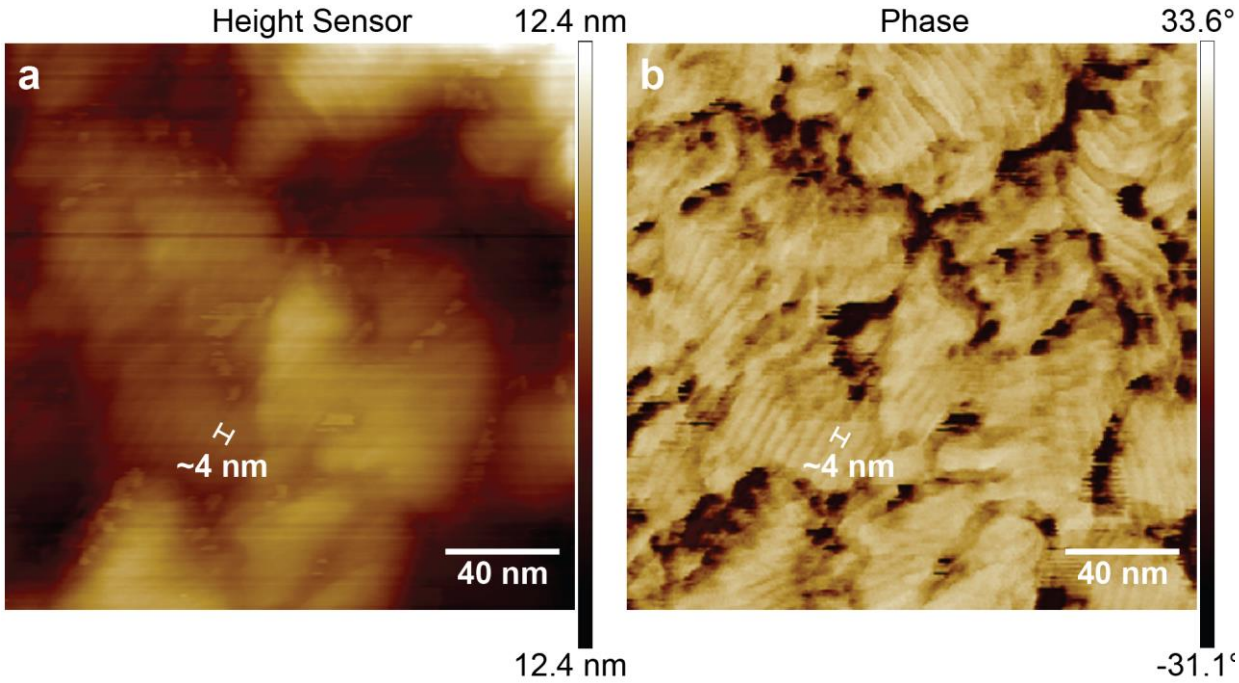

Fig. 2.S9 | AFM images of CuTOTP-OC4 macrocycle. (a) Height sensor with ~4 nm separation between edges shown. Relatively small height differences between layers of macrocycle result in relatively low contrast height sensor images. (b) AFM phase image demonstrating changing chemical interaction between tip and surface, creating oscillation lag in tapping mode. Striations correspond to ~4 nm separation, corresponding well to 40.16 Å unit cell size found by XRD. The average length of the columnar stacks is 23(6) nm (average of 30 measurements).

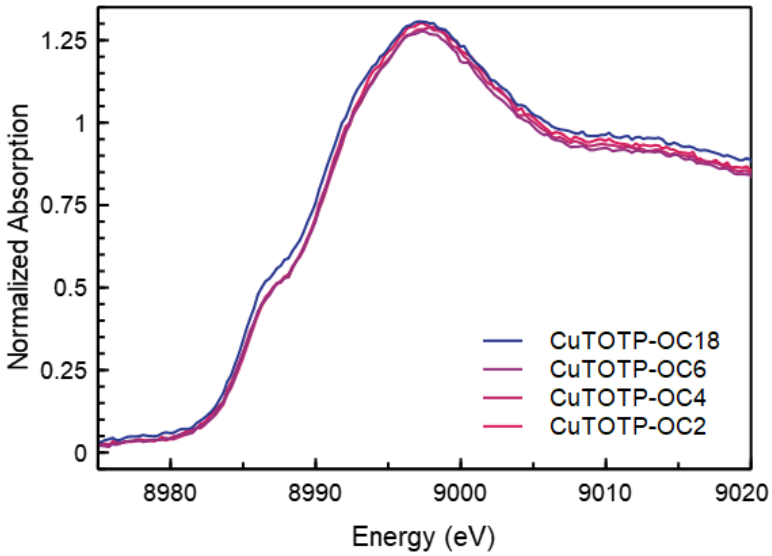

Fig. 2.S10 | Cu K-edge X-ray absorption near-edge spectra (XANES) data for CuTOTP-OR (R = C2, C4, C6, C18).

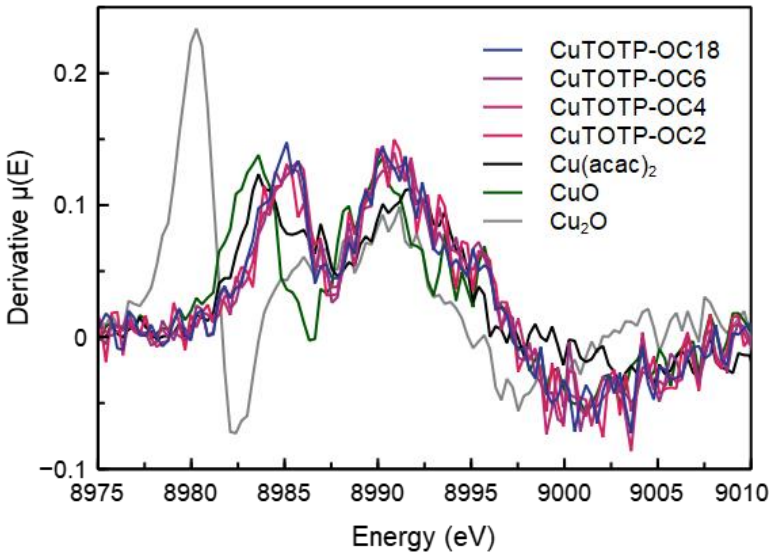

Fig. 2.S11 | First derivative of Cu K-edge XANES data for CuTOTP-OR samples and Cu(I) and Cu(II) references.

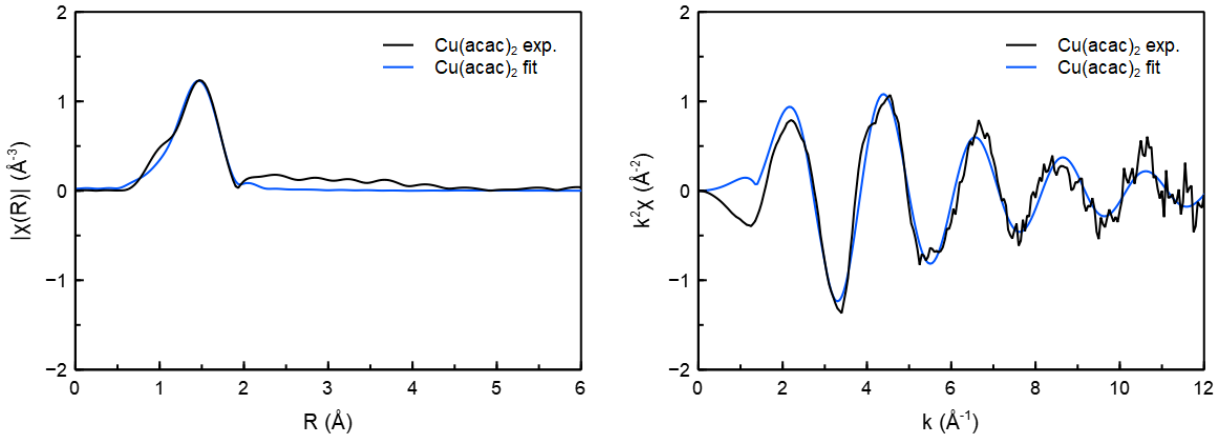

Fig. 2.S12 | Extended X-ray absorption fine structure (EXAFS) experimental data (black line) and fit (blue line) for $Cu(acac)_2$.

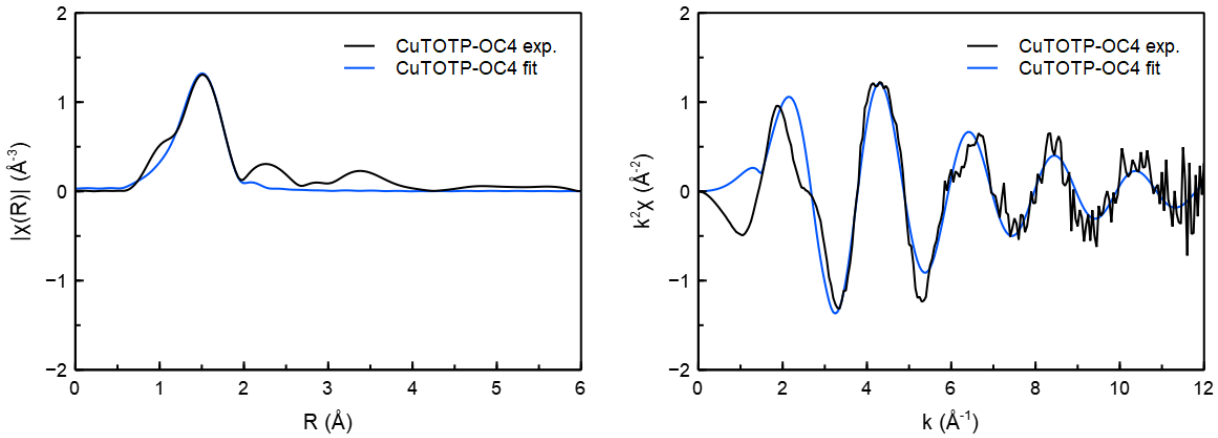

Fig. 2.S13 | Extended X-ray absorption fine structure (EXAFS) experimental data (black line) and fit (blue line) for CuTOTP-OC4.

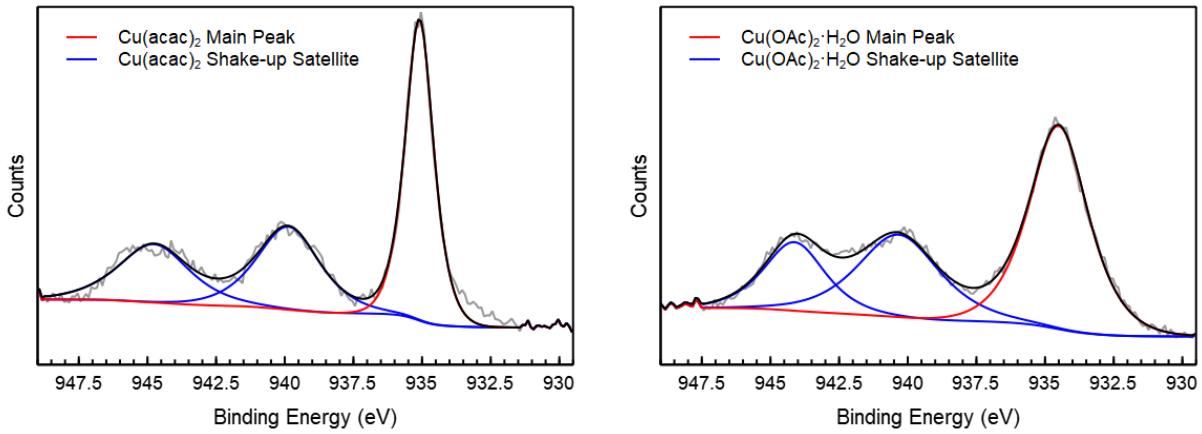

Fig. 2.S14 | Cu $2p_{3/2}$ X-ray photoelectron spectra of reference compounds Cu(II) acetylacetonate (abbreviated $Cu(acac)_2$) and Cu(II) acetate monohydrate ($Cu(OAc)_2 \cdot H_2O$). The experimental data is shown in gray and the overall fit in black. The ratio ($A1_s/B_s$) of the main peak ($A1_s$, red curves) to the shake-up satellite peak area (B_s, blue curves) was determined to be 0.9 for $Cu(acac)_2$ and 1.1 for $Cu(OAc)_2 \cdot H_2O$ (**Table 2.S3**). A summary of the curve-fitting results and data analysis are provided in **Table 2.S2**.

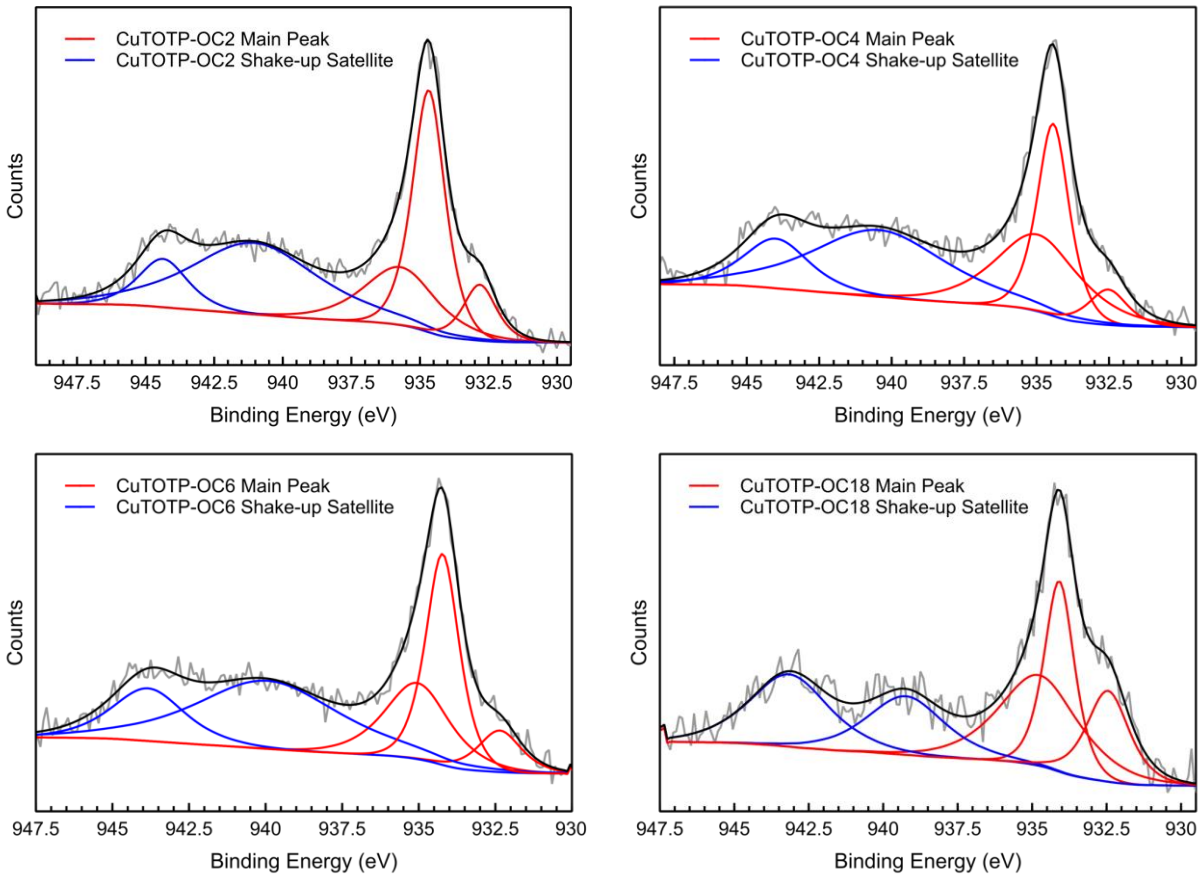

Fig. 2.S15 | Cu $2p_{3/2}$ X-ray photoelectron spectra of CuTOTP-OR (R = C2, C4, C6, C18). The experimental data is shown in gray and the overall fit in black. The ratio of the shake-up satellite area (blue curves) to the main $2p_{3/2}$ peak area (red curves) was used to estimate the Cu(II) to Cu(I) ratio. A summary of the curve-fitting results and data analysis are provided in **Table 2.S4** and **2.S5**, and a more detailed description of the analysis is described in section **2.6.5** of the Supporting Information.

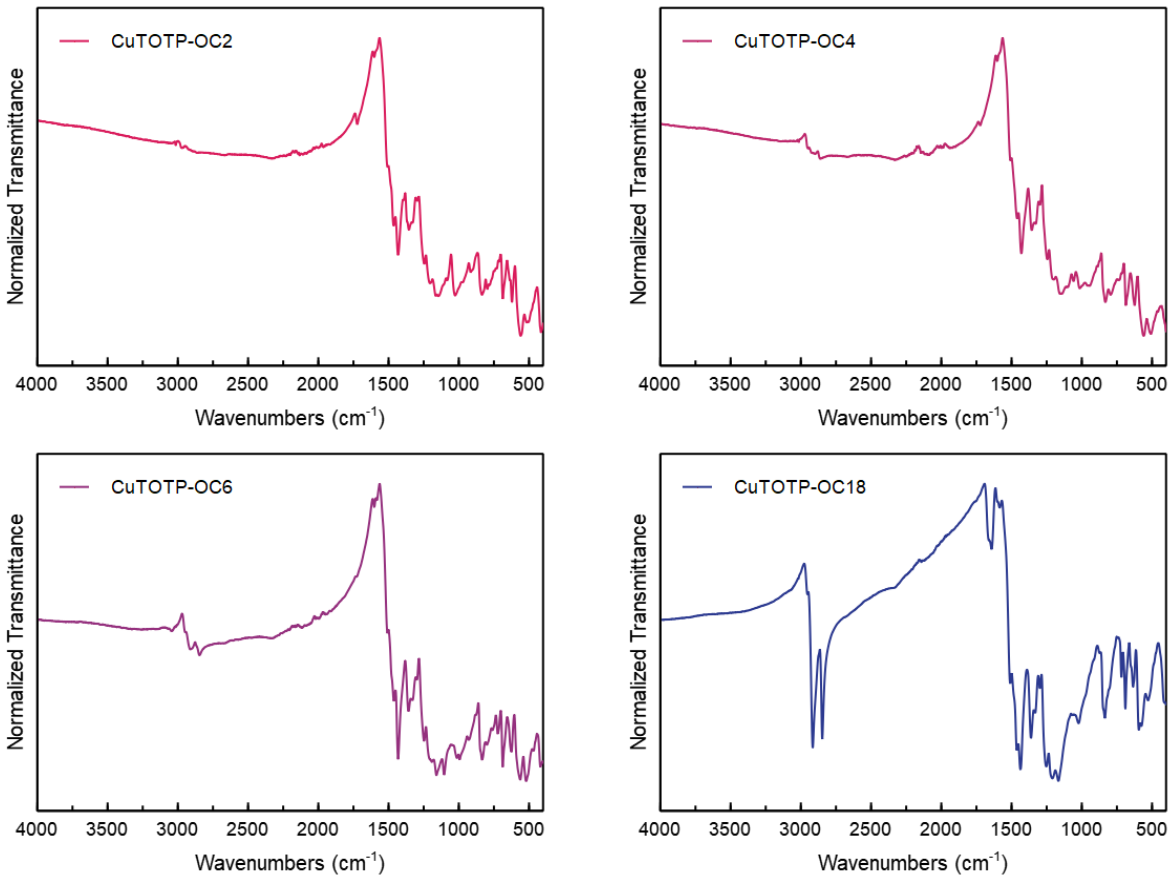

Fig. 2.S16 | Infrared spectra of CuTOTP-OR (R = C2, C4, C6, C18).

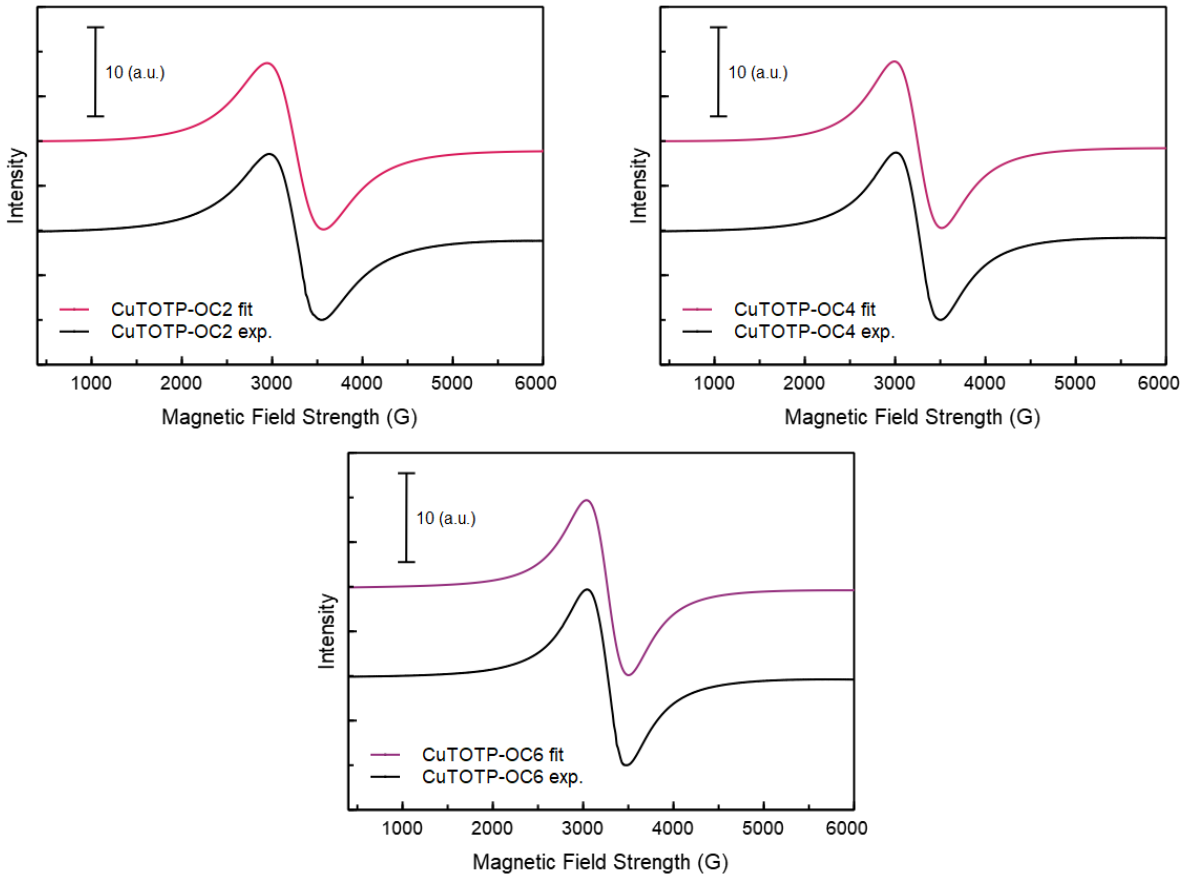

Fig. 2.S17 | Electron paramagnetic resonance (EPR) spectra of CuTOTP-OR (R = C2, C4, C6) and corresponding fits. CuTOTP-OC6, g = 2.106; CuTOTP-OC4, g = 2.116; CuTOTP-OC2, g = 2.114.

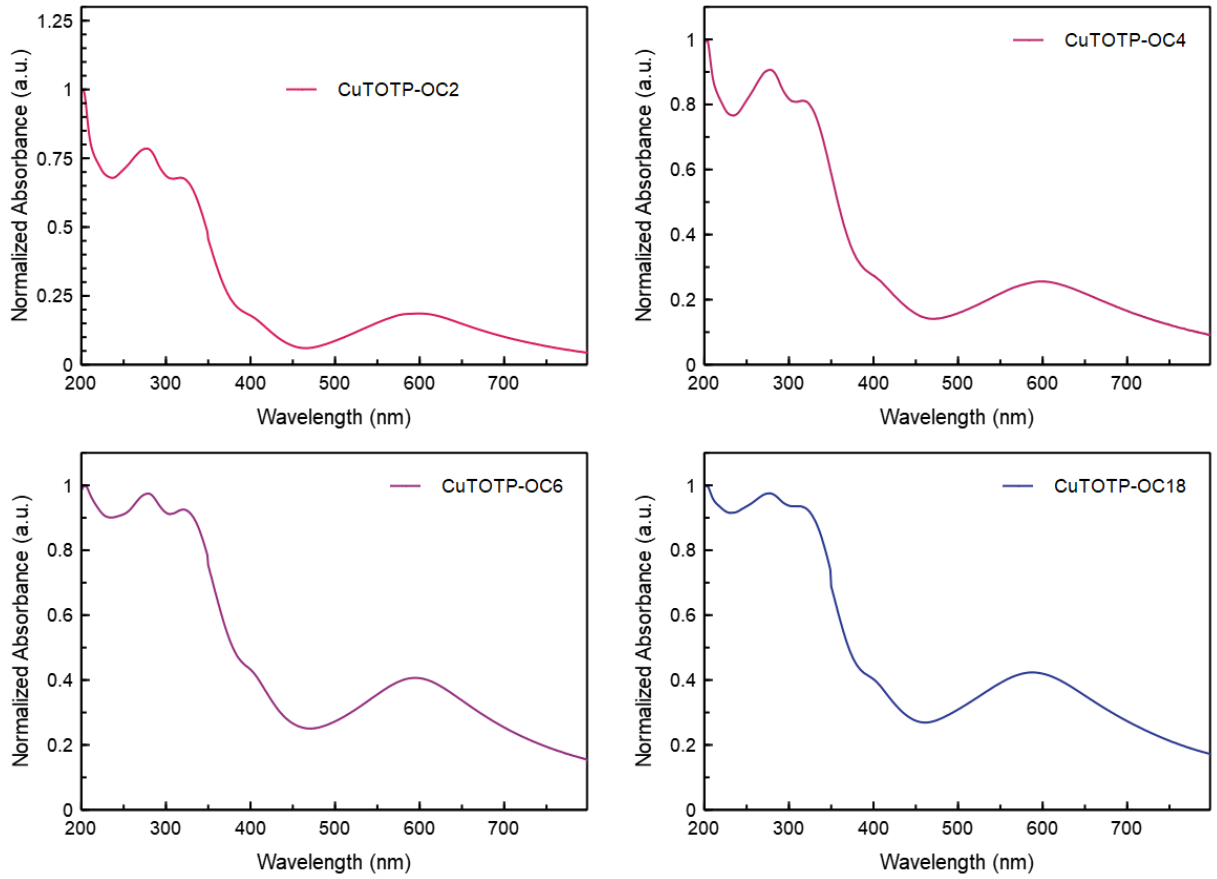

Fig. 2.S18 | UV-Vis spectra of thin films of CuTOTP-OR (R = C2, C4, C6, C18) dropcast on quartz slides.

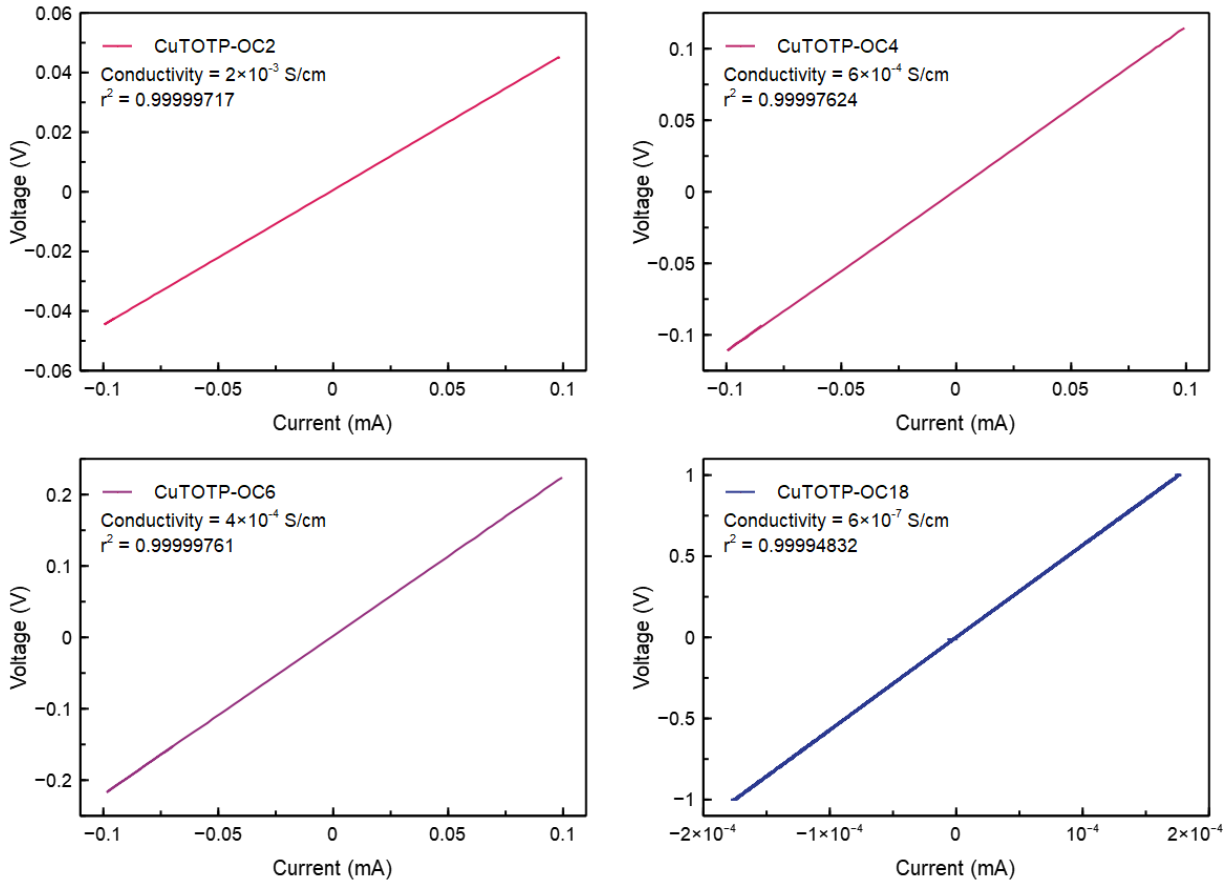

Fig. 2.S19 | I-V curves of CuTOTP-OR (R = C2, C4, C6, C18).

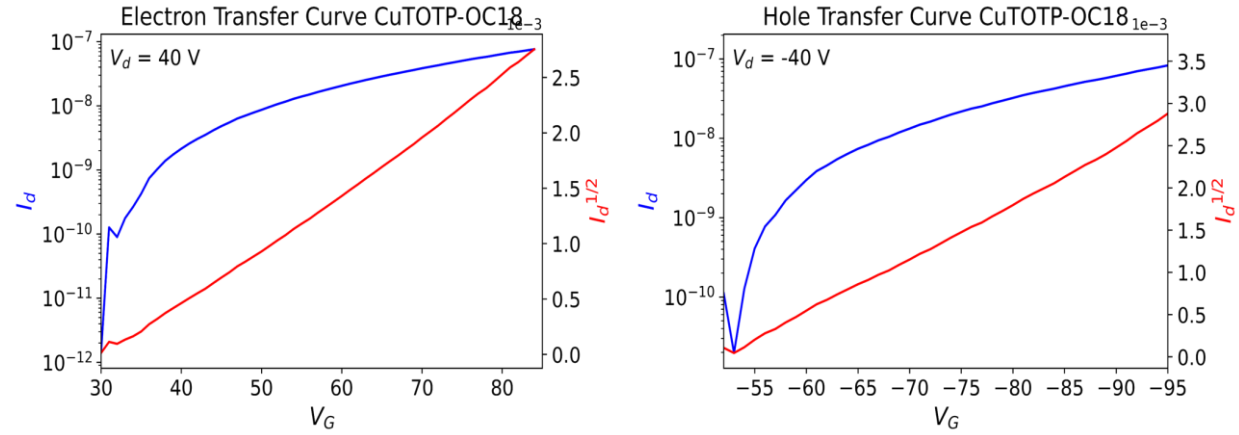

Figure 2.S20 | Representative drain current versus gate voltage curves for CuTOTP-OC18.

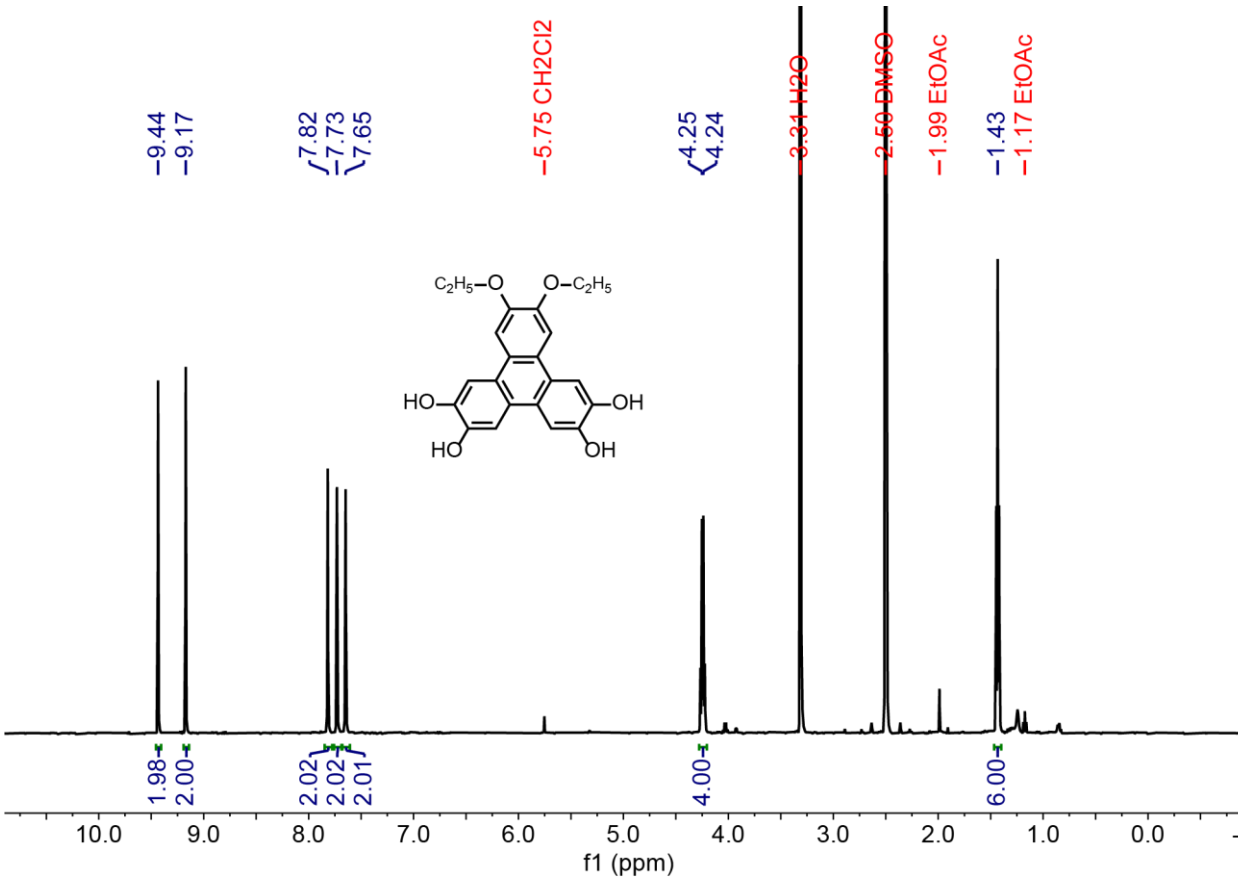

Fig. 2.S21 | The ^{1}H NMR spectrum of H_4TOTP-OC2.

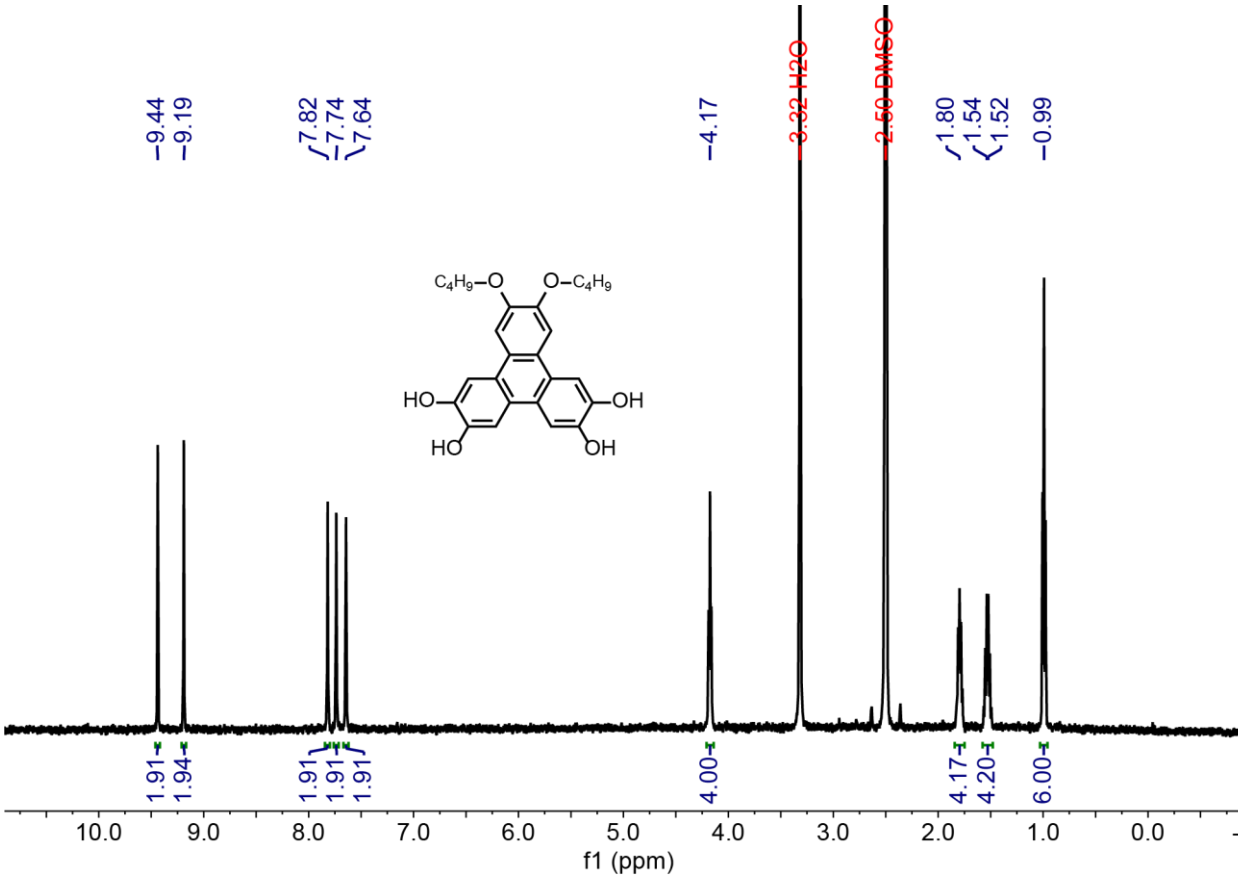

Fig. 2.S22 | The ^{1}H NMR spectrum of **H_4TOTP-OC4**.

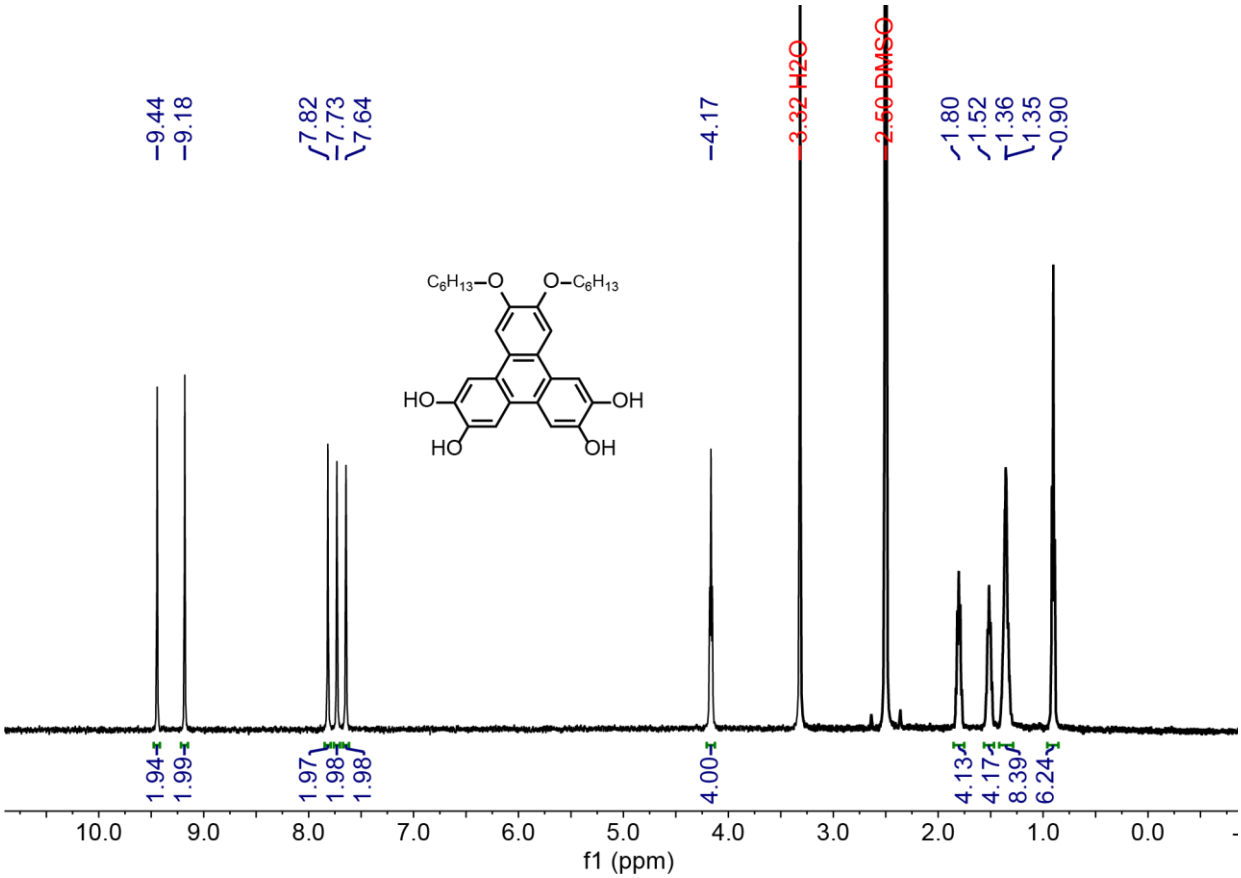

Fig. 2.S23 | The ^{1}H NMR spectrum of **H_4TOTP-OC6**.

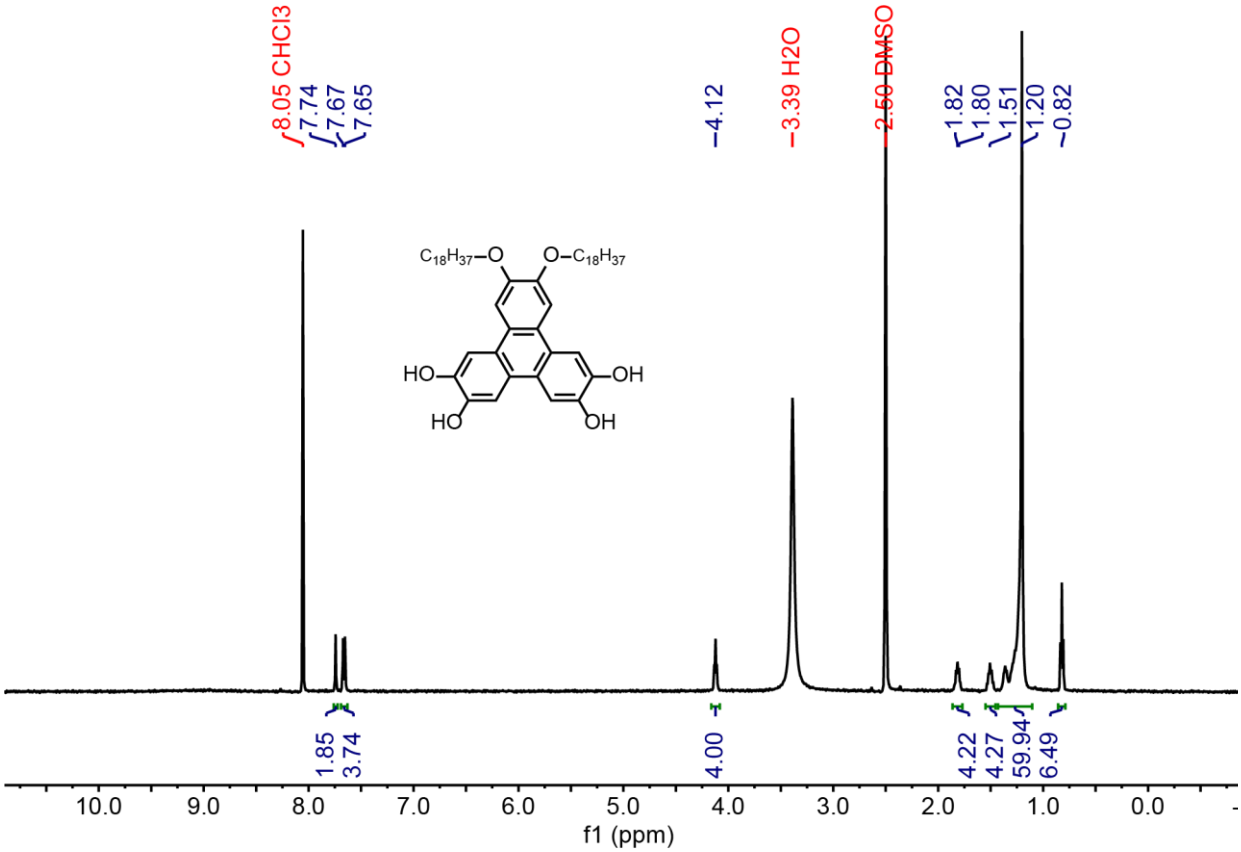

Fig. 2.S24 | The ^{1}H NMR spectrum of **H_4TOTP-OC18**.

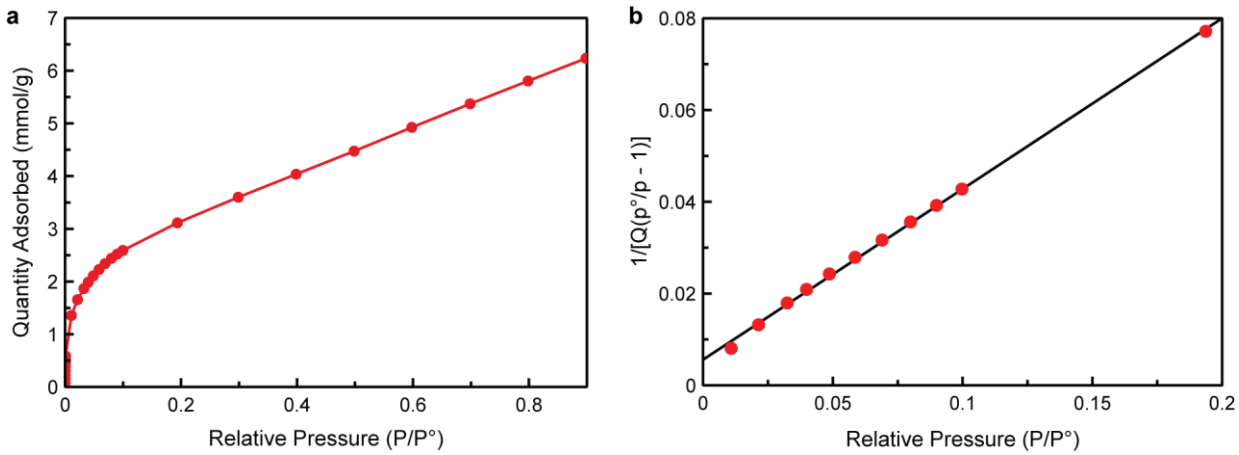

Fig. 2.S25 | a) CO_2 isotherm collected at 195 K for CuTOTP-OC2. b) A BET surface area of 226(3) m^2/g was calculated from 195 K CO_2 isotherm data.

2.6.10 References.

(1) Smith, M. K.; Powers-Riggs, N. E.; Northrop, B. H. Rational Synthesis of Bis(Hexyloxy)-Tetra(Hydroxy)-Triphenylenes and Their Derivatives. *RSC Adv.* **2014**, *4* (72), 38281–38292. https://doi.org/10.1039/C4RA06503D.

(2) Kaller, M.; TussetschlÃ¤ger, S.; Fischer, P.; Deck, C.; Baro, A.; Giesselmann, F.; Laschat, S. Columnar Mesophases Controlled by Counterions in Potassium Complexes of Dibenzo[18]Crown-6 Derivatives. *Chem. Eur. J.* **2009**, *15* (37), 9530–9542. https://doi.org/10.1002/chem.200901173.

(3) PYROGALLOL 1-MONOMETHYL ETHER. *Org. Synth.* **1946**, *26*, 90. https://doi.org/10.15227/orgsyn.026.0090.

(4) Jahrman, E. P.; Holden, W. M.; Ditter, A. S.; Mortensen, D. R.; Seidler, G. T.; Fister, T. T.; Kozimor, S. A.; Piper, L. F. J.; Rana, J.; Hyatt, N. C.; Stennett, M. C. An Improved Laboratory-Based x-Ray Absorption Fine Structure and x-Ray Emission Spectrometer for Analytical Applications in Materials Chemistry Research. *Review of Scientific Instruments* **2019**, *90* (2), 024106. https://doi.org/10.1063/1.5049383.

(5) Newville, M. Larch: An Analysis Package for XAFS and Related Spectroscopies. *J. Phys.: Conf. Ser.* **2013**, *430*, 012007. https://doi.org/10.1088/1742-6596/430/1/012007.

(6) J. Rehr, J.; J. Kas, J.; D. Vila, F.; P. Prange, M.; Jorissen, K. Parameter-Free Calculations of X-Ray Spectra with FEFF9. *Physical Chemistry Chemical Physics* **2010**, *12* (21), 5503–5513. https://doi.org/10.1039/B926434E.

(7) Fairley, N.; Fernandez, V.; Richard-Plouet, M.; Guillot-Deudon, C.; Walton, J.; Smith, E.; Flahaut, D.; Greiner, M.; Biesinger, M.; Tougaard, S.; Morgan, D.; Baltrusaitis, J. Systematic and Collaborative Approach to Problem Solving Using X-Ray Photoelectron Spectroscopy. *Applied Surface Science Advances* **2021**, *5*, 100112. https://doi.org/10.1016/j.apsadv.2021.100112.

(8) Biesinger, M. C. Advanced Analysis of Copper X-Ray Photoelectron Spectra. *Surface and Interface Analysis* **2017**, *49* (13), 1325–1334. https://doi.org/10.1002/sia.6239.

(9) Darago, L. E.; Aubrey, M. L.; Yu, C. J.; Gonzalez, M. I.; Long, J. R. Electronic Conductivity, Ferrimagnetic Ordering, and Reductive Insertion Mediated by Organic Mixed-Valence in a Ferric Semiquinoid Metal–Organic Framework. *J. Am. Chem. Soc.* **2015**, *137* (50), 15703–15711. https://doi.org/10.1021/jacs.5b10385.

(10) McCulloch, I.; Salleo, A.; Chabinyc, M. Avoid the Kinks When Measuring Mobility. *Science* **2016**, *352* (6293), 1521–1522. https://doi.org/10.1126/science.aaf9062.

(11) Choi, H. H.; Cho, K.; Frisbie, C. D.; Sirringhaus, H.; Podzorov, V. Critical Assessment of Charge Mobility Extraction in FETs. *Nature Mater* **2018**, *17* (1), 2–7. https://doi.org/10.1038/nmat5035.

(12) Day, R. W.; Bediako, D. K.; Rezaee, M.; Parent, L. R.; Skorupskii, G.; Arguilla, M. Q.; Hendon, C. H.; Stassen, I.; Gianneschi, N. C.; Kim, P.; Dincă, M. Single Crystals of Electrically Conductive Two-Dimensional Metal–Organic Frameworks: Structural and Electrical Transport Properties. *ACS Cent. Sci.* **2019**, *5* (12), 1959–1964. https://doi.org/10.1021/acscentsci.9b01006.

Chapter 3: Controlling the crystal packing and morphology of metal–organic macrocycles through side-chain modification

3.1 Introduction.

Large macrocycles that self-assemble into extended nanotubular structures provide a fertile middle ground in between molecules and materials.[1–5] As molecules, macrocycles offer processability along with the ability to tune chemical structure with atomic precision. As materials, they possess multifunctional pore channels that can be used to mimic biological water channels,[6] selectively transport molecules[7,8] and ions,[9–13] conduct electrical charge,[13] and host chemical reactions.[14,15] In addition, because the supramolecular architectures are held together by weak noncovalent interactions, these self-assembled nanotubes provide dynamic and stimuli-responsive properties.[16,17]

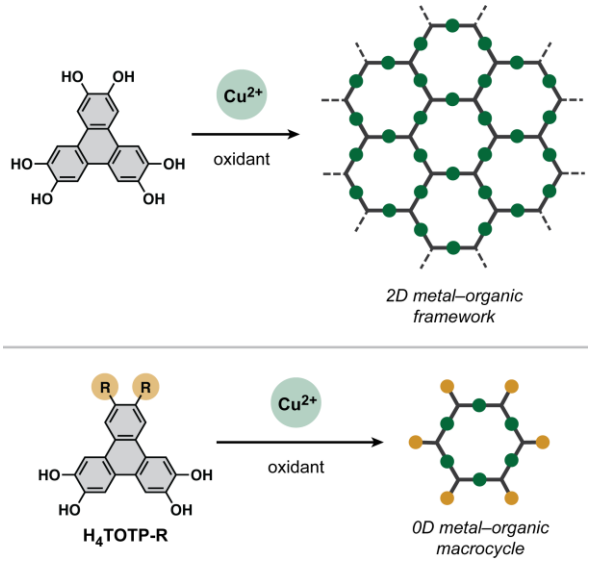

Figure 3.1. Overview of the synthesis and structure of conjugated 2D metal–organic frameworks (top) and conjugated metal–organic macrocycles (bottom). The tunable peripheral side chains (R) are highlighted in yellow.

We have been interested in macrocyclic motifs that mimic the structures of conjugated 2D metal–organic frameworks (MOFs) and covalent organic frameworks (COFs) (**Fig. 3.1**).[18] Such macrocycles should couple the benefits of supramolecular polymers (e.g., processability, stimuli-responsiveness, self-healing properties)[19–21] with the unique electronic properties of semiconducting framework materials. Indeed, we have shown that fully conjugated copper-based

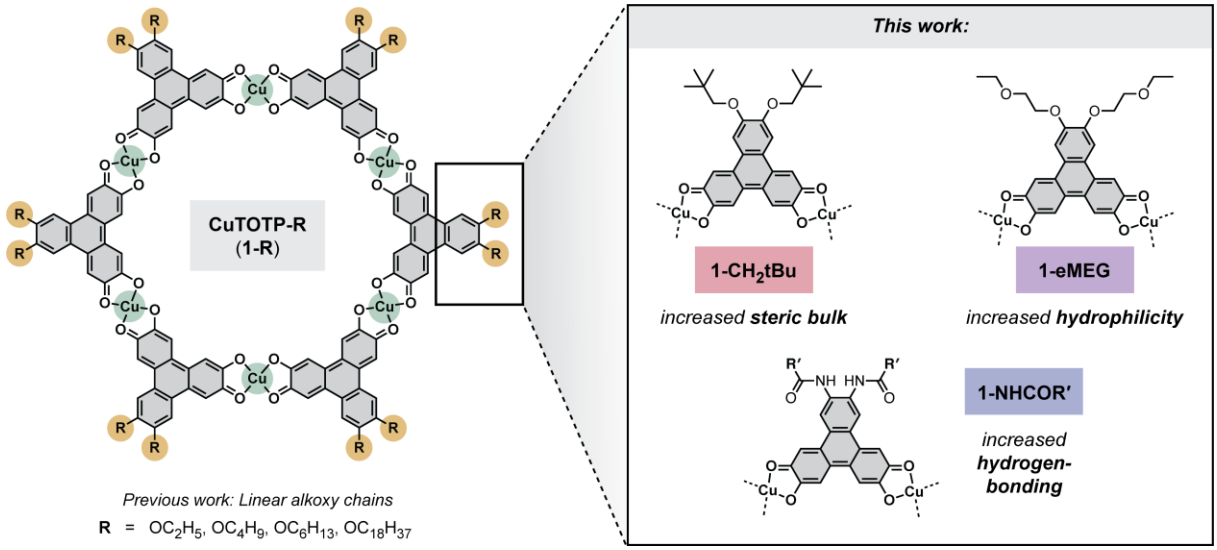

Figure 3.2. Overview of side-chain modifications in the macrocycle CuTOTP-R (**1-R**). Previous work investigated linear alkoxy side-chains of varying lengths (C2, C4, C6, and C18). In this work, we explore the effects of increased steric bulk, hydrophilicity, and hydrogen-bonding on crystal packing, crystal morphology, and materials properties.

macrocycles preserve the porosity and electrical conductivity of conjugated 2D MOFs while offering significant processability advantages.[18]

In our previous work, only linear alkoxy side-chains of varying lengths (linear C2, C4, C6, and C18) were explored. As supramolecular self-assembly is highly sensitive to molecular structure, we hypothesized that changes to the macrocycle periphery should profoundly impact the underlying π–π stacking structure and bulk materials properties, as well as the crystallization process and overall particle morphology.

To explore how the chemical identity of the peripheral side-chain impacts nanotube self-assembly, we synthesized five distinct copper macrocycles functionalized with either 1) sterically bulky branched alkoxy substituents, 2) hydrophilic ethylene glycol derivatives, or 3) hydrogen-bonding amide groups of varying chain lengths (**Fig. 3.2**). We show that while the electrical conductivity of these macrocycles appears moderately tolerant of π–π stacking disorder, it is highly sensitive to increased peripheral steric bulk. We further show that the introduction of hydrogen-bonding groups leads to more ordered packing and a dramatic increase in crystallite size. Together,

these results illustrate how side-chain engineering can be a powerful tool to modulate the underlying structure and bulk properties of conjugated metal–organic macrocycles.

3.2 Results and discussion.

3.2.1 Ligand synthesis.

Sterically bulky and hydrophilic side-chains could be installed on substituted 2,3,6,7-tetrahydroxytriphenylene ligands (H_4TOTP-R) via minor adjustments to the original synthesis route (**Scheme 3.1a**).[18,22] In our previous work, we showed that linear alkoxy chains of varying lengths (R = OC2, OC4, OC6, and OC18) could be easily attached to the ligand periphery via nucleophilic substitution. In a similar fashion, sterically bulky and hydrophilic and side-chains can be installed by reacting the starting 4,5-dibromo-1,2-diol with either neopentyl *p*-toluenesulfonate or 2-ethoxyethyl methanesulfonate, respectively. The final ligands H_4TOTP-OCH$_2$tBu and H_4TOTP-eMEG (eMEG = ethyl-capped monoethylene glycol) were obtained after Suzuki coupling, Scholl cyclization, and silyl protecting group removal (**Scheme 3.1a**; see Supporting Information for full experimental details).

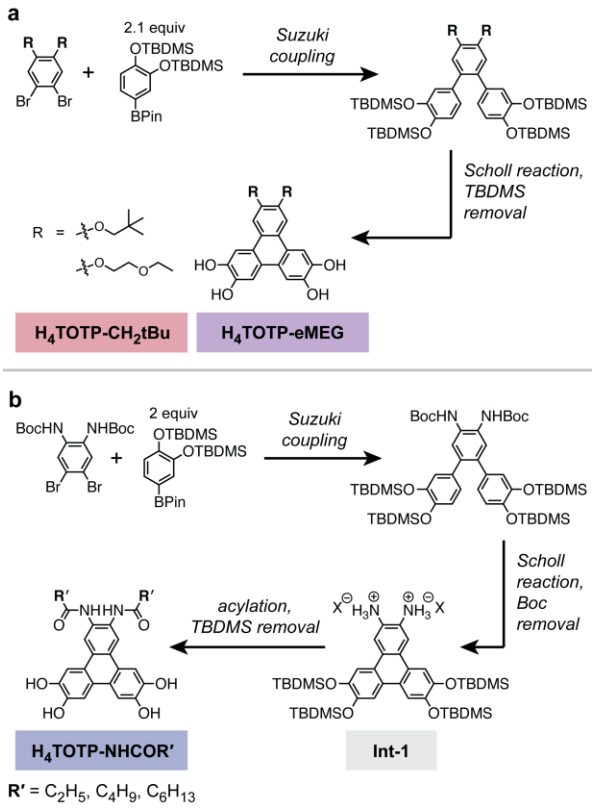

Scheme 3.1. Synthetic routes to obtain (a) sterically bulky H_4TOTP-OCH$_2$tBu and hydrophilic H_4TOTP-eMEG ligands, as well as (b) amide-functionalized H_4TOTP-NHCOR′ ligands.

In contrast, significant modifications to the original synthetic route were needed to achieve amide-functionalized ligands (**Scheme 3.1b**). Rather than using a catechol-based starting material,

we began with *tert*-butyloxycarbonyl (BOC) protected 4,5-dibromobenzene-1,2-diamine. Subsequent Suzuki coupling, Scholl cyclization, and BOC deprotection generates intermediate **Int-1**, which can be treated with acyl chlorides to form the desired amide bond. The final ligands H_4TOTP-NHCOR′ (R′ = linear C2, C4, or C6 alkyl chains) were obtained after silyl protecting group removal (see Supporting Information for full experimental details). In principle, intermediate **Int-1** should be able to react with diverse electrophiles beyond acyl chlorides, providing an opportunity for late-stage ligand diversification.

3.2.2 Impact of steric bulk and polarity on crystal packing.

Both the neopentoxy and eMEG-functionalized copper macrocycles were readily isolated as dark blue-black solids by combining $Cu(OAc)_2 \cdot H_2O$ and the ligand H_4TOTP-R (R = OCH_2tBu or eMEG) in a mixture of DMF and a cosolvent in air at room temperaure. Methanol and

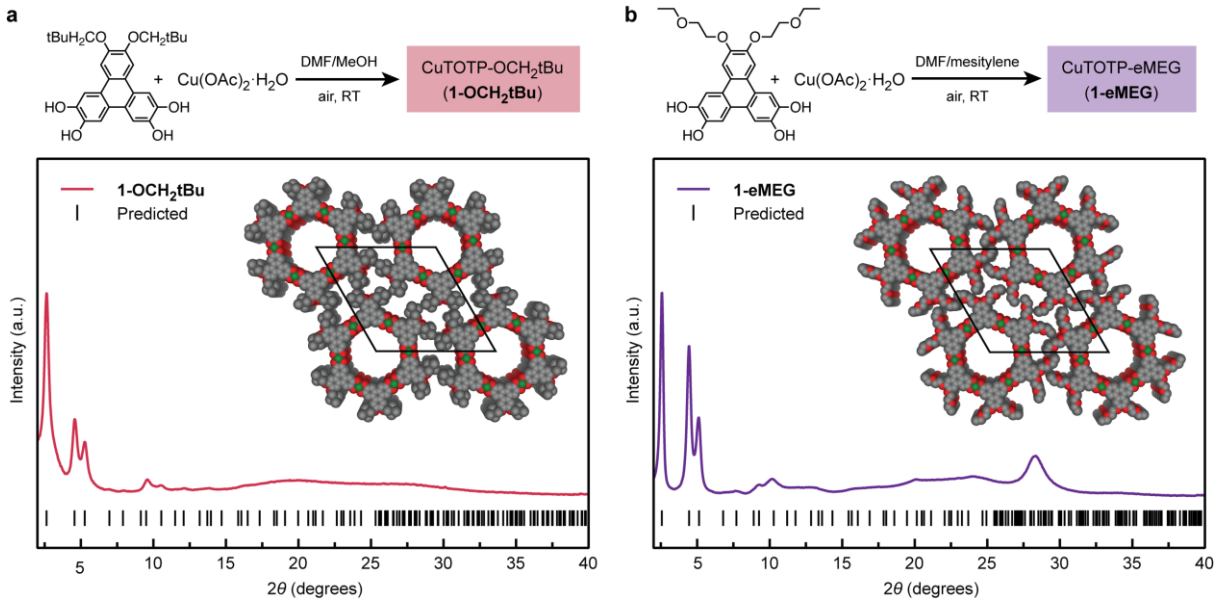

Figure 3.3. Synthesis schemes, experimental and predicted powder X-ray diffraction patterns, and structural models for (a) CuTOTP-OCH_2tBu (**1-OCH_2tBu**) and (b) CuTOTP-eMEG (**1-eMEG**).

mesitylene were used as the cosolvents for CuTOTP-OCH_2tBu (abbreviated **1-OCH_2tBu**) and CuTOTP-eMEG (abbreviated **1-eMEG**), respectively (see SI for more synthetic details).

Powder X-ray diffraction (PXRD) was used to probe how the presence of bulky neopentyl groups in **1-OCH$_2$tBu** influenced macrocycle packing (**Fig. 3.3a**). The positions of the first three peaks in the PXRD are consistent with a hexagonal unit cell ($a = b = 38.8$ Å), indicating that the macrocycles are still able to form columnar stacking structures. However, in contrast to our previously reported macrocycles, no distinct π–π stacking feature could be observed in **1-OCH$_2$tBu**. This suggests that the neopentyl groups introduce significant disorder in the π–π stacking geometry. While the exact π–π stacking distance could not be measured, we hypothesize that the neopentyl groups weaken and lengthen the interactions between macrocycles. Pressed pellet conductivity measurements show that these disruptions to the π–π stacking greatly hinder out-of-plane charge transport. Despite being similar in size to the ethoxy-functionalized macrocycle CuTOTP-OC2 ($a = b = 39.6$ Å), **1-OCH$_2$tBu** is nearly three orders of magnitude less conductive ($2(1) \times 10^{-3}$ vs. $6(2) \times 10^{-6}$ S/cm) (**Table 3.1**).[18]

Table 3.1. Average room temperature (298 K) conductivity values obtained from pressed pellets of CuTOTP-R. Values are the average of three measurements.

Sample	**Conductivity** (S cm^{-1})
1-OCH$_2$tBu	$6(2) \times 10^{-6}$
1-eMEG	$5(1) \times 10^{-4}$
1-NHCOC2	$2(1) \times 10^{-3}$
1-NHCOC4	$2(1) \times 10^{-4}$
1-NHCOC4 *(mixed phase)*	$8(4) \times 10^{-5}$
1-NHCOC6	$5(2) \times 10^{-5}$

The addition of hydrophilic oligoethylene glycol side chains has been shown to endow polythiophene and other traditional semiconducting polymers with greater ionic conductivity.[23,24] Such mixed ionic-electronic conductors have attracted strong recent interest due to emerging applications in bioelectronic, optoelectronic, and energy storage devices.[25,26] Given this prior work, we were interested in how the addition of a simple ethylene glycol derivative impacts macrocycle formation and packing.

Excitingly, in contrast to **1-OCH$_2$tBu**, the polar side-chains of **1-eMEG** do not appear to disrupt the π–π stacking (**Fig. 3.3b**). A strong π–π stacking feature at 2θ = 28.3° is observed, corresponding to a distance of ~3.2 Å. Consistent with this observation, pressed pellet conductivity measurements show that these macrocycles maintain a moderate electrical conductivity of 5(1) × 10^{-4} S/cm. Interestingly, the *a* and *b* dimensions of **1-eMEG** are only 1.3 Å larger than our previously reported CuTOTP-OC2 (39.8 Å vs. 38.5 Å), despite having a side-chain that is twice as long.[18] This may be due to the tendency of glycol side-chains to curl and bend, in contrast to the linear conformations preferred by *n*-alkyl chains.[27] Together, these results suggest that hydrophilic side-chains do not interfere with macrocycle packing, encouraging future work exploring mixed ionic-electronic conductivity in these materials.

3.2.3 Impact of hydrogen-bonding interactions on crystal packing.

The addition of hydrogen-bonding amide groups has been shown to enforce columnar stacking in shape-persistent arylene ethynylene macrocycles, enabling their self-assembly into long nanotube filaments.[10,28] In a similar way, we hypothesized that hydrogen-bonding amide groups could introduce stronger and more directional noncovalent interactions between neighboring macrocycles, facilitating the crystallization of larger particles.

The macrocycles **1-NHCOR′** (R′ = linear C2, C4, or C6 alkyl chains) were readily synthesized by combining the ligand H_4TOTP-NHCOR′ with $Cu(OAc)_2 \cdot H_2O$ in DMSO at room temperature in air. Unexpectedly, the PXRD patterns of all three macrocycles (R′ = C2, C4, C6) reveal a complex pattern that could not be indexed to a single unit cell, suggesting a mixture of phases (**Fig. 3.4a**). The presence of prominent peaks with the characteristic 1:1/√3:1/2 d-spacing ratio for a hexagonal unit cell (e.g., 2θ = 2.54, 4.42, and 5.30° for **1-NHCOC4**) suggests that these samples contain a mixture of hexagonal packing and a second, unknown packing structure.

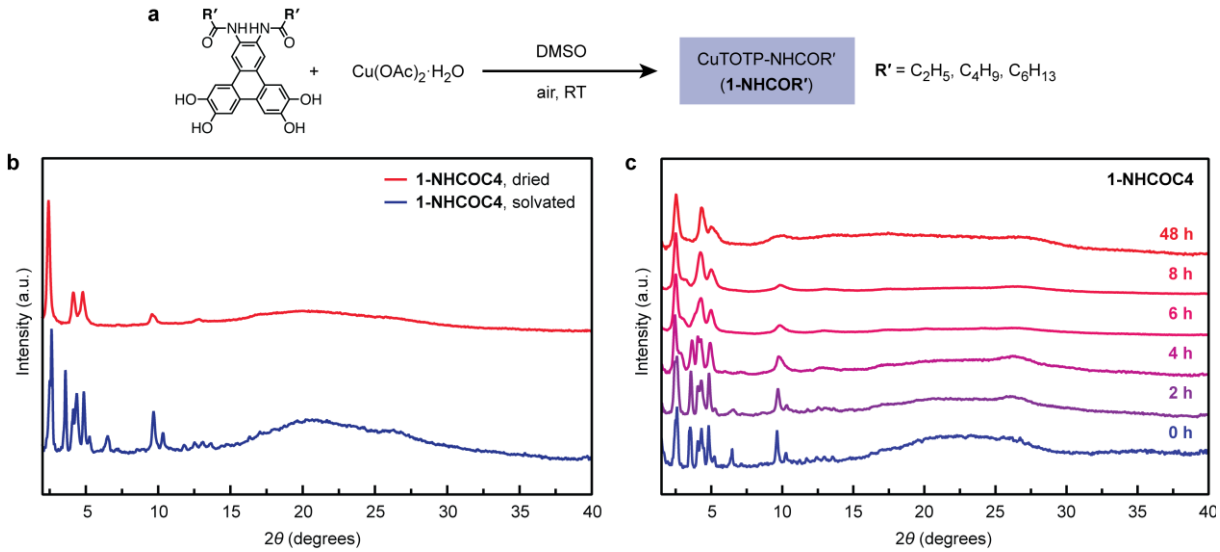

Figure 3.4. (a) Synthesis of CuTOTP-NHCOR′ (**1-NHCOR′**) macrocycles. (b) Powder X-ray diffraction (PXRD) of as-synthesized and dried **1-NHCOC4** in blue and red, respectively. The as-synthesized sample contains a mixture of phases, whereas the dried sample is a single hexagonal phase. (c) PXRD patterns tracking the phase conversion of the as-synthesized **1-NHCOC4** macrocycle over a period of 48 hours.

Partial or total conversion to a single hexagonal phase occurs upon solvent removal at room temperature, implying that the additional crystalline phases are due to alternative macrocyclic packing motifs rather than structurally distinct linear polymers or partially cyclized oligomers (**Fig. 3.4b)**. For example, while the initially filtered samples of **1-NHCOC2** and **1-NHCOC4** both show a mixture of phases, complete conversion to a single hexagonal phase is observed after air-drying at room temperature (**Fig. 3.4** and **Fig. 3.S7**). This process can be reversed through the re-addition of DMSO (**Fig. 3.S1**), again implying that these structural changes are due to the reconfiguration of dynamic noncovalent interactions rather than stronger metal–ligand bonds. We note that only partial conversion is observed for **1-NHCOC6** (**Fig. 3.S7**).

As expected, the electrical conductivity of **1-NHCOR′** decreases as the length of the insulating alkyl chain increases (**Table 3.1**). The room temperature pressed pellet conductivity of **1-NHCOC2** is $2(1) \times 10^{-3}$ S/cm, whereas the longer **1-NHCOC4** is an order of magnitude lower, at $2(1) \times 10^{-4}$ S/cm.

The hexagonal and mixed-phase **1-NHCOC4** samples provided an opportunity to probe the impact of π-stacking geometry and disorder on electrical conductivity. Surprisingly, the conductivity of the mixed-phase **1-NHCOC4** sample was within error of the pure hexagonal

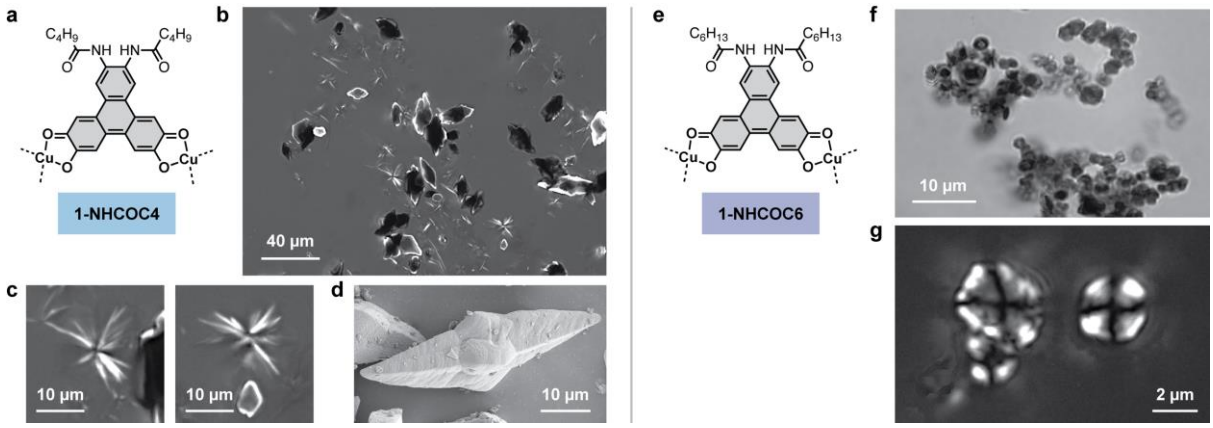

Figure 3.5. *Left:* (a) Chemical structure and (b) polarized optical microscopy image of **1-NHCOC4**. Both thin, aggregated microneedles and thick, irregular octahedra are observed. Zoomed-in (c) polarized optical microscopy and (d) scanning electron microscopy (SEM) images of the two particle morphologies. *Right:* (e) Chemical structure and (f) bright-field optical microscopy image of **1-NHCOC6**, which adopts a spherulite morphology. (g) Polarized optical microscopy image showing the Maltese cross pattern characteristic of spherulites.

phase, at 8(4) × 10^{-5} S/cm. Furthermore, both of these were comparable to **1-eMEG** (5(1) × 10^{-4} S/cm), which has a much sharper π–π stacking feature. Together, these values seem to suggest that the out-of-plane charge transport may be relatively tolerant to differences in stacking geometry, so long as there are no bulky substituents present.

Given the complexity of the initial PXRD patterns, structural elucidation of the non-hexagonal phase(s) will likely require single crystal diffraction studies. Unfortunately, the crystallites were too small for single crystal X-ray diffraction, and all attempts at electron diffraction were unsuccessful due to rapid degradation upon removal from the mother liquor. However, modeling studies suggest that the additional peaks cannot be explained by either herringbone packing (**Fig. 3.S2**) or slipped stacking (**Fig. 3.S3**), which are two of the most common packing motifs observed in the solid-state structures of conjugated organic molecules (see SI for more modeling details).[29]

3.2.4 Impact of hydrogen-bonding interactions on crystal morphology.

Excitingly, all three amide-containing macrocycles formed large, micron-sized particles that could be visualized by optical microscopy (**Fig. 5** and **Fig. S4**). This is in stark contrast to **1-OCH$_2$tBu**, **1-eMEG**, and our previously reported alkoxy-functionalized macrocycles, which precipitate as nanoparticles that are challenging to visualize by either optical or scanning electron microscopy (SEM). For example, AFM measurements on CuTOTP-OC4 showed that the columnar stacks have an average length of only 23(6) nm.[18]

The macrocycle **1-NHCOC2** formed aggregated clusters that were challenging to fully resolve by optical microscopy (**Fig. S4**). In contrast, **1-NHCOC4** formed large and well-defined particles. Two distinct crystal morphologies could be clearly visualized in **1-NHCOC4**, supporting our hypothesis that the as-synthesized sample contains two distinct phases (**Fig. 3.5b**). Specifically, both aggregates of thin microneedles (~6(3) μm average length) (**Fig. 3.5c** and **Fig. 3.S12**) as well as thick, irregular octahedra (~27(11) μm average length) were observed (**Fig. 3.5d** and **Fig. 3.S12**). The larger octahedral particles could be removed by gentle centrifugation. Powder X-ray diffraction measurements on the particles suspended in the supernatant confirmed that the smaller needle-like crystals are pure hexagonal phase material (**Fig. 3.S5**). Imaging the samples under polarized light confirmed that the individual microneedles were single crystalline, whereas the larger distorted octahedra were not. This is consistent with our PXRD studies, which showed that the structure of the non-hexagonal phase is highly sensitive to solvation state (**Fig. 3.4c**).

Finally, **1-NHCOC6** crystallizes as spherulites of approximately 2.6(5) μm in diameter (**Fig. 3.5f** and **Fig. S12**). Spherulites are densely packed spheres composed of radially oriented fibrillar crystals, which display a characteristic Maltese cross when viewed between crossed polarizers (**Fig. 3.5g**).[30] The formation of spherulites, rather than well-defined needles, may be due

to the presence of longer alkyl chains in **1-NHCOC6** that are poorly soluble in DMSO, our reaction solvent.

Overall, the crystal morphologies of **1-NHCOR′** strongly resemble those of conjugated 2D MOFs, such as $Cu_3(HHTP)_2$. Like our macrocycles, the framework $Cu_3(HHTP)_2$ typically crystallizes as thin rods or needles with the π-stacking direction oriented along the long axis.[31,32] In addition, conditions of rapid nucleation produce spherical clusters of radially oriented nanorods,[33] much like the aggregated microneedles found in **1-NHCOC4** and the spherulites in **1-NHCOC6**. Importantly, this suggests that understanding how to control the nucleation and growth of conjugated macrocycles may lead to a greater understanding of the formation of conjugated metal–organic frameworks, and vice versa.

3.3 Conclusion.

In conclusion, we have synthesized five new conjugated metal–organic macrocycles containing side-chains that vary in their steric bulk, hydrophilicity, and hydrogen-bonding ability. Despite the chemically distinct peripheral functionalities, all ligands successfully form macrocyclic structures, illustrating the versatility and robustness of this synthetic route. While the conjugated core is reminiscent of 2D metal–organic frameworks, the peripheral side-chains are a unique feature of macrocycles, and represent an exciting opportunity to tailor materials properties. We have already shown how the side-chains can be used to alter the π–π stacking structure, electrical conductivity, crystal morphology, and overall processability of these materials. Going forward, the peripheral side-chains have the potential to introduce hydrophilicity and ionic conductivity, as well as modulate the local microenvironment and reactivity of the metal center.

While quantitative structure–property relationships are limited by the lack of single crystal conductivity and diffraction data, nevertheless several qualitative conclusions can be drawn. From

these five macrocycles, it is clear that both the in-plane and out-of-plane packing structures impact electrical conductivity. In the in-plane direction, intuitively we would predict that a greater separation between macrocycles would lead to a lower conductivity, which is also what we observe. For example, the **1-NHCOR′** macrocycles demonstrate an approximately one order of magnitude decrease in conductivity with each two-carbon extension in the peripheral chain. Similar trends were observed in previous work focusing on linear alkoxy side-chains.[18] On the other hand, in the out-of-plane direction, the conclusions are more nuanced. While our studies with **1-OCH$_2$tBu** show that electrical conductivity decreases dramatically with increased peripheral steric bulk, the pressed pellet conductivity values appear less sensitive to other aspects of π–π stacking disorder. Going forward, single crystal and computational modeling studies will be needed to tease out the exact impact of the π–π stacking geometry.

Finally, a key finding from our studies is that the introduction of stronger and more directional hydrogen-bonding interactions in the π-stacking direction leads to a dramatic increase in particle size, from the nano- to the micron scale. Given the structural similarities between our macrocycles and conjugated 2D metal–organic frameworks, this finding may have implications in the crystallization and growth of 2D MOFs. The new ligand synthesis route reported here readily accommodates the late-stage installation of diverse hydrogen-bonding groups, encouraging future work along this vein.

3.4 Acknowledgements

This material is based upon work supported by the U.S. Department of Energy, Office of Science, Office of Basic Energy Sciences under Award Number DE-SC0021966. Work on the glycol-based side-chains was additionally supported by the Arnold and Mabel Beckman Foundation through a Beckman Young Investigator Award. P.H.L. and L.B.Z. were supported in part by the state of Washington through graduate fellowships from the University of Washington

Clean Energy Institute. The authors acknowledge the use of instrumentation at the following shared facilities: the Washington Research Training Testbeds, a facility operated by the University of Washington Clean Energy Institute; the Molecular Analysis Facility, a National Nanotechnology Coordinated Infrastructure (NNCI) site at the University of Washington, which is supported in part by funds from the National Science Foundation (awards NNCI-2025489, NNCI-15421010), the Molecular Engineering & Sciences Institute, and the Clean Energy Institute; and the University of Washington Department of Chemistry. The NMR facility at the UW Department of Chemistry is supported by NIH Award Number S10OD030224-01A1. Finally, we gratefully acknowledge the W. M. Keck Microscopy Center and the Keck Center Manager, Dr. Nathaniel Peters for assistance in collecting optical microscopy data.

3.5 References

(1) Bong, D. T.; Clark, T. D.; Granja, J. R.; Ghadiri, M. R. Self-Assembling Organic Nanotubes. *Angew. Chem. Int. Ed.* **2001**, *40*, 988–1011. https://doi.org/10.1002/1521-3773(20010316)40:6<988::AID-ANIE9880>3.0.CO;2-N.

(2) Balbo Block, M. A.; Kaiser, C.; Khan, A.; Hecht, S. Discrete Organic Nanotubes Based on a Combination of Covalent and Non-Covalent Approaches. In *Functional Molecular Nanostructures*; Schlüter, A. D., Ed.; Topics in Current Chemistry; Springer Berlin Heidelberg: Berlin, Heidelberg, 2005; Vol. 245, pp 89–150. https://doi.org/10.1007/b98167.

(3) Gong, B.; Shao, Z. Self-Assembling Organic Nanotubes with Precisely Defined, Sub-Nanometer Pores: Formation and Mass Transport Characteristics. *Acc. Chem. Res.* **2013**, *46*, 2856–2866. https://doi.org/10.1021/ar400030e.

(4) Strauss, M. J.; Evans, A. M.; Roesner, E. K.; Monsky, R. J.; Bardot, M. I.; Dichtel, W. R. Divergent Nanotube Synthesis through Reversible Macrocycle Assembly. *Acc. Mater. Res.* **2022**, *3*, 935–947. https://doi.org/10.1021/accountsmr.2c00062.

(5) Talukdar, D.; Kumar, J. M.; Gole, B. Self-Assembled Macrocycles: Design Strategies and Emerging Functions. *Crystal Growth & Design* **2023**, *23*, 7582–7611. https://doi.org/10.1021/acs.cgd.3c00677.

(6) Itoh, Y.; Chen, S.; Hirahara, R.; Konda, T.; Aoki, T.; Ueda, T.; Shimada, I.; Cannon, J. J.; Shao, C.; Shiomi, J.; Tabata, K. V.; Noji, H.; Sato, K.; Aida, T. Ultrafast Water Permeation through Nanochannels with a Densely Fluorous Interior Surface. *Science* **2022**, *376*, 738–743. https://doi.org/10.1126/science.abd0966.

(7) Jiang, Z.; Dong, R.; Evans, A. M.; Biere, N.; Ebrahim, M. A.; Li, S.; Anselmetti, D.; Dichtel, W. R.; Livingston, A. G. Aligned Macrocycle Pores in Ultrathin Films for Accurate Molecular Sieving. *Nature* **2022**, *60*, 58–64. https://doi.org/10.1038/s41586-022-05032-1.

(8) Zhang, G.; Lin, W.; Huang, F.; Sessler, J.; Khashab, N. M. Industrial Separation Challenges: How Does Supramolecular Chemistry Help? *J. Am. Chem. Soc.* **2023**, *145*, 19143–19163. https://doi.org/10.1021/jacs.3c06175.

(9) Helsel, A. J.; Brown, A. L.; Yamato, K.; Feng, W.; Yuan, L.; Clements, A. J.; Harding, S. V.; Szabo, G.; Shao, Z.; Gong, B. Highly Conducting Transmembrane Pores Formed by Aromatic Oligoamide Macrocycles. *J. Am. Chem. Soc.* **2008**, *130*, 15784–15785. https://doi.org/10.1021/ja807078y.

(10) Zhou, X.; Liu, G.; Yamato, K.; Shen, Y.; Cheng, R.; Wei, X.; Bai, W.; Gao, Y.; Li, H.; Liu, Y.; Liu, F.; Czajkowsky, D. M.; Wang, J.; Dabney, M. J.; Cai, Z.; Hu, J.; Bright, F. V.; He, L.; Zeng, X. C.; Shao, Z.; Gong, B. Self-Assembling Subnanometer Pores with Unusual Mass-Transport Properties. *Nat Commun* **2012**, *3*, 949. https://doi.org/10.1038/ncomms1949.

(11) Strauss, M. J.; Hwang, I.; Evans, A. M.; Natraj, A.; Aguilar-Enriquez, X.; Castano, I.; Roesner, E. K.; Choi, J. W.; Dichtel, W. R. Lithium-Conducting Self-Assembled Organic Nanotubes. *J. Am. Chem. Soc.* **2021**, *143*, 17655–17665. https://doi.org/10.1021/jacs.1c08058.

(12) Strauss, M. J.; Jia, M.; Evans, A. M.; Castano, I.; Li, R. L.; Aguilar-Enriquez, X.; Roesner, E. K.; Swartz, J. L.; Chavez, A. D.; Enciso, A. E.; Stoddart, J. F.; Rolandi, M.; Dichtel, W. R. Diverse Proton-Conducting Nanotubes via a Tandem Macrocyclization and Assembly Strategy. *J. Am. Chem. Soc.* **2021**, *143*, 8145–8153. https://doi.org/10.1021/jacs.1c02789.

(13) Louie, S.; Zhong, Y.; Bao, S. T.; Schaack, C.; Montoya, A.; Jin, Z.; Orchanian, N. M.; Liu, Y.; Lei, W.; Harrison, K.; Hone, J.; Angerhofer, A.; Evans, A. M.; Nuckolls, C. P. Coaxially Conductive Organic Wires Through Self-Assembly. *J. Am. Chem. Soc.* **2023**, *145*, 4940–4945. https://doi.org/10.1021/jacs.2c12437.
(14) Yang, J.; Dewal, M. B.; Shimizu, L. S. Self-Assembling Bisurea Macrocycles Used as an Organic Zeolite for a Highly Stereoselective Photodimerization of 2-Cyclohexenone. *J. Am. Chem. Soc.* **2006**, *128*, 8122–8123. https://doi.org/10.1021/ja062337s.
(15) Islam, M. F.; Adame-Ramirez, E.; Williams, E. R.; Kittikhunnatham, P.; Wijesekera, A.; Zhang, S.; Ge, T.; Stefik, M.; Smith, M. D.; Pellechia, P. J.; Greytak, A. B.; Shimizu, L. S. Inclusion Polymerization of Pyrrole and Ethylenedioxythiophene in Assembled Triphenylamine *Bis* -Urea Macrocycles. *Macromolecules* **2022**, *55*, 11013–11022. https://doi.org/10.1021/acs.macromol.2c02042.
(16) Norikane, Y.; Hirai, Y.; Yoshida, M. Photoinduced Isothermal Phase Transitions of Liquid-Crystalline Macrocyclic Azobenzenes. *Chem. Commun.* **2011**, *47*, 1770–1772. https://doi.org/10.1039/C0CC04052E.
(17) Sun, C.; Shen, M.; Chavez, A. D.; Evans, A. M.; Liu, X.; Harutyunyan, B.; Flanders, N. C.; Hersam, M. C.; Bedzyk, M. J.; Olvera De La Cruz, M.; Dichtel, W. R. High Aspect Ratio Nanotubes Assembled from Macrocyclic Iminium Salts. *Proc. Natl. Acad. Sci. U.S.A.* **2018**, *115*, 8883–8888. https://doi.org/10.1073/pnas.1809383115.
(18) Zasada, L. B.; Guio, L.; Kamin, A. A.; Dhakal, D.; Monahan, M.; Seidler, G. T.; Luscombe, C. K.; Xiao, D. J. Conjugated Metal–Organic Macrocycles: Synthesis, Characterization, and Electrical Conductivity. *J. Am. Chem. Soc.* **2022**, *144*, 4515–4521. https://doi.org/10.1021/jacs.1c12596.
(19) Brunsveld, L.; Folmer, B. J. B.; Meijer, E. W.; Sijbesma, R. P. Supramolecular Polymers. *Chem. Rev.* **2001**, *101*, 4071–4098. https://doi.org/10.1021/cr990125q.
(20) De Greef, T. F. A.; Smulders, M. M. J.; Wolffs, M.; Schenning, A. P. H. J.; Sijbesma, R. P.; Meijer, E. W. Supramolecular Polymerization. *Chem. Rev.* **2009**, *109*, 5687–5754. https://doi.org/10.1021/cr900181u.
(21) Aida, T.; Meijer, E. W.; Stupp, S. I. Functional Supramolecular Polymers. *Science* **2012**, *335*, 813–817. https://doi.org/10.1126/science.1205962.
(22) Smith, M. K.; Powers-Riggs, N. E.; Northrop, B. H. Rational Synthesis of Bis(Hexyloxy)-Tetra(Hydroxy)-Triphenylenes and Their Derivatives. *RSC Adv.* **2014**, *4*, 38281–38292. https://doi.org/10.1039/C4RA06503D.
(23) Giovannitti, A.; Sbircea, D.-T.; Inal, S.; Nielsen, C. B.; Bandiello, E.; Hanifi, D. A.; Sessolo, M.; Malliaras, G. G.; McCulloch, I.; Rivnay, J. Controlling the Mode of Operation of Organic Transistors through Side-Chain Engineering. *Proc. Natl. Acad. Sci. U.S.A.* **2016**, *113*, 12017–12022. https://doi.org/10.1073/pnas.1608780113.
(24) Nielsen, C. B.; Giovannitti, A.; Sbircea, D.-T.; Bandiello, E.; Niazi, M. R.; Hanifi, D. A.; Sessolo, M.; Amassian, A.; Malliaras, G. G.; Rivnay, J.; McCulloch, I. Molecular Design of Semiconducting Polymers for High-Performance Organic Electrochemical Transistors. *J. Am. Chem. Soc.* **2016**, *138*, 10252–10259. https://doi.org/10.1021/jacs.6b05280.
(25) Moser, M.; Ponder, J. F.; Wadsworth, A.; Giovannitti, A.; McCulloch, I. Materials in Organic Electrochemical Transistors for Bioelectronic Applications: Past, Present, and Future. *Adv Funct Materials* **2019**, *29*, 1807033. https://doi.org/10.1002/adfm.201807033.
(26) Paulsen, B. D.; Tybrandt, K.; Stavrinidou, E.; Rivnay, J. Organic Mixed Ionic–Electronic Conductors. *Nat. Mater.* **2020**, *19*, 13–26. https://doi.org/10.1038/s41563-019-0435-z.

(27) Moro, S.; Siemons, N.; Drury, O.; Warr, D. A.; Moriarty, T. A.; Perdigão, L. M. A.; Pearce, D.; Moser, M.; Hallani, R. K.; Parker, J.; McCulloch, I.; Frost, J. M.; Nelson, J.; Costantini, G. The Effect of Glycol Side Chains on the Assembly and Microstructure of Conjugated Polymers. *ACS Nano* **2022**, *16*, 21303–21314. https://doi.org/10.1021/acsnano.2c09464.
(28) Zhong, Y.; Yang, Y.; Shen, Y.; Xu, W.; Wang, Q.; Connor, A. L.; Zhou, X.; He, L.; Zeng, X. C.; Shao, Z.; Lu, Z.; Gong, B. Enforced Tubular Assembly of Electronically Different Hexakis(*m* -Phenylene Ethynylene) Macrocycles: Persistent Columnar Stacking Driven by Multiple Hydrogen-Bonding Interactions. *J. Am. Chem. Soc.* **2017**, *139*, 15950–15957. https://doi.org/10.1021/jacs.7b09647.
(29) Yu, P.; Zhen, Y.; Dong, H.; Hu, W. Crystal Engineering of Organic Optoelectronic Materials. *Chem* **2019**, *5*, 2814–2853. https://doi.org/10.1016/j.chempr.2019.08.019.
(30) Crist, B.; Schultz, J. M. Polymer Spherulites: A Critical Review. *Progress in Polymer Science* **2016**, *56*, 1–63. https://doi.org/10.1016/j.progpolymsci.2015.11.006.
(31) Hmadeh, M.; Lu, Z.; Liu, Z.; Gándara, F.; Furukawa, H.; Wan, S.; Augustyn, V.; Chang, R.; Liao, L.; Zhou, F.; Perre, E.; Ozolins, V.; Suenaga, K.; Duan, X.; Dunn, B.; Yamamto, Y.; Terasaki, O.; Yaghi, O. M. New Porous Crystals of Extended Metal-Catecholates. *Chem. Mater.* **2012**, *24*, 3511–3513. https://doi.org/10.1021/cm301194a.
(32) Day, R. W.; Bediako, D. K.; Rezaee, M.; Parent, L. R.; Skorupskii, G.; Arguilla, M. Q.; Hendon, C. H.; Stassen, I.; Gianneschi, N. C.; Kim, P.; Dincă, M. Single Crystals of Electrically Conductive Two-Dimensional Metal–Organic Frameworks: Structural and Electrical Transport Properties. *ACS Cent. Sci.* **2019**, *5*, 1959–1964. https://doi.org/10.1021/acscentsci.9b01006.
(33) Snook, K. M.; Zasada, L. B.; Chehada, D.; Xiao, D. J. Oxidative Control over the Morphology of $Cu_3(HHTP)_2$, a 2D Conductive Metal–Organic Framework. *Chem. Sci.* **2022**, *13*, 10472–10478. https://doi.org/10.1039/D2SC03648G.

3.6 Supporting Information

3.6.1 General materials and methods

Reagents and solvents were purchased from commercial vendors (Millipore Sigma, TCI America, Alfa Aesar, Fisher, Oakwood Chemical, Combi-Blocks) and used without purification unless otherwise noted. Deuterated solvents ($CDCl_3$, DMSO-d_6) were purchased from Cambridge Isotope Laboratories. NMR spectra were acquired on Bruker GG500 or NEO500 instruments. ^{1}H and ^{13}C NMR spectra were referenced to residual deuterated solvent peaks. Peaks corresponding to the numerous aromatic carbon atoms in the reported compounds often overlap, thereby reducing the number of observed peaks. ^{19}F NMR spectra were referenced to 1,4-difluorobenzene at δ –106.00 ppm. Mass spectrometry data of ligand intermediates were collected on a Bruker Esquire Ion Trap instrument in positive or negative ion modes as noted. High-resolution ESI-MS data for H_4TOTP-OCH2tBu, H_4TOTP-eMEG, H_4TOTP-NHCOC2, H_4TOTP-NHCOC4, and H_4TOTP-NHCOC6 were collected on an LTQ-Orbitrap XL mass spectrometer in negative ion mode.

Automated flash column chromatography was performed using a Teledyne Isco CombiFlash Rf+ with Teledyne Isco RediSep Silver, 40-60 μm, 60 Å silica gel flash columns. Manual silica plugs were conducted using SiliCycle SiliFlash Irregular P60, 40-63 μm, 60 Å silica gel.

Powder X-ray diffraction (PXRD) data were collected on a Bruker D8 Discover Powder X-ray diffractometer located in the University of Washington's Molecular Analysis Facility. Structural models were constructed in Materials Studio using the Furcate module.

Scanning electron microscopy (SEM) images were collected on a Thermo Fisher Scientific Apreo-S with LoVac scanning electron microscope with an operating voltage of 2kV at the University of Washington Molecular Analysis Facility. All samples were prepared *via* drying samples to a powder under flowing N_2 and attaching particles to carbon tape on silicon wafers.

Optical microscopy images were collected on a Leica DMI6000 inverted microscope located in the University of Washington's Keck Microscopy Center using 100X/NA1.4 and 40X/NA1.3 oil immersion objectives for **1-NHCOC2** and **1-NHCOC4** respectively and a 2X magnifier with a 100X/NA1.4 oil immersion objective for **1-NHCOC6**. Samples were prepared by synthesizing each of the **1-NHCOC2**, **1-NHCOC4**, and **1-NHCOC6** macrocycles as detailed below (S3–S4) but omitting any centrifugation or washing, then adding one drop to an Ibidi high walled chambered coverslip and imaging from underneath. Images were taken as brightfield or polarized light multifocus (i.e. focus stacking) as composites of 26–51 focal planes. Image processing and analysis were performed in LASX (Leica) and FIJI (ImageJ).

3.6.2 Macrocycle synthesis.

2.1 Synthesis of CuTOTP-OCH$_2$tBu (OCH$_2$tBu = neopentoxy): A 4 mL scintillation vial was charged with H$_4$TOTP-OCH$_2$tBu (0.010 g, 0.022 mmol, 1.00 equiv), and DMF (2 mL). Separately, a 4 mL vial was charged with copper acetate monohydrate (Cu(OAc)$_2$·H$_2$O) (0.0047 g, 0.024 mmol, 1.10 equiv) and DMF (1 mL). Both solutions were sonicated for 5 minutes, and filtered through a 0.45 μm PTFE filter, after which the ligand solution was added dropwise to the metal solution and shaken. The mixture was transferred to a 10 mL crystallization tube inside of a 250 mL jar, and MeOH (6 mL) was added to the jar and allowed to vapor diffuse into the DMF. After 7 days, the solution was centrifuged at 19000 RPM to isolate the solid product. The product was washed with 1:1 DMF:MeOH (3 × 15 mL) at room temperature via centrifugation, and then dried under flowing N$_2$ at room temperature for 18 h. The macrocycle **CuTOTP-OCH$_2$tBu** was obtained in 17% yield (0.0019 g, 0.00060 mmol) as a dark blue solid. Note this reaction was performed 8× in parallel and combined for more convenient analysis.

2.2 Synthesis of CuTOTP-eMEG: A 4 mL scintillation vial was charged with H$_4$TOTP-eMEG (0.010 g, 0.021 mmol, 1.00 equiv), and DMF (2 mL). Separately, a 4 mL scintillation vial was charged with Cu(OAc)$_2$·H$_2$O (0.0043 g, 0.021 mmol, 1.00 equiv) and DMF (2 mL). Both solutions were sonicated for 5 minutes, after which the metal solution was transferred to a 20 mL scintillation vial and the ligand solution was added dropwise and shaken, followed by addition of mesitylene (1 mL), and the vial was capped, and allowed to sit at room temperature. After 7 days, the solution was centrifuged at 19000 RPM to isolate the solid product. The product was washed with DMF (2 × 15 mL) and filtered and dried under flowing N$_2$ at room temperature for 18 h. The macrocycle **CuTOTP-eMEG** was obtained in 39% yield (0.0044 g, 0.0014 mmol) as a dark blue solid.

2.3 Synthesis of CuTOTP-NHCOC2: A 4 mL scintillation vial was charged with H$_4$TOTP-NHCOC2 (0.010 g, 0.023 mmol, 1.00 equiv), and DMSO (1 mL). Separately, a 4 mL vial was charged with copper acetate monohydrate (Cu(OAc)$_2$·H$_2$O, 0.0051 g, 0.025 mmol, 1.10 equiv) and DMSO (1 mL). Both solutions were sonicated for 5 minutes, and filtered through a 0.45 μm PTFE filter, after which the ligand solution was added dropwise to the metal solution and shaken. After 7 days, the solution was centrifuged at 19000 RPM to isolate the solid product. The product was washed with DMSO (1 × 10 mL) at room temperature via centrifugation, and then filtered and scraped onto a glass slide where it was allowed to dry in air on the bench at room temperature overnight to ensure conversion to hexagonal phase. The macrocycle **CuTOTP-NHCOC2** was obtained in 17% yield (0.0019 g, 0.00065 mmol) as a dark blue solid. Note this reaction was performed 10× in parallel and combined for more convenient analysis.

2.4 Synthesis of CuTOTP-NHCOC4: A 4 mL scintillation vial was charged with H$_4$TOTP-NHCOC4 (0.010 g, 0.020 mmol, 1.00 equiv), and DMSO (1 mL). Separately, a 4 mL vial was charged with Cu(OAc)$_2$·H$_2$O (0.0048 g, 0.022 mmol, 1.10 equiv) and DMSO (1 mL). Both solutions were sonicated for 5 minutes, and filtered through a 0.45 μm PTFE filter, after which the ligand solution was added dropwise to the metal solution and shaken. After 2 days, the solution was centrifuged at 19000 RPM to isolate the solid product. The product was washed with DMSO (1 × 10 mL) at room temperature via centrifugation, and then filtered and scraped onto a glass slide where it was allowed to dry in air on the bench at room temperature overnight to ensure conversion to hexagonal phase. The macrocycle **CuTOTP-NHCOC4** was obtained in 62% yield (0.0069 g,

0.0021 mmol) as a dark blue solid. Note this reaction was performed 10× in parallel and combined for more convenient analysis.

2.5 Synthesis of CuTOTP-NHCOC6: A 4 mL scintillation vial was charged with H_4TOTP-NHCOC6 (0.010 g, 0.018 mmol, 1.00 equiv), and DMSO (1 mL). Separately, a 4 mL vial was charged with $Cu(OAc)_2 \cdot H_2O$ (0.0041 g, 0.0201 mmol, 1.10 equiv) and DMSO (1 mL). Both solutions were sonicated for 5 minutes, and filtered through a 0.45 μm PTFE filter, after which the ligand solution was added dropwise to the metal solution and shaken. After 2 days, the solution was centrifuged at 19000 RPM to isolate the solid product. The product was washed with DMSO (1 × 10 mL) at room temperature via centrifugation, and then filtered and scraped onto a glass slide where it was allowed to dry in air on the bench at room temperature overnight to convert to hexagonal phase, but conversion was incomplete (see main text and **S5**). The macrocycle **CuTOTP-NHCOC6** was obtained in 63% yield (0.0070 g, 0.0019 mmol) as a dark blue solid. Note this reaction was performed 10× in parallel and combined for more convenient analysis.

3.6.3 Phase conversion of CuTOTP-NHCOR′.

To convert CuTOTP-NHCOC2 and CuTOTP-NHCOC4 to pure hexagonal phase, solvated samples are filtered, and the resulting paste is spread out in a thin even layer on a glass slide at room temperature in air, in an environment without strong air flow. After 24 h, samples are scraped off and PXRD demonstrates conversion to pure hexagonal phase (**Fig. S7**). When the same procedure is repeated for CuTOTP-NHCOC6, incomplete conversion is observed.

CuTOTP-NHCOC4 can convert to an alternate mixed phase if dried too quickly. If filtered samples are instead heated at 40 °C and dried under a flowing stream of N_2, they give a mixed phase (**Fig. S6**) which never fully converts to pure hexagonal phase. For the mixed phase, the 2-probe pressed pellet conductivity value across three measurements was found to be $8(4) \times 10^{-5}$ S/cm. This value is within error of the pure hexagonal phase, highlighting that these mixed phase(s) are likely macrocycles in different packing conformation(s).

3.6.4 Ligand synthesis.

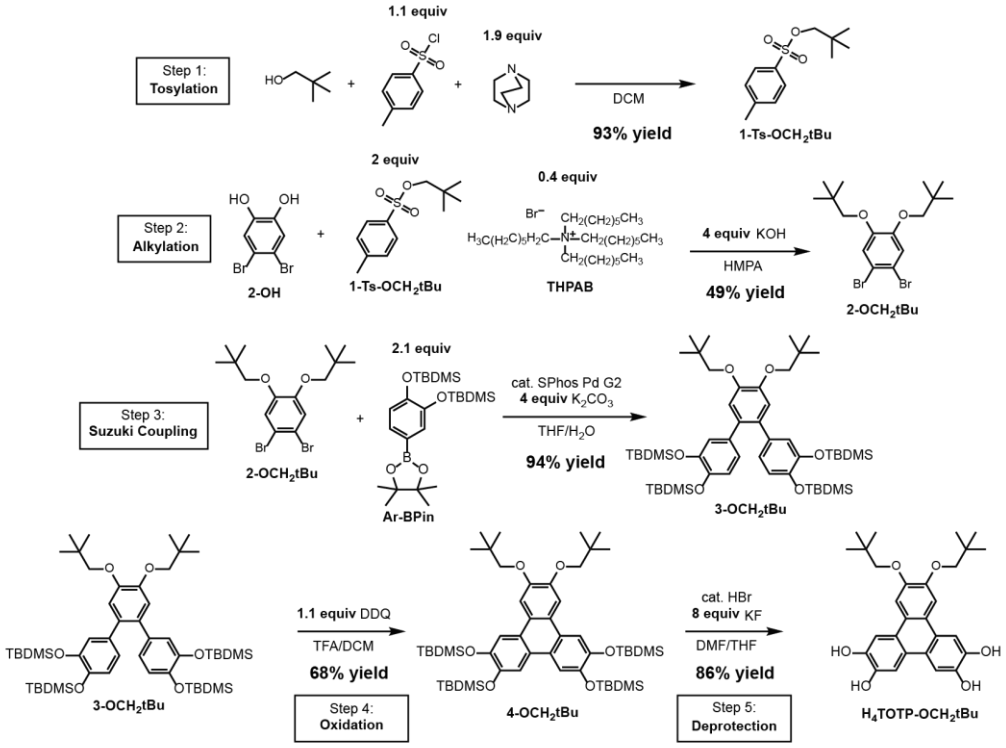

Scheme 3.S1 | Overall synthetic scheme for synthesis of H_4TOTP-OCH_2tBu. The ligand is obtained in five steps (Tosylation, Alkylation, Suzuki Coupling, Oxidation, and Deprotection). **2-OH, Ar-Bpin, 1-Ts-OCH_2tBu,** and **2-OCH_2tBu** are synthesized from previously reported procedures.[1–3] Overall synthesis based on previously reported procedures.[4]

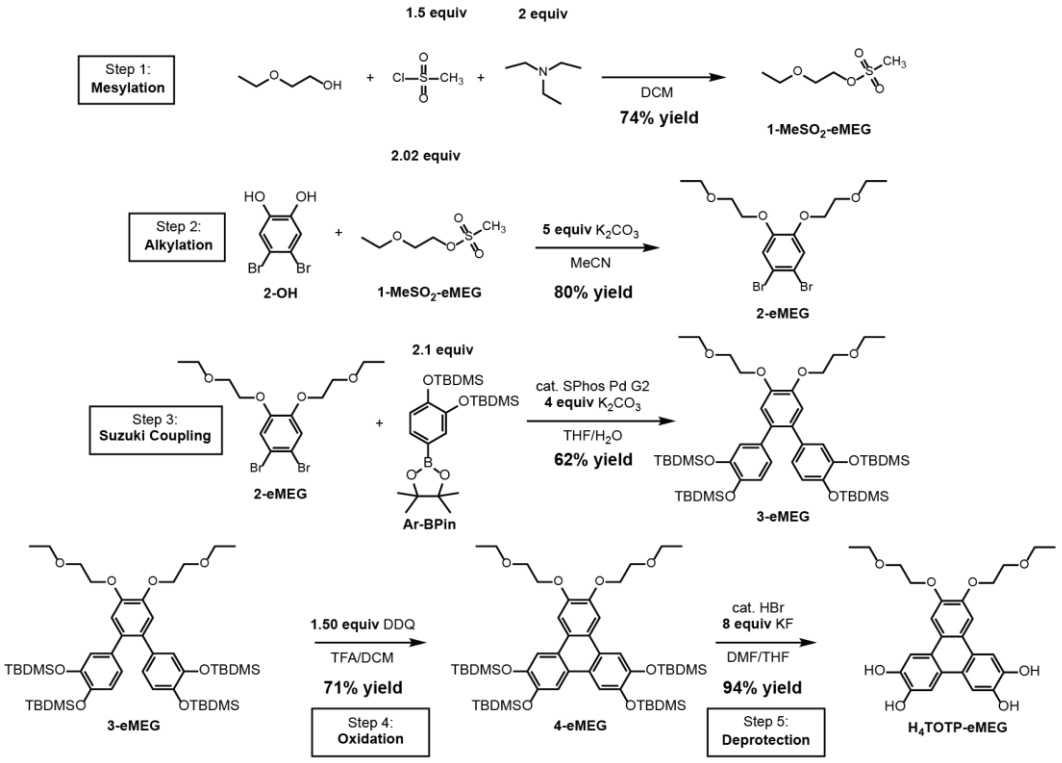

Scheme 3.S2 | Overall synthetic scheme for synthesis of H_4TOTP-eMEG. The ligand is obtained in five steps (Mesylation, Alkylation, Suzuki Coupling, Oxidation, and Deprotection). **2-OH** and **Ar-Bpin** are synthesized according to previously reported procedures.[1] Overall synthesis based on previously reported procedures.[4]

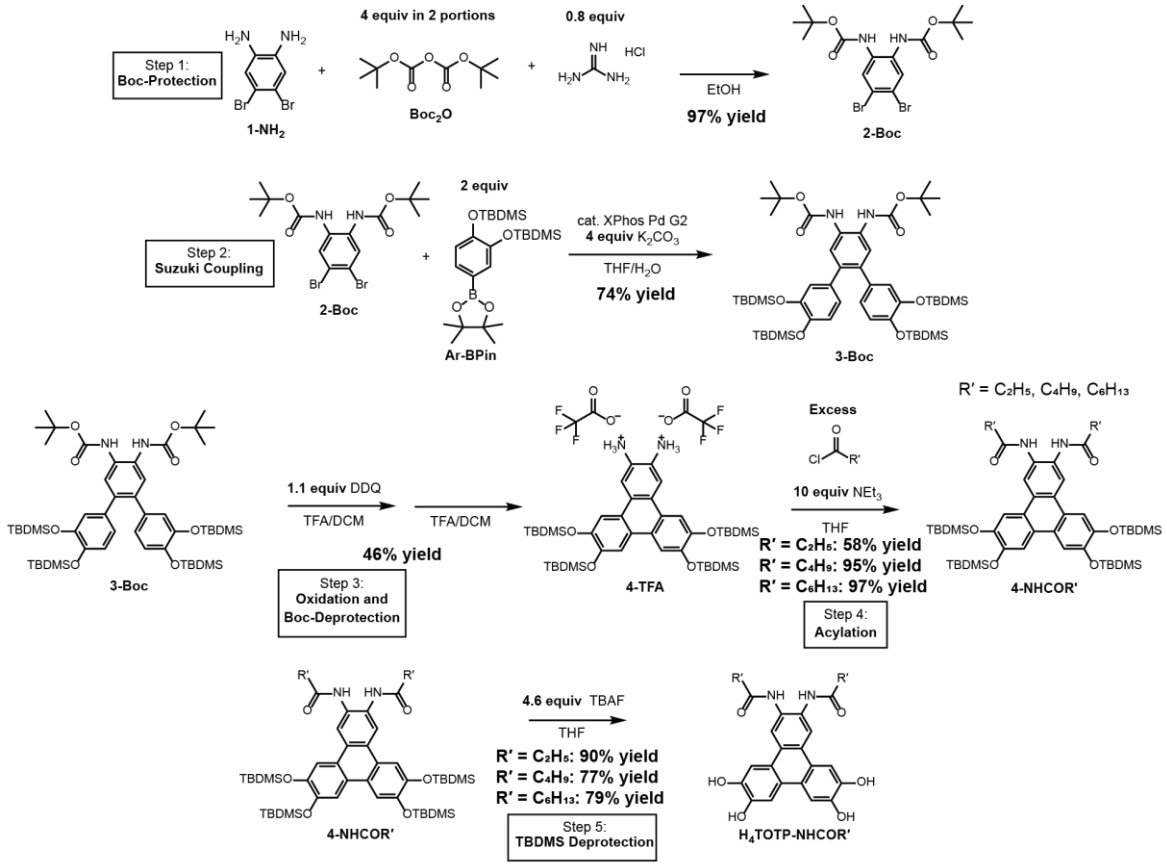

Scheme 3.S3 | Overall synthetic scheme for synthesis of H_4TOTP-NHCOR′. The ligand is obtained in five steps (Boc-Protection, Suzuki Coupling, Oxidation and Boc-Deprotection, acylation, and TBDMS deprotection). **Ar-Bpin** is synthesized based on previously reported procedures.[1] Boc-protection based on Garrido-Barros *et. al.*,[5] overall synthesis based on previously reported procedures.[4]

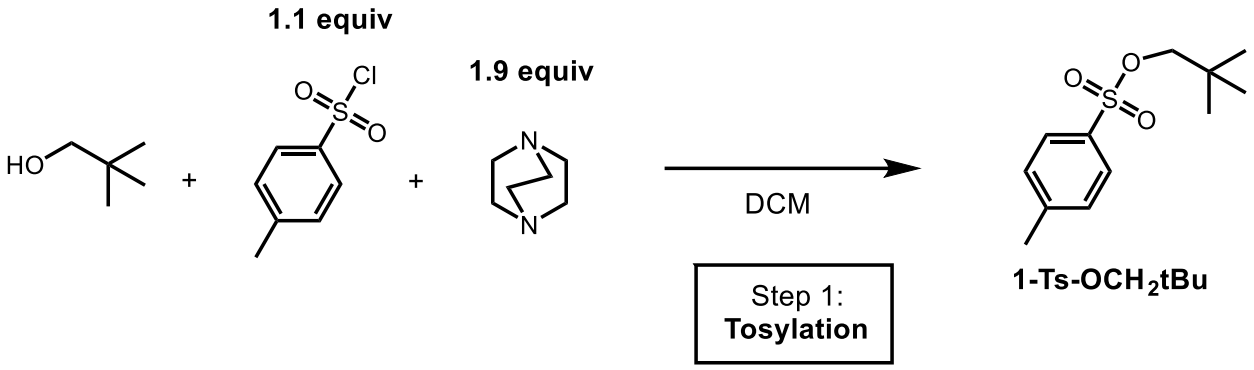

Synthesis of 1-Ts-OCH$_2$tBu. A 100 mL round bottom flask equipped with a stir bar was charged with 2,2-dimethyl-1-propanol (neopentyl alcohol, 2.00 g, 22.7 mmol, 1.00 equiv) and DCM (50 mL) and cooled to 0 °C. 1,4-diazabicyclo[2.2.2]octane (DABCO, 4.84 g, 43.1 mmol, 1.9 equiv) was then slowly added over 5 minutes while stirring, followed by slow addition of 4-toluenesulfonyl chloride (4.76 g, 25.0 mmol, 1.10 equiv). The reaction was allowed to stir for 2 h at 0 °C then warmed to room temperature and stirred for 12 h. DCM was removed *in vacuo* and the resultant oil was diluted with H_2O (50 mL) and EtOAc (100 mL). The aqueous phase was further extracted with EtOAc (2 × 100 mL). The combined organic layers were dried over $MgSO_4$ and concentrated *in vacuo* to yield **1-Ts-OCH2tBu** as a colorless oil (5.10 g, 21.0 mmol, 93% yield) and used directly in the next step without further purification. The ^{1}H NMR is consistent with previous literature reports.[2]

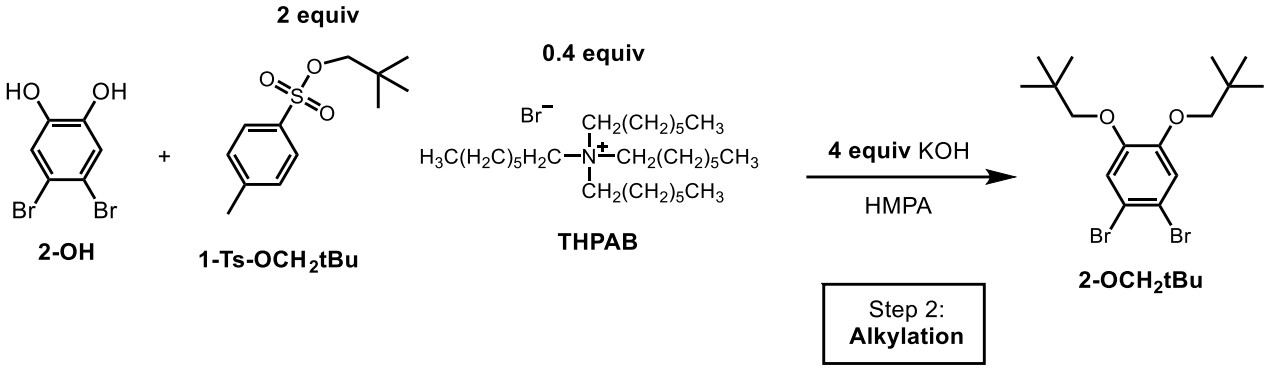

Synthesis of 2-OCH$_2$tBu. A 50 mL round bottom flask equipped with a stir bar and reflux condenser was charged with **1-Ts-OCH$_2$tBu** (5.10 g, 21.0 mmol, 2.00 equiv), hexamethylphosphoramide (HMPA, 20 mL) and sparged with N_2 for 30 minutes. To the flask, 4,5-dibromo-1,2-diol (**1-OH**, 2.82 g, 10.5 mmol, 1.00 equiv), potassium hydroxide (2.36 g, 42.0 mmol, 4.00 equiv) and tetraheptylammonium bromide (**THPAB**, 2.07 g, 4.2 mmol, 0.40 equiv) were added in that order. The solution was then sparged again with N_2 for 10 minutes and heated to 90 °C and stirred for 6 days. The reaction was cooled to room temperature and poured over H_2O (100 mL), then extracted with EtOAc (3 × 100 mL). The combined organic layers were dried over $MgSO_4$ and concentrated *in vacuo*. The resultant brown oil was subjected to filtration through a silica plug eluting with 95:5 hexanes:Et_2O to afford **2-OCH$_2$tBu** as a colorless oil (2.10 g, 5.1 mmol, 49% yield) and used directly in the next step without further purification. The ^{1}H NMR is consistent with previous literature reports.[3]

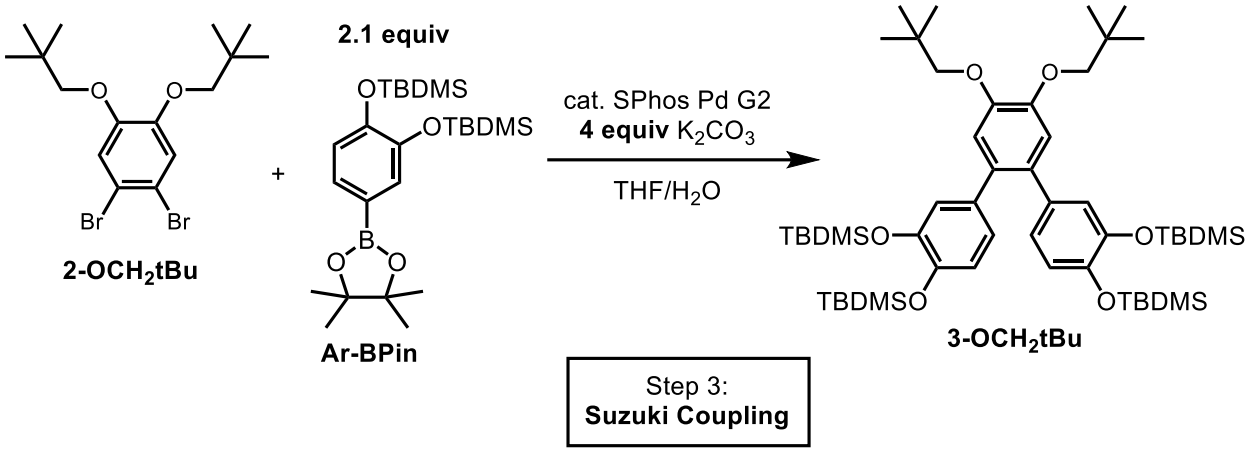

Synthesis of 3-CH_2tBu. A 250 mL round bottom flask equipped with a stir bar and reflux condenser was charged with **2-OCH2tBu** (1.20 g, 2.9 mmol, 1.00 equiv), **Ar-BPin** (2.87 g, 6.17 mmol, 2.10 equiv), H_2O (30 mL) and THF (90 mL). The solution was sparged with N_2 for 40 minutes, followed by addition of K_2CO_3 (1.63 g, 11.8 mmol, 4.00 equiv) and SPhos Pd G2 (0.042 g, 0.059 mmol, 0.0200 equiv). The solution was heated to 70 °C and stirred for 16 h. The reaction was cooled to room temperature and THF removed *in vacuo*. The solution was then diluted with Et_2O (100 mL) and H_2O (100 mL) and the aqueous layer was extracted with additional Et_2O (3 × 50 mL). The combined organic layers were dried over $MgSO_4$ and concentrated *in vacuo*. The resultant brown oil was subjected to filtration through a silica plug (Et_2O) to afford **3-OCH_2tBu** as a light brown solid (2.55 g, 2.9 mmol, 94% yield) and used directly in the next step without further purification. ^{1}H NMR (500 MHz, $CDCl_3$): δ 6.81 (s, 2H), 6.64 – 6.62 (m, 4H), 6.54 (dd, J = 2.28, 8.12, 2H), 3.65 (s, 4H), 1.07 (s, 18H), 0.97 (s, 18H), 0.93 (s, 18H), 0.18 (s, 12H), 0.06 (s, 12H) ppm. ^{13}C NMR (126 MHz, $CDCl_3$): δ 148.40, 146.25, 145.43, 135.41, 132.62, 122.93, 122.74, 120.41, 115.58, 78.91, 32.30, 26.83, 26.11, 26.09, 18.58, 18.53, -3.90, -4.04 ppm. MS (ESI/ion trap) *m/z*: $[M+Na]^+$ Calcd for $C_{52}H_{90}O_6Si_4$: 945.57; found 945.7.

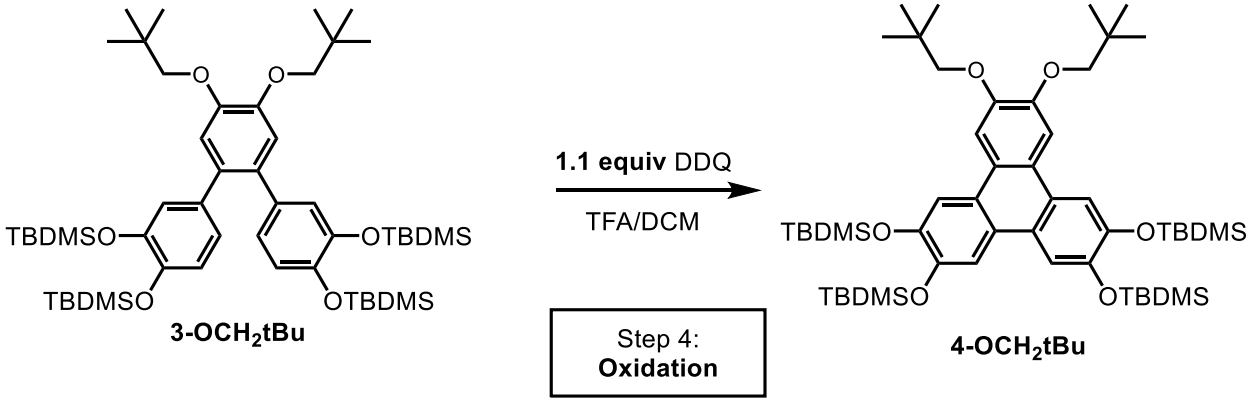

Synthesis of 4-OCH_2tBu. A 500 mL Schlenk flask equipped with a stir bar was charged with **3-OCH_2tBu** (2.67 g, 2.9 mmol, 1.00 equiv), anhydrous DCM (150 mL), and trifluoroacetic acid (15 mL). The solution was cooled to 0 °C and sparged with N_2 for 30 minutes. After sparging, 2,3-dichloro-5,6-dicyano-1,4-benzoquinone (0.72 g, 3.19 mmol, 1.10 equiv) was added under N_2 after which the solution immediately turned dark green. The reaction was kept at 0 °C for 3 h then

carefully quenched with a saturated aqueous solution of $NaHCO_3$ (~200 mL). The DCM layer was separated and washed with a saturated aqueous solution of $NaHCO_3$ (3 × 100 mL) and H_2O (3 × 100 mL). The organic layer was dried over $MgSO_4$ and concentrated *in vacuo*. The resultant brown oil was subjected to filtration through a silica plug eluting with DCM to afford **4-OCH$_2$tBu** (1.73 g, 1.9 mmol, 68% yield) and used directly in Step 5 without further purification. ^{1}H NMR (500 MHz, $CDCl_3$): δ 7.83 (s, 2H), 7.78 (s, 2H), 7.68 (s, 2H), 3.80 (s, 4H), 1.14 (s, 18H), 1.07 (s, 18H), 1.06 (s, 18H), 0.31 (s, 12H), 0.30 (s, 12H) ppm. ^{13}C NMR (126 MHz, $CDCl_3$): δ 149.57, 146.68, 146.66, 124.26, 123.98, 123.21, 114.20, 114.11, 106.28, 83.61, 79.02, 32.36, 26.87, 26.27, 26.23, 25.02, -3.88, -3.92 ppm. MS (ESI/ion trap) *m/z*: $[M+H]^+$ Calcd for $C_{52}H_{88}O_6Si_4$: 921.57; found 921.6.

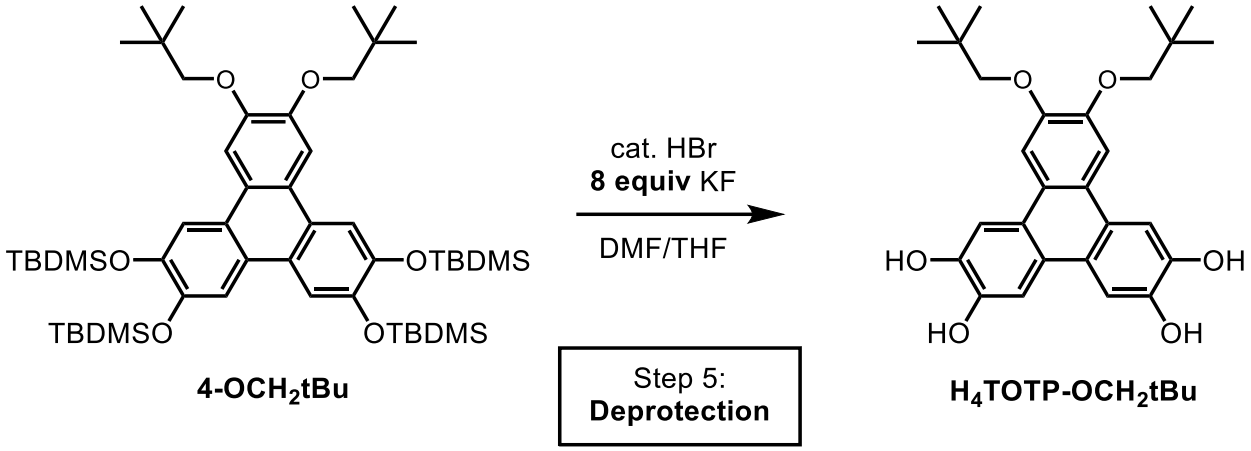

Synthesis of H$_4$TOTP-OCH$_2$tBu: A 100 mL Schlenk flask equipped with a stir bar was charged with **4-OCH$_2$tBu** (1.81 g, 2.0 mmol, 1.00 equiv), DMF (10 mL) and THF (10 mL) to create a ~0.1 M soluion in 1:1 DMF:THF, and sparged with N_2 for 30 minutes. Potassium fluoride (0.91 g, 15.7 mmol, 8.00 equiv) and 8.8 M HBr (0.089 mL, 0.79 mmol, 0.4 equiv) were then added, and the reaction was stirred at room temperature for 48 h. The flask was cooled to 0 °C, and 1 M HCl (~90 mL) was added. The reaction was then extracted with EtOAc (3 × 50 mL), and the combined organic layers were washed with H_2O (3 × 100 mL). The organic layer was then dried over $MgSO_4$ and concentrated *in vacuo*. The product was then triturated with a 1:10 mixture of Et_2O:hexanes (40 mL) to yield **H$_4$TOTP-OCH$_2$tBu** (0.74 g, 1.6 mmol, 86% yield) as a light gray solid. ^{1}H NMR (500 MHz, DMSO-*d$_6$*): δ 9.40 (s, 2H), 9.22 (s, 2H), 7.84 (s, 2H), 7.70 (s, 2H) 7.65 (s, 2H), 3.85 (s, 4H), 1.11 (s, 18H) ppm. ^{13}C NMR (126 MHz, DMSO-*d$_6$*): δ 148.21, 145.61, 145.43, 122.32, 122.21, 121.82, 108.32, 107.67, 105.16, 77.61, 31.98, 26.52 ppm. MS (ESI/ion trap) *m/z*: $[M-H]^-$ Calcd for $C_{28}H_{32}O_6$: 463.21; found 463.19.

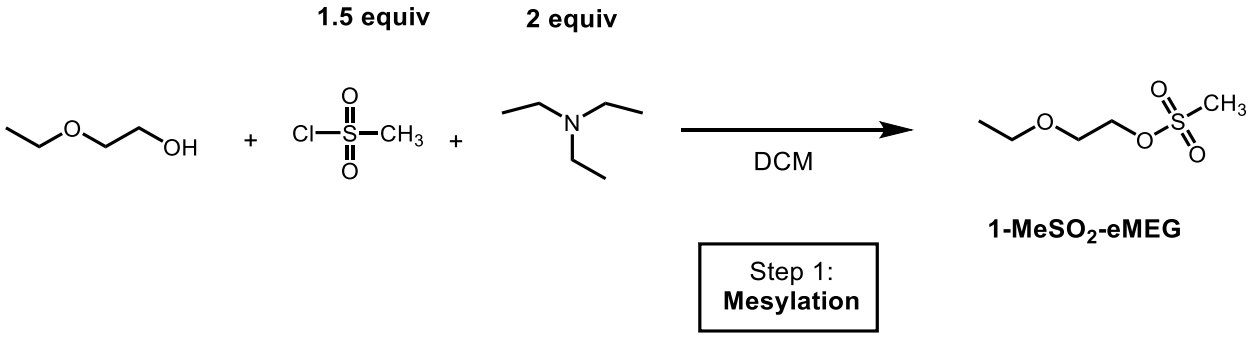

Synthesis of 1-MeSO$_2$-eMEG. A flame-dried 100 mL round bottom flask equipped with a stir bar was charged with 2-ethoxyethanol (2.00 g, 22.2 mmol, 1.00 equiv), triethylamine (4.49 g, 44.4 mmol, 2.00 equiv), and DCM (25 mL). The reaction mixture was then cooled to 0 °C and stirred under a N_2 atmosphere. Under positive N_2 pressure, methanesulfonyl chloride (3.81 g, 33.3 mmol, 1.50 equiv) was slowly added via syringe. The reaction was allowed to warm to room temperature overnight while stirring. The reaction mixture was diluted with DCM (50 mL) and extracted with 1.0 M HCl (3 × 30 mL), then washed with a saturated aqueous solution of $NaHCO_3$ (3 × 30 mL), and water (3 × 30 mL). The organic layer was dried over $MgSO_4$ and concentrated *in vacuo*. The resulting oil was dried at 40 °C under high vacuum to yield **1-MeSO$_2$-eMEG** (2.76 g, 16.4 mmol, 74% yield) as a yellow solid and used in the next step without further purification. ^{1}H NMR (500 MHz, $CDCl_3$) δ 4.39 – 4.34 (m, 2H), 3.72 – 3.65 (m, 2H), 3.55 (q, *J* = 7.0 Hz, 2H), 3.06 (s, 3H), 1.21 (t, *J* = 7.0 Hz, 3H) ppm. ^{13}C NMR (126 MHz, $CDCl_3$) δ 69.45, 68.22, 66.77, 37.66, 15.05 ppm. MS (ESI/ion trap) *m/z*: $[M+Na]^+$ Calcd for $C_5H_{12}O_4Si$: 191.04; found 190.8.

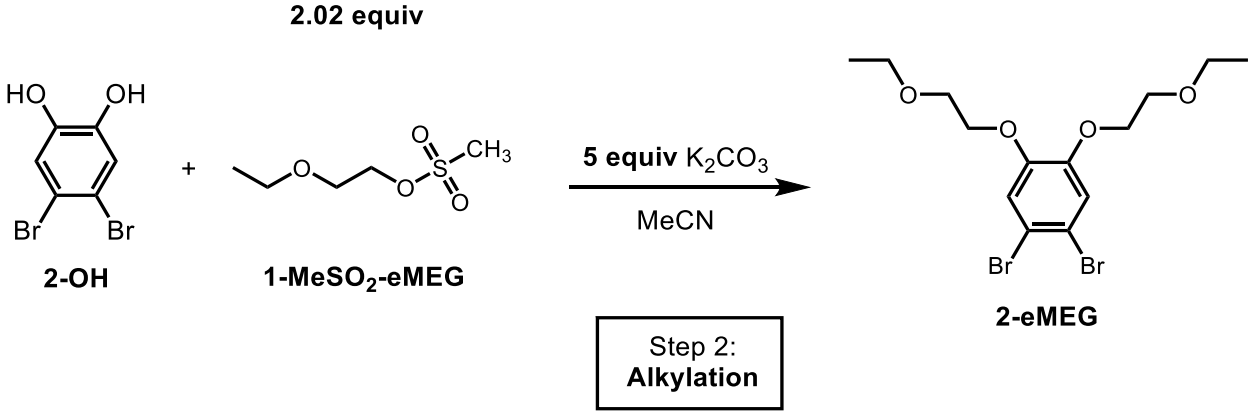

Synthesis of 2-eMEG. A flame-dried 250 mL two-neck round bottom flask equipped with a stir bar and reflux condenser was charged with 4,5-dibromobenzene-1,2-diol (2.25 g, 8.40 mmol, 1.00 equiv), K_2CO_3 (5.80 g, 42.0 mmol, 5.00 equiv), **1-MeSO$_2$-eMEG** (2.85 g, 17.0 mmol, 2.02 equiv), and acetonitrile (100 mL). The mixture was sparged with N_2 for 30 minutes and then heated at 75 °C for 48 h while stirring under an N_2 atmosphere. Following the reaction, the mixture was diluted with DCM (150 mL) and transferred to a separation funnel. The organic layer was washed with a saturated aqueous solution of $NaHCO_3$ (3 × 100 mL), and water (3 × 100 mL). The organic layer was then dried over $MgSO_4$ and concentrated *in vacuo*. The resulting liquid was dried at 60 °C under high vacuum to yield **2-eMEG** (2.78 g, 6.7 mmol, 80% yield) as a yellow solid. ^{1}H NMR

(500 MHz, $CDCl_3$) δ 7.15 (s, 2H), 4.16 – 4.09 (m, 4H), 3.82 – 3.75 (m, 4H), 3.59 (q, *J* = 7.0 Hz, 4H), 1.22 (t, *J* = 7.0 Hz, 6H) ppm. ^{13}C NMR (126 MHz, $CDCl_3$) δ 149.05, 119.27, 115.42, 69.49, 68.85, 66.95, 15.27 ppm. MS (ESI/ion trap) *m/z*: $[M+Na]^+$ Calcd for $C_{14}H_{20}Br_2O_4$: 432.96; found 433.0.

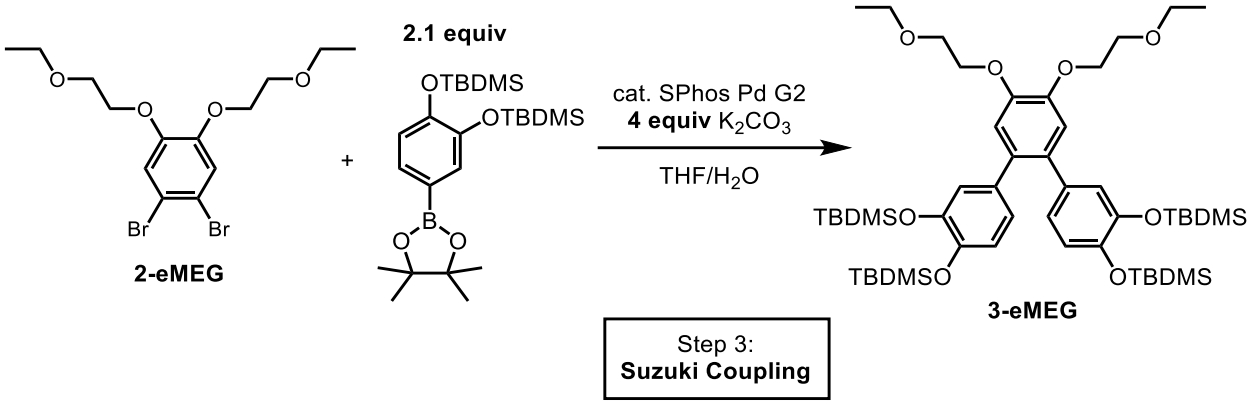

Synthesis of 3-eMEG. A 250 mL two-neck round bottom flask equipped with a stir bar and reflux condenser was charged with **2-eMEG** (1.67 g, 0.41 mmol, 1.00 equiv), **Ar-Bpin** (3.95 g, 0.85 mmol, 2.10 equiv), K_2CO_3 (2.24 g, 1.6 mmol, 4.00 equiv), THF (90 mL), and water (30 mL). The reaction mixture was sparged with N_2 for 30 minutes. Under positive N_2 pressure, SPhos Pd G2 (0.077 g, 0.11 mmol, 2.65 mol%) was added and the reaction was heated at 60 °C for 24 h with stirring. After 24 h, the mixture was diluted with diethyl ether (50 mL) and water (50 mL), and the aqueous layer was extracted with additional diethyl ether (2 × 50 mL). The combined organic layers were dried over $MgSO_4$ and concentrated *in vacuo*. The residue was triturated with MeOH. The resulting off-white solid was collected by vacuum filtration and dried under high vacuum overnight to yield **3-eMEG** (2.34 g, 2.5 mmol, 62% yield). ^1H NMR (500 MHz, $CDCl_3$) δ 6.89 (s, 2H), 6.66 – 6.60 (m, 4H), 6.53 (dd, *J* = 8.2, 2.2 Hz, 2H), 4.24 – 4.18 (m, 4H), 3.85 – 3.79 (m, 4H), 3.62 (q, *J* = 7.0 Hz, 4H), 1.23 (t, *J* = 7.0 Hz, 6H), 0.97 (s, 18H), 0.93 (s, 18H), 0.18 (s, 12H), 0.06 (s, 12H) ppm. ^{13}C NMR (126 MHz, $CDCl_3$) δ 147.93, 146.28, 145.56, 135.01, 133.63, 122.93, 122.63, 120.42, 117.49, 69.23, 66.94, 26.09, 18.57, 18.48, 15.39, -3.91, -4.03 ppm. MS (ESI/ion trap) *m/z*: $[M+Na]^+$ Calcd for $C_{50}H_{86}O_8Si_4$: 949.53; found 949.8.

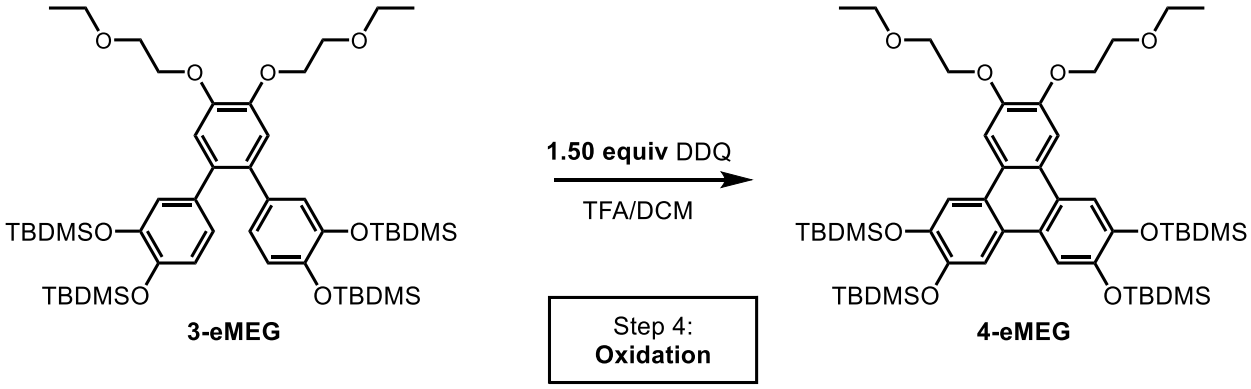

Synthesis of 4-eMEG. A 500 mL Schlenk flask equipped with a stir bar was charged with **3-eMEG** (2.08 g, 2.24 mmol, 1.00 equiv), anhydrous DCM (200 mL), and trifluoroacetic acid (20

mL). The solution was cooled to 0 °C and sparged with N_2 for 30 minutes. After sparging, 2,3-dichloro-5,6-dicyano-1,4-benzoquinone (0.76 g, 3.37 mmol, 1.50 equiv) was added under N_2 after which the solution immediately turned dark green. The reaction was kept at 0 °C for 3 h then carefully quenched with a saturated aqueous solution of $NaHCO_3$ (~200 mL). The DCM layer was separated and washed with a saturated aqueous solution of $NaHCO_3$ (5 × 100 mL) and H_2O (2 × 100 mL). The organic layer was dried over $MgSO_4$ and concentrated *in vacuo* to yield **4-eMEG** (1.47 g, 1.6 mmol, 71% yield) as a dark purple solid and used directly in Step 5 without further purification. ^{1}H NMR (500 MHz, $CDCl_3$): δ 7.81 (s, 2H), 7.80 (s, 2H), 7.78 (s, 2H), 4.38 – 4.33 (m, 4H), 3.93 – 3.86 (m, 4H), 3.67 (q, *J* = 7.0 Hz, 4H), 1.27 (t, *J* = 7.0 Hz, 6H), 1.07 (s, 18H), 1.06 (s, 18H), 0.31 (s, 12H), 0.30 (s, 12H) ppm. ^{13}C NMR (126 MHz, $CDCl_3$) δ 148.84, 146.96, 146.77, 124.14, 124.02, 114.32, 114.10, 108.56, 69.41, 69.22, 67.05, 26.22, 18.85, 18.78, 15.43, -3.86, -3.87 ppm. MS (ESI/ion trap) *m/z*: $[M+Na]^+$ Calcd for $C_{50}H_{84}O_8Si_4$: 947.80; found 947.51.

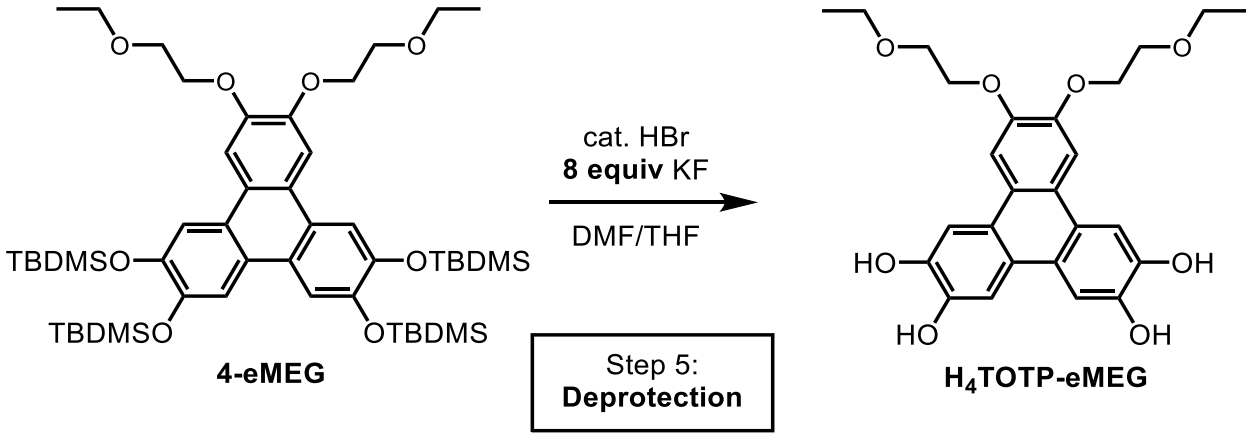

Synthesis of H_4TOTP-eMEG: A 100 mL Schlenk flask equipped with a stir bar was charged with **4-eMEG** (0.90 g, 0.97 mmol, 1.00 equiv), DMF (12.5 mL) and THF (12.5 mL) to create a solution in 1:1 DMF:THF, and sparged with N_2 for 30 minutes. Potassium fluoride (0.452 g, 7.8 mmol, 8.00 equiv) and 8.8 M HBr (0.044 mL, 0.39 mmol, 0.4 equiv) were then added, and the reaction was stirred at room temperature for 48 h. The flask was cooled to 0 °C, and 1 M HCl (75 mL) was added. The reaction was then extracted with DCM (3 × 75 mL), and the combined organic layers were washed with H_2O (2 × 50 mL). The organic layer was then dried over $MgSO_4$ and concentrated *in vacuo*, then diluted with *n*-heptane (10 mL) and concentrated again *in vacuo* to remove excess DMF. The product was then triturated with a 1:10 mixture of hexanes and Et_2O to yield **H_4TOTP-eMEG** (0.43 g, 0.91 mmol, 94% yield) as a light gray solid. ^{1}H NMR (500 MHz, DMSO) δ 9.47 (s, 2H), 9.16 (s, 2H), 7.83 (s, 2H), 7.79 (s, 2H), 7.65 (s, 2H), 4.31 (t, *J* = 4.5 Hz, 4H), 3.80 (t, *J* = 4.5 Hz, 4H), 3.58 (q, *J* = 7.0 Hz, 4H), 1.16 (t, *J* = 7.0 Hz, 6H) ppm. ^{13}C NMR (126 MHz, $CDCl_3$) δ 147.67, 145.74, 145.48, 122.78, 122.34, 121.75, 108.55, 107.67, 106.68, 68.59, 68.36, 65.86, 15.21. MS (ESI/ion trap) *m/z*: $[M-H]^-$ Calcd for $C_{26}H_{28}O_8$: 467.17; found 467.14.

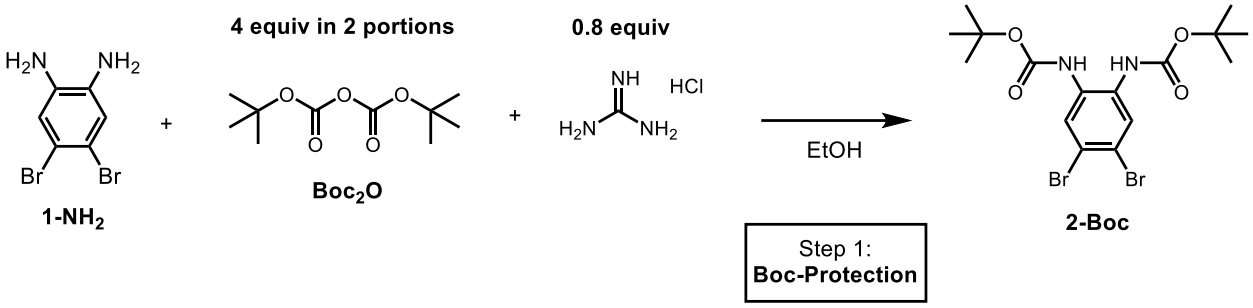

Synthesis of 2-Boc. A 500 mL round bottom flask equipped with a stir bar and reflux condenser was charged with 4,5-dibromobenzene-1,2-diamine (**1-NH$_2$**, 8.00 g, 30.1 mmol, 1.00 equiv), **Boc$_2$O** (19.71 g, 90.3 mmol, 3 equiv), guanidine hydrochloride (2.30 g, 24.6 mmol, 0.8 equiv), and EtOH (200 mL). The solution was sparged with N_2 for 30 minutes, and then heated to 50 °C and stirred for 18 h. Additional **Boc$_2$O** (6.57 g, 30.1 mmol, 1.00 equiv) was then added to drive the reaction to completion and the mixture was heated for an additional 24 h. The reaction was cooled to room temperature and EtOH removed *in vacuo*. The dark orange powder was then sonicated with water (5 × 15 mL) and washed with hexanes (5 × 20 mL). The powder was then sonicated again with water (3 × 15 mL) to remove excess guanidine hydrochloride and dried at 40 °C under high vacuum to yield **2-Boc** (13.59 g, 29.2 mmol, 97% yield) as an orange powder. ^{1}H NMR (500 MHz, $CDCl_3$): δ 8.77 (s, 2H), 7.92 (s, 2H), 1.47 (s, 18H) ppm. ^{13}C NMR (126 MHz, $CDCl_3$): δ 152.76, 130.34, 127.02, 117.28, 80.13, 27.99 ppm. MS (ESI/ion trap) *m/z*: $[M]^-$ Calcd for $C_{16}H_{22}Br_2N_2O_4$: 463.99; found 464.8.

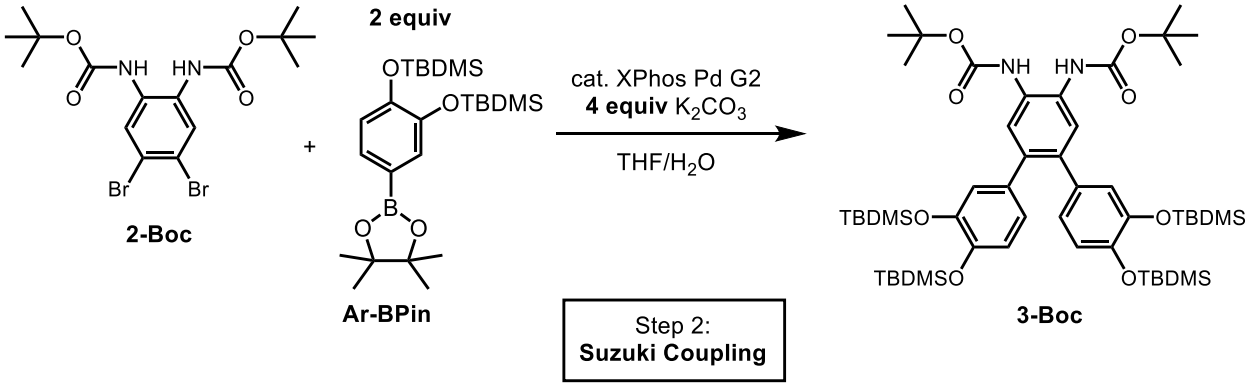

Synthesis of 3-Boc. A 250 mL round bottom flask equipped with a stir bar and reflux condenser was charged with **2-Boc** (7.00 g, 15.01 mmol, 1.00 equiv), **Ar-BPin** (13.95 g, 30.02 mmol, 2.00 equiv), H_2O (120 mL) and THF (360 mL). The solution was sparged with N_2 for 40 minutes, followed by addition of K_2CO_3 (8.30 g, 60.04 mmol, 4.00 equiv) and XPhos Pd G2 (0.236 g, 0.30 mmol, 0.0200 equiv). The solution was heated to 60 °C and stirred for 18 h. The reaction was cooled to room temperature and THF removed *in vacuo*. The aqueous phase was then extracted with DCM (3 × 100 mL) and the combined organic layers were dried over $MgSO_4$ and concentrated *in vacuo*. The product was then subjected to filtration through a silica plug (1:1 Et_2O:hexanes) and further concentrated *in vacuo*. The resultant brown solid was adsorbed to silica gel and purified by automated flash chromatography (0–10% ethyl acetate in hexanes) and concentrated *in vacuo* to

afford **3-boc** (10.87 g, 11.07 mmol, 74% yield) as a white solid. ^{1}H NMR (500 MHz, $CDCl_3$): δ 7.42 (s, 2H), 6.76 – 6.75 (s, 2H), 6.65 – 6.63 (m, 2H), 6.59 – 6.57 (m, 4H), 1.52 (s, 18H), 0.97 (s, 18H), 0.91 (s, 18H), 0.17 (s, 12H), 0.05 (s, 12H) ppm. ^{13}C NMR (126 MHz, $CDCl_3$): δ 154.08, 146.32, 145.79, 134.39, 122.81, 122.52, 120.53, 80.95, 60.53, 28.43, 26.09, 26.06, 18.56, 18.48, -3.93, -4.05 ppm. MS (ESI/ion trap) *m/z*: $[M]^-$ Calcd for $C_{52}H_{88}N_2O_8Si_4$: 980.56; found 980.4.

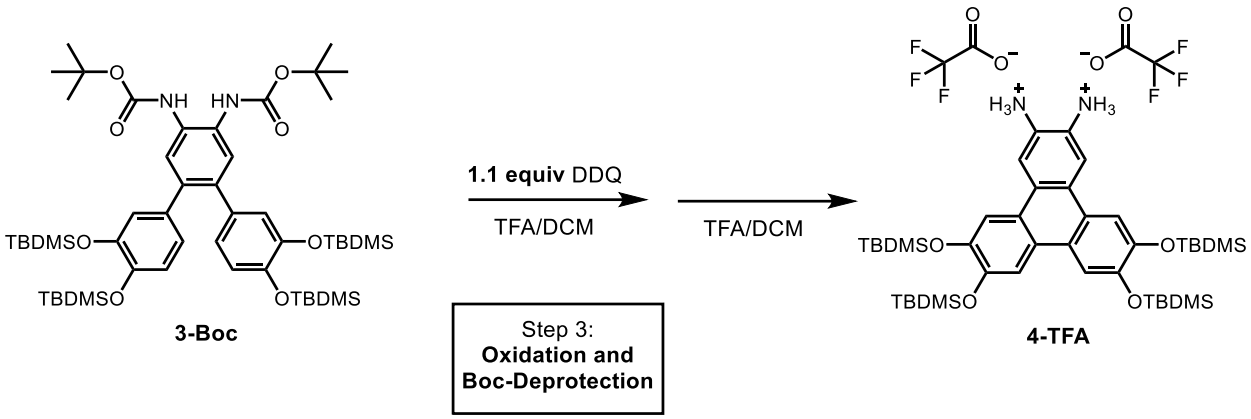

Synthesis of 4-TFA (referred to as Int-1 in the main text). A 500 mL Schlenk flask equipped with a stir bar was charged with **3-Boc** (8.30 g, 8.5 mmol, 1.00 equiv), anhydrous DCM (400 mL), and trifluoroacetic acid (40 mL). The solution was cooled to 0 °C and sparged with N_2 for 30 minutes. After sparging, 2,3-dichloro-5,6-dicyano-1,4-benzoquinone (2.11 g, 9.4 mmol, 1.10 equiv) was added under N_2 after which the solution immediately turned dark green. The reaction was kept at 0 °C for 3 h then carefully quenched with a saturated aqueous solution of $NaHCO_3$ (~200 mL). The DCM layer was separated and washed with a saturated aqueous solution of $NaHCO_3$ (3 × 100 mL) and H_2O (2 × 100 mL). The organic layer was dried over $MgSO_4$ and concentrated *in vacuo*. The resultant brown solid was then dissolved in DCM (15 mL) and TFA (15 mL) and stirred 18 h. The product was concentrated *in vacuo* and washed with cold hexanes (4 × 20 mL) to yield **4-TFA** (3.92 g, 3.9 mmol, 46% yield) as a light purple solid and used directly in Step 4 without further purification. MS (ESI/ion trap) reports the uncoordinated neutral intermediate without trifluoroacetates. ^{1}H NMR (500 MHz, $CDCl_3$): δ 8.23 – 8.20 (m, 2H), 7.79 (s, 2H), 7.66 (s, 2H), 1.05 (s, 18H), 1.00 (s, 18H), 0.31 (s, 12H), 0.25 (s, 12H) ppm. ^{13}C NMR (126 MHz, $CDCl_3$): δ 163.44 (q, J = 38.0 Hz), 149.04, 147.50, 129.91, 125.45, 122.24, 117.27, 114.97, 114.71, 114.02, 26.14, 25.81, 18.83, 18.46, -3.86, -4.29, -4.30 ppm. ^{19}F NMR (471 MHz, $CDCl_3$) δ −61.93 (s, 6F) ppm. MS (ESI/ion trap) *m/z*: $[M+H]^+$ Calcd for $C_{42}H_{70}N_2O_4Si_4$: 779.44; found 779.6.

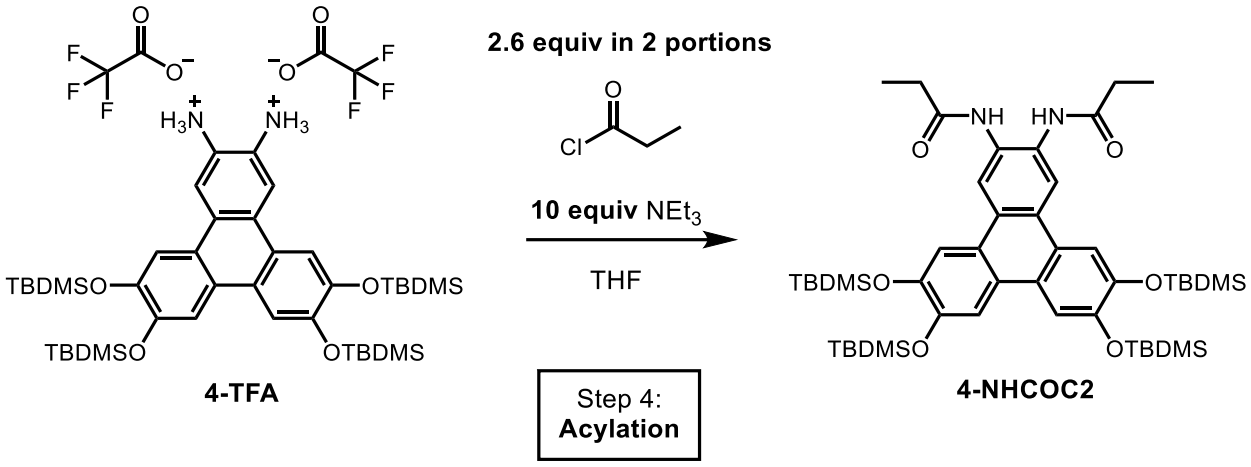

Synthesis of 4-NHCOC2. A 250 mL Schlenk flask equipped with a stir bar was charged with **4-TFA** (1.70 g, 1.69 mmol, 1.00 equiv), triethylamine (1.71 g, 16.9 mmol, 10.00 equiv), and THF (100 mL) and the solution was sparged with N_2 for 40 minutes. A solution of propionyl chloride (0.32 g, 3.5 mmol, 2.05 equiv) and THF (100 mL) was sparged with N_2 for 40 minutes and added dropwise to the flask over 1 h. The reaction was kept at 0 °C during the addition. After addition the reaction mixture was allowed to warm to room temperature and was stirred overnight. The reaction was checked for completion by ^{1}H NMR and additional propionyl chloride (0.086 g, 0.93 mmol, 0.55 equiv) was combined with THF (15 mL) and sparged for 20 minutes with N_2. The Schlenk flask was again lowered to 0 °C and the propionyl chloride solution was added dropwise and the flask was stirred an additional 18 h, warming to room temperature. The THF was removed *in vacuo* and the reaction was diluted with EtOAc (100 mL) and solid byproduct was filtered off. The reaction was then washed with brine (3 × 100 mL), and water (3 × 100 mL). The organic layer was dried over $MgSO_4$ and concentrated *in vacuo* to yield a yellow solid. The solid was recrystallized from toluene to yield **4-NHCOC2** (0.87 g, 0.98 mmol, 58% yield) as white crystals. ^{1}H NMR (500 MHz, $CDCl_3$): δ 8.36 (s, 2H), 8.18 (s, 2H), 7.86 (s, 2H), 7.77 (s, 2H) 2.42 (q, J = 7.6 Hz, 4H), 1.19 (t, J = 7.6 Hz, 6H), 1.07 (s, 18H), 1.06 (s, 18H), 0.33 (s, 12H), 0.31 (s, 12H) ppm. ^{13}C NMR (126 MHz, $CDCl_3$): δ 174.15, 147.93, 147.03, 129.44, 127.13, 124.78, 123.49, 119.38, 114.81, 114.14, 30.24, 26.24, 26.20, 18.92, 18.71, 9.59, -3.79, -3.85 ppm. MS (ESI/ion trap) *m/z*: $[M-H]^-$ Calcd for $C_{48}H_{78}N_2O_6Si_4$: 889.49; found 889.7.

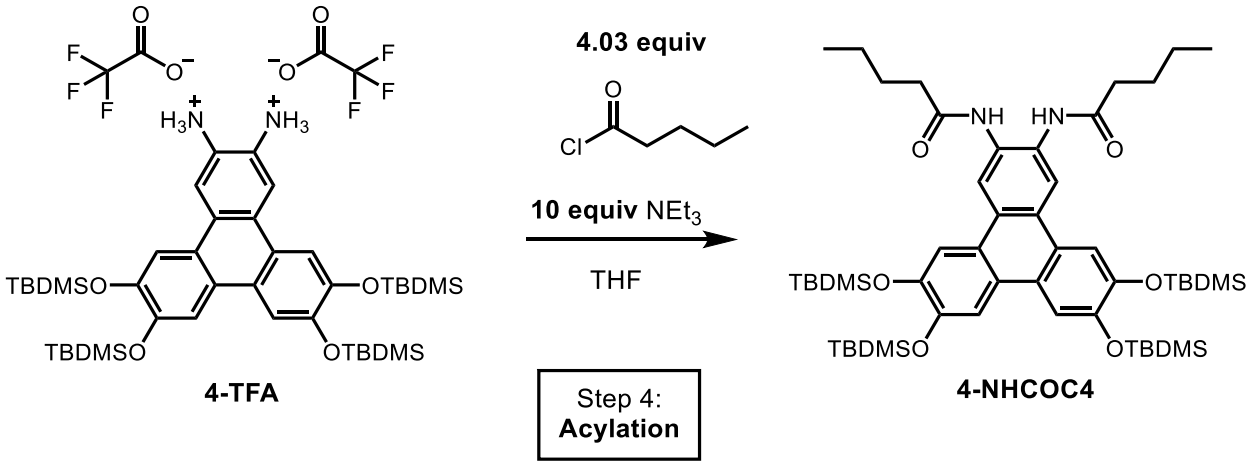

Synthesis of 4-NHCOC4. A 250 mL Schlenk flask equipped with a stir bar was charged with **4-TFA** (1.00 g, 0.99 mmol, 1.00 equiv), triethylamine (1.00 g, 9.93 mmol, 10.00 equiv), and THF (50 mL) and the solution was sparged with N_2 for 40 minutes. A solution of valeryl chloride (0.48 g, 4.0 mmol, 4.03 equiv) and THF (50 mL) was sparged with N_2 for 40 minutes and added dropwise to the flask over 1 h. The reaction was kept at 0 °C during the addition. After addition the reaction mixture was allowed to warm to room temperature and was stirred overnight. The THF was removed *in vacuo* and the reaction was diluted with EtOAc (100 mL) and solid byproduct was filtered off. The organics were washed with brine (3 × 100 mL), and water (3 × 100 mL). The organic layer was dried over $MgSO_4$ and concentrated *in vacuo* to yield **4-NHCOC4** (0.89 g, 0.94 mmol, 95% yield) as an off-white solid and used in the next step without further purification. ^{1}H NMR (500 MHz, $CDCl_3$): δ 8.34 (s, 2H), 8.23 (s, 2H), 7.86 (s, 2H), 7.77 (s, 2H) 2.37 (t, J = 7.5 Hz, 4H), 1.68 – 1.62 (m, 4H), 1.38 – 1.30 (m, 4 H), 1.07 (s, 18H), 1.06 (s, 18H), 0.90 (t, J = 7.4 Hz, 6H), 0.32 (s, 12H), 0.31 (s, 12H) ppm. ^{13}C NMR (126 MHz, $CDCl_3$): δ 173.62, 147.90, 147.02, 129.52, 127.20, 124.83, 123.45, 119.47, 114.79, 114.11, 36.98, 27.80, 26.21, 22.32, 18.87, 18.73, 13.89, -3.83, -3.85 ppm. MS (ESI/ion trap) *m/z*: $[M-H]^-$ Calcd for $C_{52}H_{86}N_2O_6Si_4$: 945.56; found 945.9.

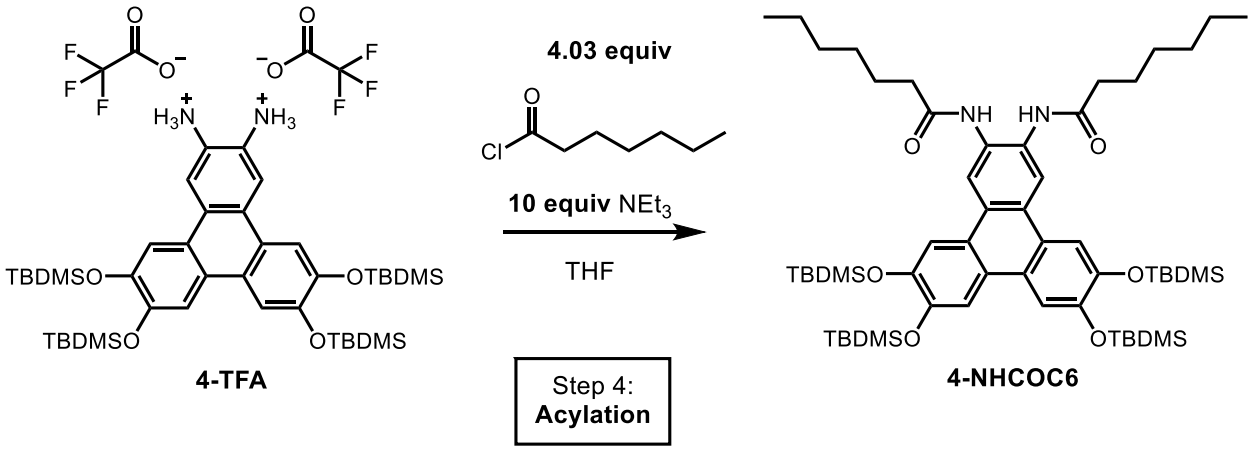

Synthesis of 4-NHCOC6. A 250 mL Schlenk flask equipped with a stir bar was charged with **4-TFA** (1.00 g, 0.99 mmol, 1.00 equiv), triethylamine (1.00 g, 9.93 mmol, 10.00 equiv), and THF (50 mL) and the solution was sparged with N_2 for 40 minutes. A solution of heptanoyl chloride (0.59 g, 4.0 mmol, 4.03 equiv) and THF (50 mL) was sparged with N_2 for 40 minutes and added dropwise to the flask over 1 h. The reaction was kept at 0 °C during the addition. After addition the reaction mixture was allowed to warm to room temperature and stirred overnight. The THF was removed *in vacuo* and the reaction was diluted with EtOAc (100 mL) and solid byproduct was filtered off. The reaction was then washed with brine (3 × 100 mL), and water (3 × 100 mL). The organic layer was dried over $MgSO_4$ and concentrated *in vacuo* to yield **4-NHCOC6** (0.97 g, 0.97 mmol, 97% yield) as an off-white solid and used in the next step without further purification. ^{1}H NMR (500 MHz, $CDCl_3$): δ 8.35 (s, 2H), 8.22 (s, 2H), 7.86 (s, 2H), 7.76 (s, 2H) 2.44 (t, *J* = 7.5 Hz, 2H), 2.37 (t, *J* = 7.6 Hz, 2H), 1.71 – 1.63 (m, 4H), 1.39 – 1.22 (m, 12H), 1.07 (s, 18H), 1.07 (s, 18H), 0.89 (t, J = 6.8 Hz, 6H), 0.33 (s, 12H), 0.31 (s, 12H) ppm. ^{13}C NMR (126 MHz, $CDCl_3$): δ 173.55, 147.85, 146.99, 129.45, 127.21, 124.80, 123.44, 119.40, 114.74, 113.98, 37.28, 31.66, 28.90, 26.20, 26.18, 25.76, 22.61, 18.84, 18.72, 14.22, -3.81, -3.83 ppm. MS (ESI/ion trap) *m/z*: $[M-H]^-$ Calcd for $C_{56}H_{94}N_2O_6Si_4$: 1001.62; found 1001.8.

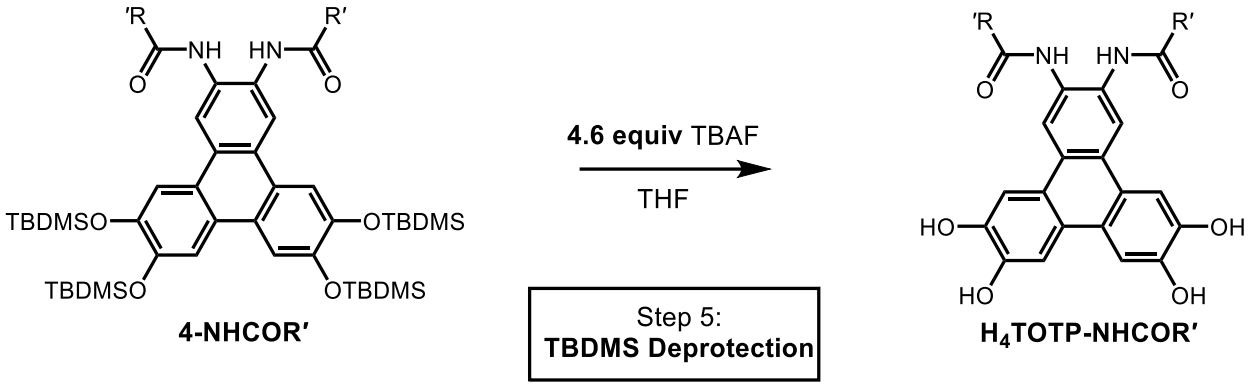

General TBDMS Deprotection procedure to synthesize H_4TOTP-NHCOC2, H_4TOTP-NHCOC4, and H_4TOTP-NHCOC6. A 20 mL scintillation vial with a septum cap equipped with a stir bar was charged with **4-NHCOR′** (0.55 mmol, 1.00 equiv) and THF (3 mL) and the solution was sparged with N_2 for 20 minutes at 0 °C. Separately, a solution of 1.0 M tetrabutyl ammonium fluoride (TBAF, 2.53 mL, 2.53 mmol, 4.6 equiv) in THF was sparged with N_2 for 20 minutes also at 0 °C. Both solutions were allowed to warm to room temperature and the TBAF solution was added dropwise to the **4-NHCOR′** solution under positive N_2 pressure, and the reaction stirred for 1 h, at which point a white precipitate formed. The reaction was quenched with glacial acetic acid (10 mL) and the THF was removed *in vacuo*. The solution was then diluted with MeCN (15 mL) and the solid was washed with acetic acid (3 × 15 mL), hexanes (3 × 15 mL), and cold EtOAc (10 mL) to yield **H_4TOTP-NHCOR′** as a white powder.

H_4TOTP-NHCOC2 was synthesized according to the general TBDMS deprotection procedure, on a 0.49 g (0.55 mmol) scale of **4-NHCOC2**. The desired product was obtained as white crystals in 90% yield (0.21 g, 0.49 mmol). ^{1}H NMR (500 MHz, $CDCl_3$): δ 9.46 – 9.44 (m, 6H), 8.61 (s, 2H), 7.77 (s, 2H), 7.65 (s, 2H), 2.46 (q, J = 7.5 Hz, 4H), 1.17 (t, J = 7.5 Hz, 6H) ppm. ^{13}C NMR (126 MHz, $CDCl_3$): δ 172.73, 146.52, 145.70, 128.86, 125.23, 122.92, 121.35, 117.75, 108.33, 108.00, 29.56, 9.80 ppm. MS (ESI/ion trap) *m/z*: $[M-H]^-$ Calcd for $C_{24}H_{22}N_2O_6$: 433.14; found 433.12.

H_4TOTP-NHCOC4 was synthesized according to the general TBDMS deprotection procedure, on a 0.83 g (0.88 mmol) scale of **4-NHCOC4**. The desired product was obtained as a white powder in 77% yield (0.34 g, 0.64 mmol). ^{1}H NMR (500 MHz, $CDCl_3$): δ 9.48 – 9.47 (m, 6H) 8.57 (s, 2H), 7.76 (s, 2H), 7.65 (s, 2H), 2.43 (t, *J* = 7.5 Hz, 4H), 1.69 – 1.63 (m, 4H), 1.44 – 1.37 (m, 4H), 0.95 (t, *J* = 7.4 Hz, 6H) ppm. ^{13}C NMR (126 MHz, $CDCl_3$): δ 171.99, 146.55, 145.70, 128.89, 125.33, 122.94, 121.28, 117.83, 108.31, 107.98, 36.16, 27.42, 21.99, 13.89 ppm. MS (ESI/ion trap) *m/z*: $[M-H]^-$ Calcd for $C_{28}H_{30}N_2O_6$: 489.20; found 489.18.

H_4TOTP-NHCOC6 was synthesized according to the general TBDMS deprotection procedure, on a 1.0 g (1.0 mmol) scale of **4-NHCOC6**. The desired product was obtained as a white powder in 79% yield (0.43 g, 0.79 mmol). ^{1}H NMR (500 MHz, $CDCl_3$): δ 9.48 – 9.46 (m, 6H) 8.57 (s, 2H), 7.76 (s, 2H), 7.65 (s, 2H), 2.42 (t, *J* = 7.4 Hz, 4H), 1.70 – 1.64 (m, 4H), 1.39 – 1.32 (m, 12H), 0.90 – 0.88 (m, 6H) ppm. ^{13}C NMR (126 MHz, $CDCl_3$): δ 171.96, 146.55, 145.69, 128.88, 125.35,

122.94, 121.28, 117.80, 108.32, 107.97, 36.48, 31.22, 28.51, 25.25, 22.14, 14.03 ppm. MS (ESI/ion trap) *m/z*: $[M-H]^-$ Calcd for $C_{32}H_{38}N_2O_6$: 489.20; found 489.18.

3.6.5 Electrochemical characterization.

All conductivity measurements were carried out using a BioLogic SP-200 Potentiostat. Conductivity measurements were run on packed pellets using a 2-electrode screw cell. A polyetheretherketone (PEEK) spacer with a 2.8 mm smooth internal diameter was prepared with threading for two brass screws to compress powders from either side.[6] The tips of the screws were polished to a flat surface 2.75 mm in diameter. Cells were prepared by screwing one screw into the PEEK spacer, then adding 8-10 mg of powder, and screwing the second screw until finger-tight, and then tightening to 0.56 Nm with a controlled torque screwdriver on both screws. Sample thicknesses were measured with calipers and were typically in the range of 200–600 μm. Cells were allowed to settle for 8 h, before re-tightening to 0.56 Nm and settling for an additional 18 h at which point I-V curves measured using a current scan (CS)

3.6.6 Supplementary tables.

Table 3.S1. Room temperature (298 K) conductivity values obtained from pressed pellets of CuTOTP-R across three measurements. Values for CuTOTP-NHCOC2, -NHCOC4, and -NHCOC6 taken after conversion to hexagonal phase unless otherwise indicated.

Sample	Conductivity (Measurement 1) (S cm^{-1})	Conductivity (Measurement 2) (S cm^{-1})	Conductivity (Measurement 3) (S cm^{-1})
CuTOTP-OCH_2tBu	6.3×10^{-6}	6.4×10^{-6}	3.2×10^{-7}
CuTOTP-eMEG	5.8×10^{-4}	5.3×10^{-4}	3.3×10^{-4}
CuTOTP-NHCOC2	2.1×10^{-3}	1.1×10^{-3}	1.5×10^{-3}
CuTOTP-NHCOC4	1.5×10^{-4}	2.6×10^{-4}	1.7×10^{-4}
CuTOTP-NHCOC4 Mixed Phase	4.2×10^{-5}	9.2×10^{-5}	1.1×10^{-4}
CuTOTP-NHCOC6	2.3×10^{-5}	6.8×10^{-5}	4.8×10^{-5}

3.6.7 Supplementary figures.

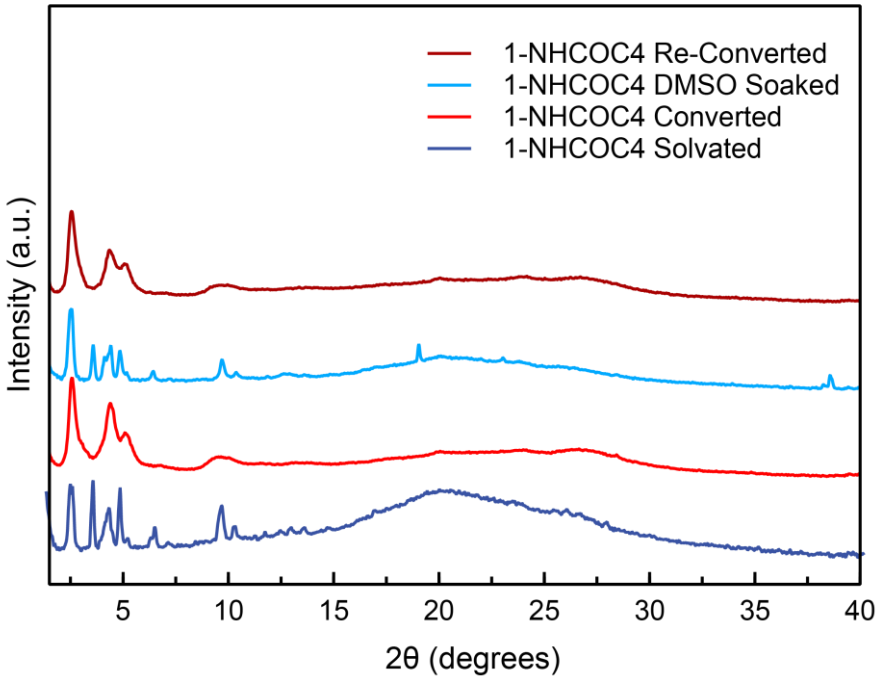

Fig. 3.S1 | PXRDs for the CuTOTP-NHCOC4 macrocycle demonstrating reversible phase transformations depending on presence of DMSO. Samples are initially solvated with multiple phases present, then convert to hexagonal phase with slow removal of DMSO. Samples can then be soaked in DMSO for several hours, whereupon multiple phases return. Conversion back to hexagonal phase is once again possible with slow drying of DMSO.

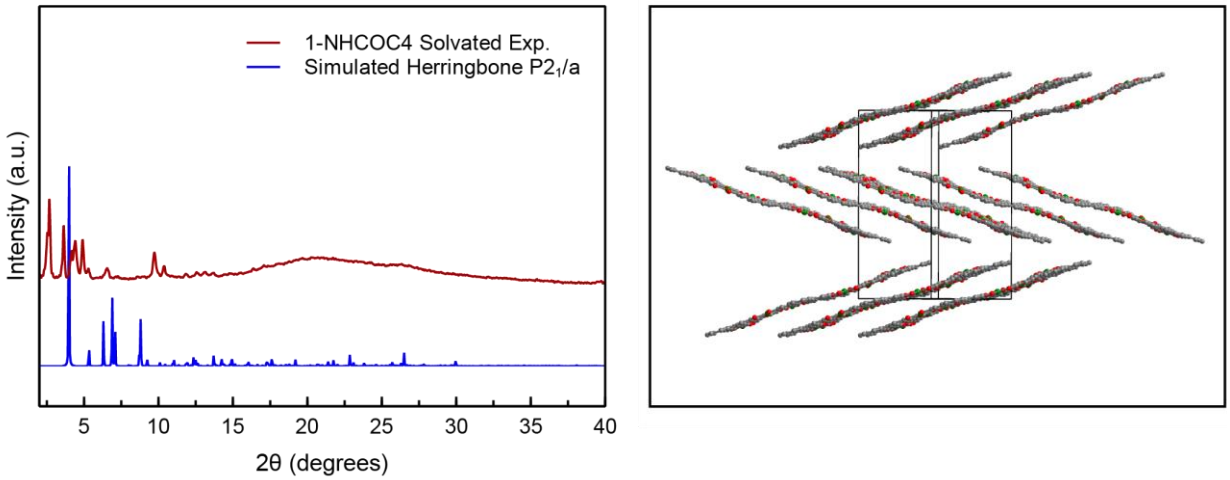

Fig. 3.S2 | Simulated PXRD and structural model of CuTOTP-NHCOC1 in herringbone packing. Structures were optimized using the Forcite module in Materials Studio, assuming a $P2_1/a$ space group. Unit cell dimensions a = 17.28 Å, b = 24.93 Å, and c = 25.62 Å. All side chains omitted in structural model image for clarity.

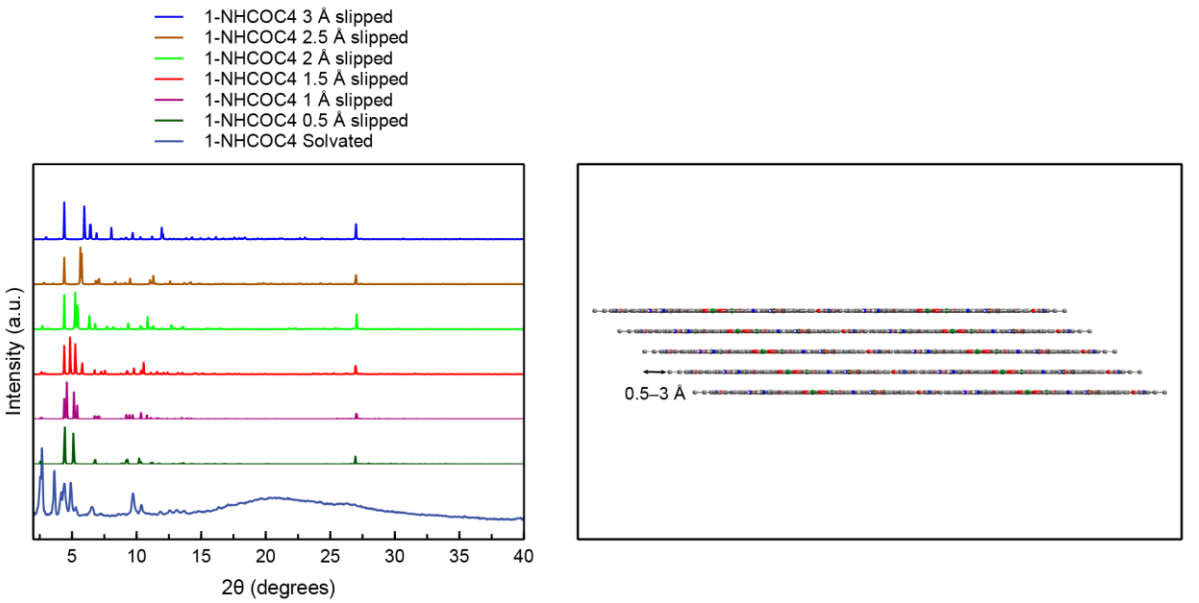

Fig. 3.S3 | PXRD of as-synthesized CuTOTP-NHCOC4**.** Other XRDs are calculated patterns from slipping the eclipsed P6/m pattern by 0.5, 1, 1.5, 2, 2.5, or 3 Å into the C2/m space group.

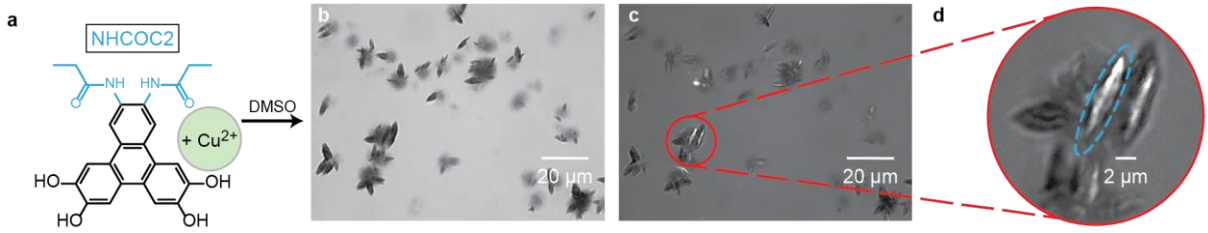

Fig. 3.S4 | Optical microscopy for the CuTOTP-NHCOC2 macrocycle. (a) schematic of synthesis for H_4TOTP-NHCOC2 ligand with Cu^{2+} in DMSO. (b) Bright field optical microscope image of CuTOTP-NHCOC2 macrocycle at 100× magnification. Image is a multifocus composite of 26 planes. (c) Polarized optical microscope image of CuTOTP-NHCOC2 macrocycle at 100× magnification. Image is a multifocus composite of 26 planes. (d) Zoom in on one particle with stronger birefringence, blue ellipse added as a guide for the eye.

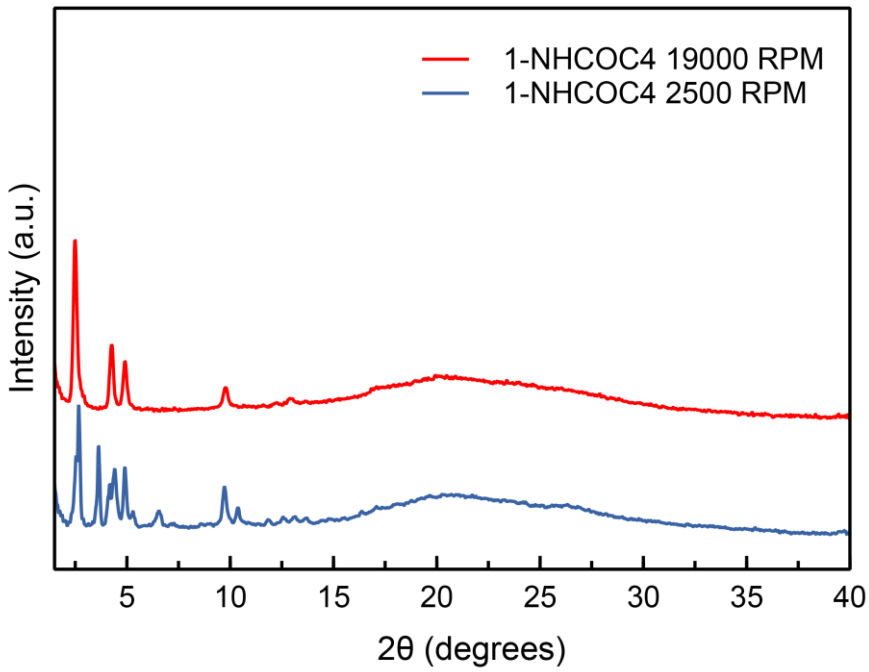

Fig. 3.S5 | PXRDs of CuTOTP-NHCOC4 after two rounds of centrifugation, initially slowly at 2500 RPM. This supernatant is decanted and PXRD is taken for the resulting solvated pellet in blue. The decanted supernatant was then re-centrifuged at 19000 RPM to collect smaller particles. Particles collected during the second round of centrifugation are then filtered and produce the solvated PXRD in red. When only small particles are collected at higher speeds, the first three peaks have a 1:1/√3:1/2 d-spacing ratio indicating a hexagonal structure. This result implies the as-synthesized sample contains multiple phases when solvated.

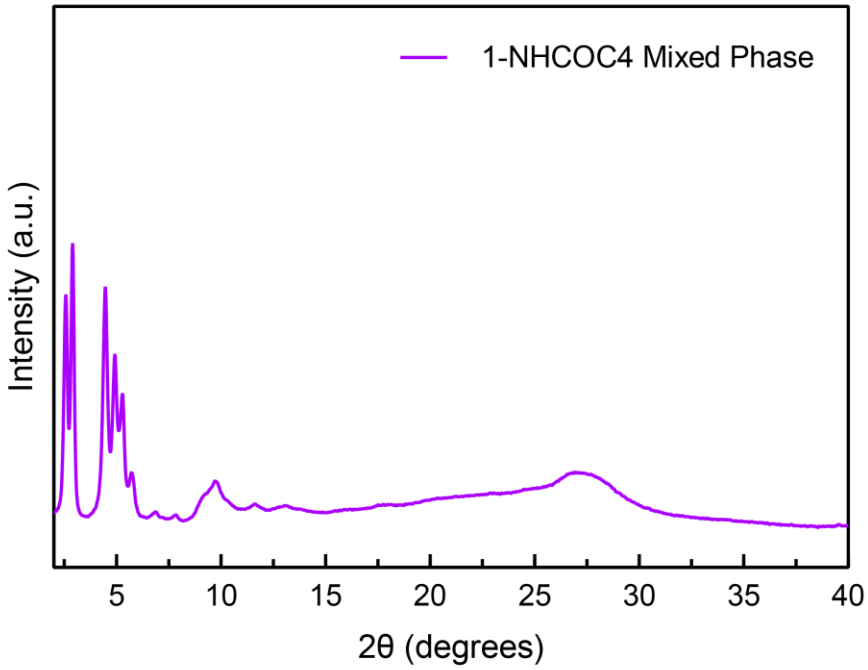

Fig. 3.S6 | PXRD of CuTOTP-NHCOC4 Mixed Phase resulting from drying from DMSO at 40 °C under a stream of flowing N_2.

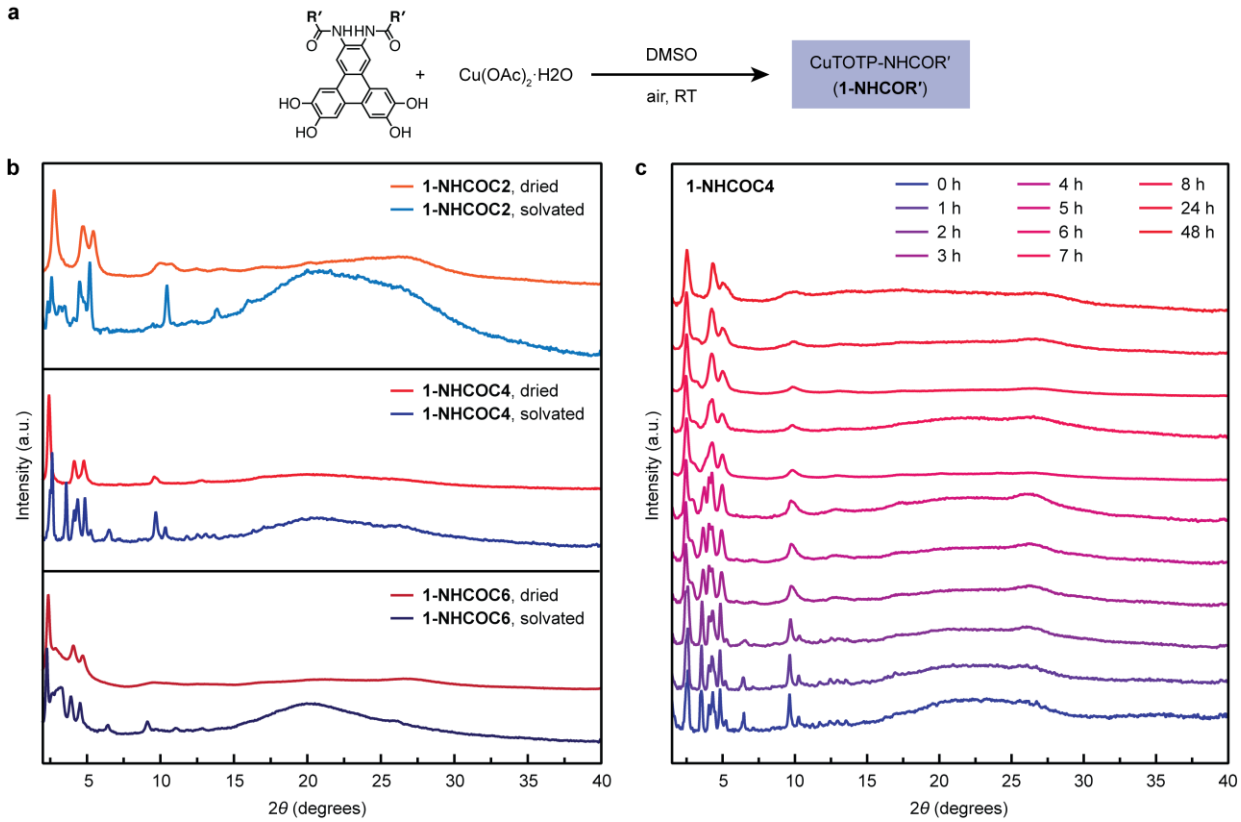

Fig. 3.S7 | (a) Synthesis of CuTOTP-NHCOR′ (**1-NHCOR′**) macrocycles. (b) Powder X-ray diffraction (PXRD) of as-synthesized and dried **1-NHCOC2** (light blue and orange), **1-NHCOC4** (blue and red), and **1-NHCOC6** (dark blue and dark red), respectively. (c) PXRD patterns tracking the phase conversion of the as-synthesized **1-NHCOC4** macrocycle over a period of 48 h.

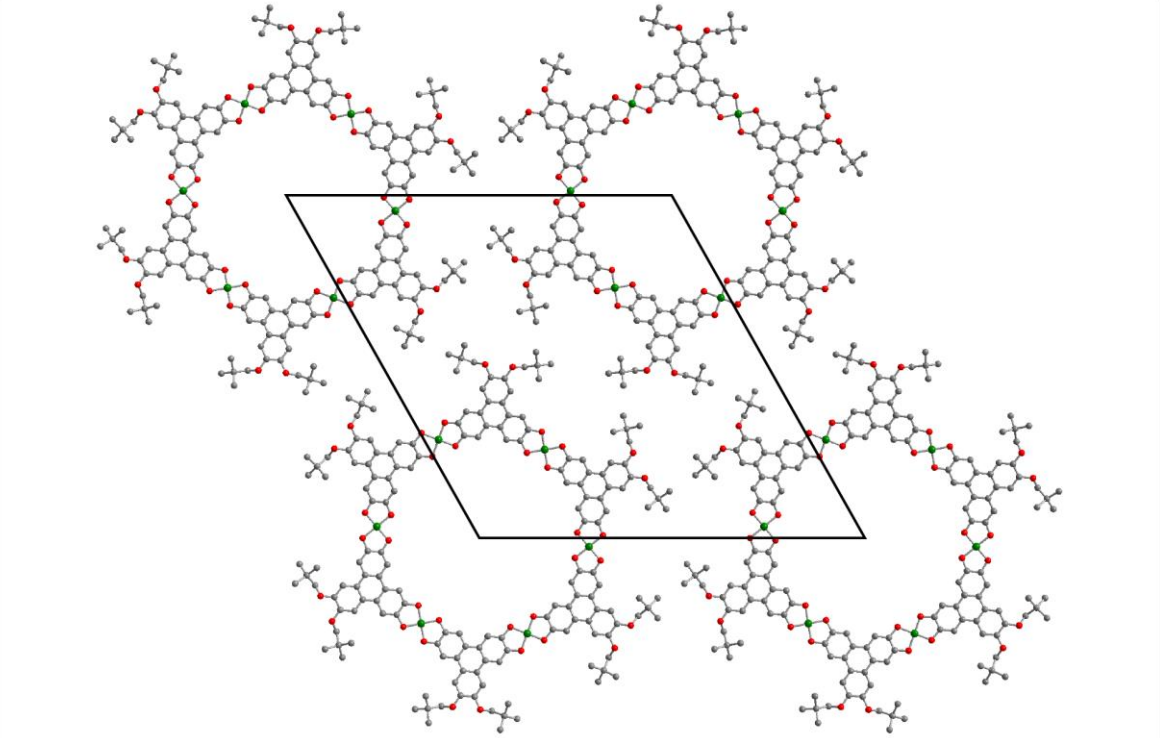

Fig. 3.S8 | Structural model of CuTOTP-OCH_2tBu. Structures were optimized using the Forcite module in Materials Studio, assuming a P6 space group. Unit cell dimensions optimized to match experimental peaks with $a = b = 38.75$ Å, and $c = 3.49$ Å (note: c was allowed to vary, but Forcite module does not account for π–π interactions, so the value is erroneous). All hydrogens bound to carbon omitted for clarity.

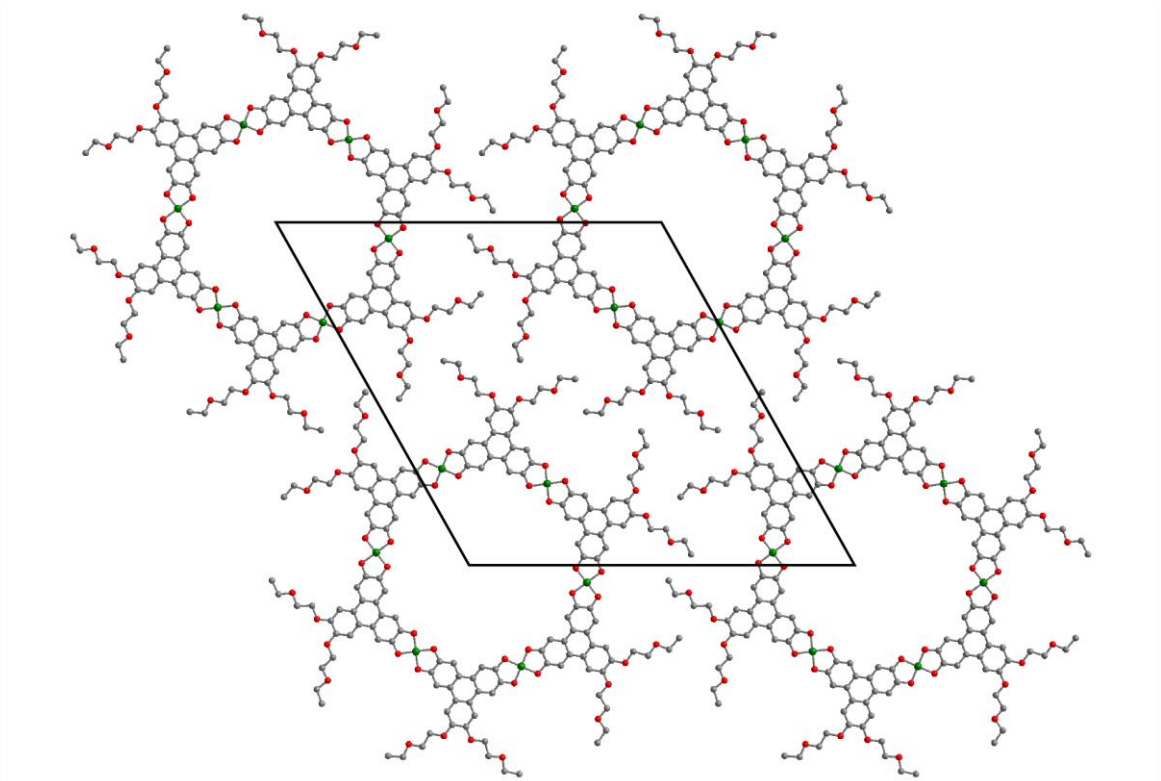

Fig. 3.S9 | Structural model of CuTOTP-eMEG. Structures were optimized using the Forcite module in Materials Studio, assuming a P6/m space group. Unit cell dimensions optimized to match experimental peaks with $a = b = 39.75$ Å, and $c = 3.15$ Å. All hydrogens bound to carbon omitted for clarity.

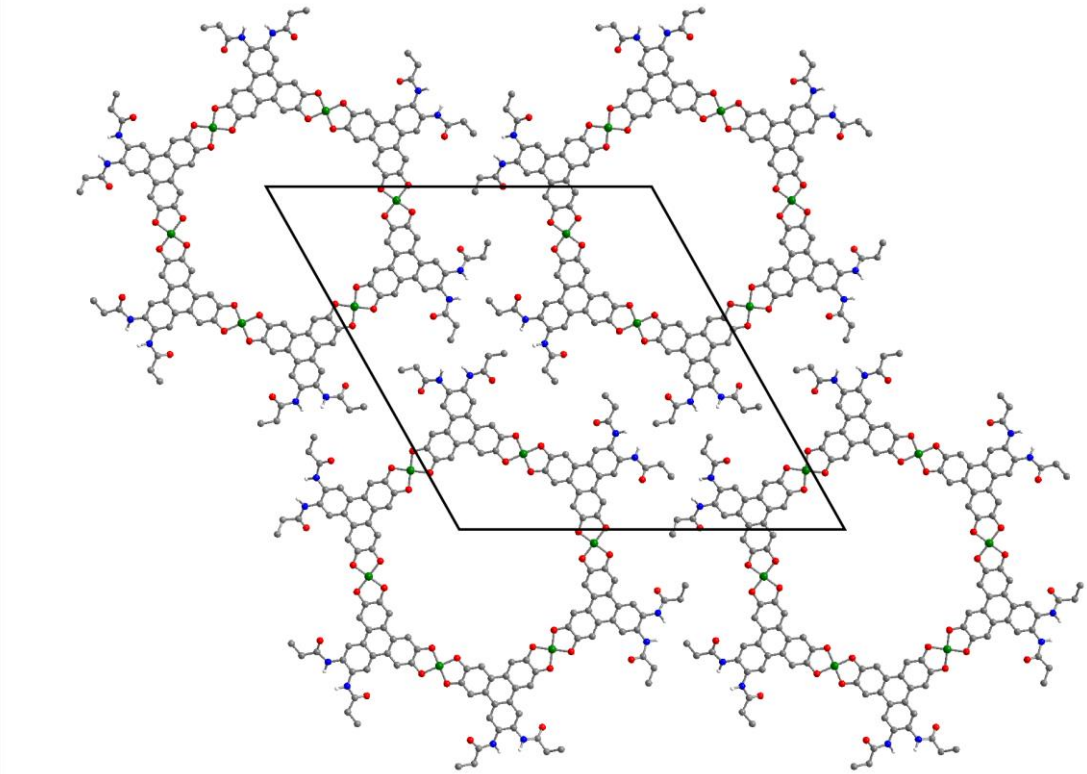

Fig. 3.S10 | Structural model of CuTOTP-NHCOC2. Structures were optimized using the Forcite module in Materials Studio, assuming a P6 space group. Unit cell dimensions optimized to match experimental peaks with $a = b = 37$ Å, and $c = 3.47$ Å (note: c was allowed to vary, but Forcite module does not account for π–π interactions, so the value is erroneous). All hydrogens bound to carbon omitted for clarity.

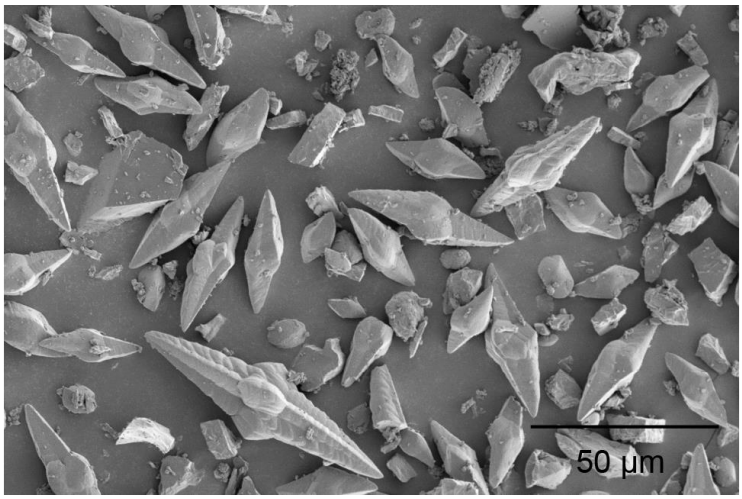

Fig. 3.S11 | Scanning electron microscope (SEM) image of CuTOTP-NHCOC4 showing the irregular octahedral particles. When the sample is dried quickly at 40 °C under a stream of flowing N_2, the particles retain their overall shape.

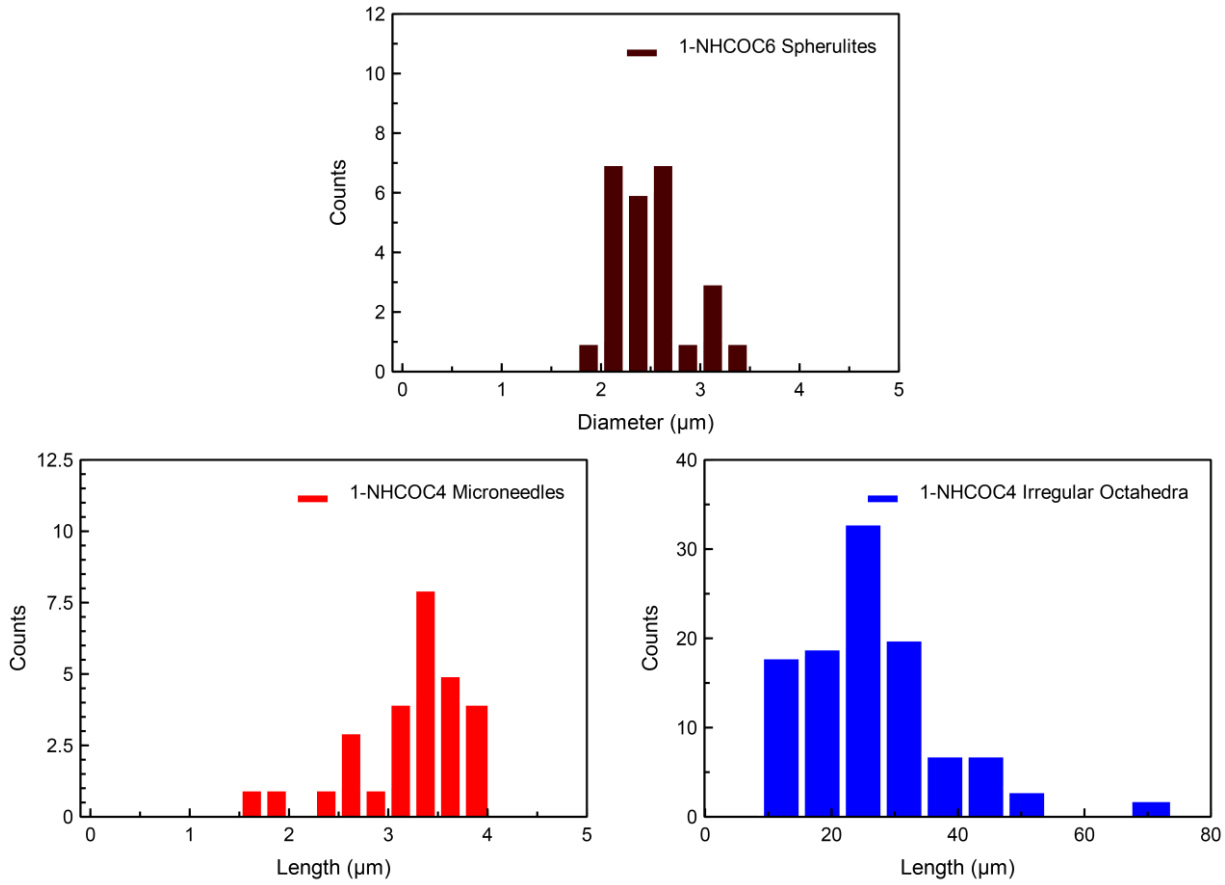

Fig. 3.S12 | Particle size distribution from optical microscopy (bright field) for **1-NHCOC6** (2.0(8) μm). Particle size distribution from optical microscopy (polarized) for **1-NHCOC4** microneedles (6(3) μm). Particle size distribution combining optical microscopy (polarized) and SEM for **1-NHCOC4** irregular octahedra (27(11) μm).

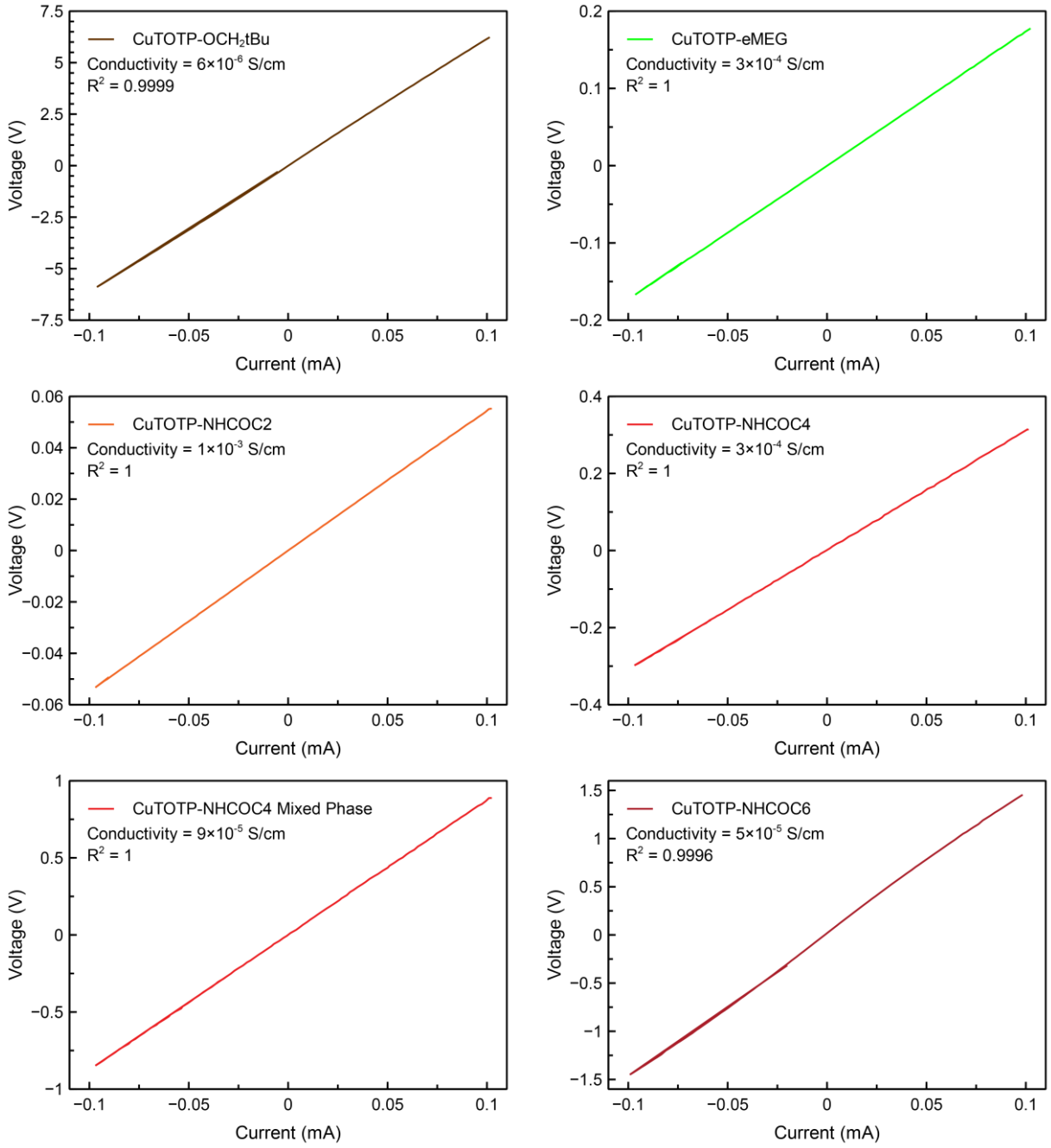

Fig. 3.S13 | Example I-V curves of CuTOTP-R (R = OCH_2tBu, eMEG, NHCOC2, NHCOC4 (hexagonal), NHCOC4 (mixed phase), NHCOC6).

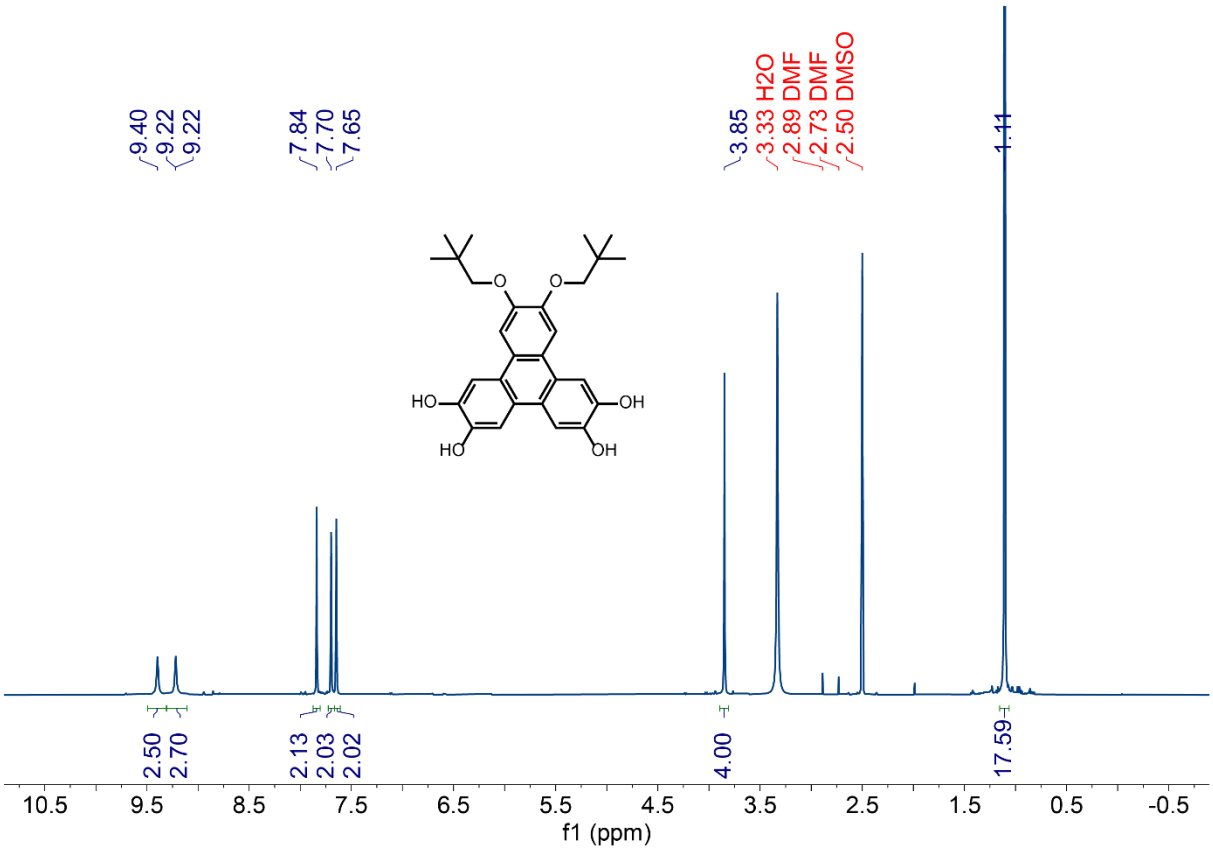

Fig. 3.S14 | The ^{1}H NMR spectrum of **H_4TOTP-OCH$_2$tBu.**

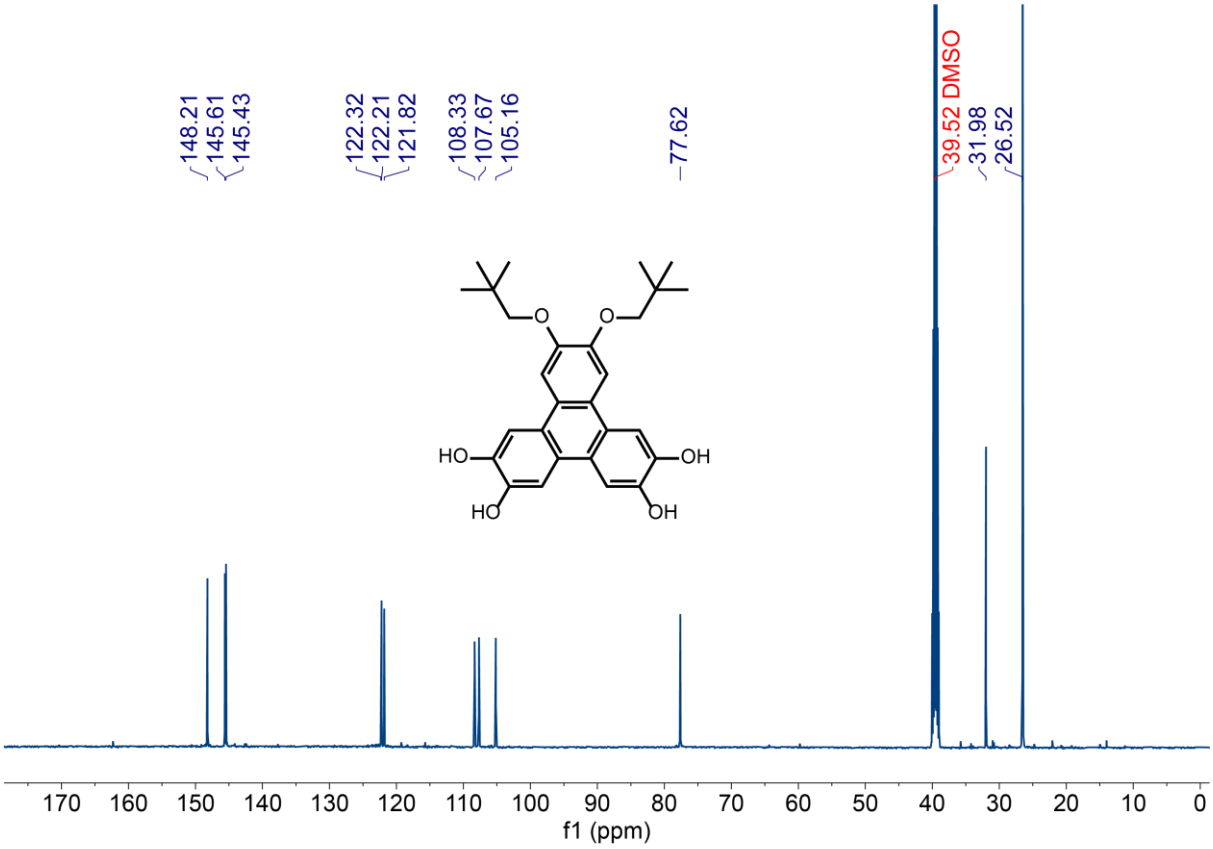

Fig. 3.S15 | The ^{13}C NMR spectrum of **H_4TOTP-OCH_2tBu.**

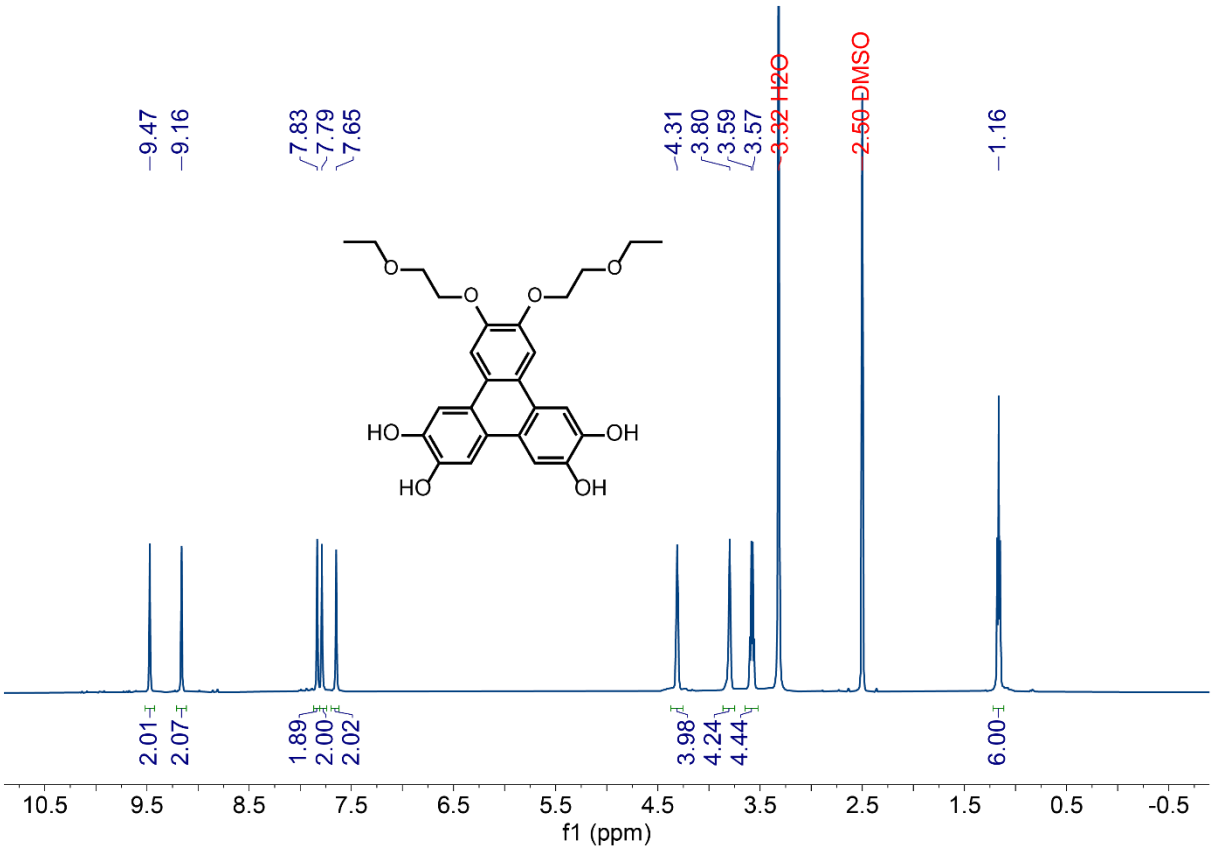

Fig. 3.S16 | The ^{1}H NMR spectrum of **H_4TOTP-eMEG**.

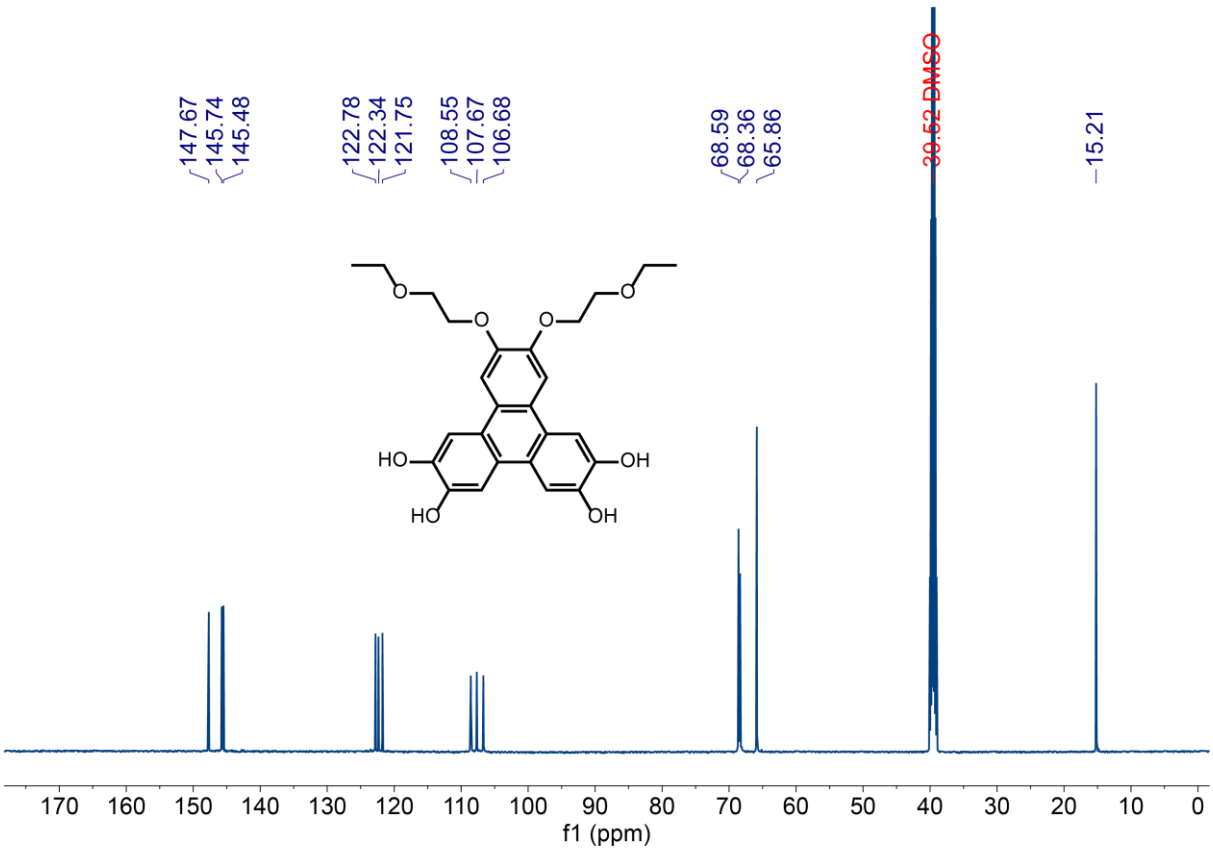

Fig. 3.S17 | The ^{13}C NMR spectrum of **H_4TOTP-eMEG**.

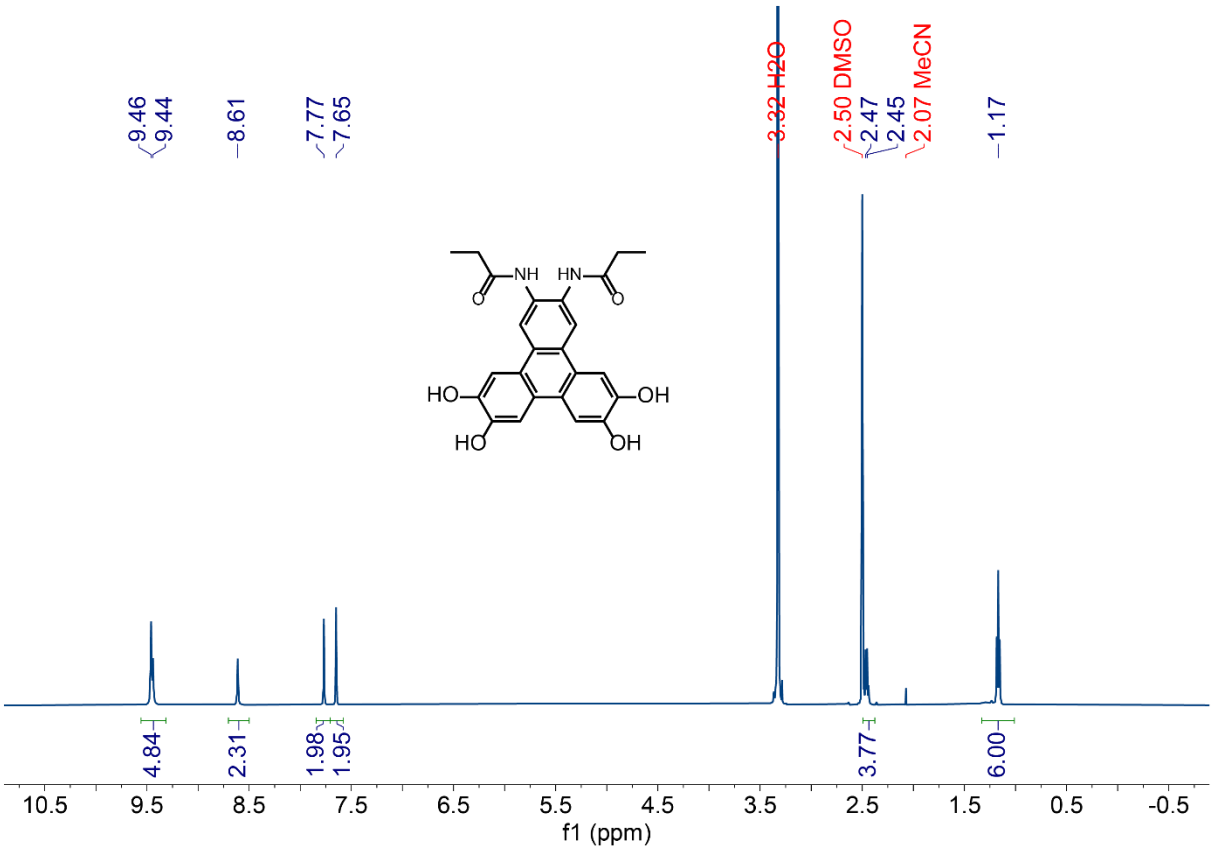

Fig. 3.S18 | The ^{1}H NMR spectrum of **H_4TOTP-NHCOC2**.

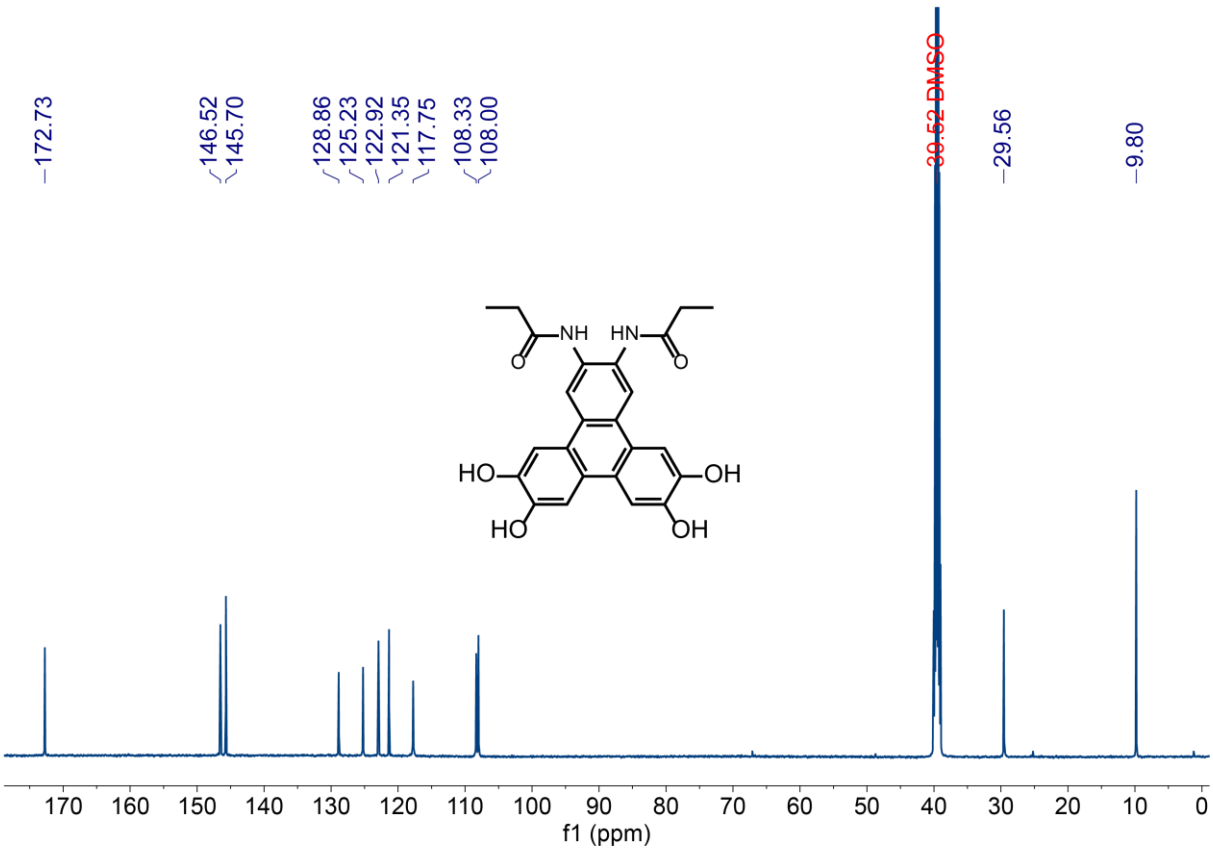

Fig. 3.S19 | The ^{13}C NMR spectrum of **H_4TOTP-NHCOC2**.

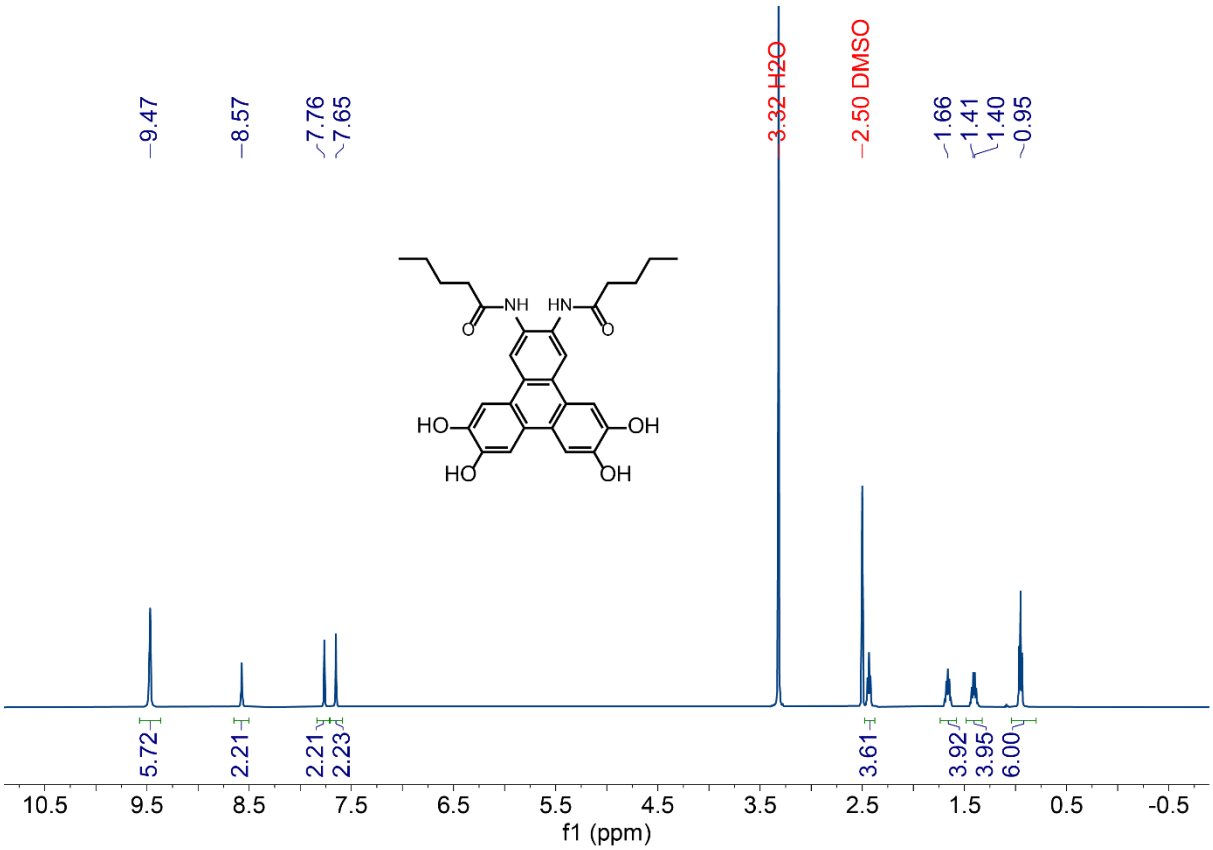

Fig. 3.S20 | The ^{1}H NMR spectrum of **H_4TOTP-NHCOC4**.

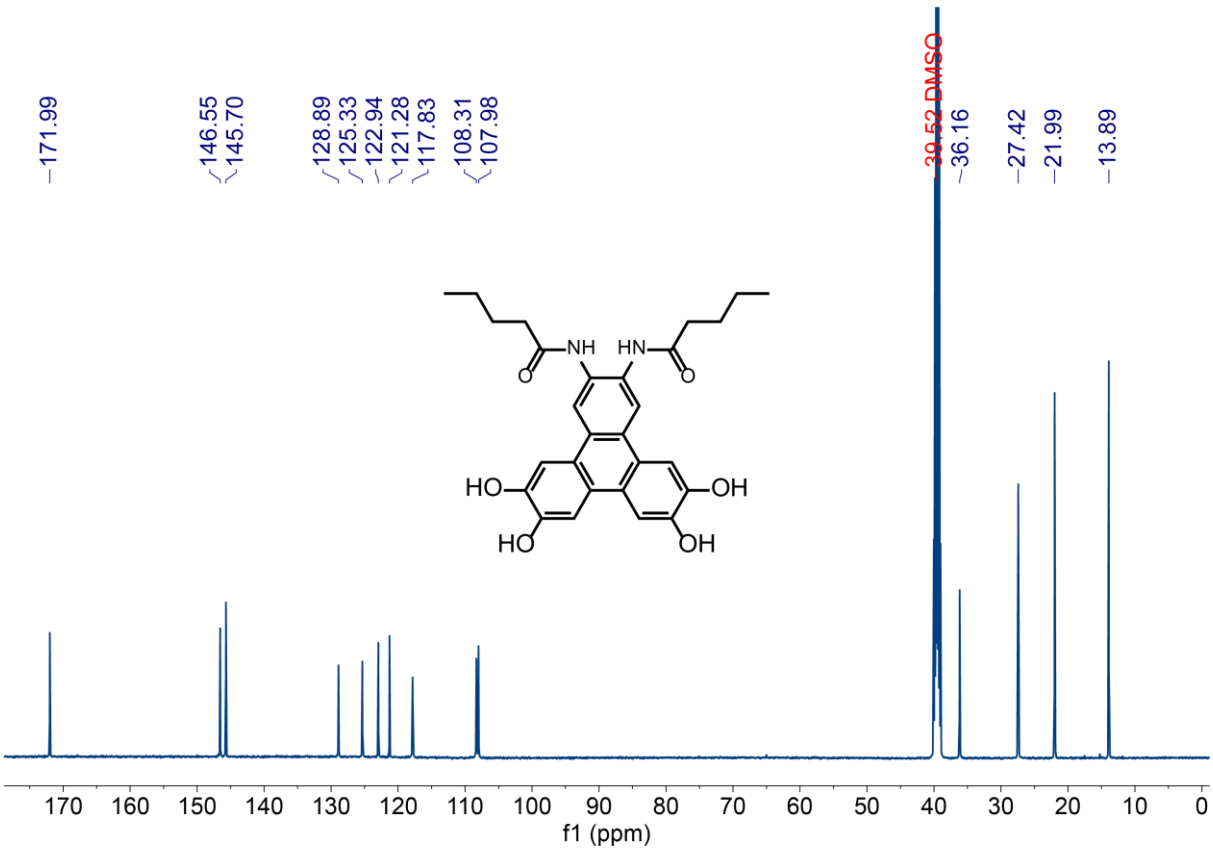

Fig. 3.S21 | The ^{13}C NMR spectrum of **H_4TOTP-NHCOC4**.

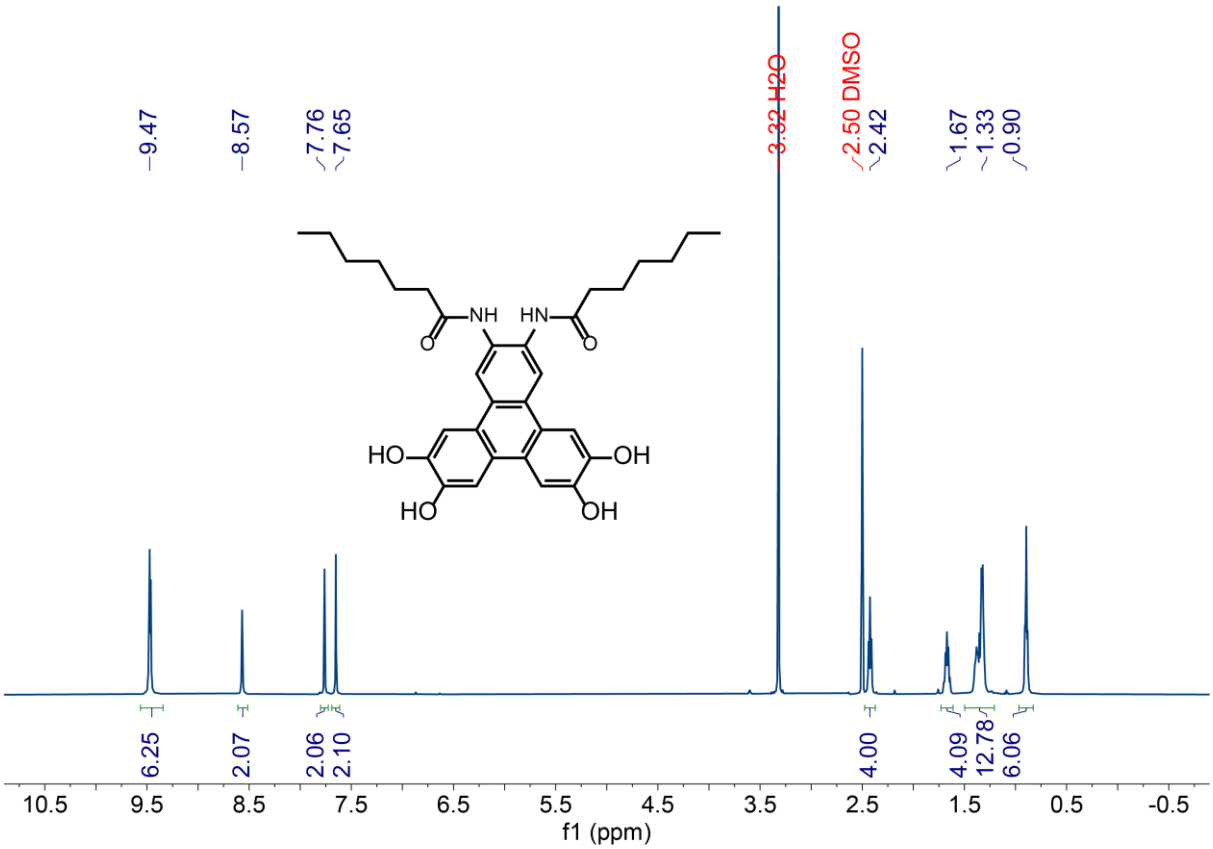

Fig. 3.S22 | The ^{1}H NMR spectrum of **H_4TOTP-NHCOC6**.

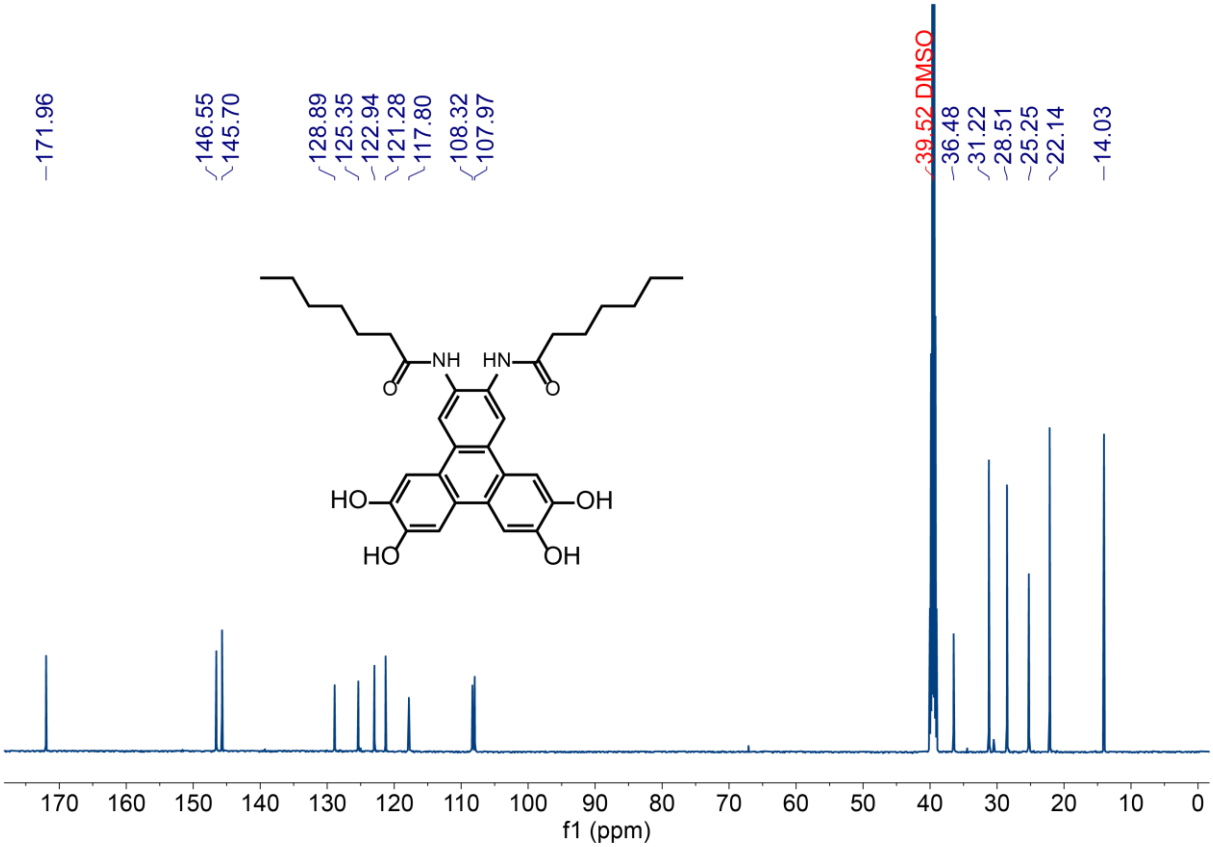

Fig. 3.S23 | The ^{13}C NMR spectrum of **H_4TOTP-NHCOC6**.

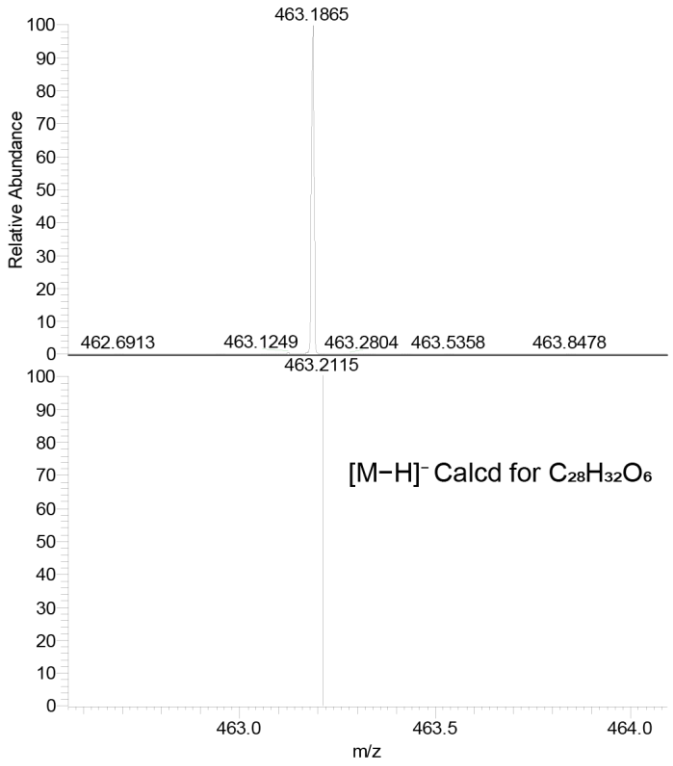

Fig. 3.S24 | Experimental (top) versus simulated (bottom) high-resolution ESI mass spectrum for H_4TOTP-OCH_2tBu $[M-H]^-$.

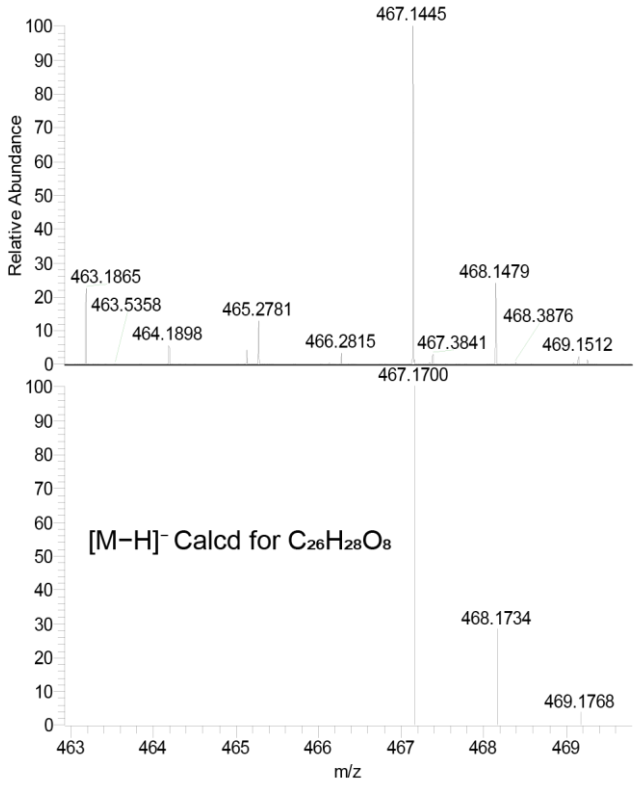

Fig. 3.S25 | Experimental (top) versus simulated (bottom) high-resolution ESI mass spectrum for H_4TOTP-eMEG $[M-H]^-$.

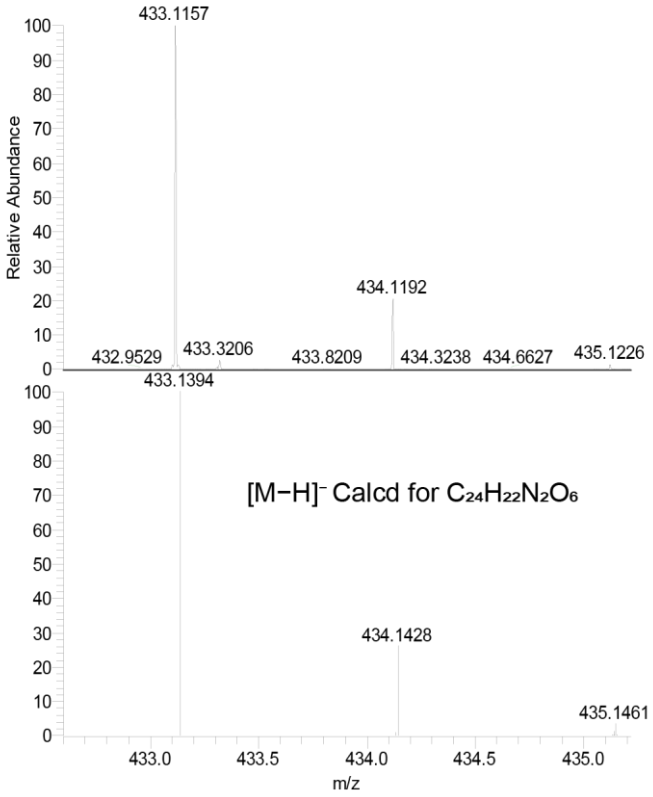

Fig. 3.S26 | Experimental (top) versus simulated (bottom) high-resolution ESI mass spectrum for H_4TOTP-NHCOC2 $[M-H]^-$.

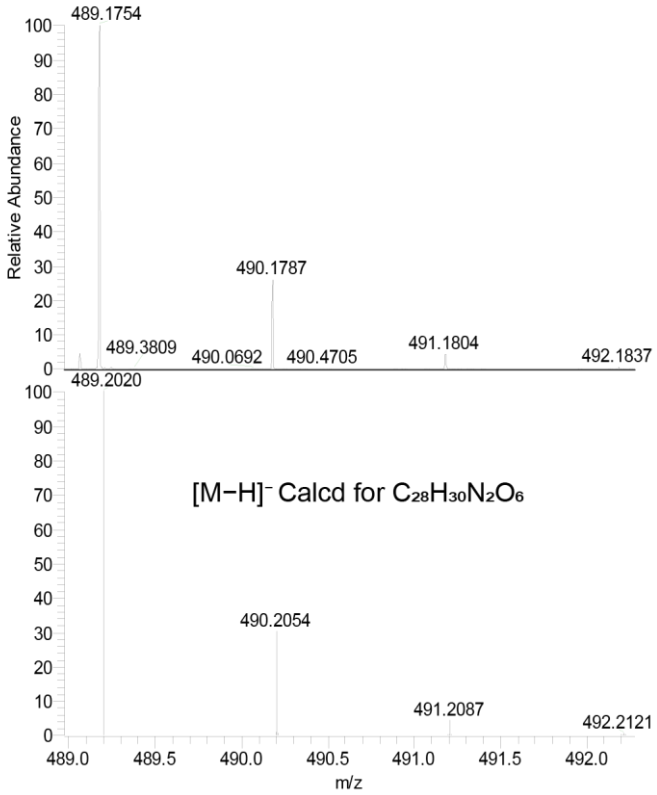

Fig. 3.S27 | Experimental (top) versus simulated (bottom) high-resolution ESI mass spectrum for H_4TOTP-NHCOC4 $[M-H]^-$.

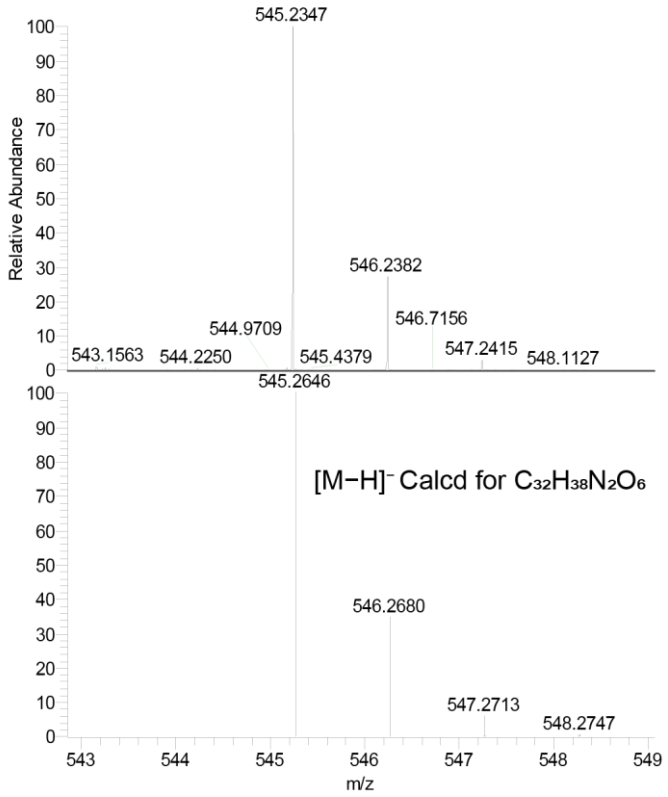

Fig. 3.S28 | Experimental (top) versus simulated (bottom) high-resolution ESI mass spectrum for H_4TOTP-NHCOC6 $[M-H]^-$.

3.6.8 References.

(1) Zasada, L. B.; Guio, L.; Kamin, A. A.; Dhakal, D.; Monahan, M.; Seidler, G. T.; Luscombe, C. K.; Xiao, D. J. Conjugated Metal–Organic Macrocycles: Synthesis, Characterization, and Electrical Conductivity. *J. Am. Chem. Soc.* **2022**, *144* (10), 4515–4521. https://doi.org/10.1021/jacs.1c12596.

(2) Tuten, B. T.; De Keer, L.; Wiedbrauk, S.; Van Steenberge, P. H. M.; D'hooge, D. R.; Barner-Kowollik, C. Visible-Light-Induced Passerini Multicomponent Polymerization. *Angewandte Chemie International Edition* **2019**, *58* (17), 5672–5676. https://doi.org/10.1002/anie.201901506.

(3) Fidan, I.; Luneau, D.; Ahsen, V.; Hirel, C. Revisiting the Ullman's Radical Chemistry for Phthalocyanine Derivatives. *Chemistry – A European Journal* **2018**, *24* (20), 5359–5365. https://doi.org/10.1002/chem.201704903.

(4) Smith, M. K.; Powers-Riggs, N. E.; Northrop, B. H. Rational Synthesis of Bis(Hexyloxy)-Tetra(Hydroxy)-Triphenylenes and Their Derivatives. *RSC Adv.* **2014**, *4* (72), 38281–38292. https://doi.org/10.1039/C4RA06503D.

(5) Garrido-Barros, P.; Gimbert-Suriñach, C.; Moonshiram, D.; Picón, A.; Monge, P.; Batista, V. S.; Llobet, A. Electronic π-Delocalization Boosts Catalytic Water Oxidation by Cu(II) Molecular Catalysts Heterogenized on Graphene Sheets. *J. Am. Chem. Soc.* **2017**, *139* (37), 12907–12910. https://doi.org/10.1021/jacs.7b06828.

(6) Darago, L. E.; Aubrey, M. L.; Yu, C. J.; Gonzalez, M. I.; Long, J. R. Electronic Conductivity, Ferrimagnetic Ordering, and Reductive Insertion Mediated by Organic Mixed-Valence in a Ferric Semiquinoid Metal–Organic Framework. *J. Am. Chem. Soc.* **2015**, *137* (50), 15703–15711. https://doi.org/10.1021/jacs.5b10385.

Appendix A: Field effect transistors (FETs) and opportunities for optimization

A1. Introduction

Organic field effect transistors (OFETs) based on organic semiconductors have garnered widespread interest for environmental sensing and health monitoring[1–3] owing to their typically good film-forming properties, flexibility, and chemical and electronic tunability. The vast majority of devices made so far are unipolar devices, meaning they either conduct electrons or holes as n- or p-type semiconductors respectively.[4] For more complex data processing capabilities, a higher density of transistors is required, which can be difficult to achieve given current fabrication methods.[5,6] Typical transistors give a binary "ON" or "OFF" state, but the number of logic states can be increased using ambipolar devices which conduct both electrons and holes, creating one "OFF" state and two distinct "ON" states, thereby increasing the number of stable states and creating a ternary transistor.[7] As shown in Chapter 2, the CuTOTP-OC18 metal–organic macrocycles demonstrate ambipolar behavior and are exciting for new applications given their high degree of chemical tunability. To realize these applications, charge mobilities must be improved to be more competitive with existing semiconducting polymers which can have electron and hole mobilities as high as 3.0 $cm^2\ V^{-1}\ s^{-1}$ for pentacene.[8] These values are obtained by alignment of pentacene in the transistor channel, and a similar alignment of the macrocyclic core may be achievable to greatly improve mobilities.

OFETs are generally composed of a gate electrode layer, dielectric layer, semiconductor layer, and deposited source and drain electrodes (Figure A1). Switching into the "ON" state is modulated by applying a voltage to the gate, generating an electric field which injects charge carriers into the channel. By applying a gate voltage with a specific polarity, electrons or holes can

Fig. A1 | Diagram of bottom gate top contact architecture organic field-effect transistor (OFET). Gate is typically silicon, dielectric is a siloxane monolayer, semiconductor is the active layer, and source and drain are gold electrodes.

accumulate at the dielectric-semiconductor interface. Externally controlled source and drain electrodes inject charge carriers necessary for accumulation. When no gate voltage is applied, there should be little to no conductance in the semiconductor due to a lack of mobile charge carriers. The so-called "field effect" as applied to organic systems is described beautifully by Mann *et. al.* in their review of organic thin film transistors.[4] The effect is shown in terms of simplified highest occupied molecular orbitals (HOMOs) and lowest unoccupied molecular orbitals (LUMOs) diagrams which are positioned relatively to the Fermi level of the source and drain electrodes. When a positive gate voltage is applied, the semiconductor's LUMO energetically aligns with the conduction band of the source electrode which injects electrons into the empty orbitals. When a positive drain bias is applied, the drain's conduction band is lowered, causing electrons to flow from source to drain. This happens in reverse when a negative gate voltage is applied. The semiconductor's HOMO aligns with the drain electrode and dumps its electrons into the conduction band, thus accumulating mobile holes. Then a negative drain voltage is applied, lowering the conduction band of the source relatively and causing hole transport from source to drain. Thus, control of gate voltage and source and drain voltage are all necessary to achieve the "ON" state for the transistor and measure charge mobility. An ambipolar device simply turns on in both cases, with positive gate and drain voltage, and with negative gate and drain voltage. For a full treatment of the underlying mathematics, please refer to other sources.[3,4,7,9]

A2. Macrocyclic alignment and potential for FET optimization

CuTOTP-OC18 macrocycles were found to have dramatically different self-assembly properties on substrates depending on the solvent and method of deposition. AFM was collected on either a Bruker ICON AFM or Oxford Instruments Cypher ES in soft tapping mode using OTESPA or TAP150Al-G tips purchased from Budget Sensors.

When a solution of CuTOTP-OC18 in chloroform or toluene are spin cast onto silicon wafers with a 300 nm wet thermal oxide layer treated with octadecyltrimethoxysilane (as in the FET fabrication in Chapter 2), no order is observable. Images are taken in tapping mode and phase data is shown in Figure A3, where lighter colored regions are the tip reacting to different chemical

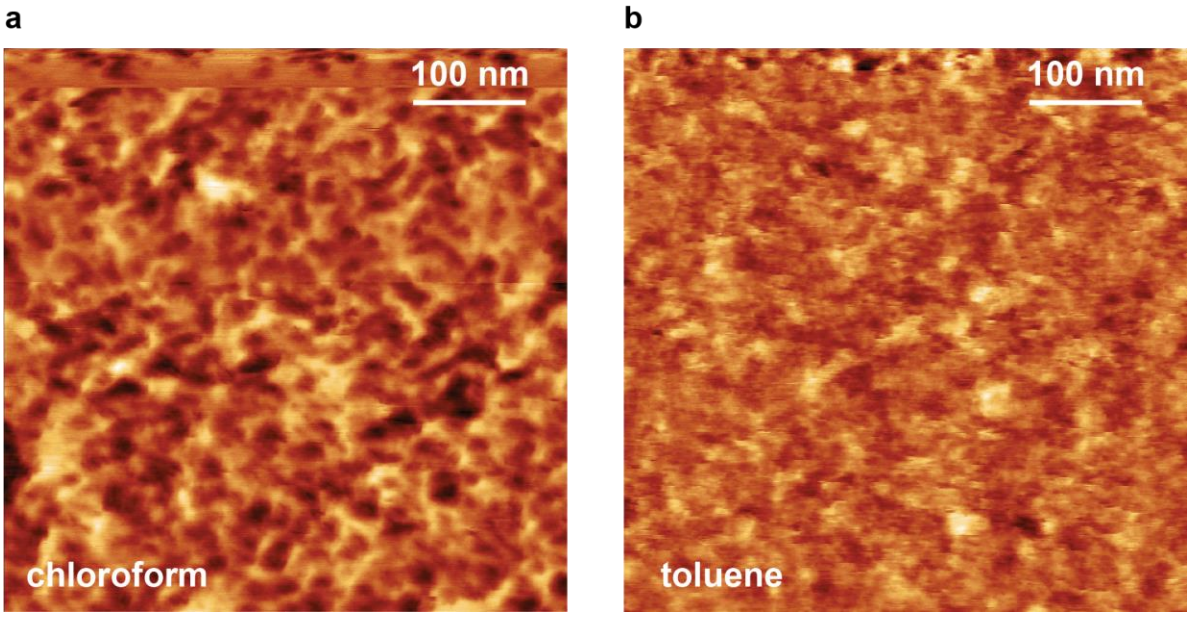

Fig. A2 | AFM Phase images of CuTOTP-OC18 spin cast on octadecyltrimethoxysilane treated Si/SiO_2 wafers. AFM taken in tapping mode. a) spin cast from chloroform at 5 mg mL^{-1}, 2500 RPM for 60 s. b) spin cast from toluene at 5 mg mL^{-1}, 2500 RPM for 60 s. Color changes indicate changes in tip interaction with the surface, but resolution is not good enough to crealy distinguish between the affects of height changes. No well-defined alignment is observed.

functionalities at the surface. At this poor resolution however, it is hard to distinguish between true phase changes and phase changes which are only a reaction to height changes.

Toluene was found to give a higher degree of long range order as compared to chloroform when drop casting onto freshly cleaved mica (Figure A3). In tapping mode with higher resolution, the color changes in phase data show the tip interacting differently with different chemical functionalities on the surface. Lines can be seen distinguishing individual nanotubes of CuTOTP-OC18 macrocycles stacked on the order of hundreds of nanometers. Distinct grain boundaries are more visible in the chloroform case where stacks of macrocycles are terminated by perpendicular

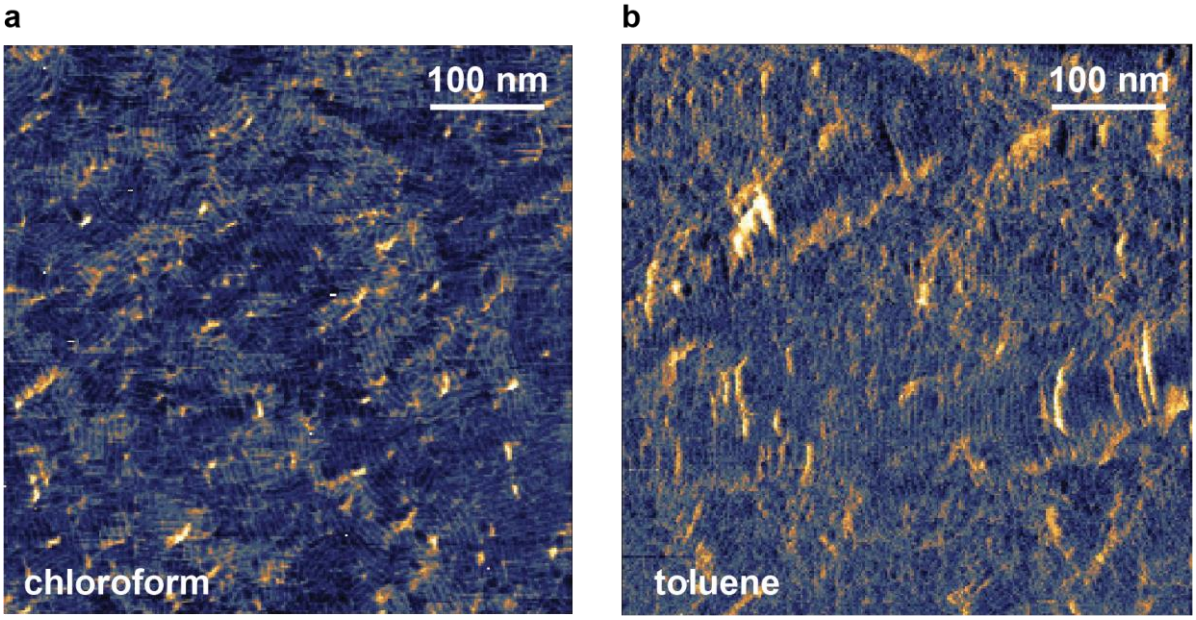

Fig. A3 | AFM Phase images of CuTOTP-OC18 drop cast on freshly cleaved mica and dried overnight before taking AFM in tapping mode. a) drop cast from chloroform, b) drop cast from toluene. Color changes indicate changes in tip interaction with the surface and outline the edges of macrocycles, where light regions correspond to peripheral groups and darker regions correspond to aromatic core. Lines are ~5 nm apart, matching with the unit cell for CuTOTP-OC18.

nanotubes, an effect much less apparent in the case of toluene. These results indicate that slower evaporation methods, higher boiling solvents, and favorable π-interactions can lead to longer range alignment. Future work will explore aligning these macrocycles in the transistor channel to increase charge mobilities.

A3. References

(1) Surya, S. G.; Raval, H. N.; Ahmad, R.; Sonar, P.; Salama, K. N.; Rao, V. R. Organic Field Effect Transistors (OFETs) in Environmental Sensing and Health Monitoring: A Review. *TrAC Trends in Analytical Chemistry* **2019**, *111*, 27–36. https://doi.org/10.1016/j.trac.2018.11.027.

(2) Bao, Z.; Locklin, J. *Organic Field-Effect Transistors*; CRC Press, 2018.

(3) Allard, S.; Forster, M.; Souharce, B.; Thiem, H.; Scherf, U. Organic Semiconductors for Solution-Processable Field-Effect Transistors (OFETs). *Angewandte Chemie International Edition* **2008**, *47* (22), 4070–4098. https://doi.org/10.1002/anie.200701920.

(4) Newman, C. R.; Frisbie, C. D.; da Silva Filho, D. A.; Brédas, J.-L.; Ewbank, P. C.; Mann, K. R. Introduction to Organic Thin Film Transistors and Design of N-Channel Organic Semiconductors. *Chem. Mater.* **2004**, *16* (23), 4436–4451. https://doi.org/10.1021/cm049391x.

(5) Jeon, J.; Kim, M. J.; Shin, G.; Lee, M.; Kim, Y. J.; Kim, B.; Lee, Y.; Cho, J. H.; Lee, S. Functionalized Organic Material Platform for Realization of Ternary Logic Circuit. *ACS Appl. Mater. Interfaces* **2020**, *12* (5), 6119–6126. https://doi.org/10.1021/acsami.9b18772.

(6) Kobashi, K.; Hayakawa, R.; Chikyow, T.; Wakayama, Y. Multi-Valued Logic Circuits Based on Organic Anti-Ambipolar Transistors. *Nano Lett.* **2018**, *18* (7), 4355–4359. https://doi.org/10.1021/acs.nanolett.8b01357.

(7) Ren, Y.; Yang, X.; Zhou, L.; Mao, J.-Y.; Han, S.-T.; Zhou, Y. Recent Advances in Ambipolar Transistors for Functional Applications. *Advanced Functional Materials* **2019**, *29* (40), 1902105. https://doi.org/10.1002/adfm.201902105.

(8) Chiu, L.-Y.; Cheng, H.-L.; Wang, H.-Y.; Chou, W.-Y.; Tang, F.-C. Manipulating the Ambipolar Characteristics of Pentacene-Based Field-Effect Transistors. *J. Mater. Chem. C* **2014**, *2* (10), 1823–1829. https://doi.org/10.1039/C3TC31546K.

(9) Wöll, C. *Physical and Chemical Aspects of Organic Electronics: From Fundamentals to Functioning Devices*; John Wiley & Sons, 2009.